

**Nearshore Bathymetry
derived from Video Imagery**

*Morfologie van de Brandingszone
afgeleid uit Video Waarnemingen*

Front cover: Intertidal morphology Noordwijk, The Netherlands
Photo by Irv Elshoff

Nearshore Bathymetry
derived from Video Imagery

PROEFSCHRIFT

ter verkrijging van de graad van doctor
aan de Technische Universiteit Delft,
op gezag van de Rector Magnificus prof.dr.ir. J.T. Fokkema,
voorzitter van het College voor Promoties,
in het openbaar te verdedigen

op dinsdag 25 november 2003 te 15.30 uur

door

Stefan Gert Jan AARNINKHOF
civiel ingenieur
geboren te Hengelo (Overijssel)

Dit proefschrift is goedgekeurd door de promotor:

Prof.dr.ir. M.J.F. Stive

Samenstelling promotiecommissie:

Rector Magnificus	voorzitter
Prof.dr.ir. M.J.F. Stive	Technische Universiteit Delft, promotor
Prof.dr. R.A. Holman	Oregon State University (Verenigde Staten)
Prof.dr. D.A. Huntley	University of Plymouth (Groot Brittannië)
Dr. B.G. Ruessink	Universiteit Utrecht
Dr.ir. J.A. Roelvink	Technische Universiteit Delft
Prof.dr.ir. J.A. Battjes	Technische Universiteit Delft
Prof.dr.ir. H.J. de Vriend	Technische Universiteit Delft

Dr. B.G. Ruessink heeft als begeleider in belangrijke mate bijgedragen aan de totstandkoming van dit proefschrift.

Published and distributed by: DUP Science

DUP Science is an imprint of
Delft University Press
P.O. Box 98, 2600 M.G. Delft
The Netherlands
Telephone: +31 15 27 85 678
Telefax: +31 15 27 85 706
Email: info@library.tudelft.nl

ISBN 90-407-2439-3

Copyright © 2003 by Stefan Aarninkhof

All rights reserved. No part of the material protected by this copyright notice may be reproduced or utilized in any form or by any means, electronic or mechanical, including photocopying, recording or by any information storage and retrieval system, without written permission from the publisher: Delft University Press

Printed in The Netherlands

Abstract

The nearshore zone, extending from the beach to water depths of about 10 meters, is of significant societal importance. A variety of functions, including the protection of the hinterland against flooding, accommodation of coastal communities, beach recreation and nature conservation, demand a careful policy to manage the coastal zone. Nearshore morphology is highly dynamic at spatiotemporal scales of hours to decades and meters to tens of kilometers, which has attracted significant research interest. It thus appears that the availability of cost-efficient methods to quantify nearshore bathymetry with high resolution in time and space would be of great value to both scientists and coastal managers.

Traditional, in-situ survey methods involving the use of ships, amphibious vehicles or jet skis provide excellent data but require major logistical commitments and often lack spatiotemporal resolution to resolve processes of interest. However, many nearshore processes have a visible signature at the sea surface, which can be monitored remotely. While perhaps of lower accuracy, remote sensing techniques offer the potential for cost-efficient, long-term data collection with high resolution in time and space. With the advent of digital imaging technology, shore-based video techniques like the advanced ARGUS system developed at Oregon State University enable the monitoring of nearshore bathymetry at spatiotemporal scales of direct management and research interest (meters-kilometers and hours-years).

Being an indirect measurement, the key issue for successful use of shore-based video monitoring techniques is the quantitative interpretation of remotely sensed information in terms of relevant hydrodynamic and morphological parameters. Coastal managers and scientists show a particular interest in the quantification of nearshore bathymetry. It is in this context that this work aims to develop and validate two complementary methods to derive intertidal and subtidal bathymetry from shore-based video imagery, and to assess the utility of these techniques for coastal management and science.

Quantification of intertidal beach bathymetry

The Intertidal Beach Mapper (IBM) determines the three-dimensional beach surface between the low-tide and high-tide shoreline contours by mapping a series of beach contours, sampled throughout a tidal cycle. IBM delineates a shoreline feature from time-averaged video imagery on the basis of the visual contrast between the sub-aerial and sub-aqueous parts of the beach. The corresponding shoreline elevation is estimated from the tide and wave conditions at the time of image collection. IBM necessarily operates on individual images, owing to the wide variety of image characteristics induced by variable hydrodynamic and atmospheric conditions at different ARGUS sites worldwide. The new method was found to be robust, generic, flexible in use and capable of resolving three-dimensional morphological features including emerging intertidal bars.

Validation of IBM against a data set of GPS-surveyed shorelines at Egmond has shown that mean vertical deviations resulting from the shoreline detection technique increase with increasing distance from the video station; deviations induced by model estimates of the corresponding shoreline elevation are relatively constant alongshore. The overall

mean vertical deviation is less than 15 cm along 85% of the 2 km study region, which corresponds to a horizontal offset of 6 m. The scatter of overall model deviations (15-20 cm) is dominated by uncertainties resulting from the shoreline detection model. Model application at three distinctive field sites confirms IBM's reasonable applicability and performance over a wide range of hydrodynamic and atmospheric conditions.

Quantification of subtidal beach bathymetry

The Subtidal Beach Mapper (SBM) quantifies surf zone bathymetry through assimilation of video-observed and model-predicted patterns of wave dissipation. SBM samples time-averaged video intensities along a cross-shore array, excludes poor-quality data and interprets the resulting intensity pattern in terms of a wave dissipation parameter. The video-derived measure of wave dissipation is compared to the corresponding model-predicted dissipation, obtained from running a common wave transformation model across a recent beach profile which is either surveyed or determined from a previous image. Updating of bathymetry is achieved by raising the bottom elevation in areas where the measured dissipation rate exceeds the computed dissipation and vice versa. Since the model includes video data with high resolution in time, it allows for nearly continuous monitoring of surf zone bathymetry. Synthetic model tests have demonstrated the applicability of SBM over a wide range of morphological configurations.

Validation of SBM along two cross-shore Egmond arrays spacing approximately 1400 m alongshore has demonstrated the model's capability to reproduce the dominant morphological changes during the first year after placing a shoreface nourishment, including the shoreward migration of the outer bar and the net accretion of sand in the nearshore part of the surf zone. The *rms* error of the vertical deviations along the entire beach profile typically amounts to 40 cm for both arrays. Marginal deviations in the order of 10 to 20 cm are found at the seaward face of the bars, which increase up to 20 to 40 cm near the bar crest. Maximum deviations up to 80 cm are found in the trough region, owing to lack of wave dissipation information. The accretion of sediment in the shallow surf zone is underestimated. The analysis of SBM sensitivity to variable parameter settings has shown that model performance is strongly governed by the user-specified time scale of profile adjustment.

The utility of IBM and SBM for coastal management and science

The availability of generically applicable, accurate and robust video interpretation models *in itself* does not guarantee the utility of video-based monitoring techniques. Useful video-based monitoring techniques also need to provide quantitative state information of direct end-users relevance. An established basic frame of reference for policy development explicitly shows the roles of operational objectives and quantitative coastal state information (or Coastal State Indicators, CSIs) in relation to decision making in the field of Coastal Zone Management (CZM). The utility of video-based monitoring techniques for coastal management is governed by their capability to quantitatively assess time series of CSIs.

The application of SBM for the monitoring of a combined beach and shoreface nour-

ishment at Egmond has resulted in high-resolution time series of the Momentary Coastline Indicator, which plays a central role in the field of Dutch CZM, and the bar crest elevation, which may be an additional measure for coastal safety. The utility of the model for coastal management directly appears from its capability to quantify the Momentary Coastline Indicator, provided that SBM-based estimates are sufficiently accurate. At the moment, CZM procedures to evaluate coastal safety do not account for an operational objective involving the CSI bar crest elevation. IBM-derived intertidal bathymetrical maps have enabled the quantification of time series of low-tide and high-tide beach width, as well as intertidal volumetric changes. To assess the utility of these CSIs in direct support of CZM, it is necessary to demonstrate that CSIs correlate to variations in the Momentary Coastline Indicator so that they contribute to an established operational objective. Alternatively, CSIs should address additional operational objectives for smaller-scale coastal variability, driven by public and economic demands on beach recreation.

The scientific utility of video-derived coastal state information is particularly revealed by its contribution to studies involving model improvement and data-model integration. Detailed observations of the evolution of morphological parameters like shoreline location, intertidal beach volume and bar crest elevation provide enhanced opportunities for improvement and validation of process-based models and enable development of sophisticated data-driven model concepts (including neural networks) to describe coastal morphodynamics. The use of video-derived morphological parameters for model improvement and data-model integration purposes is expected to be one of the focal points of ARGUS-based research in the nearby future.

In summary, it is concluded that the ARGUS video technique provides unique opportunities for cost-efficient, synoptic and long-term monitoring of coastal environments at spatiotemporal scales of meters to kilometers and days to years. In Egmond, this was particularly observed from a remarkable spatial coherence of morphological changes during the first and second year after implementation of a combined beach and shoreface nourishment, showing an unexpected, highly persistent shoreline perturbation immediately north of the light house. Traditional survey techniques do not easily account for these smaller scales. With local beach and shoreface nourishments becoming the most important measure for coastal interventions, the importance of smaller-scale CSIs within the field of CZM is expected to increase. It is a challenge for both coastal managers and scientists to derive appropriate quantitative state information from ARGUS video imagery and to facilitate a sound embedding of this information in policy development cycles.

Samenvatting

De kustzone van het duin tot een waterdiepte van ongeveer 10 meter vertegenwoordigt een grote maatschappelijke waarde. De zone biedt ruimte voor een breed scala aan functies, waaronder de bescherming van het achterland tegen overstromingen, huisvesting, recreatie en natuur. Duurzaam behoud van deze functies stelt hoge eisen aan het beheer van de kustzone. De zone wordt tevens gekarakteriseerd door grote morfologische veranderingen op tijdschalen van uren tot decennia en over afstanden van meters tot tientallen kilometers. Van oudsher heeft een belangrijk deel van het wetenschappelijk kustonderzoek zich gericht op de beschrijving van deze morfodynamiek. Het blijkt dus dat zowel kustbeheerders als kustonderzoekers belang hechten aan het monitoren van het kuststelsel en derhalve baat zouden hebben bij de beschikbaarheid van goedkope, nauwkeurige technieken om de morfologie van de brandingszone te meten, met een hoge resolutie in tijd en ruimte.

Traditionele *in situ* meettechnieken, gebaseerd op het gebruik van schepen, amfibische voertuigen of jet-skis, leveren uitstekende data, maar gaan gepaard met grote operationele en logistieke inspanningen. Daarnaast is hun resolutie in tijd en ruimte veelal onvoldoende voor het monitoren van kleinschalige kustprocessen. Echter, het geval wil dat veel kustprocessen direct of indirect waarneembaar zijn aan het wateroppervlak. Dit opent de weg voor de toepassing van remote sensing technieken. Hoewel de nauwkeurigheid van remote sensing technieken wellicht minder is dan die van *in situ* metingen, bieden ze de mogelijkheid voor het inwinnen van langetermijn datasets met een hoge resolutie in tijd en ruimte, tegen lage kosten. Voor het monitoren van morfologische veranderingen in de brandingszone kan gebruik gemaakt worden van volautomatische videot technieken, zoals het geavanceerde ARGUS videosysteem ontwikkeld door Oregon State University.

Remote sensing technieken leveren per definitie een indirecte meting. Voor het succesvol toepassen van video monitoring technieken ligt de crux dan ook in de kwantitatieve vertaalslag van remote sensing informatie naar relevante hydrodynamische en morfologische parameters, zoals stroomsnelheden of bodemligging. Kustbeheerders en kustonderzoekers hechten met name aan het meten van de bodemligging in de brandingszone. Om die reden is in het kader van dit werk een tweetal complementaire methodes ontwikkeld voor de bepaling van de bathymetrie van het intergetijdestrand en de brandingszone uit videobeelden. Beide methodes zijn getest aan de hand van veldmetingen. Daarnaast is de bruikbaarheid van beide methodes voor kustbeheer en kustonderzoek aan de orde gesteld.

Bepaling van de bathymetrie van het intergetijdestrand

De Intertidal Beach Mapper (IBM) brengt het driedimensionale strandoppervlak tussen de hoog- en laagwater lijn in kaart door de bepaling van een aantal strandcontouren op verschillende momenten gedurende een getijcyclus. Op basis van het visuele contrast tussen het droge en natte strand extraheert IBM de horizontale positie van de kustlijn uit tijdgemiddelde videobeelden. De bijbehorende hoogteligging van de kustlijn wordt geschat aan de hand van de getij- en golfcondities ten tijde van de inwinning van het videobeeld. Vanwege variabele beeldkarakteristieken als gevolg van veranderende hy-

droodynamische, morfologische en atmosferische condities op verschillende ARGUS sites werkt IBM noodzakelijkerwijs op individuele beelden. De nieuw ontwikkelde methode is robuust, generiek en flexibel in gebruik. Daarnaast is zij in staat om driedimensionale morfologische structuren (zoals droogvallende banken) in kaart te brengen.

IBM is gevalideerd aan de hand van een kustlijn-dataset, ingemeten met behulp van een GPS-systeem. Hieruit kwam naar voren dat de gemiddelde verticale fout veroorzaakt door het kustlijn-detectiemodel toeneemt met de afstand tot het videostation; de verticale fout als gevolg van de schatting van de hoogteligging van de kustlijn is relatief constant in kustlangse richting. De totale, gemiddelde verticale fout bedraagt minder dan 15 cm langs 85% van het 2 km lange studiegebied, wat overeenkomt met een horizontale fout van ongeveer 6 m. De variabiliteit van de modelafwijkingen (15-20 cm) wordt gedomineerd door onzekerheden in het detectiemodel. De toepassing van IBM op een drietal sterk verschillende ARGUS sites heeft laten zien dat het model goede resultaten levert over een breed scala aan hydrodynamische, morfologische en atmosferische condities.

Bepaling van de bathymetrie van de brandingszone

De Subtidal Beach Mapper (SBM) bepaalt de bodemligging in de brandingszone door assimilatie van patronen van golfdissipatie, verkregen uit videowaarnemingen en modelberekeningen. SBM bemonstert tijdgemiddelde video intensiteiten langs een kustdwarse raai, selecteert de data van goede kwaliteit and interpreteert het verkregen intensiteitsprofiel in termen van een golfdissipatie parameter. Het golfdissipatiepatroon afgeleid uit video wordt vergeleken met de overeenkomstige golfdissipatie, berekend met behulp van een gangbaar golftransformatiemodel op basis van een recent bodemprofiel. Dit profiel is verkregen uit een recente meting, danwel de toepassing van SBM op een recent videobeeld. De bodemligging wordt geactualiseerd door de waterdiepte te verminderen in gebieden waar de gemeten dissipatie de berekende dissipatie overschrijdt en vice versa. Aangezien het model gebruik maakt van video data met een hoge temporele resolutie is het mogelijk om bodemveranderingen in de brandingszone bijna vol-continu te monitoren. Synthetische model tests hebben laten zien dat SBM toepasbaar is over een breed scala van morfologische configuraties.

Validatie van SBM langs twee kustdwarse raaien in Egmond op een onderlinge afstand van ongeveer 1400 m kustlangs heeft aangetoond dat het model in staat is om de dominante morfologische veranderingen gedurende het eerste jaar na aanleg van een gecombineerde strand- en vooroeversuppletie te reproduceren. Dit betreft met name de kustwaartse verplaatsing van de buitenste bank en de aanzanding in het ondiepe deel van de brandingszone. De *rms* fout van de verticale afwijkingen langs het gehele kustprofiel bedraagt 40 cm voor beide raaien. Op de zeewaartse flank van de brekerbanken zijn de afwijkingen marginaal in de orde van 10 tot 20 cm. De fouten nemen toe tot zo'n 20-40 cm rond de banktop. Maximale afwijkingen tot 80 cm treden op in de troggen, als gevolg van de afwezigheid van brekende golven. De aanzanding van sediment in de ondiepe brandingszone is onderschat. Tenslotte is uit een gevoeligheidsanalyse naar voren gekomen dat het gedrag van SBM in hoge mate bepaald wordt door de tijdschaal van de bodemaanpassingen. Deze tijdschaal wordt door de gebruiker gespecificeerd.

De bruikbaarheid van IBM en SBM voor kustbeheer en kustonderzoek

De beschikbaarheid van algemeen toepasbare, nauwkeurige en robuuste video interpretatie methodes is *op zichzelf* geen garantie voor de bruikbaarheid van video monitoring technieken. Een goede bruikbaarheid vereist tevens dat een kustmonitoring techniek informatie levert die relevant is voor eindgebruikers. Een ingeburgerde referentiekader-systematiek voor beleidsontwikkeling toont expliciet de rol van operationele doelstellingen en kwantitatieve toestandsinformatie (ofwel Coastal State Indicators, CSIs) in relatie tot besluitvorming door kustbeheerders. De bruikbaarheid van video monitoring technieken ten behoeve van kustbeheer wordt bepaald door de mate waarin ze in staat zijn om tijdseries van CSIs te genereren.

De toepassing van SBM voor het monitoren van een gecombineerde strand- en voor-oever-suppletie te Egmond heeft geresulteerd in een hoge-resolutie tijdserie van de Momentane Kustlijn Indicator, die een centrale rol speelt binnen het Nederlandse kustbeheer. Daarnaast is een tijdserie van bankhoogtes gegenereerd, die beschouwd kan worden als een toegevoegde maat voor kustveiligheid. De bruikbaarheid van SBM ten behoeve van kustbeheer blijkt rechtstreeks uit het gegeven dat het model in staat is de Momentane Kustlijn Indicator te kwantificeren uit video beelden, aangenomen dat het model dit doet met voldoende nauwkeurigheid. Binnen de huidige beheerspraktijk ten aanzien van kustveiligheid bestaat geen operationele doelstelling die gebruik maakt van de CSI bankhoogte.

De toepassing van IBM heeft geleid tot een dataset van maandelijkse intergetijde bodems, op basis waarvan tijdseries gegenereerd zijn van de strandbreedte bij hoog- en laagwater, alsmede de volumeveranderingen op het intergetijdestrand. De bruikbaarheid van deze CSIs ten behoeve van kustbeheer is vastgesteld als aangetoond kan worden dat veranderingen in de strandbreedte of het volume van het intergetijdestrand correleren met veranderingen in de Momentane Kustlijn Indicator, waardoor ze bijdragen aan een bestaande operationele doelstelling. Bij wijze van variant kunnen de genoemde CSIs ook worden gekoppeld aan kustdynamische processen op kleinere tijden en ruimteschalen, waarbij de operationele doelstelling bijvoorbeeld wordt afgeleid uit publieke en economische eisen ten aanzien van recreatie.

De wetenschappelijke bruikbaarheid van CSIs afgeleid uit video blijkt uit de bijdrage aan studies gericht op model verbetering of data-model integratie. Gedetailleerde waarnemingen van de ontwikkeling van morfologische parameters als kustlijnlocatie, intergetijde strandvolume en bankhoogte bieden nieuwe kansen voor de verbetering en validatie van procesmodellen en banen de weg voor de ontwikkeling van geavanceerde data-gedreven model concepten (inclusief neurale netwerken) ter beschrijving van de morfodynamiek van kustsystemen. Wij voorzien dat het gebruik van morfologische informatie afgeleid uit videobeelden ten behoeve van de verbetering van procesmodellen en data-model integratie één van de speerpunten zal zijn van het ARGUS onderzoek in de komende jaren.

Samenvattend wordt gesteld dat de ARGUS videoteknik unieke mogelijkheden biedt voor het synoptisch monitoren van de kustzone over afstanden van meters tot kilometers en op tijdschalen van dagen tot jaren, tegen lage kosten. In Egmond bleek dit met name uit de waargenomen morfologische veranderingen gedurende de eerste twee jaar

na aanleg van een gecombineerde strand- en vooroeversuppletie, welke een opmerkelijke ruimtelijke coherentie vertoonden. Daarnaast lieten de videometingen onverwachts een zeer persistente kustlijnverstoring zien juist ten noorden van de vuurtoren. Dit morfologisch gedrag op kleinere tijd- en ruimteschalen is niet eenvoudig te meten met traditionele meetmethodes. Nu het kustbeheer lokale strand- en vooroeversuppleties heeft omarmd als de belangrijkste maatregel voor ingrepen in de kustzone verwachten wij dat het belang van kleinschaliger CSIS gaat toenemen. Voor zowel kustbeheerders als kustonderzoekers ligt er de uitdaging om ARGUS videobeelden te gebruiken voor het verkrijgen van relevante, kwantitatieve informatie over de kustzone, en deze informatie op een effectieve manier in te zetten bij het ontwikkelen en evalueren van kustbeleid.

Contents

Abstract	v
Samenvatting	ix
1 Introduction	1
1.1 Motivation	1
1.2 Remote sensing of nearshore bathymetry	2
1.3 Monitoring the nearshore with Argus video	4
1.3.1 Background	4
1.3.2 Image processing	7
1.3.3 The analysis of Argus video data	11
1.4 Research objectives and outline of this thesis	13
2 Quantification of intertidal beach bathymetry	15
2.1 Introduction	15
2.1.1 Motivation and approach	15
2.1.2 Objectives and outline of this chapter	17
2.2 Shoreline identification from exposure images	18
2.2.1 Background of the shoreline detection model	18
2.2.2 Shoreline detection based on pixel clustering	19
2.3 The elevation of video-derived shorelines	23
2.3.1 Background of the shoreline elevation model	23
2.3.2 Assessment of the still water level at the shoreline	24
2.3.3 Modelling wave set-up at zero water depth	25
2.3.4 Empirical quantification of the swash height	35
2.4 Investigation of IBM model performance	36
2.4.1 Introduction	36
2.4.2 Model validation against GPS surveyed shorelines	37
2.4.3 Comparison of IBM to alternative shoreline detection models	42
2.4.4 Discussion on IBM behaviour and performance	45
2.4.5 Furthering IBM performance and applicability	48
2.5 Conclusions	49

3	Quantification of subtidal beach bathymetry	53
3.1	Introduction	53
3.1.1	Motivation	53
3.1.2	Approach	54
3.1.3	Objectives and outline of this chapter	55
3.2	The Breaker Intensity Model (BIM)	57
3.2.1	Introduction	57
3.2.2	Pre-processing of time-averaged intensity data	58
3.2.3	Quantitative scaling of video intensity data	60
3.2.4	Investigation of various model-predicted measures of wave dissipation	66
3.2.5	Sensitivity analysis BIM parameter settings	69
3.2.6	Discussion on BIM performance	72
3.2.7	Conclusions	73
3.3	Quantification of water depth from video observations of wave breaking	74
3.3.1	A model to map subtidal bathymetry: Approach	74
3.3.2	Model formulations BAM	75
3.3.3	Evaluation of model behaviour against synthetic data	78
3.3.4	Discussion on BAM behaviour and applicability	86
3.4	Validation of Subtidal Beach Mapper	87
3.4.1	Introduction	87
3.4.2	Validation of SBM at Egmond: Heuristic approach	88
3.4.3	SBM sensitivity to variable parameter settings	92
3.4.4	Discussion on SBM performance Egmond	95
3.5	Discussion on SBM behaviour	97
3.5.1	General characteristics of present SBM behaviour	97
3.5.2	Furthering SBM performance and applicability	98
3.6	Conclusions	100
4	Video monitoring in support of Coastal Zone Management	103
4.1	Introduction	103
4.1.1	Motivation and approach	103
4.1.2	Objectives and outline of this chapter	104
4.2	The Egmond site: Coastal system and management issues	104
4.2.1	Nearshore processes at Egmond	104
4.2.2	Coastal Zone Management at Egmond	106
4.2.3	A framework to evaluate the utility of video monitoring in support of Coastal Management	107
4.3	Video-based assessment of intertidal CSIs	109
4.3.1	Data set of intertidal bathymetries	109
4.3.2	Video-observed evolution of intertidal CSIs Egmond	111
4.4	Video-based assessment of subtidal CSIs	113
4.4.1	Data set of subtidal beach profiles	113
4.4.2	Video-observed evolution of subtidal CSIs Egmond	117

4.5	Discussion on the utility of Argus	118
4.6	Conclusions	122
5	Conclusions	125
	Bibliography	129
A	Photogrammetry	139
A.1	Geo-referencing of oblique video data	139
A.2	Calibration of intrinsic camera model parameters	140
B	Detailed aspects of the shoreline detection model	143
B.1	Preprocessing of raw intensity data	143
B.2	Filtering histograms of scaled intensities	143
B.3	Assessment of dry-wet contrast in pixel intensities	146
B.4	Empirical demands on shoreline persistency	146
C	Formulation and implementation of the inner surf zone model	149
C.1	Background inner surf zone model	149
C.2	Model formulations	150
C.2.1	Time averaged momentum balance equation	150
C.2.2	Time averaged mass balance equation	153
C.2.3	Bore velocity	153
C.3	Solving the model equations	153
D	Formulations wave transformation model	155
E	Video-based shoreline detection models	157
E.1	ShoreLine Intensity Maximum (SLIM) model	157
E.2	Artificial Neural Network (ANN) model	158
E.3	Colour Channel Divergence (CCD) model	159
	List of Figures	161
	List of Tables	165
	List of Symbols	167
	Acknowledgements	171
	Curriculum Vitae	175

Chapter 1

Introduction

1.1 Motivation

The nearshore zone, extending from the beach to water depths of about 10 meters, is of significant societal importance. For instance, more than half of the US population lives within 80 kilometers of the shoreline and beaches are nowadays the primary recreational destination for domestic and foreign tourists (Thornton et al., 2000). Similarly, almost half of the European population lives within 50 km of the sea (Fragakis, 2002). In Spain, for instance, tourist spending at beaches in the Gulf of Cadiz justifies annual maintenance costs of more than 250 US\$/m for beach nourishments (Munoz-Perez et al., 2001). Besides its unquestionable economic and recreational value, the nearshore zone also contributes importantly to coastal safety. Nearshore sand bars are responsible for the depth-induced dissipation of wave energy off the shoreline, thus reducing the impact of direct wave attack at the dunefoot during storm events; and in the Netherlands, the protection of the low-lying, densely-populated hinterland against flooding is, amongst others, guaranteed by means of a sediment buffer in the nearshore zone (e.g., De Ruig, 1998). Effective management of a variety of coastal functions like safety, recreation, nature, shipping, fishery and others demands a sound understanding of the morphological behaviour of a coastal system and regular monitoring of its present state. The latter is complicated by morphological variability at time scales of days to seasons, which obscures the observation of coastal evolution at time scales of primary management interest (years - decades).

Apart from these management interests, the nearshore zone also embodies a significant research interest. With variations of morphology at temporal scales of hours to centuries and spatial scales of meters to hundreds of kilometers (De Vriend, 1997; Stive et al., 2002), it is probably the most dynamic region of any coastal environment. Coastal scientists have studied the morphodynamics of beaches over a wide range of spatiotemporal scales, including small-scale ripple formation (Thornton et al., 1998; Gallagher et al., 1998), storm-driven shoreline erosion events (List & Farris, 1999; Sallenger et al., 2001), seasonal fluctuations in beach morphology (Wright & Short, 1984; Lippmann & Holman, 1990; Komar, 1998; Stive & Reniers, 2003), cyclic sand bar behaviour at the time scale of years (Wijnberg, 1995; Ruessink et al., 2003b), (inter-)decadal oscillations

of the dunefoot position (Guillén et al., 1999; Ruessink & Jeuken, 2002), chronic beach erosion at time scales of years to decades (e.g., Kaminsky et al., 1997) and the evolution of coastal systems at geological time scales (e.g., Beets et al., 1992). High-resolution measurement techniques are necessary to resolve small-scale coastal processes at spatiotemporal scales in the order of (tens of) meters and hours to days, whereas the collection of long-term data sets is of decisive importance to study large-scale coastal behaviour at spatial scales of 1 - 100 km and temporal scales of months to decades (De Vriend et al., 1993).

Thus, both researchers and coastal managers will benefit from techniques to monitor coastal evolution at a variety of spatiotemporal scales. Present-day techniques to do so should primarily satisfy two functional requirements. First, they have to provide data with high resolution in time and space to resolve small-scale morphological processes at spatiotemporal scales in the order of (tens of) meters and days to weeks. Second, they have to be cost-efficient in operation to enable the collection of long-term data sets. In-situ measurement techniques do not meet these functional demands. Bathymetric survey techniques involving the use of ships, amphibious vehicles (Birkemeier & Mason, 1984) or jet skis (Dugan et al., 2001a) provide excellent bathymetrical data, but require major logistical commitments. Likewise, locally deployed wave and current sensors provide high-quality point measurements of the current wave and flow field, but lack synoptic coverage and are expensive to maintain in a hostile environment. In other words, in-situ techniques cannot deliver efficiently information on coastal evolution at spatiotemporal scales of direct research and management interest (meters-kilometers and hours-years).

Fortunately, many nearshore processes have a visible signature at the sea surface, which can be monitored remotely. While perhaps of lower accuracy, remote sensing techniques offer the potential for cost-efficient, long-term data collection with high resolution in time and space. In contrast to in-situ sampling techniques, remote data collection continues - and may even be most informative - during rough wave conditions. Being an indirect measurement, the key issue for every remote sensing technique is the quantitative interpretation of remotely sensed information in terms of relevant physical parameters, like coastal bathymetry. The development of robust, generically applicable techniques to do so on a routinely basis is still in its infancy.

The research and management context described above provides the basis for the formulation of the central aim and main objectives of this work (Section 1.4). Before that, the use of video data is motivated on the basis of an overview of remote sensing techniques commonly applied for the monitoring of nearshore bathymetry (Section 1.2) and the video system used here is introduced (Section 1.3).

1.2 Remote sensing of nearshore bathymetry

Remote sensing techniques have served a wide range of coastal monitoring purposes, including studies on land use, environmental issues and the mapping of coastal topography. For the monitoring of bathymetrical evolution at spatiotemporal scales of meters to kilometers and days to years, the remote sensing techniques most commonly applied

are radar and video, either space-borne, airborne or shore-based (see Hamm et al., 2002, for a review). In this section, we present a brief overview of recent applications of these techniques, to enable the selection of the most suitable option for this study. Monitoring techniques involving the penetration of the water column by a remotely transmitted signal (e.g., Irish & Lillycrop, 1999; Clarke & Werner, 2003) are not considered here, since they rely on moderately high water clarity. Owing to large turbidity values and high concentrations of suspended sediment, the applicability of these techniques in the nearshore zone is rather limited.

Space-borne monitoring systems allow for the quantification of subtidal bathymetric features on the basis of surface current modulations observed from Synthetic Aperture Radar (Greidanus, 1997; Wensink et al., 1998) or straightforward wavelength estimates derived from optical video imagery (Leu et al., 1999). Space-borne radar imagery was further used for the large-scale mapping of intertidal beach bathymetry at several UK tidal inlets (Mason et al., 1999, 2001).

Like space-borne systems, airborne photogrammetry (e.g., Rooney et al., 2003; Kuriyama, 2003) and airborne topographic LIDAR (e.g., Sallenger et al., 2001; Thornton et al., 2003) cover space scales of tens of kilometers and time scales of years, enabling the quantification of shoreline evolution and the analysis of sediment budgets. At spatiotemporal scales of several kilometers and months to years, extensive data sets of time-averaged shore-based video observations (Holman & Sallenger, 1986) were used to analyze planform beach evolution (Lippmann & Holman, 1990; Van Enkevort & Ruessink, 2001), adopting wave-breaking induced bright intensity patterns as a proxy for the underlying beach bathymetry. Time-averaged airborne video imagery (Worley et al., 1997; Lippmann & Kannan, 2003) and time-averaged X-band radar (Ruessink et al., 2002a) were used for similar purposes.

In contrast to space-borne systems, airborne and particularly shore-based monitoring techniques allow for the implementation of high-frequency data collection schemes (up to several Hz), to facilitate high-resolution monitoring of coastal changes. Most data interpretation techniques developed in this context aimed to quantify nearshore bathymetry from remote observations of the wave field, using shore-based radar (McGregor et al., 1998; Bell, 1999), airborne video (Dugan et al., 2001b) or shore-based video imagery (Stockdon & Holman, 2000). The wave characteristics thus obtained can be converted into water depth with the help of the linear dispersion equation. High-resolution, shore-based video imagery was also used for the quantification of shoreline evolution and intertidal beach morphodynamics. The key element driving these techniques is their capability to delineate a shoreline feature (Plant & Holman, 1997; Aarninkhof & Roelvink, 1999; Kingston et al., 2003; Turner et al., 2000; Alport et al., 2001) from multiple images throughout a tidal cycle.

Space-borne monitoring techniques are typically associated with spatiotemporal scales of tens of kilometers and several years. Although modern space-borne imagery may provide spatial resolutions well below 10 m, it cannot provide the dynamic information offered by motion imagery (like video). Airborne as well as shore-based radar and video monitoring systems typically offer a spatial coverage of 1-5 km, with a resolution in the order of 0.5-20 m. If deployed permanently, shore-based systems cover a wide range of time scales (hours-years).

Table 1.1: *Characterization of remote sensing techniques commonly used for the monitoring of changes of coastal bathymetry. ‘+’ (‘+/-’) symbols indicate that a particular technique has been applied with good (fair) results. Empty boxes denote situations that were incorporated in the overview presented here.*

Aspect	Radar		Video	
	Space-borne	Airborne & Shore-based	Space-borne	Airborne & Shore-based
Temporal scale	years	days-years	years	days-years
Temporal resolution	months	hours	months	hours
Spatial scale	$10^3 - 10^5$ m	$10^0 - 10^3$ m	$10^3 - 10^5$ m	$10^0 - 10^3$ m
Spatial resolution	5 – 25 m	5 – 10 m	5 – 25 m	0.5 – 20 m
Shorelines	+	+/-	+/-	+
Intertidal bathymetry	+/-	+/-		+
Subtidal bathymetry	+/-	+	+/-	+

Comparing the characteristics of the different monitoring techniques (Table 1.1), we consider *shore-based, optical video imagery* as the most suitable remote sensing technique for the purpose of *long-term, high-resolution monitoring* of morphodynamic processes in the nearshore zone. Fixed, shore-based platform installations offer the advantages of good spatiotemporal resolutions, in combination with cost-efficient, long-term data sampling with minimum operational difficulties as regard to station housing, power and data transmission. Airborne monitoring methods essentially also offer good spatiotemporal resolutions and embody a great potential for military applications (mounted on unmanned aerial vehicles, Holland et al., 2002), however their frequent use for long-term, high-resolution monitoring purposes demands significant logistic efforts, involving high costs. Space-borne monitoring techniques lack temporal resolution for application in the highly dynamic nearshore zone, where vertical changes in bathymetry of more than 1 m may occur over time spans as short as a few hours (Holland & Puleo, 2001). Although we recognize that radar embodies distinctive advantages over video techniques, like its ability to operate at night and in adverse weather conditions as well as its ability to provide a synoptic, direct measure of sea surface velocity (McGregor et al., 1998), we prefer the use of video because of its lower costs and complexity, the ease of visual interpretation of video data as compared to radar images and the considerable experience gained over the last 20 years from nearshore video monitoring projects worldwide. Shore-based video imaging, in particular the ARGUS system developed at Oregon State University (<http://cil-www.oce.orst.edu:8080/>), is therefore adopted in this thesis.

1.3 Monitoring the nearshore with Argus video

1.3.1 Background

The ARGUS video program, developed at the Coastal Imaging Lab, Oregon State University, involves the installation of unmanned, automated video stations at sites of

scientific interest (Holman et al., 1993). The first station was deployed at Yaquina Head, Oregon, in June 1992 and the program now includes 13 permanent research stations, with another 12 ARGUS video stations mounted at sites of coastal management interest (Figure 1.1). The motivation for setting up an extensive network of research stations was to examine the morphological response of a wide range of natural beaches to forcing by waves and tides. The network presently includes steep and shallow sloping beaches, high and low tidal ranges, energetic and calm environments as well as different sediment types.

An ARGUS monitoring station typically comprises five video cameras, spanning a 180° field of view and covering a 3-6 km coastal stretch, depending on the station elevation and the focal length of the camera lenses. Data sampling is usually hourly, although any schedule can be specified. Video data are temporarily stored on the computer on site, which communicates to the outside world by phone line or a permanent internet connection. As the process of data collection and return is fully automated, costs of operation are virtually zero.

Each standard hourly collection usually consists of three types of images, collected for each of the station's cameras (Figure 1.2). A snapshot image (Figure 1.2a) serves as simple documentation of conditions but offers little quantitative information. Ten

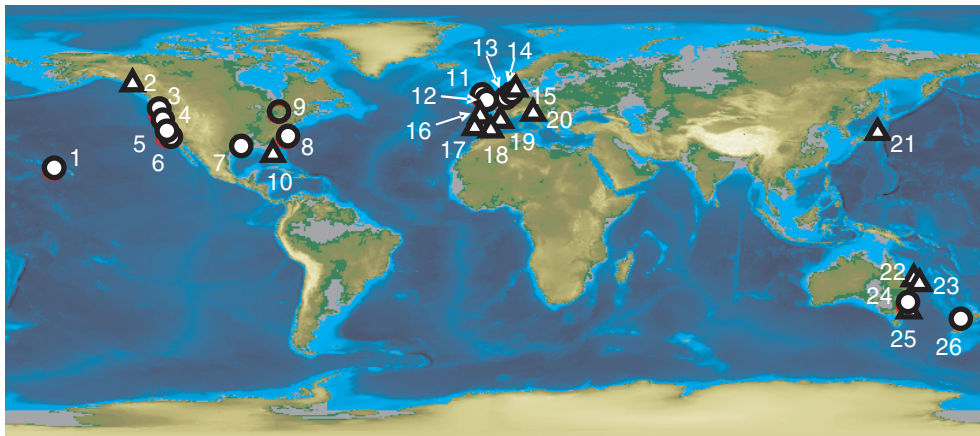


Figure 1.1: *The “ARGUS world”. Overview of ARGUS video stations worldwide, featuring sites of research interest (white circles), sites of management interest (white triangles) and a former ARGUS site (open circle). The Argus Research Programme, initiated and coordinated by Oregon State University, presently comprises stations in the USA (Waimea Bay HI [1], Yaquina Head OR [3], Monterey Bay CA [4], Blacks Beach, La Jolla, CA [5], Scripps, La Jolla CA [6], Bay St. Louis MS [7], Duck NC [8] and a former station at Lake Erie [9]), the UK (Droskyn Point [11] and Teignmouth [12]), the Netherlands (Noordwijk [13] and Egmond [14]), Australia (Palm Beach [24]) and New Zealand (Muriwai Beach [26]). Commercial stations were deployed in the USA (Homer AL [2] and Lake Worth FL [10]), the Netherlands (Egmond lighthouse [15]), Spain (Santander [16], Trafalgar [17], Carchuna [18] and Barcelona [19]), Italy (Lido di Dante [20]), Japan (Miyazaki [21]) and Australia (Goldcoast [22], Tweed Heads [23] and Wamberal lagoon [25]).*

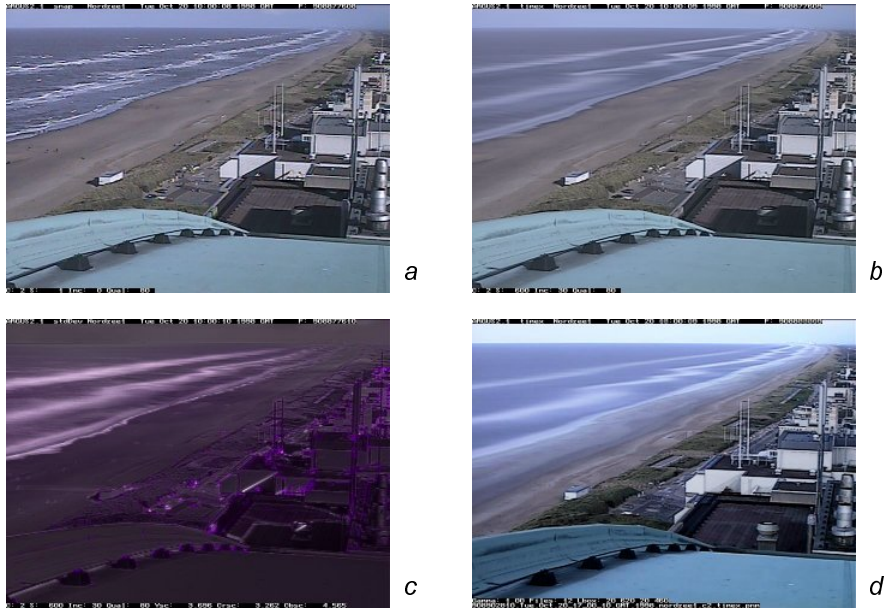


Figure 1.2: Overview of standard ARGUS image types: (a) snapshot, (b) time exposure, (c) variance and (d) daytimex image.

minute time exposures of the nearshore wave field (Figure 1.2b) average out natural modulations in wave breaking to reveal a smooth band of white which has been shown to be an excellent proxy for the underlying, submerged sand bar topography (Lippmann & Holman, 1989; Van Enckevort & Ruessink, 2001). Time exposures also ‘remove’ moving objects from the field of view, such as ships, vehicles and people. Variance images (Figure 1.2c) help identify regions which are changing in time (like the sea surface), from those which may be bright, but are unchanging (like the dry beach). Once per day, a so-called daytimex image (Figure 1.2d) is generated by averaging all time exposure images to provide a tide-averaged characterization of the bar morphology. Being averaged over all daylight hours, daytimex images show relatively stable illumination conditions,

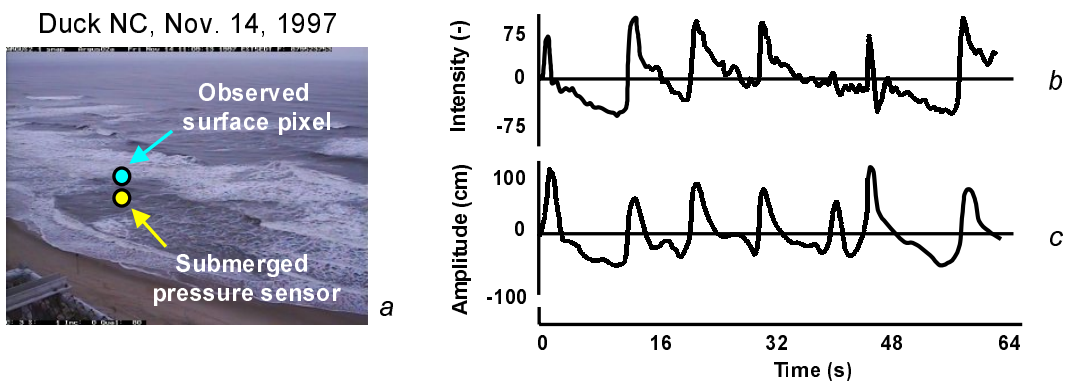


Figure 1.3: Time series of pixel intensities (b) sampled from Duck, camera 3 versus wave height (c) measured by a pressure sensor (after Lippmann & Holman, 1991).

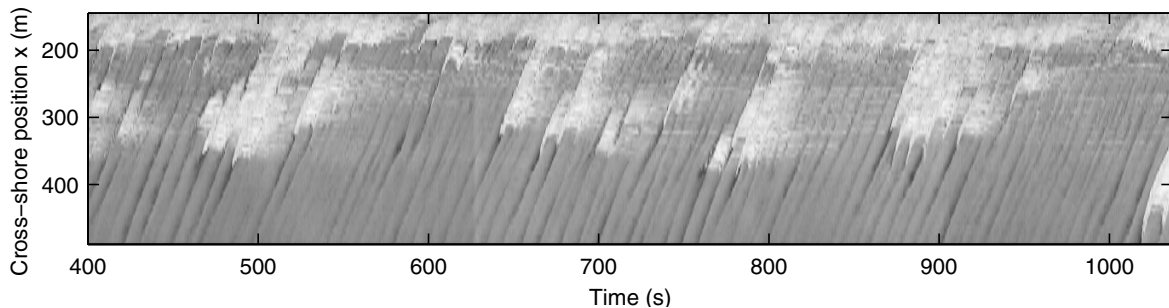


Figure 1.4: *Example of cross-shore intensity timestack sampled from Duck camera 3 d.d. 14/11/1997, GMT 17 hr. The cross-shore axis is positive off-shore.*

which make them highly suitable for the creation of animations that are used to provide qualitative insight in the morphodynamic behaviour of an ARGUS field site.

Besides time-averaged video data, data sampling schemes can be designed to collect time series of image intensities, typically at 2 Hz. As an example, Figure 1.3 shows the strong correlation which is commonly observed between a time series of pixel intensities and the wave height signal obtained from a wave gauge at the same location (after Lippmann & Holman, 1991). The small phase lag between the two indicates that maximum intensities correspond to the white, foam covered face of the breaking wave, which precedes the passage of the actual wave top. Comparisons for non-breaking waves, which are visually observed owing to the dark face of a shoaling wave, also show strong coherence, but often a larger, yet fixed, phase difference.

In extension of this approach, time series of pixel intensities can be sampled along a cross-shore or an alongshore array, which yields a so-called timestack image (space-time image, Figure 1.4). The dark, slightly curved patterns represent individual waves propagating onshore. The slope of the wave traces can be used to determine the approximate speed of the shoreward progressing waves, before these are dissipated through wave breaking at the shoreline (around cross-shore position $x = 170$ m)¹. The work presented in this thesis is based on time exposure, variance and timestack images.

1.3.2 Image processing

Quantification of image features requires accurate geo-referencing of oblique video data and a good understanding of the cross-camera variation of pixel resolutions. These aspects are described through the relationship between image coordinates (u, v) and the corresponding real world location (x, y, z) , which has been well established for application with the ARGUS video system (Holland et al., 1997). The relation between image and real world coordinates is defined by means of the camera location (x_c, y_c, z_c) , the effective focal length f (which directly relates to the camera horizontal field of view δ , Lippmann & Holman, 1989) and the camera orientation, defined through three camera angles, namely the tilt τ , azimuth ϕ and roll σ (Figure 1.5). The angles τ , ϕ and σ rep-

¹By ARGUS convention, the cross-shore x-axis is positive off-shore and the alongshore y-axis is rotated 90 degrees counterclockwise

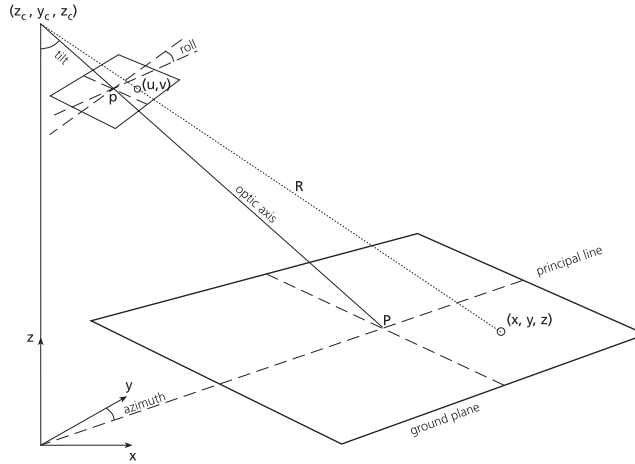


Figure 1.5: *Geo-referencing of oblique video data. Relation between image coordinates (u, v) and real world coordinates (x, y, z) .*

represent the rotation with respect to the vertical z axis, the orientation in the horizontal xy -plane and the rotation of the focal plane with respect to the horizon, respectively. Standard photogrammetric procedures enable the transformation from (x, y, z) to (u, v) to be expressed by means of the collinearity equations

$$u = \frac{L_1x + L_2y + L_3z + L_4}{L_9x + L_{10}y + L_{11}z + 1} \quad (1.1a)$$

and

$$v = \frac{L_5x + L_6y + L_7z + L_8}{L_9x + L_{10}y + L_{11}z + 1}. \quad (1.1b)$$

where coefficients $L_1 - L_{11}$ are linear functions of seven unknowns (τ, ϕ, σ) , (x_c, y_c, z_c) and f (Appendix A.1). These seven unknowns can be solved with the help of a set of reference points (also called Ground Control Points, or GCP's) with known image and real world coordinates. Although this procedure allows for the determination of the camera location (x_c, y_c, z_c) , Holland et al. (1997) found that more accurate coordinate transformations are obtained by constraining the camera position to the surveyed values. In that way, only two GCP's are needed to solve for four unknown angles $(\tau, \phi, \sigma$ and $\delta)$. Accounting for more than two GCP's yields an over-determined system of equations, which allows for the determination of a least-squares solution and (95%) confidence intervals on the angles τ, ϕ, σ and δ .

The procedure for geo-referencing described so far is valid for use with a distortion-free lens and square image pixels. The equipment presently used for ARGUS video imaging violates these conditions. In practice, video-observed pixel locations generally exhibit a radial distortion Δr with respect to the theoretically rectangular pixel grid (u, v) , while individual pixels may be slightly non-square as a result of small differences in sampling frequency between the camera and the image acquisition hardware. Before application of Eq. (1.1), raw video images need to be corrected for pixel non-squareness

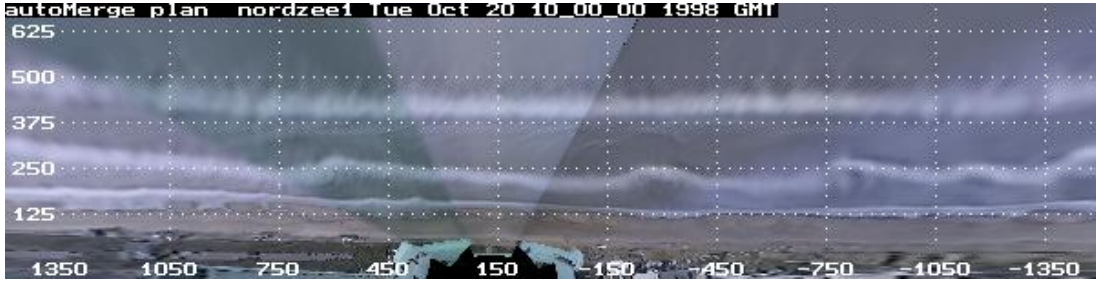


Figure 1.6: *Merged, plan-view image of Noordwijk, The Netherlands d.d. 20/10/1998 at 10:00 GMT. The image spans 3000 m in the alongshore direction, with the dry beach at the lower side and the cross-shore axis positive offshore. Bright intensity patterns reflect the submerged morphology, showing a linear outer bar at about 400 m offshore and a fairly irregular inner bar at about 250 m offshore.*

(using scale factors λ_u and λ_v) and radial lens distortion (involving distortion coefficients k_1 and k_2 , and the image center coordinates u_0 and v_0). The values of these six intrinsic camera model parameters are determined by calibrating the system hardware in the laboratory with the help of a control points test image (Holland et al., 1997), preceding the actual system installation in the field (Appendix A.2).

Geo-referencing video images of all cameras composing an ARGUS station yields a geometry solution (i.e. a four-angle vector $[\tau, \phi, \sigma, \delta]$) for each camera, which remains unchanged as long as the camera orientation is unaffected. With the help of such a geometry solution, oblique video data can be rectified through inversion of Eq. (1.1), according to

$$\begin{bmatrix} L_1 - L_9u & L_2 - L_{10}u & L_3 - L_{11}u \\ L_5 - L_9v & L_6 - L_{10}v & L_7 - L_{11}v \end{bmatrix} \begin{bmatrix} x \\ y \\ z \end{bmatrix} = \begin{bmatrix} v - L_4 \\ v - L_8 \end{bmatrix}. \quad (1.2)$$

Eq. (1.2) essentially involves a transformation of two-dimensional oblique pixel coordinates (u, v) to three-dimensional real world coordinates (x, y, z) , which implies that the system is under-determined. This problem is usually overcome by assuming the real world z -coordinate to be constant, preferably at the measured tidal level. Rectification of oblique images sampled from all five cameras composing the Noordwijk station and subsequent merging of the individual results yields a so-called plan view image (Figure 1.6), which readily allows for the measurement of length scales of morphological features observed in the field.

The theoretical accuracy of video cameras is governed by the nearly rectangular dimensions of a pixel footprint, approximated as (Lippmann & Holman, 1989)

$$L_c(x, y) = R(x, y) \left(\frac{\delta}{N_u} \right) \quad (1.3a)$$

and

$$L_a(x, y) = \frac{R(x, y)}{\cos(\tau(x, y))} \left(\frac{\delta}{N_u} \right), \quad (1.3b)$$

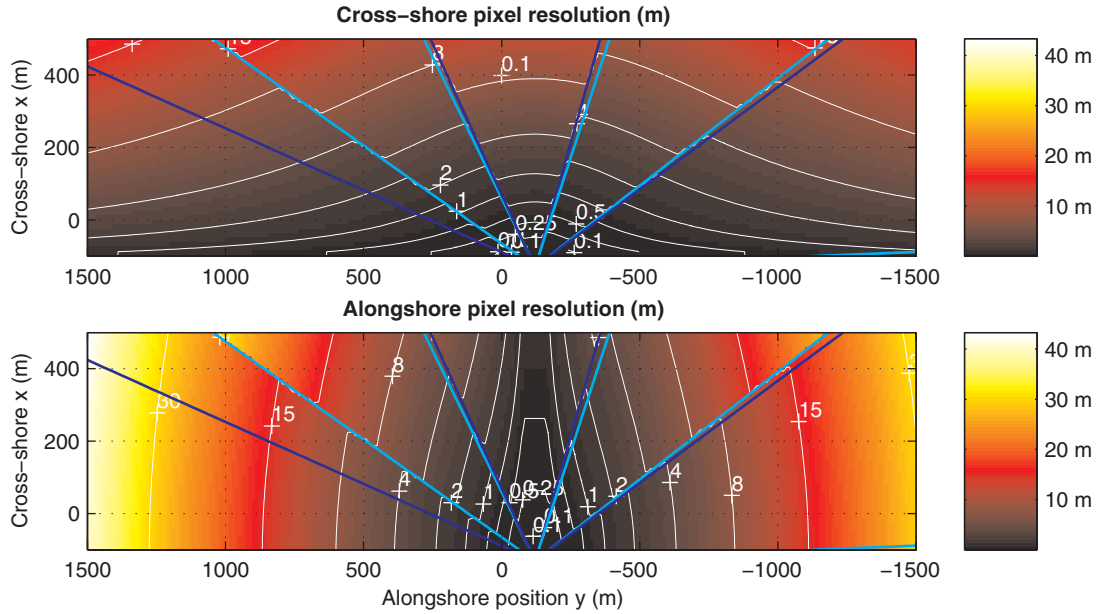


Figure 1.7: *Pixel resolution maps for the five-camera configuration of Egmond station “Jan van Speyk” (May 1999). Spatially varying cross-shore (upper panel) and along-shore (lower panel) dimensions of a pixel footprint, quantified across a coastal region of 600 m length cross-shore and 3000 m alongshore. The positive x -axis is pointing seaward, while the horizontal y -axis is positive towards the south. The video station is located near $(x, y) = (-130, -120)$ m, elevated at about 43 m above mean sea level and equipped (from north to south) with 12.5, 9, 6, 9 and 12.5 mm lenses.*

where L_c (L_a) is the cross-bore (boresight) size of a single pixel, N_u the number of horizontal pixels composing the image, R the distance between the camera and the location (x, y) of interest and the angle δ is given in radians. The spatially varying dimensions L_c and L_a thus obtained are projected on cross- and alongshore oriented coordinate axes, which yields maps that show the spatial distribution of cross-shore and alongshore pixel resolutions (Figure 1.7). The latter characterization of video accuracy is physically more meaningful for coastal applications. Cross-bore resolutions happen to be fairly constant, as can be seen from the cross-shore resolutions of the outer cameras 1 and 5 and the alongshore resolutions of the middle camera 3. Video accuracy in boresight sense, on the other hand, rapidly decreases with increasing distance from the video station, as most clearly observed from the rapidly decreasing alongshore pixel resolutions for the outer cameras 1 and 5. For the five-camera Jan van Speyk configuration at Egmond (the Netherlands) shown in Figure 1.7, shorelines (located around cross-shore coordinate $x = 0$ m) can be measured with a cross-shore (alongshore) accuracy in the order of 0.5-2 (0.5-30) m, while the cross-shore (alongshore) pixel resolution in the bar regions (around $x = 300$ m) typically amounts 4-8 (1-30) m.

Van Enkevort (2001) presents an excellent analysis of the errors involved with the procedures for geo-referencing and image rectification. Using the 95% confidence intervals around the computed geometry angles ($\phi, \delta, \tau, \sigma$), she finds angular deviations

below $\approx 0.2^\circ$ for τ and ϕ and within $\approx 1^\circ$ for δ and σ , indicating that the methodology for geo-referencing generally yields consistent results. Even though the absolute value of the error in τ may be relatively small, Van Enkevort (2001) shows that the accuracy of the rectification procedure is dominated by errors in τ , yielding positional errors in the order of five times the dimensions of a pixel footprint for a stand-alone τ offset of 0.2° . Fortunately however, the procedure for geo-referencing was found to be self-correcting, in the sense that errors in a single angle are compensated by an offset of the other angles, yielding a total positional error in the order of the pixel accuracy. As projection errors associated with an inaccurate estimate of the rectification level (typically the measured tidal level) were found to be an order of magnitude smaller than the dimensions of a pixel footprint, Van Enkevort (2001) concludes that image errors are of pixel magnitude and mainly result from random calibration errors.

1.3.3 The analysis of Argus video data

ARGUS video imagery has been used to study a wide range of beaches and coastal processes (Holman et al., 1993), including the phenomenological analysis of nearshore morphodynamics, the quantification of nearshore hydrodynamic processes and the mapping of intertidal and subtidal beach bathymetry. A brief overview of ARGUS-based work in these three categories is presented here.

Ten minute time exposures of the nearshore zone generally show bright intensity patterns which correspond to locations where waves preferentially break. Lippmann & Holman (1989) have shown these patterns to reflect the underlying submerged beach bathymetry, although modulations of the breaker bar position with varying tide level and incident wave height may induce a considerable offset (up to 30 m) between the surveyed and video-observed bar location. This can, however, be corrected empirically (Van Enkevort & Ruessink, 2001) or with the help of a neural network (Kingston et al., 2000). Rectified time exposure images thus show bright intensity patterns which readily enable the phenomenological analysis of coastal morphodynamics. This type of analysis was exploited to quantify the spatial and temporal variability of nearshore sand bar morphology at Duck, USA (Lippmann & Holman, 1990) and Noordwijk, Netherlands (Van Enkevort & Ruessink, 2003a,b), to study the (cyclic) behaviour of alongshore (Wijnberg & Holman, 1997; Alexander, 2001) and transverse (Konicki & Holman, 2000) bars, to investigate the morphological response of a coastal inlet to a limited series of storm events (Morris et al., 2001) and to assess the spacing of beach cusps (Holland et al., 1998) and rip currents (Symonds et al., 1997; Ranasinghe et al., 1999, 2000) at natural beaches. The long-term, high-resolution, phenomenological analysis of beach behaviour at various video sites worldwide has revealed some of the mysteries of surf zone morphodynamics, uncovering much unexpected behaviour.

The second category of ARGUS analysis methods concerns methods to assess near-shore hydrodynamics processes including wave characteristics, flow velocities and swash processes. High-frequency (2 Hz) time series of pixel intensities were used to quantify the phase speed and incident angle of shoreward progressing waves (Lippmann & Holman, 1991), and to investigate the statistics of wave breaking and wave-breaking modulation across the nearshore (Lippmann & Holman, 1992). Using a visible signa-

ture at the sea surface (traces of persistent foam or turbulent cells of roughened water), timestack images allow for the monitoring of wave-induced alongshore (Chickadel & Holman, 2002a; Chickadel et al., 2003) and cross-shore (Chickadel & Holman, 2002b) currents, as well as tide-induced flow velocities in a coastal inlet system (Davidson & Morris, 2002). Timestack images of swash run-up (Holland & Holman, 1993) and high-frequency snapshot imagery (Holland & Holman, 1997) were deployed to study wave run-up characteristics on natural beaches (Holland et al., 1995) and the hydro- and morphodynamics of the swash region (Holland & Puleo, 2001). Video capabilities in the swash zone nowadays include the quantification of two-dimensional, intra-wave maps of flow velocities obtained from particle image velocimetry (PIV) techniques (Puleo et al., 2000; Holland et al., 2001), which have, among others, been used to estimate detailed friction coefficients throughout the swash zone (Puleo & Holland, 2001). Quantification of hydrodynamic processes from video strongly relies on the visibility of individual wave crests and flow signatures at the sea surface, which in turn depend on the local pixel resolution (governed by lens characteristics and the distance to the camera), the dominant wave climate (with long-period, long-crested swell being relatively well resolved by video) and the atmospheric conditions (with frequent rain and fog being disadvantageous for successful analysis). So far, the algorithms to quantify hydrodynamic processes were mostly developed and tested on the basis of video data collected at Duck NC, USA. Their applicability to field sites with strongly different hydrodynamic and morphologic characteristics is subject to present research, within frameworks like the EU-funded CoastView project.

The third category of ARGUS analysis routines aims to quantify beach bathymetry from video observations. This generally involves separate approaches for the sub-aerial, intertidal and subtidal beach, respectively. Automated video systems enable the monitoring of morphological changes at the sub-aerial beach with the help of shadowing techniques (Holman et al., 1991). The quantification of intertidal beach bathymetry usually relies on the mapping of video-derived shorelines throughout a tidal cycle. The shoreline detection methods developed so far delineate a shoreline feature from spatial gradients in intensity in rectified time exposure images (Davidson et al., 1997), the location of the shoreline break (Plant & Holman, 1997; Madsen & Plant, 2001), the intensity difference between low- and high-tide images (Alexander, 2001) or the visually observed difference in time-averaged variance (*pers. comm.* K.T. Holland, NRL-SSC, MS, USA) or color characteristics (Aarninkhof & Roelvink, 1999; Kingston et al., 2003; Turner et al., 2000) between pixels intensities at the dry and wet beach. Holland & Holman (1997) quantify intertidal bathymetry on a 10 m by 10 m grid using trinocular stereogrammetry at intra-wave time scales. Except for the trinocular technique, most shoreline models adopt the measured tidal level as a proxy for the shoreline elevation, although some models (Davidson et al., 1997; Plant & Holman, 1997) apply a site-specific correction to the estimated shoreline elevation. The development of a generic shoreline elevation model needs further exploration. Video-based models to quantify subtidal bathymetry are relatively scarce, especially compared to the wide variety of shoreline detection models developed so far. The subtidal bathymetry mappers²

²In the context of this work, ‘mapper’ refers to a technique to quantify coastal bathymetry from

presently available estimate local water depth from video observations of wave celerity (Stockdon & Holman, 2000) or wave breaking (Aarninkhof et al., 1997). Our limited capabilities at this point are particularly surprising in view of the vast importance of bathymetrical data for many applications, including the scientific analysis of nearshore morphodynamics, the development of management strategies for coastal safety and the use of numerical models to simulate nearshore hydro- and morphodynamics.

Inspired by advanced capabilities of electro-optical sensors, nearshore circulation models and the environmental characterization algorithms summarized above, present-day developments also focus on setting up an integrated, real-time monitoring system for nearshore environments (Holland et al., 2002), involving the quantification of subtidal bathymetry, shoreline evolution, wave characteristics and currents.

1.4 Research objectives and outline of this thesis

Motivated by (i) a research and management interest in the monitoring of coastal evolution at spatiotemporal scales of (tens of) meters and days to years and (ii) the absence of techniques to quantify inter- and subtidal bathymetry from remote video observations at the start of this study (Subsection 1.3.3), the central aim of this work is *to quantify nearshore bathymetry from shore-based video imagery at spatiotemporal scales of direct management and research interest (meters-kilometers and hours-years)*. To achieve this central aim, three main objectives are pursued:

1. To develop robust methods to extract inter- and subtidal beach bathymetry from shore-based video imagery,
2. to determine the accuracy of these methods through calibration and validation against existing bathymetric data sets, and
3. to assess the utility of video-based monitoring techniques, particularly methods to quantify inter- and subtidal bathymetry, for application in support of coastal management and science.

Chapters 2 and 3 form the core part of this thesis, directly addressing Objectives 1 and 2 through development and validation of new model concepts to map inter- and subtidal beach bathymetry, respectively:

- The Intertidal Bathymetry Mapper (Chapter 2) analyzes time exposure images to delineate a shoreline feature from the visible contrast between the dry and wet beach and estimates the associated shoreline elevation from the hydrodynamic conditions at the time of image collection. This yields a contour line at the beach surface. Mapping a time series of contour lines throughout a tidal cycle allows for the quantification of intertidal beach bathymetry. Model performance is evaluated against a data set of GPS-surveyed shorelines at Egmond, the Netherlands. Besides, video images from three distinctive ARGUS sites are used to compare

the performance of our model to the results obtained from alternative shoreline detection techniques.

- The Subtidal Beach Mapper (Chapter 3) operates on time-averaged video images, which show wave breaking induced bright intensity bands as a visible signature of the underlying beach topography. Wave dissipation maps, computed from common wave transformation models, show similar patterns, with dissipation rates that increase with decreasing water depth. The model developed here updates surf zone bathymetry through assimilation of video-derived and model-predicted patterns of wave dissipation. This demands a fundamental understanding of the process of wave breaking as observed from video imagery and the availability of a robust assimilation code, which are both developed in the first part of Chapter 3. In the second part, the Subtidal Beach Mapper is tested against a one-year bathymetric data set acquired during the first year after nourishing a beach at Egmond.

The two models are presented in separate chapters since their approaches to quantify bathymetry fundamentally differ and they largely operate on different parts of the beach profile, which makes them complementary by nature. There is however an interesting link between both models. Because of the spatial overlap at high tide, when the subaqueous intertidal beach is also part of the computational domain of the Subtidal Beach Mapper, information on the elevation of the intertidal beach can be used as a shoreward boundary condition of the model to quantify subtidal beach bathymetry.

During the development of both models, emphasis is put on their generic character, to facilitate model applicability at a variety of ARGUS sites. However, the availability of generically applicable, accurate and robust video interpretation models *in itself* does not guarantee the utility of video-based monitoring techniques. This is also determined by the model's capability to address problems of end-user interest. The utility issue is specifically addressed in Chapter 4, which evaluates the potential of video-based monitoring techniques, particularly the methods to quantify inter- and subtidal beach bathymetry for coastal research and management purposes (Objective 3). To that end, the new models developed in Chapters 2 and 3 are evaluated in a Coastal Zone Management context, focussing on the morphological evolution of a nourished beach at Egmond. The overall conclusions of this study are summarized in Chapter 5.

Chapter 2

Quantification of intertidal beach bathymetry

2.1 Introduction

2.1.1 Motivation and approach

This chapter¹ addresses Objectives 1 and 2 of this thesis (Section 1.4) for the nearshore area situated between the low and high tide beach contours. This is achieved by (i) the development of a model to quantify intertidal beach bathymetry from shore-based video imagery, and (ii) the assessment of model accuracy through validation against field measurements and a comparison to alternative models. Models to quantify intertidal beach bathymetry from video imagery generally delineate a shoreline feature from oblique or plan view images and estimate the associated elevation from the hydrodynamic conditions at the time of image collection. This yields an alongshore elevation contour of the intertidal beach. Mapping a time series of contour lines throughout a tidal cycle enables the composition of the three-dimensional beach surface between the shoreline contours at low and high tide. This approach assumes morphological changes at spatial scales of tens to hundreds of meters to be small over the period of data sampling (typically 6-10 hours).

The first generation of shoreline detection models (Plant & Holman, 1997; Janssen, 1997; Davidson et al., 1997) originated from the time that ARGUS stations collected gray-scale images only. These models aimed to identify a characteristic pattern in the distribution of gray-scale pixel intensities sampled across the swash zone. The SLIM model (Plant & Holman, 1997; Madsen & Plant, 2001) was typical of this approach, using the visually observed shoreline break ('ShoreLine Intensity Maximum', SLIM) as a proxy for the location of the shoreline. Application of the SLIM model was found to be highly robust, easy to automate and to perform well at beaches with a well-pronounced and discrete SLIM feature. These criteria are met at steep (reflective) beaches with

¹This chapter is based on Aarninkhof, S.G.J., Turner, I.L., Dronkers, T.D., Caljouw, M. and Nipius, L. (2003). A video-based technique for mapping intertidal beach bathymetry. *Coastal Engineering* 49, pp. 275-289

mild to rough wave conditions. However, SLIM features are often diffuse or absent at mildly sloping (dissipative) beaches with emerging sand bars. This initiated the development of alternative shoreline detection models, which were still based upon gray-scale image information, but differed from the SLIM approach in that the location of the shoreline was estimated from a characteristic feature in the correlogram of the cross-shore intensity and variance profile (Janssen, 1997) or spatial gradients in intensity levels in rectified images (Davidson et al., 1997). The absence of a well-pronounced gray-scale contrast between pixel intensities sampled from sub-aerial and sub-aqueous regions of the beach often complicated or prevented unambiguous application of the latter models. A further difficulty with the gray-scale models was that a site-dependent correction to estimate the shoreline elevation was generally required (e.g., Plant & Holman, 1997; Davidson et al., 1997).

Holland & Holman (1997) avoided the problem of estimating the shoreline elevation from the hydrodynamic conditions at the time of image collection by utilizing trinocular (three view) stereogrammetry. In a small scale application, they detected the instantaneous location of the shoreward edge of the swash (hereafter referred to as the waterline) across a 10 m by 10 m foreshore region from snapshot images sampled at 10 Hz. Mapping multiple waterlines throughout one or more swash cycles enabled the quantification of foreshore topography with a vertical accuracy between 1 and 3 cm, thus allowing for the detection of small-scale morphological changes. The applicability of this technique at spatial scales of one to several kilometers is however limited, owing to the operational and logistical commitments involved with the use of multiple video stations with overlapping camera views. In summary, the shoreline detection models developed until 1997 either lacked generic applicability, were complicated to use or failed to cover spatiotemporal scales of coastal management interest.

The introduction of color ARGUS imagery in 1997 has initiated the development of a second generation of shoreline detection models. Color video images show a visual contrast between the sub-aqueous and sub-aerial beach. This is induced by the rapid attenuation of wavelengths from the red end of the light spectrum at a water covered surface, as compared to those from the blue end (Kingston et al., 2003). This effect increases in areas of large sediment concentrations, like the swash zone. At the dry beach, in contrast, the red light component is comparatively unaffected for similar lighting conditions, which yields the visual contrast between both areas. Several models have been developed to delineate a shoreline feature from this color contrast, involving pixel clustering techniques (Aarninkhof & Roelvink, 1999), an artificial neural network approach (Kingston et al., 2003), or observations of color band convergence (Turner et al., 2000). This thesis presents the development and validation of the pixel clustering approach.

The model developed in this chapter (hereafter referred to as the Intertidal Beach Mapper, or IBM) operates on standard oblique time exposure images, which average over waterline oscillations induced by individual waves and wave groups. Time exposure images allow for the detection of a time-averaged waterline (hereafter referred to as shoreline), situated in the swash region between the sub-aqueous inner surf zone and the sub-aerial dry beach. This approach is successful as long as the detection model identifies a consistent shoreline location within the swash zone, insensitive to variable

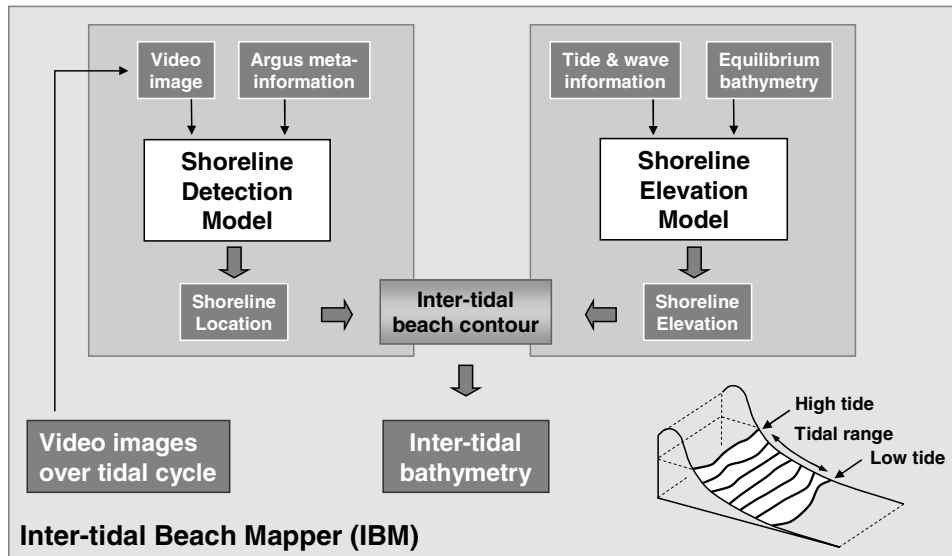


Figure 2.1: *Mapping intertidal beach bathymetry from a set of shorelines, derived from time-averaged video observations throughout a tidal cycle.*

hydrodynamic conditions and beach slopes. To enable the interpretation of video-derived shorelines as contour lines of the beach surface, the corresponding elevation of each shoreline needs to be quantified as well. In the context of this work, this has been done on the basis of the measured hydrodynamic conditions at the time of image collection.

2.1.2 Objectives and outline of this chapter

This chapter presents the IBM model, which quantifies intertidal beach bathymetry by mapping video-derived shoreline contours throughout a tidal cycle. Thus, further detailing the Objectives 1 and 2 of this thesis (Section 1.4), the sub-objectives of this chapter are:

- To develop a technique to delineate a shoreline feature from standard time-averaged video imagery. This involves setting up a model to discriminate the dry beach from the wetted inner surf zone, based on the clustering of pixel intensities sampled at the shoreward and seaward side of the shoreline.
- To develop a method to estimate the associated shoreline elevation from the measured hydrodynamic conditions at the time of image collection. The shoreline elevation model should account for the effects of storm surge, tide, wave set-up and swash.
- To assess the accuracy of the overall IBM model, which is obtained by combining the techniques to quantify the shoreline location and elevation. This involves the validation of IBM results against a data set of GPS-surveyed shorelines.

The layout of IBM (Figure 2.1) directly reflects the first and second sub-objective specified above. IBM consists of two sub-models, the Shoreline Detection Model and the Shoreline Elevation Model. The Shoreline Detection Model investigates the intensity characteristics of a region of interest covering both the sub-aerial and the sub-aqueous beach. If this yields distinctive clusters of dry and wet pixels, the location of the shoreline is determined in between both. The Shoreline Elevation Model estimates the associated water level at the shoreline, making use of the tide and wave conditions at the time of image collection. Application of IBM throughout a tidal cycle yields a set of contour lines, that enable the composition of the three-dimensional beach surface between the shoreline contours at low and high tide.

In the remainder of this chapter, the development of the Shoreline Detection Model (Sub-objective 1) and the Shoreline Elevation Model (Sub-objective 2) is described in Sections 2.2 and 2.3, respectively. The third sub-objective of this chapter is addressed in Section 2.4 by quantitatively assessing IBM performance against a data set of GPS-surveyed shorelines at Egmond and the comparison of IBM results at three distinctive ARGUS sites worldwide to the output of three alternative shoreline detection models. Section 2.4 includes a discussion on the behaviour and performance of IBM at different sites worldwide and also presents suggestions for furthering IBM performance. This chapter concludes (Section 2.5) with a summary of our findings in the context of the three sub-objectives driving the development of IBM.

2.2 Shoreline identification from exposure images

2.2.1 Background of the shoreline detection model

Time-averaged video observations of the nearshore zone generally show a visual contrast between the sub-aerial and sub-aqueous parts of the beach, which reflects different pixel intensity characteristics at both parts. On the basis of an inspection of representative video images collected at different ARGUS stations worldwide, it was found that a well-pronounced distinction between the sub-aqueous and sub-aerial parts of the beach is observed from time-averaged video imagery as:

1. A color distinction. This distinction mechanism is particularly associated with bright, sunny days (Figure 2.2a). Pixel intensities sampled from the sea surface represent blue colors, whereas the color characteristics of pixel intensities sampled at the sub-aerial beach vary from yellow/white (Gold Coast, Australia) to reddish (Palm Beach, Australia) to gray/brownish (Egmond and Noordwijk, Netherlands), likely depending on the sedimentological characteristics of the beach.
2. A luminance (or brightness) distinction. This distinction mechanism is associated with low altitudes of the sun and overcast days (Figure 2.2b). Reflection of downwelling sky radiance causes the sea surface to be relatively bright as compared to the dark surface of the dry beach. These conditions were frequently found at Teignmouth (UK) and Miyazaki (Japan), but were also occasionally observed at the Dutch beaches and at Duck (NC, USA).



Figure 2.2: *Time exposure images of Noordwijk, Netherlands, collected d.d. 04/12/1998 at 10:00 GMT (a) and 06/12/1998 at 10:00 GMT (b). The images represent typical conditions that allow for color-based (a) and luminance-based (b) shoreline detection.*

The key observation here is that both situations yield a clustering of pixels sampled at the sub-aqueous and sub-aerial beach, induced by contrasting color or luminance characteristics. Discrimination of the two clusters allows for the identification of the shoreline at the interface of the sub-aqueous and sub-aerial beach. In the remainder of this section, these clusters are referred to as the wet and dry cluster, consisting of wet and dry pixels sampled from the sub-aqueous and sub-aerial regions of the beach, respectively.

2.2.2 Shoreline detection based on pixel clustering

The IBM shoreline detection model aims to discriminate clusters of dry and wet pixels, based on distinctive intensity values in terms of color or luminance. Color video images are generally encoded in RGB space, where the color and luminance of each pixel are defined as a mixture of the primary colors Red, Green and Blue (RGB). By nature, RGB space combines color and luminance information, which hampers the applicability of RGB images to identify shorelines on the basis of either color or luminance information. The IBM detection model therefore converts pixel intensities within a region of interest covering both the sub-aerial and sub-aqueous beach to HSV (‘Hue Saturation Value’) color space, which treats color (hue, saturation) and luminance (brightness) information separately (e.g., Russ, 1995). The HSV color space corresponds better to how people experience color than the RGB color space does. Hue is defined along the surface of the HSV definition cone (Figure 2.3) and ranges between 0 and 1, running through the color spectrum from red (hue = 0) via orange, yellow, green (hue = 0.5), blue, purple and back to red (hue = 1) again. The saturation, also ranging between 0 and 1, is 0 for black and white, while adopting a value 1 for the primary (red, green, blue) and secondary (cyan, magenta, yellow) colors. The value information incorporates the brightness level and also ranges between 0 and 1, with 0 (1) representing black (white).

The IBM detection methodology is illustrated on the basis of the example image of Noordwijk presented in Figure 2.2a. Pixel intensity values are sampled within the region

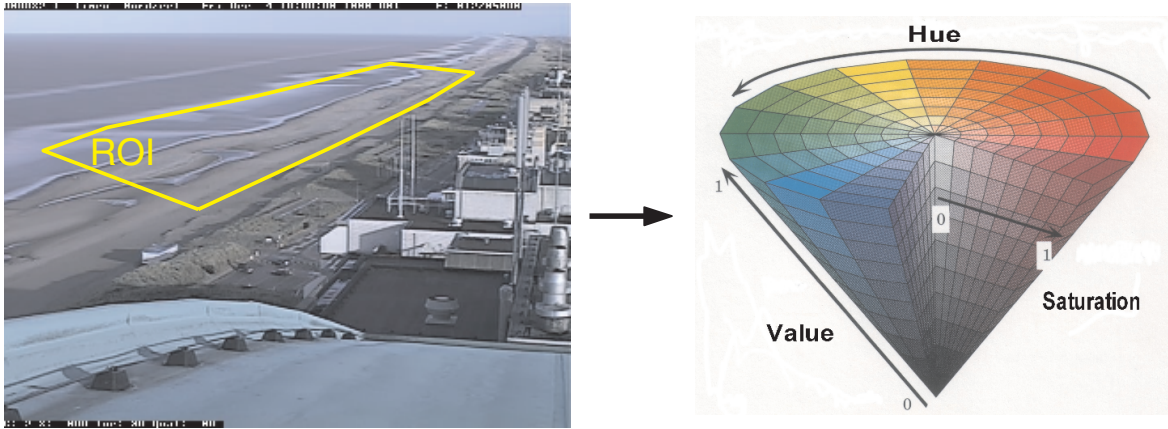


Figure 2.3: Conversion of image intensities within a region of interest (ROI) covering both the sub-aerial and sub-aqueous beach from RGB to HSV color space. Noordwijk, 04/12/1998 GMT 10 hr.

of interest shown in Figure 2.3. Categorization of these intensities in hue-saturation space yields the clustering presented in Figure 2.4a. Raw pixel intensities were filtered to remove outliers and scaled between 0 and 1 to improve contrast between the dry and wet clusters (Appendix B.1). For this image, dry (wet) pixels are typically associated with a hue of 0.55 (0.20) and a saturation of 0.20 (0.70). The key issue now is to determine a discriminator criterion to separate these two clusters.

The determination of a discriminator criterion is obscured by the spiky appearance of the histogram of scaled intensities (Figure 2.4a). Iterative low-pass filtering of the spiky data (Appendix B.2) yields a smooth histogram with two well-pronounced peaks P_{dry}

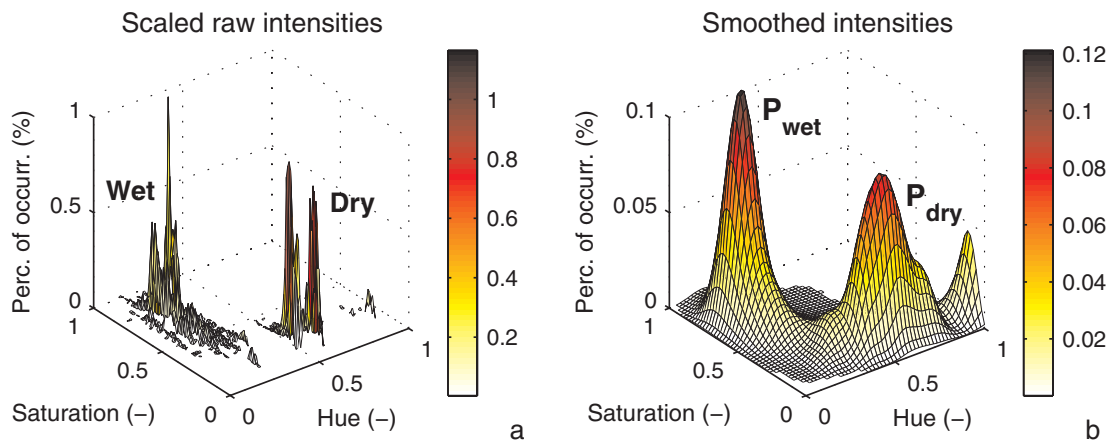


Figure 2.4: Clustering of pixel intensities in hue-saturation space. Histogram of Noordwijk pixel intensity data (04/12/1998 GMT 10 hr.) before (a) and after (b) iterative low-pass filtering. The filtered histogram shows a local maximum situated at its hue=1 border, which is excluded from further analysis.

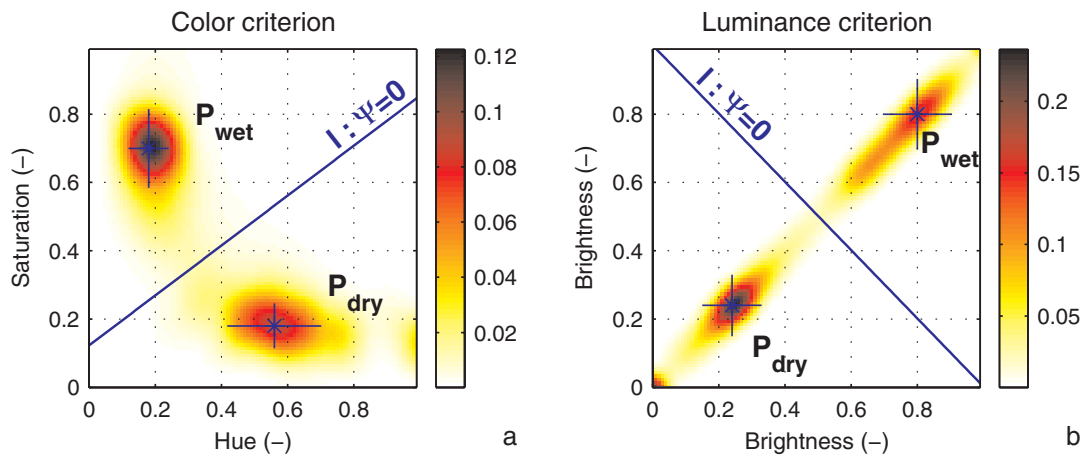


Figure 2.5: Filtered histogram of pixel intensities and the resulting discrimination function Ψ , in the color (a) and luminance (b) domain. The histograms originate from IBM application to the images shown in Figure 2.2.

and P_{wet} , which mark the locations of the clusters of dry and wet pixels (Figure 2.4b). To avoid the identification of non-representative clusters, local maxima situated at the borders of the color or luminance domain (Figure 2.4) do not qualify for further analysis. The filtered histogram thus obtained is used to define a line separating the clusters of dry and wet pixels. This line crosses the saddle point of the filtered histogram with an orientation perpendicular to the line connecting P_{dry} and P_{wet} . The location of this line is corrected for a minor artificial offset of the location of the saddle point, induced by the filtering of two peaks of non-equal size (Appendix B.2).

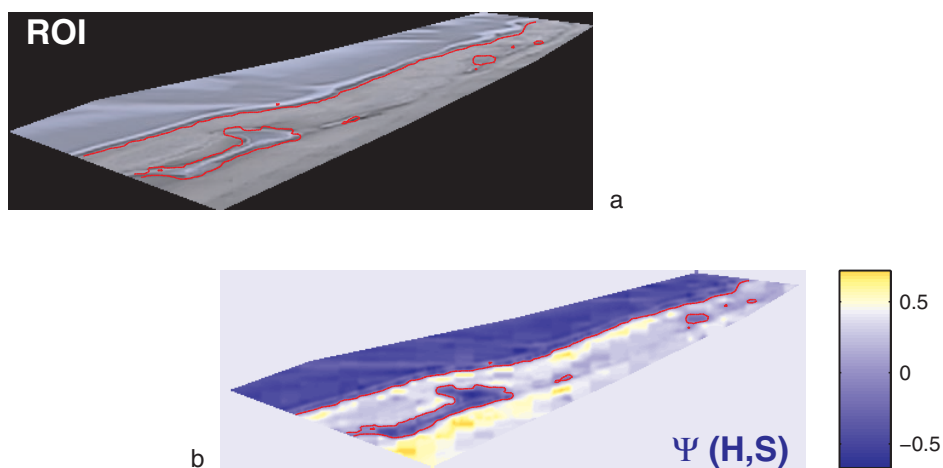


Figure 2.6: Shoreline detection on the basis of pixel intensity clustering. Identification of the shoreline at the interface of dry and wet pixels (a), categorized by application of Ψ to individual pixels within the region of interest (b). Bright colors relate to positive Ψ (sub-aerial beach), dark colors to negative Ψ (sub-aqueous beach).

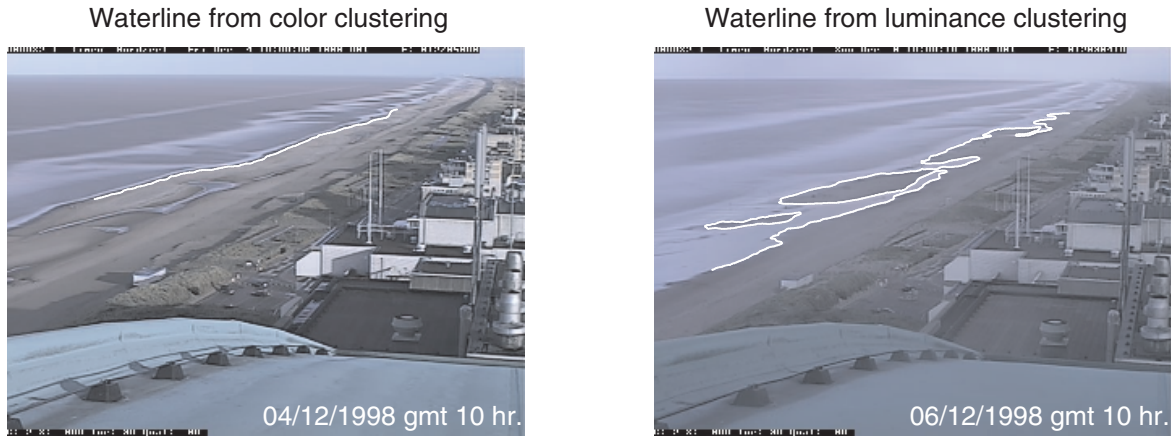


Figure 2.7: *Video-based estimates of the shoreline location at Noordwijk, Netherlands, determined from the color (a) and luminance (b) contrast of pixel intensity characteristics sampled at the sub-aerial and sub-aqueous beach.*

When applied to an arbitrary video image, the detection model performs these operations on intensity data in both the two-dimensional color and one-dimensional luminance domain. The relative spread of pixel intensities within each cluster (Appendix B.3) is determined to assess the dry-wet contrast observed in the color and luminance domain. The domain providing the best contrast is adopted for further analysis. Examples of filtered histograms in plan view, representing the cases of color-based and luminance-based distinction, are shown in Figure 2.5. Notice that the detection model evaluates the luminance criterion in two-dimensional space, to enable the use of a single numerical code.

The discrimination line l is mathematically described as $l : I_y = p_1 I_x + p_2$, where I_x and I_y represent hue/saturation for color-based discrimination (Figure 2.5a) and value/value for luminance-based discrimination (Figure 2.5b). With the help of l , a discriminator function $\Psi(I_x, I_y)$ is defined such that $\Psi = 0$ along l :

$$\Psi(I_x, I_y) = p_1 I_x + p_2 - I_y \quad (2.1)$$

Evaluation of Eq. (2.1) for all scaled intensity data yields a Ψ value for any pixel within the region of interest. Pixel intensities at the sub-aerial (sub-aqueous) beach are associated with positive (negative) Ψ , for both color-based and luminance-based based cluster distinction. Thus, on the basis of the sign of Ψ , individual pixels can be categorized as being dry or wet (Figure 2.6b).

With the help of surface contour techniques, the location of the shoreline is calculated from the location of the $\Psi = 0$ elevation contours. The result may show erroneous contours at the sub-aerial beach (Figure 2.6a), which are associated with the irregular intensity characteristics of features like water-filled, detached runnel systems or vehicles on the beach. These are removed through application of empirical demands on shoreline persistency in both real-world and pixel space (Appendix B.4). Example results representing color-based and luminance-based shoreline detection at Noordwijk are shown

in Figure 2.7, demonstrating the models' capability to resolve three-dimensional morphology including emerging intertidal bars. The performance of the overall IBM model is quantitatively assessed in Section 2.4, after a description of the Shoreline Elevation Model in the next section.

2.3 The elevation of video-derived shorelines

2.3.1 Background of the shoreline elevation model

This section introduces a model to estimate the elevation of video-derived shorelines (Section 2.1). Like the shoreline detection model, the elevation model aims to estimate the elevation of a specific beach contour identified from standard video imagery. Different concepts for shoreline detection may therefore demand the use of different elevation models or different model parameter settings. As our detection model aims to identify the shoreline location from time-averaged video observations, the elevation model has to account for all physical processes that affect the instantaneous location of the waterline during the ten minutes of time exposure (Janssen, 1997). These processes are the offshore tidal level, wind-induced or surge set-up, breaking-induced wave set-up and swash oscillations (Figure 2.8).

Starting point for the shoreline elevation model is the assumption that video-based shoreline detection techniques identify a beach contour at some location x_{sl} within the swash zone of width Δx_{osc} (i.e. the gray-shaded area in Figure 2.8). x_{sl} does not necessarily coincide with the ten minute time- (hence wave-group) averaged waterline location x_{avg} , but rather represents a location associated with a certain level of swash

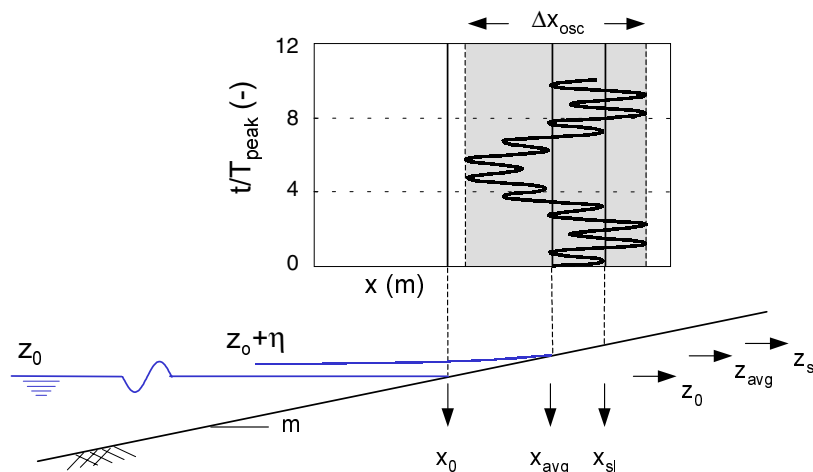


Figure 2.8: *Physical processes affecting the instantaneous waterline location. Artificial timestack of swash run-up on a plane beach with slope m , for an energy spectrum dominated by short waves with peak period T_p and long waves with a period $7T_p$. The instantaneous waterline elevation is affected by the offshore water level z_0 outside the surf zone, the breaking induced wave set-up η and an oscillatory component at the time scale of individual waves and wave groups.*

exceedence (Figure 2.8). Accounting for the hydrodynamic processes involved, the formulation for the corresponding water level z_{sl} at x_{sl} reads

$$z_{sl} = z_0 + \eta_{sl} + K_{osc} \frac{\eta_{osc}}{2} \quad (2.2)$$

where z_0 is the tide- and wind-induced offshore water level without the contribution of wind-generated waves, η_{sl} is the wave-breaking induced mean rise of the water level at the shoreline (hereafter referred to as wave set-up) and η_{osc} represents the vertical swash excursion, related to waterline oscillations at the time scale of individual waves and wave groups. The swash parameter K_{osc} is an empirical coefficient that accounts for the level of swash exceedence as associated with the beach contour returned from a particular shoreline detection model. Positive K_{osc} imply that z_{sl} exceeds z_{avg} , indicating that x_{sl} is located shoreward of x_{avg} , in the region of low swash exceedence.

The three terms z_0 , η_{sl} and η_{osc} that contribute to z_{sl} (Eq. 2.2) will be further addressed in the next three sub-sections. The settings of K_{osc} will be determined from model calibration against field data, as discussed in Section 2.4.

2.3.2 Assessment of the still water level at the shoreline

The offshore water level z_0 is affected by tidal variations Δz_{tide} above a vertical reference level $z = z_{ref}$, the storm surge elevation Δz_{storm} and local wind set-up Δz_{wind} . Δz_{storm} refers to the large scale elevation of the mean water level induced by atmospheric pressure gradients and associated wind fields (CERC, 1984), while Δz_{wind} represents the additional, local water level rise due to wind shear stresses acting on the water body between the measurement pole and the shoreline.

$$z_0 = z_{ref} + \Delta z_{tide} + \Delta z_{storm} + \Delta z_{wind} \quad (2.3)$$

The shoreline elevation preferably adopts locally measured water level data, i.e. measured within a distance of order 10 km from the field site of interest, to estimate the combined contribution of Δz_{tide} and Δz_{storm} . These data account for storm surge induced rises of the mean water level, which may well exceed 1 m along the Dutch coast (e.g., Houwman, 2000), and even rise in excess of several meters along US coastlines (CERC, 1984). Without locally measured water level data, the combined effect of Δz_{tide} and Δz_{storm} can be computed from tide and storm surge models. In the absence of any measured water level and wind data, the elevation model necessarily relies on astronomically predicted tidal levels to approximate Δz_{tide} , thus ignoring the potentially large contribution of storm surges.

The term Δz_{wind} accounts for an additional, local, wind-induced rise of the water level on top of the tide and storm surge related elevation measured at the nearest tidal station. The importance of Δz_{wind} increases with increasing distance between the field site and the water level measurement station, and increasing wind speed. The contribution of Δz_{wind} can be estimated quantitatively from a momentum balance equation, which shows onshore directed wind shear stresses, compensated by offshore directed bottom shear stresses and a sloping water surface. For a measurement station at 10 km offshore and an onshore wind speed of 20 m/s (Beaufort 8-9), this approach

yields for a representative Dutch coastal profile a Δz_{wind} of 6 cm. It is concluded that the contribution of Δz_{wind} is negligible if the water level measurement station is located within 10 km off-shore of the site of interest.

2.3.3 Modelling wave set-up at zero water depth

The dissipation of wave energy induces a rise of the mean water level across the surf zone, referred to as wave set-up. Parametric wave transformation models (Appendix D) are commonly used to describe this wave height decay and associated wave set-up across the surf zone. Validation studies show good model performance in terms of the cross-shore varying wave set-up, for both flume experiments (e.g., Nairn et al., 1990; Reniers & Battjes, 1997) and field conditions (e.g., Garcez Faria et al., 2000).

The shoreline elevation model relies on parametric wave models to predict the decay of H_{rms} and associated wave set-up throughout the surf zone. Estimating η_{sl} (Eq. 2.3) at zero water depth directly from a parametric wave model is, however, not straightforward, since parametric wave models are known to fail in shallow water depth, where the actual wave height exceeds the maximum wave height due to lack of dissipation mechanisms (Battjes & Janssen, 1978). It is for this reason that an operational morphological model like Delft Hydraulics' coastal profile model Unibest-TC (Bosboom et al., 1997) limits its computational domain on the basis of a dimensionless non-linearity parameter T_{nl} , defined as

$$T_{\text{nl}} = T_{\text{p}} \sqrt{\frac{g}{h}} \quad (2.4)$$

where T_{p} is the peak period, g is the gravitational acceleration and h is local water depth. Calculations in shallow water are ceased if T_{nl} exceeds a user-defined threshold value. For a default threshold of 40, the shoreward end of the computational domain is set a location x_{end} , with a water depth of 20 (60) cm for $T_{\text{p}} = 5$ (10) s. This model deficiency hampers the straightforward application of parametric wave models in the context of the shoreline elevation model, which demands an estimate of η_{sl} at zero water depth. An additional hydrodynamic model is necessary to bridge the gap between x_{end} and x_{avg} (Figure 2.8). The latter model (hereafter referred to as the inner surf zone model) is developed here, based on the self-similarity of hydrodynamic processes in the inner surf zone. The inner surf zone model will be described and tested in the remainder of this subsection.

Background of the inner surf zone model

The inner surf zone model is based on the assumed self-similarity of bores propagating onshore through the inner region of the surf zone. The term 'inner region' originates from Svendsen et al. (1978), who describe the breaking wave motion on gently sloping sandy beaches and differentiate between a so-called outer and inner region (Figure 2.9). In the outer region the initial, highly unsteady breaking (ranging from spilling to plunging) takes place over a relatively short horizontal distance of several times the water depth at the breaking point. In the inner region, a relatively well-organized motion develops. The breaking motion is fully turbulent, while the mean motion is quasi-steady.

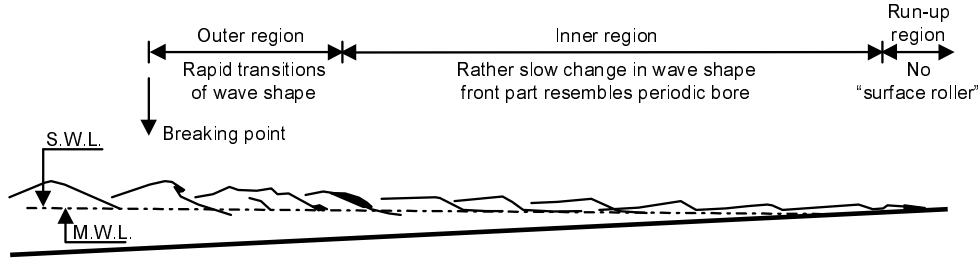


Figure 2.9: *Wave characteristics in the surf zone (after: Svendsen et al., 1978).*

If the depth continues to decrease, the quasi-steady breaking motion (or ‘bore motion’) is maintained until the shoreline is reached.

Detailed flume experiments by Stive (1980) confirm the self-similarity of bores in the inner region as observed by Svendsen et al. (1978). The experiments were carried out in a wave flume of 55 m length, 1 m width and 1 m height, on a plane, concrete beach with a 1:40 slope. Experiments were restricted to two (regular) wave conditions, which are referred to as Test 1 and Test 2 (Table 2.1). The two tests represent ‘spilling’ and ‘plunging’ wave breaking, respectively. Stive (1980) presents his findings on the water motion in shoreward propagating bores in the inner surf zone by means of detailed plots, which show the surface elevation and flow velocity as a function of intra-wave time (Figure 2.10a).

Stive (1980) found that the wave shapes propagating onshore are highly similar, as inferred from the observation that velocities of different characteristic points at the wave front tend to coincide. This conservation of wave shape even holds for waves that originate from different deep water conditions. The water motion throughout the inner surf zone is strongly locally controlled, as can be seen from a nearly constant ratio of wave height over mean water depth. He concluded that his detailed measurements agree encouragingly well with the Peregrine & Svendsen (1978) conceptual model of a quasi-steady breaking wave (Figure 2.10b), which provides further ground for the concept of self-similarity in the inner surf zone.

Instead of solving the commonly-used energy and momentum balance equations (Appendix D) up to zero water depth, our inner surf zone model quantifies the wave height decay and associated wave set-up directly from a system of balance equations describing the depth-controlled, self-similar surface elevation and fluid motion in the inner region as observed by Peregrine & Svendsen (1978) and Stive (1980). The model describes an onshore-propagating bore that passes a location x at time $t = 0$ (Figure 2.11). The bore motion is periodic with period T . The upper layer is located above

Table 2.1: *Overview of wave conditions flume experiments by Stive (1980).*

	Profile	H_0 (m)	H_b (m)	T (s)	L_0 (m)	H_0/L_0 (-)
Test 1	Plane beach	0.159	0.178	1.79	5.00	0.032
Test 2	Plane beach	0.142	0.226	3.00	14.04	0.010

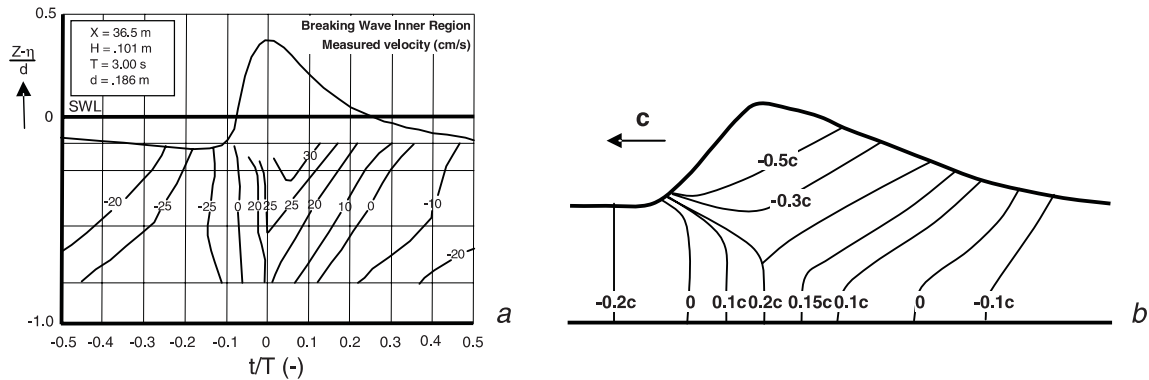


Figure 2.10: *Intra-wave surface elevation and flow velocity of an inner surf zone bore. Detailed flume measurement (Test 2 by Stive, 1980) of a breaking wave entering the inner surf zone (a) and interpretation by Stive (1980) of the Peregrine & Svendsen (1978) model of a quasi-steady breaking wave (b).*

trough level and features a bore with height H_2 , propagating onshore with velocity V over a sloping bottom with elevation z_b . The lower layer with thickness H_1 , extending from the bottom to the trough level, features a net offshore mass flux to balance the onshore mass flux in the upper layer. Depth-controlled self similarity of the water motion causes H_1 , H_2 , and V to decrease with decreasing water depth.

To describe the inner surf zone bore motion, we choose to parameterize the instantaneous layer thickness and flow velocities on the basis of detailed flume experiments by Stive (1980) and to integrate the resulting expressions over the wave period T , to enable the formulation of the time-averaged mass and momentum balance equations in terms of H_1 , H_2 and V . These steps are described below.

Parameterization of layer thickness and flow velocities

This subsection presents non-dimensional parameterizations for the instantaneous layer thickness h_2 and flow velocity v_2 of the upper layer above trough level, as well as the thickness h_1 and velocity v_1 of the lower layer, extending from the bottom to the trough level. The parameterizations are based on the detailed flume experiments by Stive (1980) described above and his interpretation of the Peregrine & Svendsen (1978)

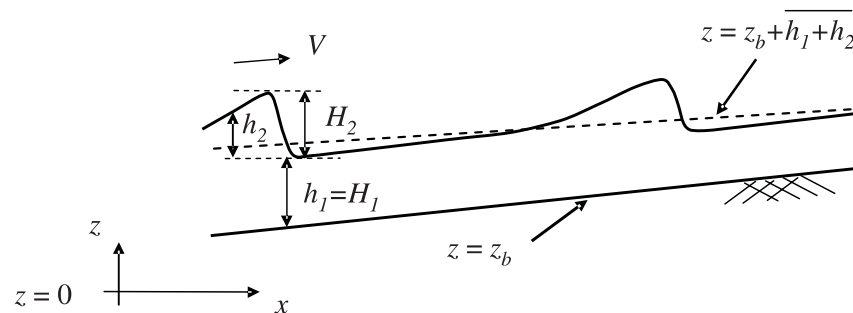


Figure 2.11: *Definition sketch inner surf zone model.*

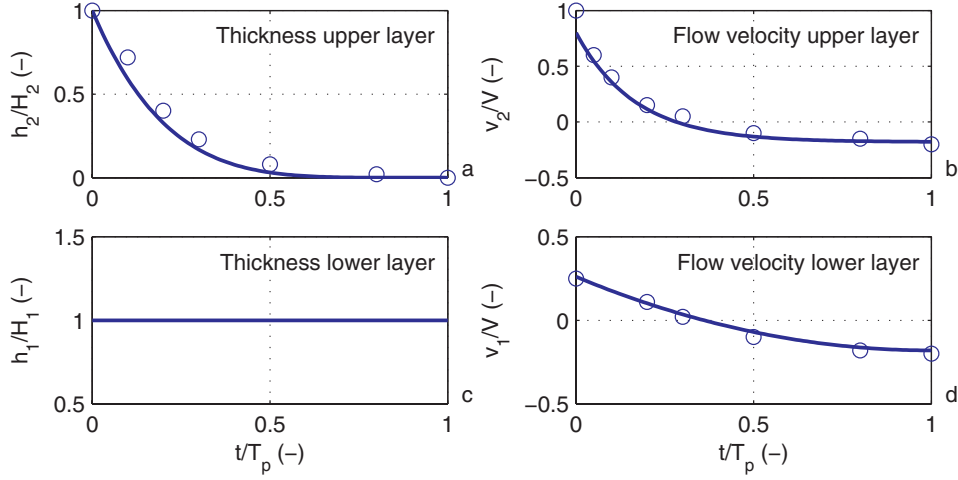


Figure 2.12: *Parameterizations of intra-wave layer thickness (a,c) and flow velocity (b,d) for the upper and lower layer respectively. The parameterizations are plotted against observations (o), derived from detailed flume experiments by Stive (1980) and his interpretation of the Peregrine & Svendsen (1978) model of a quasi-steady breaking wave.*

model of a quasi-steady breaking wave (Figure 2.10). The Stive (1980) Test 2 results are interpreted in depth-averaged sense, which yields ground-truth measurements of the variation of the non-dimensional layer thickness h_1/H_1 (h_2/H_2) and flow velocity v_1/V (v_2/V) of the lower (upper) layer over the wave period T . On the basis of these measurements (denoted by circles in Figure 2.12), the instantaneous layer thickness and flow velocity are parameterized as

$$\frac{h_1}{H_1} = 1 \quad (2.5a)$$

$$\frac{h_2}{H_2} = (1 - t_*)^{a_1} \quad (2.5b)$$

$$\frac{v_1}{V} = a_2 (1 - t_*)^2 + a_3 \quad (2.5c)$$

$$\frac{v_2}{V} = a_4 e^{a_5(1-t_*)} + a_6 \quad (2.5d)$$

where t_* denotes the intra-wave time t/T . To match the Stive (1980) results, the model coefficients are set at $a_1 = 5$, $a_2 = 0.44$, $a_3 = -0.18$, $a_4 = 0.0024$, $a_5 = 6$ and $a_6 = -0.18$. The four parameterizations are visualized in Figure 2.12. The thickness h_2/H_2 of the upper layer shows the arrival of a bore at $t_* = 0$, which induces maximum onshore flow velocities in both the upper and the lower layer. After passage of the bore, the thickness h_2/H_2 and velocity v_2/V of the upper layer rapidly decrease. The velocity v_1/V of the lower layer gradually decreases to become negative, owing to the seaward directed return flow. The intra-wave lower layer thickness h_1/H_1 of the lower layer is constant over time.

Some prudence is required in the application of these parameterizations. Firstly, the formulations according to Eq. (2.5) assume the velocity field to be depth-uniform. This assumption holds reasonably well in the wake region after passage of the bore, however it is certainly violated during the actual passage. Secondly, the magnitude of the flow velocities in the bore itself are largely unknown. The ‘measured’ v_2/V directly after passage of the bore is based on extrapolation of the velocity distribution presented in Figure 2.10b, whereas the value $v_2/V = 1$ at $t_* = 0$ is theoretical. The parameterized value $v_2/V = 0.8$ at $t_* = 0$ reflects the latter uncertainty.

Formulation of the model equations

Integration of the instantaneous expressions (2.5) over the wave period T yields the time-averaged fluxes of mass and momentum in both layers, formulated in terms of three unknowns H_1 , H_2 and V . Balance equations for the conservation of mass and momentum in the overall two-layer system provide two conditions for the inner surf zone model. The system of equations is closed through the assumption of a shallow water approximation for V . The three model equations are briefly addressed here; reference is made to Appendix C for a detailed description of the formulation and implementation of the inner surf zone model.

The time averaged momentum balance equation is formulated on the basis of the conservation of horizontal momentum within an inner surf zone control volume, extending from the bottom to the water surface and bordered by vertical planes. Assuming steady state conditions and neglecting long-wave induced weakly varying acceleration terms, the balance equation for horizontal momentum reads:

$$\begin{aligned} & \frac{\partial}{\partial x} \int_0^1 \int_{z_b}^{z_b+h_1+h_2} p dz dt_* + \frac{\partial}{\partial x} \int_0^1 \int_{z_b}^{z_b+h_1} \rho v_1^2 dz dt_* + \frac{\partial}{\partial x} \int_0^1 \int_{z_b+h_1}^{z_b+h_1+h_2} \rho v_2^2 dz dt_* + \\ & + \int_0^1 p_b \frac{\partial z_b}{\partial x} dt_* + \int_0^1 \tau_b dt_* = 0 \end{aligned} \quad (2.6)$$

where z_b is the local bottom elevation (Figure 2.11), ρ is the density of water and $p = \rho g (z_b + h_1 + h_2 - z)$ is the instantaneous hydrostatic pressure for the vertical range $z_b < z < z_b + h_1 + h_2$, $p_b = \rho g (h_1 + h_2)$ is the hydrostatic pressure near the bottom, $\frac{\partial z_b}{\partial x}$ is the local beach slope and τ_b is the bottom friction, modelled as $\tau_b = \frac{1}{2} \rho f_w v_1 |v_1|$, where f_w is a friction coefficient. In this equation, the first term represents the net contribution of the hydrostatic pressure to the transfer of momentum to the inner surf zone control volume and the second and third term reflect the fluxes of horizontal momentum through the upper and lower layers, respectively. The fourth and fifth term account for the forces effectuated by the sloping bottom and bottom friction.

Conservation of mass at the time scale of the wave period T demands that the net shoreward mass flux above trough level is compensated by a net seaward mass flux in the lower layer,

$$\int_0^1 \int_{z_b}^{z_b+h_1} (\rho v_1) dz dt_* = \int_0^1 \int_{z_b+h_1}^{z_b+h_1+h_2} (\rho v_2) dz dt_* \quad (2.7)$$

Although we realize that the turbulent bore will be strongly aerated hence will have a smaller density, a constant value ρ has been used here. The system of equations is closed through the assumption of a shallow water approximation for V ,

$$V = \sqrt{gh_{\text{bore}}} = \sqrt{g(H_1 + \delta H_2)} \quad (2.8)$$

where h_{bore} is the water depth at the bore crest and δ is an empirical bore velocity coefficient, which accounts for uncertainties in the magnitude of h_{bore} . The coefficient δ will be used for calibration purposes.

Substitution of the intra-wave parameterizations (2.5) in the balance equations (2.6) and (2.7), and accounting for the shallow water approximation for V (Eq. 2.8) yields a system of two coupled, first order differential equations in two unknowns H_1 and H_2 . The equations can be solved numerically, starting from seaward boundary conditions for H_1 and H_2 . This has been achieved by the use of a forward stepping integration method, for which the finite difference terms of the balance equations are formulated in terms of their first order Taylor approximations. Model results obtained from (i) a stand-alone application of the inner surf zone model and (ii) an integrated application where the inner surf zone model is used to extend the computational domain of a conventional parametric wave model to zero water depth are discussed under the next two headers.

Stand-alone calibration and validation of the inner surf zone model

The inner surf zone model has been tested against the flume experiments by Stive (1980), in terms of the predicted bore height decay and associated rise of the mean water level throughout the inner surf zone. Following Stive (1980), the extent of the inner surf zone is determined from the measured data as the region of approximately constant wave height over water depth ratio, which yields a seaward boundary at $x = 38.5\text{m}$ ($x = 39.5\text{m}$) for Stive Test 1 (Test 2). Boundary conditions for the inner surf zone model are derived from the measured wave height (H_{bc}), wave set-up (η_{bc}) and bottom elevation (z_{bc}) at these locations and the still water level z_{SWL} in the flume, by means of

$$H_2 = H_{\text{bc}} \quad (2.9a)$$

$$H_1 = z_{\text{SWL}} + \eta_{\text{bc}} - (z_{\text{bc}} + \int_0^1 h_2 dt_*) \quad (2.9b)$$

Eq. (2.9)a equates the bore height H_2 to the measured wave height H_{bc} , expressing that the upper layer represents the water motion above trough level. The associated H_1 is derived from the demand of continuity of the water surface, by stating that the mean depth at the seaward boundary of the inner surf zone model matches the measured mean depth (Eq. 2.9b). On the basis of known H_1 and H_2 , V can be found from Eq. (2.8). The system thus obtained does not necessarily guarantee conservation of mass

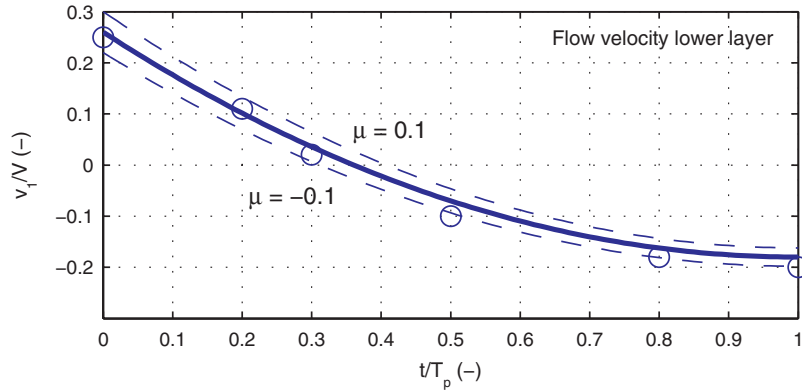


Figure 2.13: *Sensitivity of lower layer flow field to tuning parameter μ .*

at the seaward boundary, because of a possible mismatch between the measured wave conditions and the parameterized inner surf zone conditions. To ensure conservation of mass, a parameter μ is included, which affects the parameterization of the flow velocity in the lower layer (Eq. 2.5c) according to

$$\frac{v_1}{V} = \left(1 + \frac{\mu}{2}\right) \cdot a \cdot (1 - t_*)^2 + (1 - \mu) \cdot c \quad (2.10)$$

A positive μ reduces the net return flow in the lower layer, through an increase in v_1/V during passage of the bore and a reduction of v_1/V in the wake region afterwards. A negative μ reversely affects the flow velocity. Variations of μ over a small range between -0.10 and 0.10 yields modified velocity values that still fit reasonably well with the detailed flume measurements (Figure 2.13). Hence, small values of μ do not violate the starting point of self-similarity of the water motion in the inner region, particularly given the assumptions adopted earlier on parameterization of the instantaneous flow velocity and layer thickness.

The model has been applied to predict bore height decay and associated rise of the mean water level across the inner surf zone for the two test cases described by Stive (1980). To account for mass conservation at the seaward boundary, the model applied minor corrections to the parameterization of the flow field in the lower layer ($\mu = 0.015$ and 0.008 for Test 1 and Test 2, respectively), showing that the parameterized inner surf zone hydrodynamics fit well with the measured wave conditions at the seaward boundary. Standard parameter settings $f_w = 0.01$ and $\delta = 1$ were used for both test cases. The model returns excellent results in terms of bore height decay and wave set-up for both test cases (Figure 2.14), albeit that the slightly decreasing slope of the water surface towards zero water depth (Test 1) was not reproduced. Good performance of the inner surf zone model for Test 1 is particularly encouraging as the parameterizations of the intra-wave layer thickness and flow velocity (Eq. 2.5) were based on Test 2 measurements only.

A concise sensitivity analysis has demonstrated that the behaviour of the inner surf zone model shows limited sensitivity to variable settings of the calibration parameters f_w and δ . Variation of f_w over the range 0.0025-0.10 yields predicted η at zero water depth that differ less than 0.1 cm compared to the results presented in Figure 2.14.

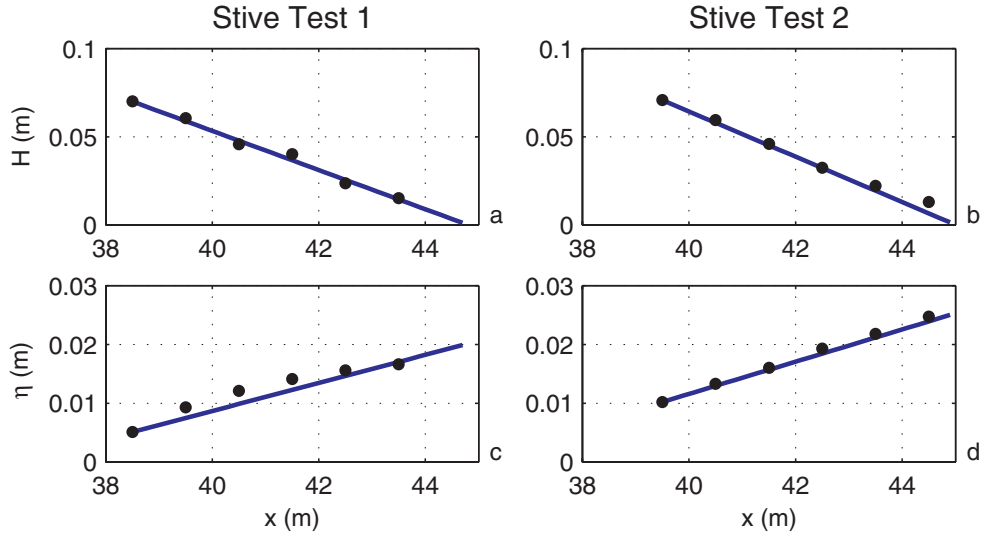


Figure 2.14: Calibration and validation of the inner surf zone model. Model predicted bore height decay (a,b) and wave set-up (c,d) against flume measurements by Stive (1980), Test 1 (a,c) and 2 (b,d).

This corresponds to a minor cross-shore shift of the location of zero water depth in the order of 2-4 cm. Wave set-up across the surf zone slightly increases with increasing f_w . Variation of δ over the range 0-2 yields variations of η in the order of plus or minus 0.5 cm, corresponding to horizontal shifts of about 20 cm in terms of the location of zero water depth. Wave set-up increases with increasing δ . It is concluded that model behaviour in terms of η is less sensitive to f_w as compared to δ .

Operational use of the inner surf zone model

Operational use of the inner surf zone model demands its embedding within the overall context of a parametric wave transformation model. The wave decay model used here consists of two balance equations to describe the transformation of organized wave energy (Battjes & Janssen, 1978) and roller energy (Nairn et al., 1990; Stive & De Vriend, 1994) through the surf zone, using the Baldock et al. (1998) formulation for the dissipation of organized wave energy (see Appendix D). This model is used to predict the wave transformation from deep water across the surf zone up to a point where the non-linearity parameter T_{nl} (Eq. 2.4) exceeds a threshold value. At that point, the inner surf zone model takes over to predict wave height decay and the associated wave set-up towards zero water depth. To avoid artificial (hence unrealistic) gradients, it is important to realize a smooth transition between both models.

At the seaward end of the inner surf zone model, the boundary conditions for H_1 and H_2 according to Eq. (2.9) apply, albeit that H_{bc} , η_{bc} and z_{bc} are derived from the parametric model output rather than field or flume measurements. For the situation with irregular waves considered here, H_{rms} is used as a measure for H_{bc} . The stand-alone model application discussed before readily showed that this approach may violate

Table 2.2: *Overview of wave conditions flume experiments by Boers (1996).*

	Profile	$H_{rms}(m)$	$T_{peak}(s)$	$L_0(m)$	H_0/L_0
Test 1a	Barred beach	0.111	2.05	6.56	0.017
Test 1b	Barred beach	0.146	2.03	6.43	0.023
Test 1c	Barred beach	0.073	3.33	17.31	0.0042

the condition of mass conservation at the seaward boundary, which resulted in the introduction of the correction parameter μ (Eq. 2.10), operating on the parameterization of the flow velocity in the lower layer. This methodology is adopted here to achieve the operational coupling of the two models, in the sense that μ is evaluated along a transition zone Δx_{trans} , ranging from $T_{nl} = 20$ to $T_{nl} = 40$. The latter typically marks the shoreward end of the computational domain of parametric wave models. The seaward boundary of the inner surf zone model is set at the location along Δx_{trans} that returns a minimum absolute value of μ , thus facilitating a smooth transition between both models on the basis of a best match between both water motions.

The operational applicability of the inner surf zone model has been investigated on the basis of experiments, carried out in a wave flume of 40 m length, 0.80 m width and 1.05 m height on a fixed, barred beach profile (Boers & Van de Graaff, 1995; Boers, 1996). The experiments involved three irregular wave conditions, which are referred to as Test 1a, 1b and 1c, respectively (Table 2.2). In terms of wave steepness, Tests 1a and 1b are within the range of wave conditions measured by Stive (1980). Test 1c represents waves of lower steepness.

The inner surf zone model runs were performed with standard parameter settings $f_w = 0.01$ and $\delta = 1$ as obtained from calibration of the stand-alone inner surf zone model against the Stive (1980) experiments. Small μ values well below 0.02 were found at the seaward boundary of the inner surf zone model for all three test cases, confirming the good fit of the parameterized water motion of the inner surf zone model with the hydrodynamics of the parametric wave model. In the case of Test 1c, the seaward limit of Δx_{trans} was set to $T_{nl} = 30$, to prevent the inner surf zone model from starting too far seaward. The results (Figure 2.15) show a smooth extension of the calculated wave height decay and associated wave set-up towards zero water depth. The wave height predicted by the inner surf zone model is small as compared to the corresponding values found from the parametric model, over the entire range of δ considered here. It is therefore concluded that the inner surf zone model indeed enhances wave height decay near the shoreline, thus alleviating the problem that parametric wave transformation models meet at very shallow water depths.

Discussion on the inner surf zone model

In this subsection, we have developed a hydrodynamic model to describe the water motion in the inner surf zone. In operational mode, the inner surf zone model is used to extend the applicability of parametric wave transformation models up to zero water

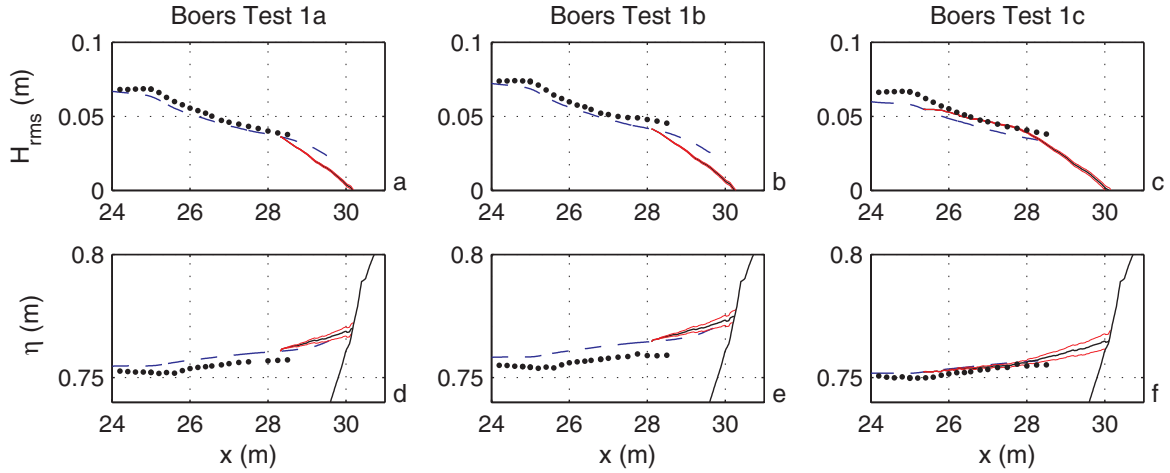


Figure 2.15: *Operational use of the inner surf zone model. Combined application of a standard parametric wave model (Appendix D), extended with the inner surf zone model to continue computations towards zero water depth. Model-predicted wave height decay (a,b,c) and wave set-up (d,e,f) against measured data reported by Boers (1996), Test 1a (a,d), Test 1b (b,e) and Test 1c (c,f). Each plot contains the results of the parametric wave model (dashed line), the inner surf zone model (solid line) and the measured data (dotted line). The thin bands surrounding the solid line - hardly visible in the wave height plots (a,b,c) - represent the variability of inner surf zone model results for δ ranging between 0 and 2.*

depth. The inner surf zone model relies on a parameterization of the water motion, derived from flume experiments by Stive (1980) and a conceptual model of a quasi-steady breaking wave based on Peregrine & Svendsen (1978). Although developed on the basis of detailed measurements of regular waves, the model has demonstrated good behaviour when tested in operational mode against flume experiments by Boers (1996), involving random waves. This can be understood from the depth-controlled self-similarity of the surface elevation and fluid motion in the inner surf zone.

The inner surf zone model shows a rapid decay of wave energy near the shoreline as compared to parametric wave transformation models. As the variability of the computed inner surf zone wave height decay for δ ranging between 0 and 2 (Figure 2.15) is only marginal as compared to the H_{rms} difference between the parametric wave model and the inner surf zone model, it is concluded that the increased wave dissipation rates at very shallow water are primarily driven by the inherent dynamics of the inner surf zone model, embedded in the depth-controlled parameterizations of the intra-wave surface elevation and flow velocity.

So far, the inner surf zone model has not yet been tested over a wide range of random wave conditions, incident at beaches with different slopes. The Stive (1980) flume experiments which provided the starting point for model development span a range of wave height over wave length ratios varying between 0.01 and 0.03. Although model application to Test 1c of the experiments by Boers (1996), characterized by a wave height over wave length ratio of 0.0042, showed realistic behaviour, it is largely

unknown yet to what extent the parameterizations according to Eq. (2.5) apply to situations with very short or long waves. This aspect needs further consideration. A first implication of model application to wave conditions outside the Stive range was already observed, by means of a manual modification of T_{nl} at the seaward end of Δx_{trans} , for application of the inner surf zone model in operational model to Test 1c of Boers (1996). The latter modification, however, has only limited effect on the wave set-up at zero water depth, and hence does not limit model applicability within the framework of this thesis.

2.3.4 Empirical quantification of the swash height

The time-varying oscillation of the waterline on a beach, hereafter referred to as swash, results from standing waves, induced by the reflection of incident waves off the shoreline (e.g., Miche, 1951; Guza & Thornton, 1985). The kinematics and vertical excursion of the swash motion have been extensively studied, for both monochromatic waves (Hunt, 1959; Battjes, 1974) and broadband swash (e.g., Goda, 1975; Huntley et al., 1977; Guza & Thornton, 1982; Holland et al., 1995). On natural beaches the swash amplitude at incident wave periods (frequency $f > 0.05$ Hz) is typically saturated (that is, does not increase with increasing offshore significant wave height H_0), while swash at infragravity frequencies (0.004 - 0.05 Hz) is unsaturated and increases with H_0 (Guza & Thornton, 1982; Holman & Sallenger, 1985; Ruessink et al., 1998b). To quantify the contribution of oscillations at incident and infragravity frequencies to the overall swash height η_{osc} (Eq. 2.2) at the shoreline, we adopt empirical formulations for the sea swell swash height R_{ss} and the infragravity swash height R_{ig} .

On the basis of 154 video-based run-up time series, sampled during a 3-week field experiment at Duck NC (USA), Holman & Sallenger (1985) found the normalized infragravity swash height R_{ig}/H_0 and the normalized sea swell swash height R_{ss}/H_0 both to be linearly related to the Iribarren number ξ_o as

$$\frac{R_{ig}}{H_0} = 0.53\xi_o + 0.09 \quad (2.11)$$

$$\frac{R_{ss}}{H_0} = 0.69\xi_o - 0.19 \quad (2.12)$$

where $\xi_o = \tan(m)/\sqrt{H_0/L_0}$, m is the local foreshore slope and L_0 is the deep water wave length, determined with the peak period T_p . m can be set iteratively, based on a site-specific initial estimate of m and a set of IBM-derived shorelines at low and high tide. Eqs. (2.11) and (2.12) were obtained for ξ_o varying between 0.5 and 3.5. Stockdon et al. (2002) confirm reasonable applicability of these empirical relationships over a range of particularly reflective natural beaches. Analyzing 45 run-up time series sampled at a low-sloping, dissipative beach at Terschelling (Netherlands), Ruessink et al. (1998b) however find a significantly stronger dependency between R_{ig}/H_0 and ξ_o , parameterized as

$$\frac{R_{ig}}{H_0} = 2.20\xi_o + 0.02 \quad (2.13)$$

The Ruessink et al. (1998b) data set has ξ_o ranging between 0.05 and 0.35. The increase in the constant of proportionality compared to Eq. (2.11) is attributed to the saturation of the higher infragravity frequencies for situations with small ξ_o . To accommodate both dissipative and reflective conditions, Ruessink et al. (1998b) suggest a relationship

$$\frac{R_{ig}}{H_0} = 0.65 \tanh(3.38\xi_o), \quad (2.14)$$

which reduces to Eq. (2.13) for highly dissipative conditions. For more reflective conditions, Eq. (2.14) attains a constant value of 0.65, closely matching the relationship reported by Raubenheimer & Guza (1996) but underestimating the parameterization according to Holman & Sallenger (1985) for ξ_o greater than 1.05. The validity of Eq. (2.14) in the transitional range between dissipative and reflective conditions could not unambiguously be established because of a lack of measured data in the ξ_o range between 0.2 and 0.6. Being the only parameterization for R_{ig} that caters for both dissipative and reflective conditions, it is adopted here for use with the shoreline elevation model.

In search of the quantification of R_{ss} , the shoreline elevation model adopts Eq. (2.12) after Holman & Sallenger (1985). To prevent the occurrence of negative R_{ss}/H_0 , which would be obtained for small ξ_o outside the measured range of Holman & Sallenger (1985), R_{ss}/H_0 is set to zero for ξ_o below 0.275

$$\frac{R_{ss}}{H_0} = 0.69\xi_o - 0.19 \quad \text{for } \xi_o > 0.275 \quad (2.15a)$$

$$\frac{R_{ss}}{H_0} = 0 \quad \text{for } \xi_o < 0.275, \quad (2.15b)$$

thus ignoring the short-wave contribution to swash oscillations during highly dissipative conditions ($\xi_o < 0.275$). The latter can be justified from the measurements by Ruessink et al. (1998b), who found an average ratio of infragravity to total swash height R_{ig}/R of 0.85. As both R_{ig} and R_{ss} are determined as a fraction of the offshore significant wave height H_0 defined as 4σ , where σ is the standard deviation of the sea surface elevation, the overall η_{osc} can be calculated as

$$\eta_{osc} = \sqrt{R_{ig}^2 + R_{ss}^2} \quad (2.16)$$

where R_{ig} and R_{ss} are obtained from the empirical parameterizations (2.14) and (2.15), respectively. The result obtained from Eq. (2.16) is used to estimate z_{sl} (Eq. 2.2), applying a swash parameter K_{osc} to account for the level of swash exceedence as associated with the beach contour obtained from the shoreline detection model. The validation of IBM including the assessment of best parameter settings for K_{osc} for Egmond is described in the next section.

2.4 Investigation of IBM model performance

2.4.1 Introduction

In the previous Sections 2.2 and 2.3, the two sub-models that compose IBM were described individually and - if necessary - tested in stand-alone mode. In this section,

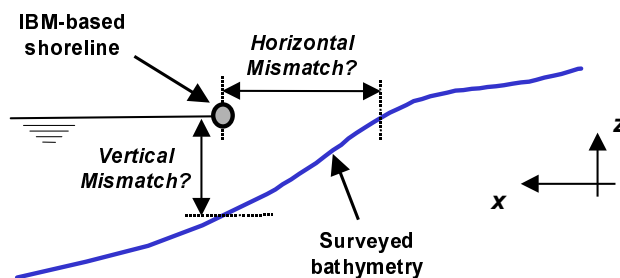


Figure 2.16: *Assessment of IBM model accuracy on the basis of bathymetrical data. Example mismatch between an IBM-derived beach contour and a surveyed bathymetry. It remains unclear whether the deviation originates from the shoreline detection model (causing a horizontal offset) or the shoreline elevation model (inducing a vertical offset).*

the performance of the overall model IBM is tested against a data set of GPS-surveyed shorelines at a nourished beach at Egmond (Subsection 2.4.2) and compared to the results obtained from alternative shoreline detection techniques (Subsection 2.4.3). In this validation section, the focus is on the quantification of model inaccuracies. The background and morphological evolution of the Egmond nourishment is further described in Chapter 4, based on the results obtained from the intertidal beach mapper described here and the subtidal beach mapper, presented in Chapter 3.

2.4.2 Model validation against GPS surveyed shorelines

Overall IBM model performance is governed by deviations resulting from either the shoreline detection model or the shoreline elevation model. The aim of this subsection is to address the accuracy of both sub-models individually, and thus to assess which sub-model primarily governs IBM model performance. This cannot be achieved on the basis of common beach elevation maps $(x, y, z)_b$, since deviations between the video-derived beach contour and the surveyed bathymetry cannot be attributed to either one of the sub-models (Figure 2.16). Instead, we need field measurements of the shoreline, resolving its time-averaged location and elevation during the ten minutes of time-exposure for image collection. In this study, IBM model performance is therefore assessed on the basis of a data set of GPS-surveyed shorelines.

A data set of 52 measured shorelines was collected at a nourished beach in front of the Egmond boulevard, during the periods November 29-30, 1999 and March 14-15, 2000 (Caljouw, 2000; Nipius, 2002). The shoreline surveys were conducted by driving a differential GPS system, mounted on a four-wheel drive vehicle, over a distance of approximately 2 km alongshore, at the shoreward end of the swash zone. This yields a data set of beach contours with an expected vertical accuracy of less than 10 cm. The surveys were carried out on a half-hourly basis, simultaneously with the recording of time-averaged video images by the five-camera ARGUS video station, mounted at 43 m above sea level on top of the Egmond lighthouse 'Jan van Speyk'. Offshore wave conditions (H_{rms0} , T_p and θ_0) were measured with a directional wave buoy at IJmuiden, located approximately 15 km to the south of the nourished site. Offshore tidal levels

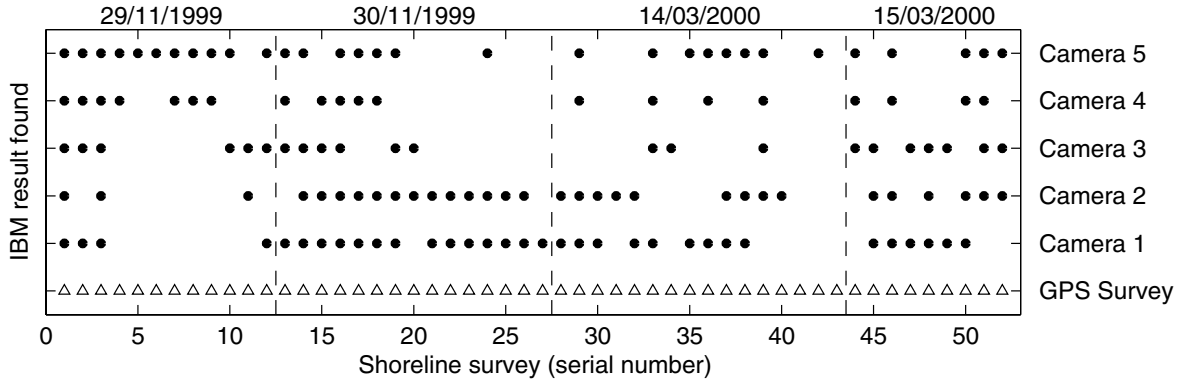


Figure 2.17: *Overview of the Egmond data set for IBM validation. Triangles denote the 52 GPS-surveyed shorelines, conducted over four different days. The filled circles indicate the images that allowed for the reliable detection of a video-derived shoreline.*

are found from interpolation in water level data collected at tidal stations located 15 km north and south of Egmond. During the experiment, $H_{\text{rms}0}$ ranged between 0.6 and 2.3 m, while the offshore tidal level spanned a range between -0.7 and 1.0 m with respect to the Dutch datum NAP.

IBM was used to map shorelines from all 260 images collected concurrently with the field measurements. On the basis of visual inspection, 137 shorelines were accepted for further analysis (Figure 2.17). Lacking recent information on the surf zone bathymetry, η_{sl} (Eq. 2.2) was estimated by running the inner surf zone model in operational mode on an equilibrium beach profile (Dean, 1977). Janssen (1997) has shown that this simplification introduces only minor deviations of order 1-2 cm in terms of η_{sl} . The foreshore slope m at the intertidal beach is set at a fixed value 1:40 for Egmond. The settings of m affect the slope of the equilibrium profile and the value of ξ_0 , hence the empirical estimate of η_{osc} . Deviations between the video-based and GPS-surveyed shorelines are evaluated on a grid with 2 m alongshore spacing.

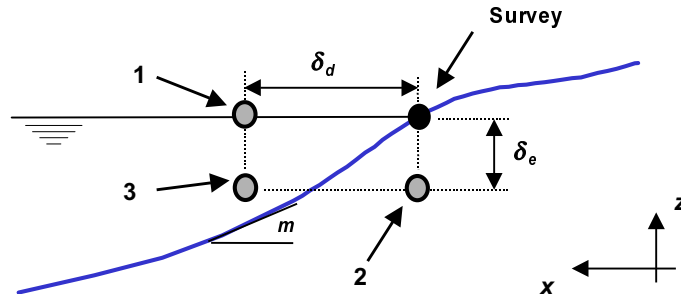


Figure 2.18: *Assessment of IBM model accuracy against GPS-surveyed shorelines. Quantification of model deviations by means of detection and elevation induced offsets δ_d and δ_e . Scenario 1 represents perfect performance of the elevation model, Scenario 2 represents perfect performance of the detection model and Scenario 3 the general case with non-zero δ_d and δ_e .*

To enable separate assessment of the two sub-models' performance, deviations between modelled and surveyed shorelines are quantified as a horizontal offset δ_d , induced by the shoreline detection model, and a vertical offset δ_e , induced by the elevation model (Figure 2.18),

$$\delta_d(y, t) = x_v(y, t) - x_s(y, t) \quad (2.17)$$

$$\delta_e(y, t) = z_v(y, t) - z_s(y, t), \quad (2.18)$$

where $x_s(y, t)$ is the surveyed shoreline position x (positive offshore) at alongshore location y and time t , and $x_v(y, t)$ the corresponding shoreline position derived from video. Similarly, $z_v(y, t)$ ($z_s(y, t)$) represents the shoreline elevation obtained from video (field survey). To facilitate the comparison, both deviations are interpreted as vertical offsets δz_d and δz_e , which demands the mapping of δ_d on a vertical plan using the foreshore beach slope m , assuming m to be small such that $\tan(m) \approx m$:

$$\delta z_d(y, t) = m \cdot \delta_d(y, t) \quad (2.19)$$

$$\delta z_e(y, t) = \delta_e(y, t) \quad (2.20)$$

Quantification of the overall model error as $\delta z = \sqrt{(\delta z_d)^2 + (\delta z_e)^2}$ would yield an upper limit of the model accuracy. This can be explained with the help of Figure 2.18. In the case of a perfect estimate of the shoreline elevation (Scenario 1, $\delta_e = 0$), δz is entirely governed by the detection induced error δ_d . In the case of perfect estimate of the shoreline location combined with a poor elevation estimate (Scenario 2), the opposite occurs. In general, both δ_d and δ_e will be non-zero. If δ_d and δ_e have opposite signs, errors resulting from both sub-models compensate each other. This situation occurs, for instance, if a seaward offset of the video-derived location of the shoreline is compensated by an underestimated shoreline elevation (Scenario 3). In other words, an IBM-derived shoreline can be fairly close to the actual *bathymetry*, even though it is relatively far from the GPS-surveyed *shoreline*. To account for this mechanism of mutual error compensation, the overall error $\delta z(y, t)$ is determined as the sum of δz_d and δz_e ,

$$\delta z(y, t) = \delta z_d(y, t) + \delta z_e(y, t). \quad (2.21)$$

The individual performance of the detection (elevation) model is quantified by means of the mean $\mu_{\delta z_d}$ ($\mu_{\delta z_e}$) and standard deviation $\sigma_{\delta z_d}$ ($\sigma_{\delta z_e}$) of δz_d (δz_e) across all shoreline estimates, as a function of the alongshore location y (Figure 2.19). The number of shorelines contributing to the statistics at a certain location y^* varies with the location along the shore. Statistics were only determined if at least ten shorelines were found in y^* , out of a maximum of 52. As a result, 4.3% of the grid points, all located in overlap regions between cameras or at the northern end of the area of interest, were excluded from the statistical analysis.

The results show negative $\mu_{\delta z_d}$ along virtually the entire area of interest, indicating that video-derived shorelines are located landward of the surveyed shorelines. In an absolute sense, the detection induced deviations $\mu_{\delta z_d}$ are well below 20 cm (with a relatively constant $\sigma_{\delta z_d}$ of about 15 to 20 cm) along a major part of the area of interest, except for the far-field region to the north of the video station. Application of the elevation model typically yields mean deviations $\mu_{\delta z_e}$ up to 10 cm, with a $\sigma_{\delta z_e}$ in the

Table 2.3: *Characterization of IBM model deviations. Percentage of area of interest with $|\mu_{\delta z}|$ below threshold value.*

Criterion	Area that obeys criterion
$ \mu_{\delta z} < 5 \text{ cm}$	39.8%
$ \mu_{\delta z} < 10 \text{ cm}$	64.4%
$ \mu_{\delta z} < 15 \text{ cm}$	85.5%
$ \mu_{\delta z} < 20 \text{ cm}$	91.1%
$ \mu_{\delta z} < 25 \text{ cm}$	94.0%

order of 10 to 15 cm. The local increase in $\mu_{\delta ze}$ and $\sigma_{\delta ze}$ near $y = 800 \text{ m}$ is related to the presence of a local seaward morphological extension (clearly visible on plan view images of November 29, 1999), which induces a local increase in z_s , hence negative $\mu_{\delta ze}$.

Similar patterns are observed when considering the overall model performance in terms of the mean $\mu_{\delta z}$ and standard deviation $\sigma_{\delta z}$ of δ_z across all shoreline estimates

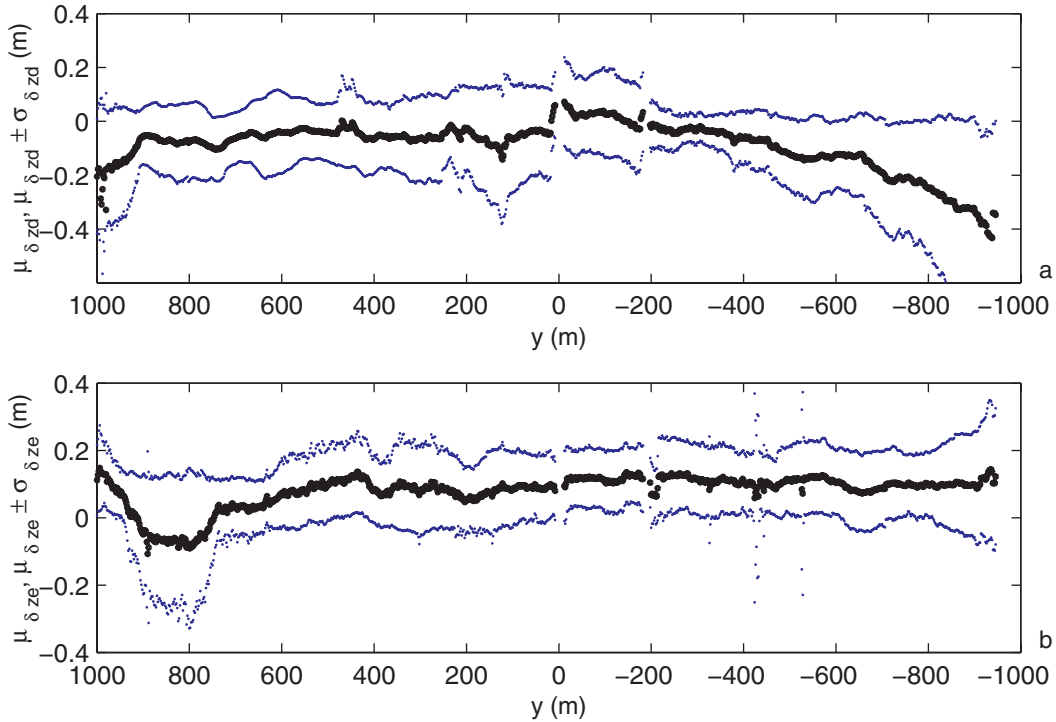


Figure 2.19: *Error quantification IBM per sub-model. Mean and standard deviation of the detection (a) and elevation induced (b) vertical offsets δz_d and δz_e , across all shoreline estimates. Bold dots represent the mean offset as a function of the location alongshore, fine dots visualize the scatter representing the mean \pm the standard deviation. The positive y-axis is pointing south, with the video station being located around $y = -120 \text{ m}$.*

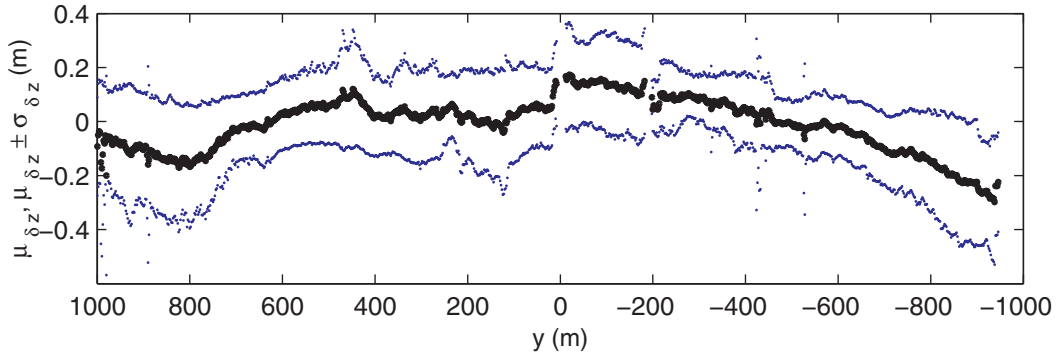


Figure 2.20: *Error quantification IBM overall model. Mean and standard deviation of the overall vertical offsets δ_z over time. Bold dots represent the mean offset as a function of the location alongshore, fine dots visualize the scatter representing the mean \pm the standard deviation. The positive y -axis is pointing south, with the video station being located around $y = -120$ m.*

(Figure 2.20), albeit that the absolute magnitude of the deviations decreases owing to the mutual compensation of errors resulting from the individual sub-models. μ_{δ_z} typically amounts to 10 to 20 cm along the entire region of interest, except for the far-field region north of the video station where $|\mu_{\delta_z}|$ increases locally up to 30 cm. In absolute sense, μ_{δ_z} is less than 15 cm along 85% of the 2 km wide area of interest (Table 2.3), which corresponds to a horizontal offset of 6 m. With σ_{δ_z} in the order of 15 to 20 cm throughout most of the region of interest, the scatter of results is fairly constant, with larger values again found in the far-field region to the north and the non-uniform area near $y = 800$ m.

The results presented so far were obtained with a setting 1.20 for the swash parameter K_{osc} (Eq. 2.2). To assess IBM model sensitivity to variable K_{osc} , Table 2.4 summarizes model performance for different K_{osc} , quantified by means of the *rms* error of the detection induced δz_d (Eq. 2.19), the elevation induced δz_e (Eq. 2.20) and the overall offset δz (Eq. 2.21), involving a total number of 29551 samples that compose the entire data set of 137 video-based shorelines. The modelled shoreline elevation increases with increasing K_{osc} , which yields a decrease in the *rms* value of δz_e for K_{osc} ranging

Table 2.4: *Sensitivity of IBM model performance to variable K_{osc} .*

K_{osc}	<i>rms</i> (δz_d) [m]	<i>rms</i> (δz_e) [m]	<i>rms</i> (δz) [m]
0.20	0.194	0.209	0.318
0.50	0.194	0.153	0.259
0.80	0.194	0.122	0.211
1.00	0.194	0.125	0.190
1.20	0.194	0.148	0.182
1.40	0.194	0.182	0.188

from 0.2 to 1. For K_{osc} above 1, the *rms* value of δz_e increases, indicating that the modelled shoreline elevation increasingly exceeds the surveyed elevation. However, the combined error, quantified by means of the *rms* value of δz , further decreases for K_{osc} values in exceedence of 1. This reflects the mechanism of mutual error compensation noted earlier: A landward offset of the video-derived shoreline location as regard to the surveyed location is compensated by an associated overestimate of the modelled shoreline elevation as compared to the surveyed elevation. Minimum deviations in terms of δz_e are obtained with a parameter setting $K_{\text{osc}} = 1.2$, which is the value adopted here. The optimum value $K_{\text{osc}} = 1.2$ suggests that IBM identifies a shoreline near the higher end of the swash run-up, which is confirmed in the next sub-section.

2.4.3 Comparison of IBM to alternative shoreline detection models

In continuation of the model validation against the data set of GPS-surveyed Egmond shorelines (Sub-section 2.4.2), IBM model behaviour and performance is further investigated on the basis of a comparison of the results obtained from the application of four video-based shoreline detection models at three distinctive ARGUS field sites worldwide (Aarninkhof et al., 2002). Besides IBM, this analysis involves the application of

- the SLIM model (Plant & Holman, 1997; Madsen & Plant, 2001), which determines the location of the wave breaking induced ShoreLine Intensity Maximum (SLIM) as a proxy for the shoreline. The SLIM model operates on grayscale video data.
- the ANN model (Kingston et al., 2003), which adopts an Artificial Neural Net (ANN) to delineate a shoreline from differences in the color characteristics of pixels located at the dry and wet beach. The ANN model can be considered a non-linear version of IBM.
- the CCD model (Turner et al., 2000; Turner & Leyden, 2000). The Color Channel Divergence (CCD) model utilizes the divergence of the red, green and blue color bands in the swash zone, induced by the high reflectivity of ambient light at wave lengths corresponding to blue colors from the ocean surface.

A brief background on these model concepts is provided in Appendix E. The four shoreline detection models were applied to identify shorelines from a data set of 43 time exposure images collected at Duck NC, 26 images collected at Teignmouth and 44 images

Table 2.5: *Characterization of hydrodynamic regime per field site.*

Field site	H_0 (m)	T_p (s)	m (-)	ξ_o (-)
Duck NC (USA)	0.3-4.0	7-12	1:8-1:12	0.62-2.00
Egmond (NL)	0.4-3.5	4-9	1:30-1:50	0.12-0.27
Teignmouth (UK)	0.3-2.0	4-10	1:10-1:100	0.09-0.91



Figure 2.21: *Time exposure image of Duck NC (USA), Teignmouth (UK) and Egmond (NL), showing the dissimilar morphological characteristics of the field sites involved in the comparison analysis of shoreline detection models.*

sampled from the Egmond station ‘Jan van Speyk’. Each field site features unique characteristics as regard to the (intertidal) morphology (Figure 2.21) and hydrodynamic regime, characterized by representative ranges of H_0 , T_p and m , and the resulting ξ_o (Table 2.5). The entire data set of 113 images spans seven different days, each accompanied with the measured tide and wave conditions offshore and detailed survey data of intertidal beach bathymetry. Survey data are interpolated to data grids with an alongshore (cross-shore) spacing of 10 (5) m. At Duck, the cross-shore grid spacing was refined to 2 m because of the steep beach face.

Application of the four detection models to the testbank described above yields 92, 86, 98 and 59 video-derived shorelines for the IBM, SLIM, ANN and CCD model, respectively. This forms a data set of 335 shorelines in the horizontal plane, which were interpolated to data grid coordinates (x_i, y_i) . To enable the evaluation of model performance in terms of the vertical deviation between video-derived and surveyed beach contours, we determine the mean surveyed elevation $\langle z_s \rangle$ along each individual shoreline by averaging the surveyed beach elevations $z_s(x_i, y_i)$ involved. The corresponding modelled shoreline elevation z_{sl} is estimated with the help of the shoreline elevation model developed in Section 2.3, using an optimal K_{osc} value for each of the four detection techniques. Optimal K_{osc} settings for each detection technique were found from a linear regression analysis of z_{sl} against $\langle z_s \rangle$, across all three field sites. The regression analysis yields K_{osc} of 1.37, -0.28, 0.40 and 0.92 for the IBM, SLIM, ANN and CCD mod-

Table 2.6: *Performance of each shoreline detection model, quantified by means of the rms value of Δz_i per site.*

Model	Duck NC	Teignmouth	Egmond
IBM	0.14	0.39	0.17
SLIM	0.39	0.67	0.44
ANN	0.16	0.27	0.23
CCD	0.11	-	0.35

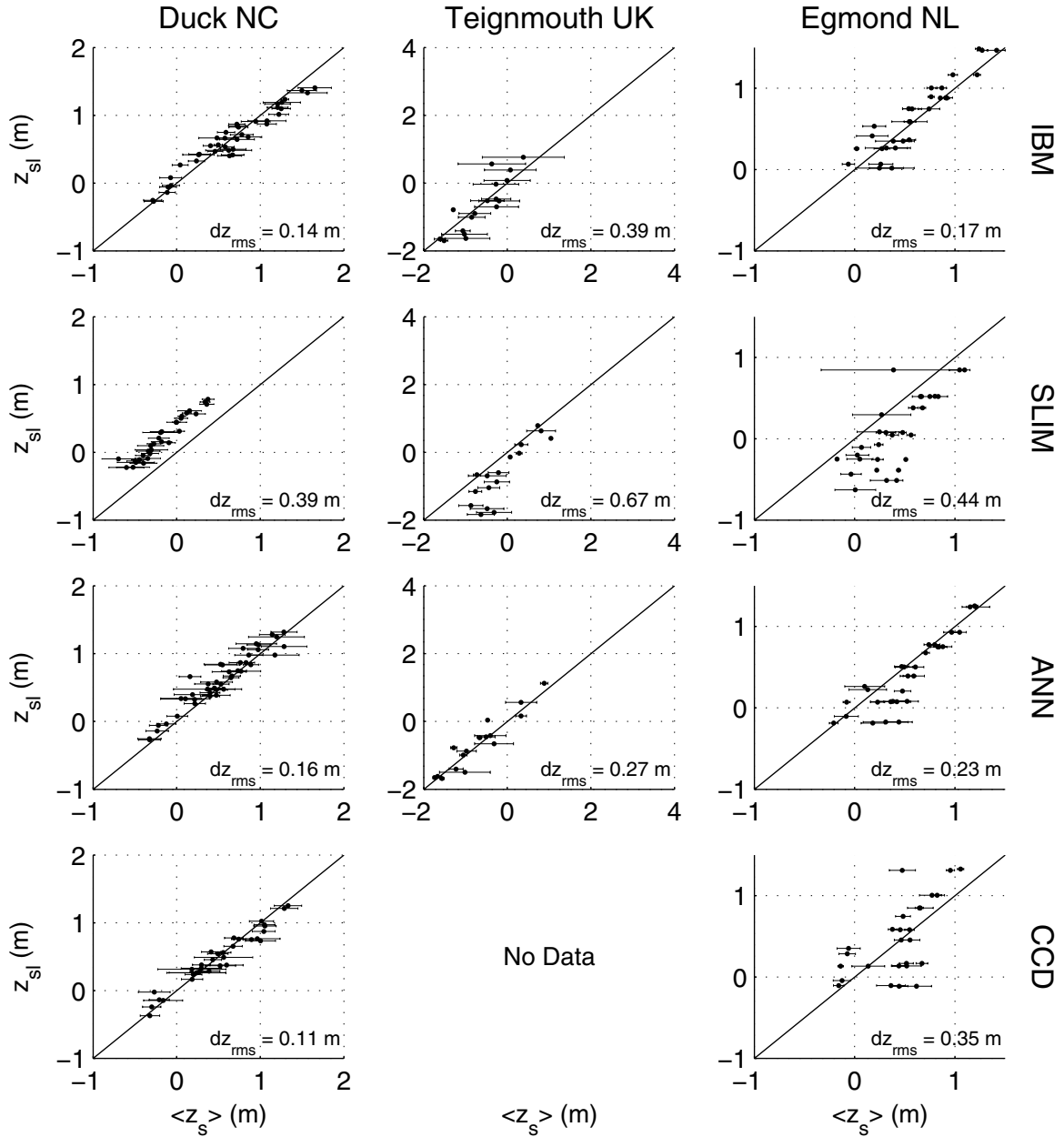


Figure 2.22: Performance of shoreline detection models at Duck NC, Teignmouth and Egmond. Assessment of model accuracy on the basis of z_{sl} versus $\langle z \rangle$. The horizontal error bands around $\langle z \rangle$ represent the standard deviation of the surveyed bottom elevations $z(x_i, y_i)$ along each video-derived shoreline located at (x_i, y_i) .

els, respectively, confirming that IBM identifies a shoreline near the higher end of the swash run-up. The overall performance of each shoreline detection model is quantified by means of the *rms* value of vertical shoreline offsets Δz_i per site (Table 2.6, see also Figure 2.22), where Δz_i is calculated as

$$\Delta z_i = \langle z_s \rangle - z_{sl}. \quad (2.22)$$

With *rms* errors of less than 20 cm, IBM shows good performance at Duck and Egmond. Owing to poor image quality with hardly any color contrast between dry and wet, the *rms* error of the IBM results at Teignmouth increases up to 37 cm. This behaviour matches the observations for the SLIM and ANN model, while the CCD model does not return any results at all at Teignmouth. Considering the deviations of all four shoreline detection models investigated here, it is concluded that IBM shows second best performance across the entire range of sites, closely behind its non-linear equivalent ANN, the latter yielding better results at Teignmouth. These observations demonstrate the generic applicability of IBM over a wide range of hydrodynamic, morphological and atmospheric conditions.

2.4.4 Discussion on IBM behaviour and performance

In this section, IBM was applied in the context of a validation study at Egmond and a comparative study involving the use of IBM and three alternative shoreline detection models at three distinctive field sites worldwide. Both studies involved the analysis of many time exposure images sampled over a wide range of hydrodynamic, morphological and atmospheric conditions, which yields a considerable scattering of the peak locations of the filtered clusters of dry and wet pixels in both the color and luminance domain (Figure 2.23). Both domains show an overlap region where clusters of dry as well wet pixels may be located. It is therefore not possible to identify a generic distinction criterion with fixed settings in hue/saturation or value space, for application to time exposures image from any ARGUS station worldwide. Instead, the detection model necessarily determines a distinction criterion for every single image, which facilitates the model's generic applicability. Successful applications at several ARGUS field sites

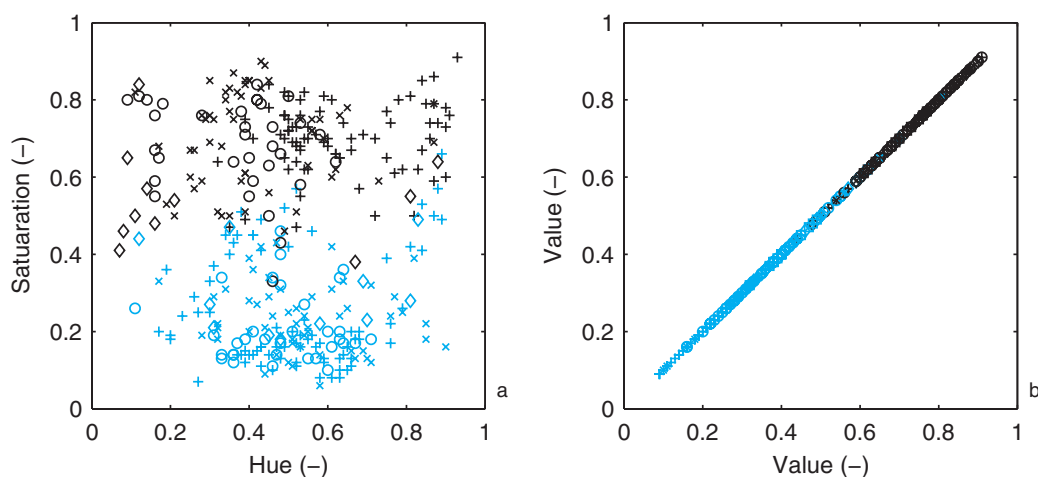


Figure 2.23: Variability of the location of the filtered clusters of dry (gray) and wet (black) pixels in the color (a) and luminance (b) domain. Scattering of peak locations for 191 shorelines mapped at Egmond, Netherlands (+), 74 shorelines at the Goldcoast, Australia (o), 78 shorelines at Duck NC, USA (x), 56 shorelines at Teignmouth, UK (\diamond) and 12 shorelines at Miyazaki, Japan (\square).

worldwide, including Miyazaki (Suzuki et al., 2002), Goldcoast (Dronkers, 2001; Turner et al., 2003), Barcelona (Guillén et al., 2002) and Egmond (Aarninkhof et al., 2000), confirm the potential of IBM for generic use.

The IBM model results show a tendency towards a seaward shift of the video-derived shoreline location in regions close to the camera station, as can be seen from the less negative values of $\mu_{\delta_{zd}}$ (Figure 2.19a). Similar behaviour was observed from the application of the ANN model at the Goldcoast (Turner & Leyden, 2000). Besides, Dronkers (2001) questions the consistency of the mixed application of a color-based and luminance-based distinction criteria. Both observations demand a further exploration of the physical background of the shoreline characteristic as identified from time-averaged video imagery.

Model validation against a data set of GPS-surveyed shorelines at Egmond has shown that mean vertical deviations, in an absolute sense, are less than 15 cm (corresponding to a mean horizontal offset of 6 m) along more than 85% of the overall area of interest, which covers 2 km alongshore. Model deviations increase with increasing distance from the video station. The bulk statistics on the overall data set of 29551 shoreline samples (Table 2.7) demonstrate that the detection induced mean vertical deviation of -8.5 cm (reflecting a landward offset of the video-derived shoreline location) is largely compensated by an elevation induced positive offset of 7.8 cm (indicating that the modelled shoreline elevation exceeds the surveyed elevation). The scatter of the overall model deviations is dominated by uncertainties resulting from the shoreline detection model, as can be seen from the standard deviations reported in Table 2.7. The overall model deviations $\mu \pm \sigma$ found here are of same order of magnitude as the vertical excursion of the oscillating swash motion, consistent with the fact that that IBM identifies shorelines within the swash region on the basis of time-averaged video images.

The increase in $|\mu_{\delta_{zd}}|$ and $\sigma_{\delta_{zd}}$ with increasing distance from the video station can be explained by a lack of representativeness of the discriminator function Ψ for the far-field regions of the area of interest. The present version of IBM samples pixel intensities directly from oblique images. Owing to a decrease in the resolution (Figure 1.7) in the far field (i.e., each pixel covers a larger area), far-field information is relatively poorly represented. Consequently, the histogram of image intensities (Figure 2.5) and the discriminator function resulting from that are dominated by near-field intensity characteristics, which negatively affects model performance in the far-field. Besides, atmospheric effects are anticipated to predominantly affect image clarity, hence model performance, in the far field. Poor model performance in the far-field to the north of

Table 2.7: *Bulk statistics (mean and standard deviation) on the overall data set of 29551 Egmond shoreline samples.*

Parameter	μ (m)	σ (m)
δz_d (detection model)	-0.085	0.174
δz_e (elevation model)	0.078	0.126
δz (overall model)	-0.007	0.182

the video station is further explained from the presence of buildings, which obscure the camera view at the dry beach, thus further limiting the opportunities for pixel clustering through a decrease in the size of the cluster of dry pixels.

Apart from imperfections in the shoreline detection and elevation models, the model accuracy reported here is also affected by the survey data. This observation concerns the survey method rather than the fundamental measurement accuracy of the differential GPS system (1-2 cm), which is an order of magnitude better than the model accuracy found here. IBM assumes constancy of the time-averaged shoreline elevation during the ten minutes of time exposure for image collection. So an ideal shoreline measurement would be surveyed along a perfectly horizontal track. This is hard to achieve in the field where the instantaneous location of the waterline is permanently affected by oscillating swash motions over a complex intertidal bathymetry. The 137 GPS-surveyed shorelines sections that were used to quantify the offset of the corresponding 137 IBM derived shorelines show a *mean* standard deviation of 4.7 cm, stating that the scatter values $\sigma_{\delta z}$ reported here are partly explained from variabilities in the ground truth data.

The model comparison study (Subsection 2.4.3) has demonstrated the generic applicability of the shoreline elevation model developed here. This involves the use of model-dependent settings of the swash parameter K_{osc} , confirming our qualitative observation that different video-based shoreline detection concepts each identify a different shoreline characteristic from time-averaged video imagery. The stand-alone calibration of K_{osc} against a data set of GPS-surveyed Egmond shorelines yields a best setting $K_{\text{osc}} = 1.2$, whereas the calibration on the basis of the multi-site application involving Duck, Teignmouth and Egmond resulted in a best setting $K_{\text{osc}} = 1.37$. This increase can be explained from the inclusion of two additional sites in the comparison study, yielding best K_{osc} settings of 1.49, 1.56 and 1.22 for Duck, Teignmouth and Egmond, respectively. The Egmond value however closely matches the best setting $K_{\text{osc}} = 1.2$, found from the stand-alone Egmond calibration.

The calibration of four different shoreline detection models at three distinctive ARGUS field sites has resulted in a relatively large K_{osc} for IBM as compared to alternative models, indicating that IBM identifies a shoreline feature near the higher end of the region of wave run-up. Field observations of swash motions show that maximum swash exceedence levels ζ decrease with increasing spectral width ϵ_s of the swash spectrum in the range $0.75 < \epsilon_s < 1$ (Holland & Holman, 1993). This dependence however decreases with decreasing levels of swash exceedence, yielding a 2% exceedence level $\zeta_{2\%}$ which is virtually insensitive to variable ϵ_s conditions. This implies that detection methods like the SLIM model which identify a shoreline at the seaward side of the swash zone have to deal with this natural variability in ϵ_s . In contrast, color-based methods, particularly IBM, tend to identify a shoreline further onshore, in regions of lower swash exceedence levels which are less affected by the natural variability in ϵ_s . This makes model results consistent and contributes to the relatively good performance of the color-based shoreline detection models.

Apart from the fact that IBM identifies a shoreline near the upper end of the swash run-up, the large optimal K_{osc} found here also suggests that the empirical swash formulations which form the basis of the shoreline elevation model tend to underestimate the real-world vertical swash excursion. The latter may well be the case, as Eq. (2.15) ig-

nores the short-wave contribution R_{ss} at dissipative beaches ($\xi_o < 0.275$). For reflective conditions characterized by $\xi_o > 1.05$, the Ruessink et al. (1998b) parameterization for infragravity swash (Eq. 2.13) underestimates the Holman & Sallenger (1985) relationship. Both aspects contribute to an underestimate of the real-world vertical swash excursion over a wide range of ξ_o , which is compensated by the large K_{osc} settings found here. Besides, it may be questioned whether a generic parameterization of R_{ig} and R_{ss} as a function of local short-wave parameters (quantified through ξ_o) is achievable at all. On the basis of the analysis of wave observations in intermediate water depths, Herbers et al. (1995) found that the amount of infragravity energy not only depends on ξ_o , but also on large-scale morphology like shelf width. Further exploration of the Herbers et al. (1995) findings goes beyond the scope of this thesis. We conclude that model- and (preferably) site-dependent calibration of K_{osc} accounts for uncertainties in both the location of the shoreline feature identified from time-averaged video imagery and the associated elevation estimated from the empirical parameterizations for the vertical swash excursion.

2.4.5 Furthering IBM performance and applicability

Furthering the performance and applicability of IBM may be achieved by improving the accuracy of the shoreline detection model, by improving the accuracy of the elevation model or by improving the operational usability of the model. The potential for furthering each of these three elements is discussed here.

To improve the accuracy of the shoreline detection model, it is recommended to focus future research efforts on

- Enhancing IBM performance in the far field through better representation of far-field pixel intensities in the procedure to determine the discriminator function Ψ . The present model operates on oblique images, which induces a poor representation of far-field pixel intensities, owing to decreasing pixel resolutions. By sampling pixel intensities from plan-view rectified images, the number of pixels per unit area is constant, which yields a balanced distribution of near- and far-field pixels. The discriminator function thus obtained may provide improved far-field performance.
- Eliminating the inconsistency of IBM Gold Coast results as induced by the application of combined color and luminance criteria (Dronkers, 2001). This can be achieved through integration of the two distinction criteria, by determining Ψ in 3-dimensional color space (*pers. comm.* O. Chic, CSIC, Barcelona, Spain). This model improvement involves an integrated approach on the three color bands hue, saturation and value, rather than separate analyses in the color and luminance domains. As a first step, the IBM graphical user interface can be extended with an option that allows the user to specify the criterion he prefers to use (that is, color, luminance, or both).

Optimal performance of the shoreline elevation involved the use of relatively large K_{osc} , which was attributed to an underestimate of the vertical swash excursion η_{osc} . Improving the shoreline elevation model at this point demands a reconsideration of the

empirical expressions for the vertical swash excursion R_{ig} and R_{ss} , at infragravity and incident wave frequencies, respectively. First, the Ruessink et al. (1998a) expression for R_{ig} adopted here is known to underestimate the Holman & Sallenger (1985) parameterization in the range of large ξ_o above 1.05, even though it closely matches the Raubenheimer et al. (1996) formulation for reflective conditions. An improved parameterization of R_{ig} should fit field measurements of η_{osc} over a wider range of ξ_o , covering both dissipative and reflective conditions. Second, the estimate of η_{osc} would benefit from the inclusion of an empirical parameterization of R_{ss} during dissipative conditions. The present model ignores the contribution of R_{ss} for ξ_o below 0.275. Extension of the empirical expression for R_{ss} towards small ξ_o cannot be achieved through a linear extension of the relationship between R_{ss}/H_0 and ξ_o (which effectively reflects a $\sqrt{H_0}$ dependence of R_{ss}), as the incident band swash is saturated for low ξ_o . An improved parameterization for saturated R_{ss} should express a dependence on the peak period T_p and the local foreshore slope m (Battjes, 1974; Guza & Thornton, 1982) instead.

As regards the operational applicability of IBM, the key issue is to lower the manual effort that is required for image analysis. As a first step, this can be achieved by operating the model on merged, plan-view images instead of individual, oblique images. This may yield improved model performance in the far field (see above), and also reduces the manual effort, as it allows for a simultaneous analysis of all cameras of an ARGUS video station, rather than a one-by-one analysis of individual images. This approach relies, however, on the availability of a technique for the color balancing of images sampled from neighbouring cameras, such that the discriminator function Ψ applies to all individual images that compose the merged plan view. A provisional technique to do so (developed at NRL, Stennis Space Center, MS, USA) shows reasonable performance as regards color balancing. However, it also loses much of the image contrast provided by the individual images. The applicability of this technique within the context of IBM has not been investigated yet. As a second step, the operational use of IBM can be automated by incorporating pre-existing knowledge on the intertidal beach bathymetry. Madsen & Plant (2001) exploit this approach by using a recent bathymetry and the actual tidal level to narrow the search area where their SLIM model could possibly identify the shoreline. Any shoreline features identified outside this search region are excluded from further analysis. The applicability of this concept within the context of IBM depends on aspects like the accuracy of IBM, the alongshore variability of the shorelines typically found at the site of consideration, and the resolution of useful images in time with respect to the morphodynamic activity of the site of interest. These aspects need detailed exploration before the application of IBM can be automated.

2.5 Conclusions

The work presented in this chapter addresses the main objectives 1 and 2 of this thesis (Section 1.4) for the intertidal part of the beach, through development and validation of a new model to map intertidal beach bathymetry from shore-based video imagery and the tide and wave conditions offshore. To that end, three sub-objectives were formulated as a guideline for model development (Subsection 2.1.2). These sub-objectives are evaluated here.

To develop a technique to delineate a shoreline feature from standard time-averaged video imagery

- To delineate a shoreline feature from time-averaged video imagery, a detection model was developed which determines the shoreline location from the visual contrast between the sub-aerial and sub-aqueous parts of the beach. To distinguish between these parts, the model explores the clustering of pixel intensities in both the color and luminance domains.
- The comparison of surveyed and image-derived shorelines shows that the detection model identifies a shoreline feature near the higher end of the wave run-up.
- In the absence of a generic discriminator function that separates between sub-aerial and sub-aqueous pixels over a wide range of hydrodynamic and atmospheric conditions at different sites, the detection model necessarily determines a distinction criterion for every single image.
- The new detection model is robust, generic, flexible in use and capable of resolving three-dimensional morphological features including emerging intertidal bars.

To develop a method to estimate the associated shoreline elevation at the time of image collection

- To estimate the vertical level of the video-derived shoreline feature, a shoreline elevation model was developed which accounts for the effects of tide- and storm-induced water level variations outside the surf zone, wave set-up at zero water depth and swash oscillations at infragravity and incident wave frequencies.
- To quantify wave set-up at zero water depth, a new wave propagation model is presented, based on the self-similarity of bores in the inner surf zone. The new inner surf zone model carries the potential to extend process-based sediment transport computations up to zero water depth, which would be highly beneficial for the use of common coastal profile models.
- To quantify the vertical excursion of the swash oscillations, empirical parameterizations were adopted involving the offshore wave height and period, and the intertidal beach slope.

To assess the accuracy and applicability of the Intertidal Beach Mapper

- Model validation against a data set of GPS-surveyed shorelines has shown that detection-induced mean vertical deviations increase with increasing distance from the video station. Deviations are generally well below 20 cm, with a fairly constant scatter in the order of 15-20 cm.
- Elevation-induced mean vertical deviations are in the order of 10 cm (with a scatter of 10-15 cm) and relatively constant alongshore.

- Uncertainties associated with the two sub-models tend to compensate for each other. The resulting mean vertical deviation is less than 15 cm along 85% of the 2 km study region, which corresponds to a horizontal offset of 6 m. The scatter of overall model deviations (15-20 cm) is dominated by uncertainties resulting from the shoreline detection model.
- Model application at three distinctive field sites worldwide confirms IBM's reasonable applicability and performance over a wide range of hydrodynamic and atmospheric conditions.

In summary, horizontal deviations in the order of the dimensions of the swash zone and reasonable model applicability over a range of hydrodynamic, morphological and atmospheric conditions enable the use of IBM for the monitoring of coastal changes at the time scale of weeks to months. An example of the latter, including a discussion on its utility for coastal scientists and managers, is treated in Chapter 4.

Chapter 3

Quantification of subtidal beach bathymetry

3.1 Introduction

3.1.1 Motivation

This chapter addresses the main objectives 1 and 2 of this thesis (Section 1.4) for the subtidal part of the beach, by means of the development of a model to quantify surf zone bathymetry from shore-based video imagery and the assessment of model accuracy through validation against a one-year bathymetric data set acquired at a multiple-barred beach. Most model concepts developed so far exploit radar-based (McGregor et al., 1998; Bell, 1999), video-derived (Stockdon & Holman, 2000; Dugan et al., 2001b) or directly measured (Holland, 2001) estimates of the incident wave frequency σ and wave number k to quantify local water depth h from the linear dispersion equation,

$$\sigma - uk = \sqrt{gk \tanh(kh)} \quad (3.1)$$

where u is the mean velocity magnitude. Neglecting the mean velocity u , Eq. (3.1) reduces to a simplified expression $c^2 = gh$ in shallow water ($h/L_0 < 0.05$). Although these models have shown good performance along deeper sections of the nearshore zone, they meet difficulties in the surf zone owing to the non-linearity of the wave field in shallow water. Stockdon & Holman (2000), for instance, report a great amount of variability in depth estimates at Duck in a barred region between the shoreline and the -3 m depth contour. Besides, it is largely unexplored yet whether video-based techniques to estimate wave properties, which were mostly developed and tested at Duck, also perform well at field sites with strongly different hydrodynamic and morphologic characteristics. Instead of using wave celerity as a visible signature of the underlying beach topography, our model estimates water depth from standard time-averaged video observations of wave breaking.

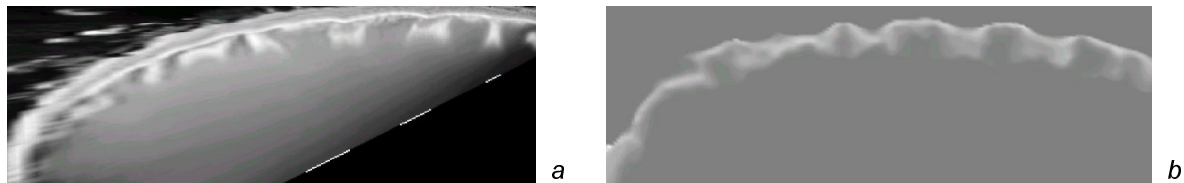


Figure 3.1: *Video observation (a) and model prediction (b) of wave breaking at Palm Beach, Australia (after Reniers et al., 2001). Figure 3.1a shows a plan view time-exposure image of Palm Beach, where the dry beach is located at the upper side. Figure 3.1b shows the model-predicted wave dissipation, quantified in terms of roller energy E_r divided by the squared phase speed c^2 . The latter was obtained from a wave model, which accounts for the effect of wave groupiness and corresponding infragravity waves on morphological development (Reniers et al., 2000, 2003).*

3.1.2 Approach

Time-averaged video observations of the nearshore zone show the process of wave breaking as one or more white alongshore bands of high intensity, which correspond to the preferential locations of depth-induced wave breaking (Figure 3.1). These bands have been shown to reflect the underlying bar morphology (e.g., Lippmann & Holman, 1989; Van Enckevort & Ruessink, 2001), at least in terms of bar position. So video patterns of wave dissipation provide an indirect measurement of submerged surf zone morphology, with high image intensities corresponding to shallow areas like sand bars.

Over the last few decades, various model concepts have been developed to describe the transformation of wave energy through the surf zone. Parametric wave models (e.g., Battjes & Janssen, 1978; Thornton & Guza, 1983), in which random waves are simplified to a single representative wave height, period and direction, are particularly popular because of their computational ease and their capability to accurately predict the decay of wave energy across a known beach topography (e.g., Thornton & Guza, 1983; Battjes & Stive, 1985). Wave dissipation rates increase in shallow areas, where waves are breaking due to depth limitation. Thus, similar to video observations, model predicted wave dissipation maps of the surf zone provide an indirect estimate of submerged morphology, with high-dissipation regions corresponding to shallow areas like sand bars. An example of the match between video-observed and model-predicted patterns of wave dissipation is shown qualitatively in Figure 3.1.

The first model to quantify subtidal bar bathymetry from video observations of wave breaking is presented by Aarninkhof et al. (1997). In a cross-shore approach, Aarninkhof et al. (1997) relate time-averaged image intensities to a wave parameter containing the turbulent kinetic energy E_r in the aerated roller at the face of a breaking wave and the phase speed c . On the basis of a single image, subtidal bar bathymetry is quantified through inverse modelling of a video-derived approximation of the wave dissipation characteristic E_r/c^2 . To improve model accuracy, individual estimates of bar bathymetry, obtained from multiple video images sampled throughout a tidal cycle, are combined with the help of a statistical filtering technique (Knaapen, 1996).

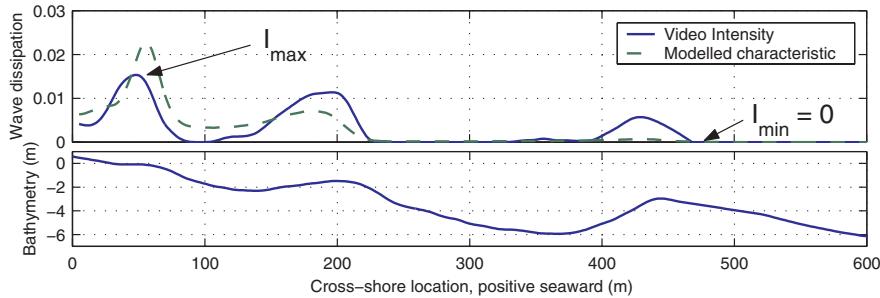


Figure 3.2: *Normalized cross-shore image intensity profile (solid line) versus normalized modelled wave characteristic $\frac{E_r}{c^2}$ (dashed line). Example of mismatch between different peaks (Station Egmond Coast3D, 18/10/1998 GMT 13 hr).*

Model application to the single-barred beach at Duck, NC, yielded bathymetry estimates with deviations of 10-20 cm at the crest of the bar, and mean differences of 30-40 cm across the bar. Application to the multiple barred beach at Noordwijk (The Netherlands) was less successful. This was attributed to a qualitative mismatch between the cross-shore variation of the selected wave parameter E_r/c^2 and the image intensity values. The relative magnitude of the intensity maxima over the two bars was often found to be opposite to the maxima of E_r/c^2 (Figure 3.2), which induced erroneous estimates of subtidal beach bathymetry.

The new model concept developed in this chapter (hereafter referred to as the Subtidal Beach Mapper, SBM) aims to extend existing capabilities to map surf zone bathymetry to a wider range of morphological configurations, particularly beaches with multiple sand bars. To that end, the techniques to interpret image intensities of wave breaking and to transform them into water depth are thoroughly revised. In stead of quantifying subtidal bathymetry from a single image (cf. Aarninkhof et al., 1997), SBM adopts a time-dependent approach by operating on a time sequence of video images, so that the dominant signal in the evolution of video-observed patterns of wave breaking exceeds the noise level. Starting from an initial coastal profile $z_b(x, t_0)$ measured at time t_0 , and the actual tide and wave conditions at time t , SBM compares a model-computed wave dissipation measure $D_c(x)$ to the corresponding video-derived wave dissipation measure $D_o(x)$. A mismatch between $D_c(x)$ and $D_o(x)$ is taken to imply that $z_b(x, t_0)$, which was used to determine $D_c(x)$, differs from the actual bathymetry $z_b(x, t)$. Based on the deviations between $D_c(x)$ and $D_o(x)$, the bathymetry is updated to optimize the match between $D_c(x)$ and $D_o(x)$. This process is referred to as the updating of bathymetry through assimilation of $D_o(x)$ and $D_c(x)$. Successive video images are used to model the evolution of bathymetry at time scales of days to years.

3.1.3 Objectives and outline of this chapter

This chapter presents a new model named SBM, which updates beach bathymetry through assimilation of video-derived and model-predicted patterns of wave dissipation. Thus, in further detailing of the main objectives 1 and 2 of this thesis (Section 1.4), the sub-objectives of this chapter are

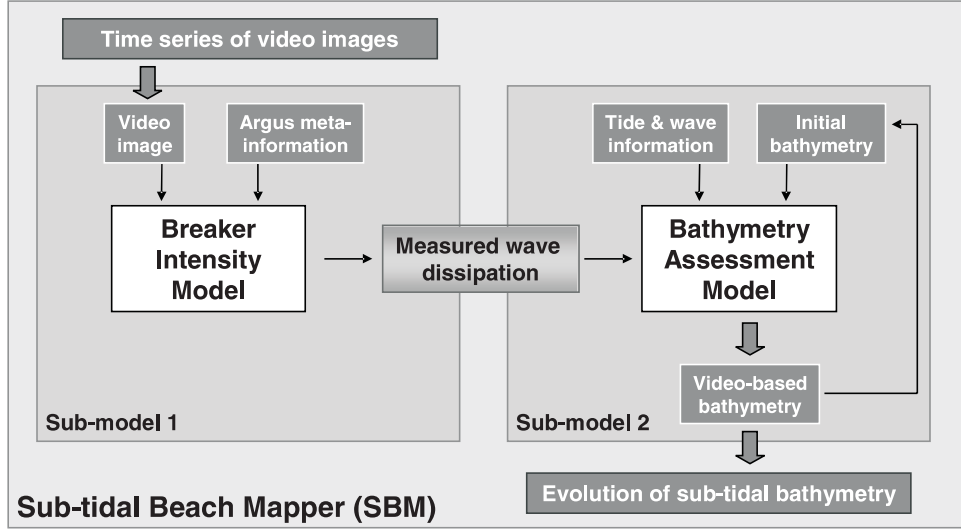


Figure 3.3: *Quantification of subtidal beach bathymetry. Interaction between the Breaker Intensity Model (BIM) and the Bathymetry Assessment Model (BAM).*

1. To develop a methodology to interpret *good-quality* video observations of wave breaking, to enable a quantitative comparison of video-derived and model-predicted measures of wave dissipation. This demands the set-up of operational criteria to verify image quality, a detailed analysis of the process of wave breaking as observed from video imagery and the identification of the model-predicted measure of wave dissipation that shows best correspondence to time-averaged video observations of wave breaking.
2. To develop a methodology to quantify the temporal evolution of subtidal beach bathymetry through assimilation of video-derived and model-predicted measures of wave dissipation. This involves the use of a wave transformation model to compute the dissipation of wave energy across the surf zone and the design of a robust assimilation code to modify beach bathymetry on the basis of differences between the computed and video-observed wave dissipation rates.
3. To assess SBM accuracy by means of a validation of model results against a bathymetric data set, acquired over a one-year period at a multiple-barred beach.

The layout of SBM (Figure 3.3) directly reflects the first and second sub-objective specified above. SBM consists of two sub-models, the Breaker Intensity Model (BIM) and the Bathymetry Assessment Model (BAM). BIM samples intensity data from time-averaged ARGUS video images, verifies data quality and normalizes the pre-processed intensity data to obtain a normalized video-derived measure of wave dissipation $D_{o,n}(x)$, which provides the video-derived input for BAM. Starting from $z_b(x, t_0)$ and the tide and wave conditions at the time of image collection, BAM uses a standard wave transformation model to compute $D_c(x)$, determines the associated $D_o(x)$ by scaling $D_{o,n}(x)$ with the incoming wave energy flux and updates bathymetry through assimilation of $D_c(x)$ and $D_o(x)$. Coastal profiles $z_b(x, t)$ thus obtained provide the starting point for consecutive

bathymetry updates, which involves the use of successive video images to model the temporal evolution of nearshore bathymetry.

In the remainder of this chapter, the development and stand-alone testing of the sub-models BIM (reflecting sub-objective 1) and BAM (reflecting sub-objective 2) is described in Sections 3.2 and 3.3, respectively. The two models presently operate on a one-dimensional, cross-shore grid, although the concept in itself also allows for application to two-dimensional field situations. It is explicitly stated that the investigation of the match between video-derived and model-computed measures of wave dissipation and the analysis of BIM performance at a multiple-barred beach (Subsection 3.2.4) are performed in terms of normalized dissipation measures $D_{o,n}$ and $D_{c,n}$. The analysis of BAM behaviour and its application in the context of SBM (Section 3.3 and further) are performed in terms of D_o and D_c .

The third sub-objective of this chapter is addressed in Section 3.4, by means of a quantitative assessment of SBM performance against a bathymetric data set, sampled during the first year after nourishing a beach at Egmond. The analysis of SBM performance shows that deviations between the computed and measured bathymetrical evolution are strongly related to the model's time scale of profile adjustment, which is primarily governed by the morphological model parameters. The latter observation confirms the importance of the sensitivity analysis of SBM parameters, also described in Section 3.4. Section 3.5 presents a discussion on some general characteristics of SBM behaviour and the opportunities for furthering SBM performance. This chapter is finalized (Section 3.6) with a summary of our findings with respect to the three sub-objectives driving the development of SBM.

3.2 The Breaker Intensity Model (BIM)

3.2.1 Introduction

The Breaker Intensity Model (BIM) aims to automatically sample and process time-averaged video data to find a normalized wave dissipation pattern $D_{o,n}(x)$, which allows for a quantitative comparison to various normalized model-predicted measures of wave dissipation $D_{c,n}(x)$. In operational mode, BIM follows a five-step approach to obtain $D_{o,n}(x)$:

1. Sampling of raw video data from time-averaged video images;
2. Pre-processing of the raw video data: Noise removal and correction for background illuminations;
3. Verification of data quality through application of acceptance criteria;
4. Removal of the effect of persistent foam from the intensity data;
5. Normalization of the pre-processed video data;

To arrive at an operation model to perform these five steps, three research issues need further consideration:

- Pre-processing of raw, time-averaged video data. The quality – hence usefulness – of ARGUS time exposure images varies with the atmospheric and hydrodynamic conditions. The analysis of longer-term time series of video images therefore demands the availability of a technique for the pre-processing of video data. The latter involves the removal of noise, correction for background illuminations and the application of acceptance criteria on data quality. The methodology for pre-processing is described in Sub-section 3.2.2.
- Correction for the effect of persistent foam. The white intensity bands observed from good-quality time-averaged video images are affected by wave breaking as well as persistent foam. The latter refers to persistent bubbles and foam that remain at the sea surface after passage of the breaking wave and are not directly related to the process of wave breaking. Persistent foam is visible at time-averaged video images but not predicted by common wave propagation models. Thus, to relate video-derived and model-computed measures of wave dissipation, the wave breaking induced part of the video intensity signal needs to be isolated by removing the contribution of persistent foam. This demands detailed investigation of the process of wave breaking as observed from video imagery, which is done on the basis of a limited data set of intra-wave timestack images, sampled at Duck, NC (USA). This approach yields a technique to remove the effect of persistent foam on the basis of time-averaged video information only (Sub-section 3.2.3). Normalizing the intensity data thus obtained yields $D_{o,n}(x)$, which acts as the input for BAM.
- Assessment of the model-computed measure of wave dissipation that relates best to $D_{o,n}(x)$. This issue is investigated empirically for various model-predicted measures of wave dissipation, on the basis of the application of BIM to field data collected during the Coast3D field experiments at the multiple-barred beach at Egmond, Netherlands (Sub-section 3.2.4).

It is explicitly stated that the detailed investigation on the basis of timestack images (second issue) and the assessment of various model-predicted measures of wave dissipation (third issue) concern one-time activities. In operational mode, BIM processes time-averaged video data only and provides the outcome $D_{o,n}(x)$ to BAM for further processing. The overall performance of BIM is discussed in Subsection 3.2.6.

3.2.2 Pre-processing of time-averaged intensity data

ARGUS video data are collected on an hourly basis irrespective of the hydrodynamic, light and weather conditions. Robust application of SBM therefore demands an objective methodology to remove poor-quality images from the data set and to remove (as much as possible) noise from the intensity signal in the selected high-quality images. For both we use a technique developed by Alexander (2001), in which a cross-shore intensity profile is described in terms of a background intensity level I_0 , a trend m_I and a variable number of peak features, each associated with wave breaking over a sand bar or at the

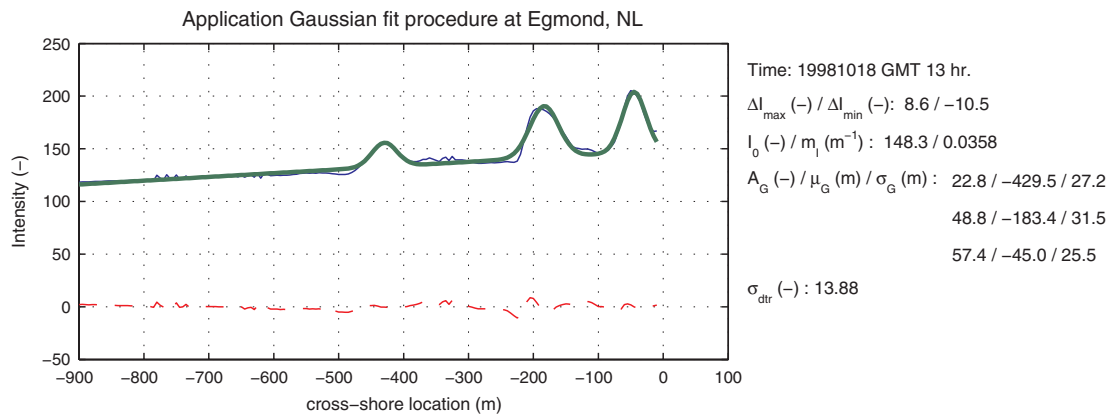


Figure 3.4: *Example of the Gaussian fit technique to a cross-shore intensity profile at Egmond, Netherlands. The peaks around $x = -430$ m, $x = -180$ m and $x = -50$ m represent wave breaking at the outer, inner and intertidal bar, respectively; the peak at $x = -50$ m is the shoreline break. The thin line is I_v , the thick line shows I_G . The dashed line is $I_v - I_G$.*

shoreline. Alexander (2001) finds that these peak features can be described well by a Gaussian $G(x)$ type curve of intensity

$$G(x) = A_G \cdot e^{-\left(\frac{x-\mu_G}{\sigma_G}\right)^2} \quad (3.2)$$

where A_G , μ_G and σ_G represent a measure for the height, mean location and width, respectively, of a dissipation peak. Thus, the Gaussian approximation I_G of the video-based cross-shore intensity profile is described as

$$I_G(x) = I_0 + m_I \cdot x + \sum_{i=1}^{N_G} G_i(x) \quad (3.3)$$

where N_G is the number of Gaussian peaks. The settings of the Gaussian parameters A_G , μ_G and σ_G for each of the dissipation peaks are obtained from a convolution analysis of the raw, video-based intensity profile I_v with a limited series of Gaussian shapes (Alexander, 2001). The number of Gaussian shapes to be fitted matches the number of regions of distinct wave breaking over breaker bars or at the shoreline. These regions are determined from a threshold procedure, stating that a wave breaking induced intensity peak should involve an intensity increase of at least 35% of the difference between the maximum and minimum value of I_v . The procedure developed by Alexander (2001) results in a smooth approximation of I_v (Figure 3.4) and was found to effectively filter noise from the raw intensity data. It is also observed that the Gaussian approximation filters the intensity dip immediately seaward of the regions of wave breaking, which is related to the dark face of shoaling waves at the onset of breaking (Stockdon & Holman, 2000). This is a favorable characteristic, because the dip does not relate to any physical process incorporated in wave transformation models.

In addition to the noise removal, I_G allows for the definition of objective criteria to accept video data for further processing. We decided to reject an image intensity profile when one or more of the following criteria was met:

- I_0 is lower than a threshold value $I_{0,\min}$, indicating poor lighting conditions or nighttime images;
- the deviation $\Delta I = I_v - I_G$ exceeds a positive threshold value ΔI_{\max} , indicating a poor fit of I_G to I_v ;
- the amplitude A_G of the highest Gaussian peak does not exceed a threshold value $A_{G,\min}$, indicating poorly-pronounced dissipation peaks;
- the standard deviation σ_G of the widest Gaussian peak exceeds a threshold value $\sigma_{G,\max}$, indicating unrealistically wide dissipation peaks;
- the standard deviation σ_{dtr} of the detrended intensity profile does not exceed a threshold $\sigma_{\text{dtr},\min}$, again indicating non-pronounced dissipation patterns.

To illustrate this approach, the values of these filtering parameters for the example profile shown above are included in Figure 3.4. The minimum value of ΔI is not taken into consideration, since this generally coincides with the intensity dip at the onset of wave breaking, which is meant to be removed by pre-processing of the raw video data. Based on an application of Eq. (3.3) to video images collected at Egmond (Van Enckevort & Ruessink, 2001), default values were empirically set to $I_{0,\min} = 120$, $\Delta I_{\max} = 15$, $A_{G,\min} = 20$, $\sigma_{G,\max} = 100$ m and $\sigma_{\text{dtr},\min} = 5$.

Being sampled at the sea surface, an image intensity profile I_G that passes these criteria embodies a background illumination level plus an intensity increase in areas of wave breaking, induced by bubbles and foam. We assume the wave breaking related component $I(x)$ of $I_G(x)$ to be described by

$$I(x) = \sum_{i=1}^{N_G} G_i(x) \quad (3.4)$$

This effectively means that background illuminations as described by $I_0 + m_1 x$ are removed. Further processing of $I(x)$ involves a correction for the effect of persistent foam, which is described in the next sub-section.

3.2.3 Quantitative scaling of video intensity data

The image intensity profile $I(x)$ obtained after pre-processing is affected by bubbles and foam associated with the roller at the face of a breaking wave, as well as persistent foam drifting at the water surface. Thus, to relate pixel intensities to a model-predicted measure of wave dissipation, we need to isolate the roller induced contribution to $I(x)$ by removing the intensity contribution of persistent foam. This can be achieved through application of a reduction factor $f_{\text{red}}(x)$ to $I(x)$, which reflects the relative importance

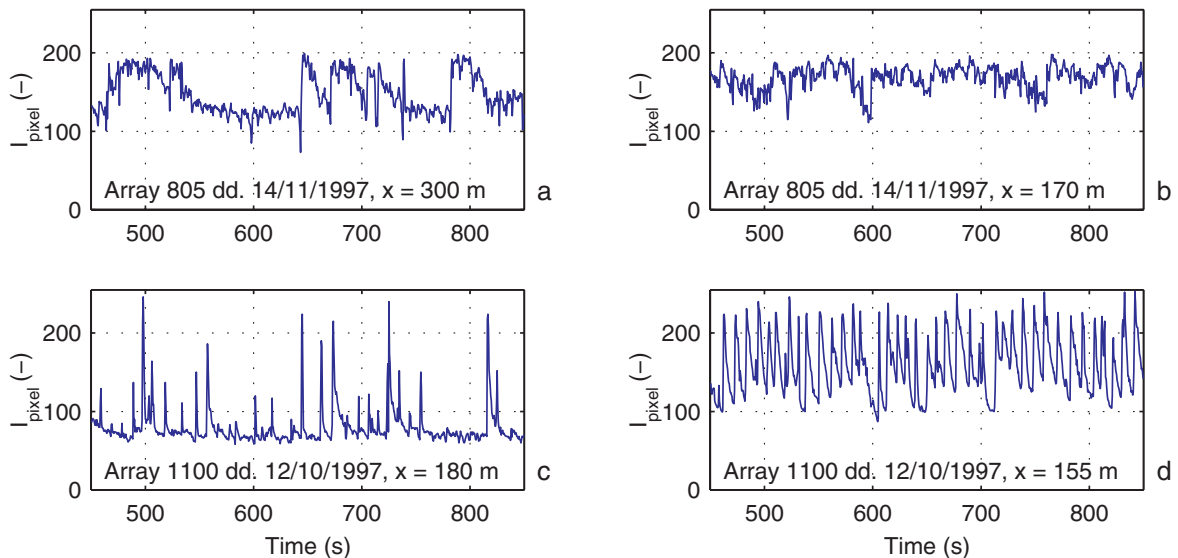


Figure 3.5: *Time series of pixel intensities during SandyDuck Experiment 1997. The time series presented here are sampled at (a,b) Array $y = 805$ m and (c,d) Array $y = 1100$ m, and show typical results at (a,c) the onset of breaking and (b,d) in the region of saturated breaking.*

of roller induced pixel intensities as a fraction of the combined intensity impact of the wave roller plus persistent foam, as a function of the cross-shore location x :

$$I_{\text{rol}}(x) = f_{\text{red}}(x) \cdot I(x) \quad (3.5)$$

Quantification of $f_{\text{red}}(x)$ demands a detailed investigation of the process of wave breaking as observed from video. This can be done by considering intensity time series sampled at 2 Hz in individual pixels (Figure 3.5). Such a time series is obtained by taking a slice from a timestack image (Figure 1.4) at some cross-shore location x . Generally, pixel time series show a roughly constant intensity level at deep water, in absence of any wave breaking. In the region of initial wave breaking, individual breaking events initiate a sudden increase in the intensity level (Figures 3.5a and 3.5c). Occasionally, this rise is preceded by an intensity dip related to the dark face of a wave near the onset of breaking (Stockdon & Holman, 2000). As air bubbles, trapped in the water column during wave breaking, escape they may cause persistent wave foam which causes the water surface to be white after the passage of the turbulent roller. The latter processes govern the time scale of the intensity drop after passage of a breaking wave (i.e. the length of the ‘tail’ of a breaker as observed from the intensity time series). Figures 3.5a and 3.5c show typical examples of a slow and rapid intensity drop, respectively.

Further onshore, wave breaking intensifies with decreasing water depth. Consequently, the time window between wave breaking events (or ‘intensity bursts’) narrows and the fraction of breaking waves Q_b increases. If the decay time scale is relatively large with respect to the wave period T_p , breaking waves catch up with the persistent foam of the preceding breaker, yielding a relatively constant signal of high intensity in case of saturated breaking (Figure 3.5b). If the decay time scale is relatively small with

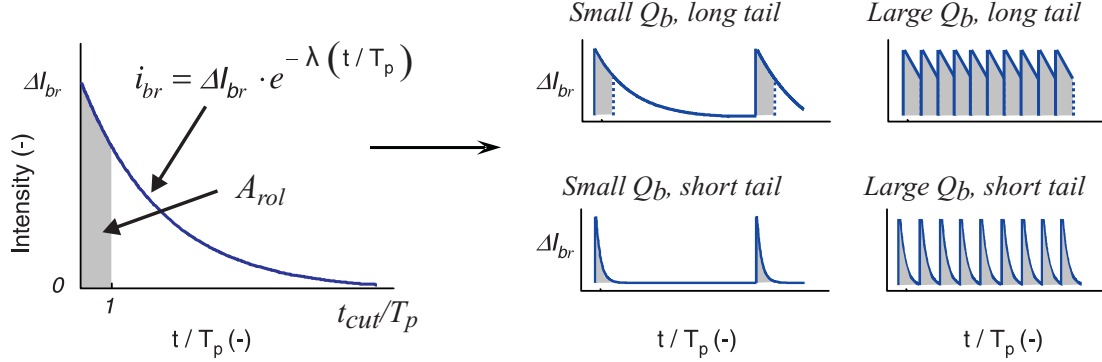


Figure 3.6: *Description of an individual wave breaker in BIM. Intensity increase in a single pixel during the passage of a wave breaker, induced by the wave roller (gray-shaded area) and persistent foam (blank area). At $t = t_{cut}$ the next breaker arrives. The four sub-plots at the right hand side reflect the four situations that are typically observed from timestack images (Figure 3.5).*

respect to T_p , pixel intensities drop before the arrival of the next breaker, yielding a strongly peaked intensity signal (Figure 3.5d).

A ten minute time-averaged video observation of nearshore wave breaking is based on many snap shot observations of breaking and non-breaking waves. To quantify the time-averaged roller induced contribution to $I(x)$, we need to model the video registration of an individual breaker, assess what part of the signal is roller related and average the roller induced contribution over time while accounting for the cross-shore varying fraction of breaking waves. Based on the analysis of timestack images presented above, we describe the video registration following the passage of an individual breaker as a pixel intensity signal i_{br} above the background level (Figure 3.6)

$$i_{br} = \Delta I_{br} \cdot e^{-\lambda\left(\frac{t}{T_p}\right)} \quad (3.6)$$

where ΔI_{br} is the initial intensity increase at the time of the arrival of the breaker, t is time and λ is a non-dimensional decay factor accounting for the time scale of the intensity decay after passage of the roller, relative to the wave period T_p . The roller induced contribution to $i_{br}(t)$ is separated from the persistent foam induced part by assuming that $i_{br}(t)$ is roller related for $0 < t \leq T_p$, and induced by persistent foam for $t > T_p$. In Figure 3.6 the integrated roller induced contribution A_{rol} to $i_{br}(t)$ is shaded gray for the four typical video conditions discussed here, that is long/short tail breaking (small and large λ , respectively) in combination with initial/saturated breaking (small and large Q_b , respectively, see Figure 3.5).

The analytical breaker intensity model introduced above is adopted as a starting point to quantify the roller induced increase of $I(x)$, as a fraction of the overall increase of $I(x)$. Suppose that the pixel intensity signal i_{br} of a single breaker at location x is cut off at $t = t_{cut}$ (Figure 3.6) due to the arrival of the next breaker. Based on our assumption of i_{br} being roller induced for $0 < t < T_p$, the integrated roller related contribution A_{rol} to the increase of $I(x)$ reads

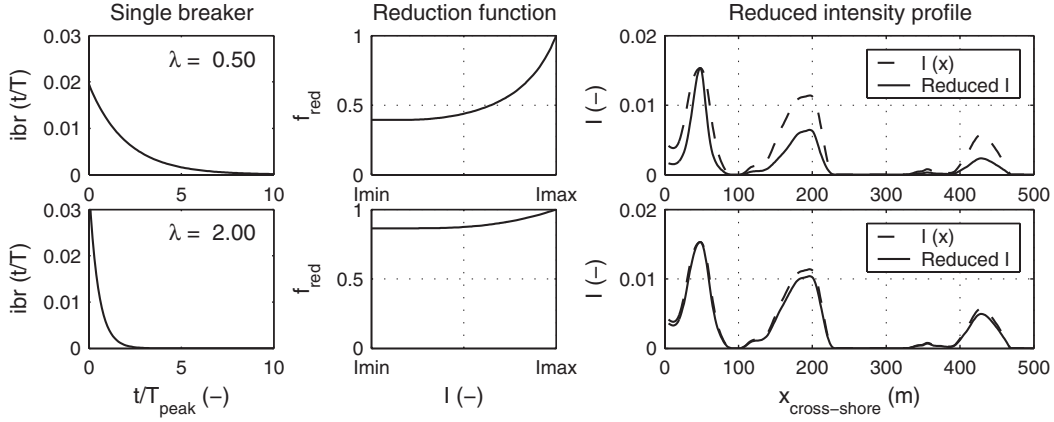


Figure 3.7: Conceptual BIM behaviour for different levels of persistent foam pollution. The left-hand plots show the analytical representation of a foam-polluted roller (upper plot, $\lambda = 0.5$) and a clean roller (lower plot, $\lambda = 2$). The middle plots show f_{red} as a function of I , indicating that persistent foam polluted intensities need a larger reduction. The resulting scaled intensity profiles are shown in the right-hand plots.

$$A_{\text{rol}} = \int_0^{T_p} \Delta I_{br} \cdot e^{-\lambda\left(\frac{t}{T_p}\right)} dt = \frac{T_p \Delta I_{br}}{\lambda} (1 - e^{-\lambda}), \quad (3.7)$$

The integrated combined contribution A_{br} of both the roller and persistent foam to the increase of $I(x)$ reads

$$A_{br} = \int_0^{t_{\text{cut}}} \Delta I_{br} \cdot e^{-\lambda\left(\frac{t}{T_p}\right)} dt = \frac{T_p \Delta I_{br}}{\lambda} \left(1 - e^{-\lambda\left(\frac{t_{\text{cut}}}{T_p}\right)}\right), \quad (3.8)$$

Eq. (3.8) shows that A_{br} depends on $t_{\text{cut}}(x)$, which represents the time t/T_p that the next breaker arrives, hence reflects the cross-shore varying fraction of breaking waves. An expression for $t_{\text{cut}}(x)$ can be found from the constraint that the combined intensity impact of the roller plus the persistent foam should yield a time-averaged intensity increase $I(x) - I_{\text{min}}$ for any location x along the cross-shore array, where I_{min} is the minimum intensity along $I(x)$. Adopting a wave-averaged approach where $t_{\text{cut}}(x)$ is constant in time throughout the ten minutes of time exposure for the collection of $I(x)$, this constraint can be formulated as

$$\frac{A_{br}}{t_{\text{cut}}} = I - I_{\text{min}} \quad \Leftrightarrow \quad t_{\text{cut}}(x) = \frac{T_p \cdot \Delta I_{br}}{\lambda (I(x) - I_{\text{min}})} \left(1 - e^{-\lambda\left(\frac{t_{\text{cut}}}{T_p}\right)}\right) \quad (3.9)$$

which yields an implicit expression for $t_{\text{cut}}(x)$ as a function of ΔI_{br} , which is unknown yet. The value of ΔI_{br} can be quantified by assuming saturated wave breaking conditions at the location of maximum intensity I_{max} , so that $t_{\text{cut}} = T_p$ for $I(x) = I_{\text{max}}$. Our earlier assumption of i_{br} being roller induced for $0 < t < T_p$ then implies that the time-averaged intensity increase $I_{\text{max}} - I_{\text{min}}$ is entirely induced by the wave roller,

$$\frac{A_{\text{rol}}}{T_p} = I_{\text{max}} - I_{\text{min}} \quad \Leftrightarrow \quad \Delta I_{br} = \frac{\lambda}{1 - e^{-\lambda}} (I_{\text{max}} - I_{\text{min}}) \quad (3.10)$$

Substitution of Eq. (3.10) into Eq. (3.9) allows to iteratively solve for $t_{\text{cut}}(x)$ and ΔI_{br} , which then enables the quantification of A_{rol} and A_{br} from Eqs. (3.7) and (3.8). Finally, the reduction factor f_{red} (Eq. 3.5) is determined from the ratio of A_{rol} and A_{br} , expressing the relative importance of roller induced pixel intensities:

$$f_{\text{red}}(x) = \frac{A_{\text{rol}}}{A_{\text{br}}(x)} \quad (3.11)$$

The definition of f_{red} according to Eq. (3.11) effectively implies a reduction of $I(x)$ for $I(x) < I_{\text{max}}$, to account for roller induced pixel intensities only. Model behaviour is illustrated in Figure 3.7 for different values of the decay factor λ . With decreasing values of λ , the raw intensity signal is increasingly obscured by persistent foam, which consequently yields a stronger reduction. While mean intensities are low, the reduction function is approximately constant. With increasing mean intensities, individual breakers start overlapping, which can be considered as an inherent correction mechanism of foam related intensities. Consequently, the reduction function increases up to a value of one at $I = I_{\text{max}}$, where wave breaking is saturated and no reduction is needed.

Calibration against data from SandyDuck experiment 1997

The methodology to remove persistent foam was tested against a limited data set of good quality timestack images, collected as part of the SandyDuck experiment (Birkemeier & Holland, 2001; Stockdon & Holman, 2000) conducted during September and October 1997 at the U.S. Army Corps of Engineers Field Research Facility (FRF) near Duck, NC. During the experiment, 18 cross-shore beach profiles with an alongshore spacing of approximately 50 m were surveyed on a daily basis, using the Coastal Research Amphibious Buggy (CRAB). Wave data (significant wave height H_{m0} , peak period T_p and the mean wave angle $\bar{\theta}_0$) for this period were obtained from an array of wave gauges located in 8 m water depth, slightly north-east of the FRF pier. Tide data were obtained from a tide gauge located at the end of the pier. Video data were collected hourly with a five camera ARGUS station on top of a tower 43 m above sea level.

Calibration of BIM involves the parameterization of λ (Eq. 3.6), which governs the time scale of the intensity decay after passage of a breaking wave. The analysis of ARGUS timestack images collected during the SandyDuck experiment (Figures 3.5b and 3.5d) has shown that increasing values of λ are associated with an increase in the peakedness of the time-varying intensity signal at saturated breaking, during the ten minutes of time exposure for image collection. Standardly collected ARGUS variance images (Figure 1.2c) provide a measure for the variability of the intensity signal during the collection of a time exposure image, hence the peakedness of the intensity signal. We therefore relate λ to the standard deviation σ_I of the intensity signal at saturated breaking ($I = I_{\text{max}}$), normalized with the time-averaged pixel intensity I_{max} at that location.

To parameterize λ as a function of σ_I/I_{max} , it is necessary to set up a calibration data set of measured λ against σ_I/I_{max} . It is hard to estimate λ directly from the type of intensity time series shown in Figure 3.5. We therefore follow an indirect approach by estimating the ratio t_{cut}/T_p in the region of initial wave breaking, based on which

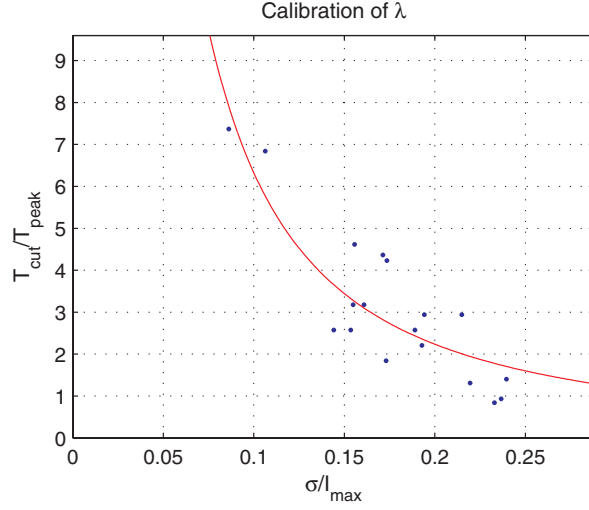


Figure 3.8: Calibration of persistent foam parameters of intensity interpretation model against data from SandyDuck Experiments 1997. The shape of the best-fit curve (Eq. 3.14) is chosen on physical grounds, demanding that the ratio t_{cut}/T_p approaches infinity (zero) for small (large) values of σ_I/I_{max} .

λ can be quantified. The ratio t_{cut}/T_p is visually estimated such that the integrated intensity contribution A_{est} of the breaker of interest has nearly reached its theoretical maximum contribution A_{∞} , which equals

$$A_{\infty} = \int_0^{\infty} \Delta I_{br} \cdot e^{-\lambda\left(\frac{t}{T_p}\right)} dt = \frac{T_p \Delta I_{br}}{\lambda} \quad (3.12)$$

Assuming that $A_{\text{est}}/A_{\infty} = 0.99$ and taking into account Eq. (3.8), λ can be expressed as a function of t_{cut}/T_p according to

$$\frac{T_p \Delta I_{br}}{\lambda} \left(1 - e^{-\lambda\left(\frac{t_{\text{cut}}}{T_p}\right)}\right) = 0.99 \frac{T_p \Delta I_{br}}{\lambda} \quad \Leftrightarrow \quad \lambda = -\frac{\ln(1 - 0.99)}{\frac{t_{\text{cut}}}{T_p}} \quad (3.13)$$

Parameterization of t_{cut}/T_p as a function of video-observed variables thus enables the quantification of λ . On the basis of the considerations given above, the ratio t_{cut}/T_p is parameterized as a function of σ_I/I_{max} at saturated breaking, by means of an empirical expression of the form

$$\frac{t_{\text{cut}}}{T_p} = \frac{1}{p \left(\frac{\sigma_I}{I_{\text{max}}}\right)^b} \quad (3.14)$$

where p and b are calibration parameters. Small values of σ_I/I_{max} (i.e. long tails) cause t_{cut}/T_p to become very large, whereas the ratio t_{cut}/T_p approaches zero if σ_I/I_{max} becomes infinite. Both observations are in accordance with the physics of the process of consideration. On the basis of 18 visual estimates of t_{cut}/T_p and the corresponding σ_I/I_{max} quantified from the 18 intensity timestacks involved, BIM was calibrated

by adopting parameter settings $b = 1.5$ and $p = 5$ for model application at Duck (Figure 3.8). Substitution of Eq. (3.14) in Eq.(3.13) finally yields the parameterized expression for λ :

$$\lambda = -p \cdot \ln(1 - 0.99) \cdot \left(\frac{\sigma_I}{I_{\max}} \right)^b \quad (3.15)$$

where $b = 1.5$ and $p = 5$ for application at Duck. Notice that the arbitrarily chosen ratio $A_{\text{est}}/A_{\infty} = 0.99$ does not affect model behaviour, as a different choice would be compensated by a different setting of p .

In summary, the application of BIM to a pre-processed intensity profile $I(x)$ removes the effect of persistent foam from the intensity data through application of a spatially-varying reduction function f_{red} (Eq. 3.5), which yields the cross-shore distribution of roller related image intensities I_{rol} . The latter will be used as a starting point for the comparison of video-derived and model-computed measures of wave dissipation, as investigated in the next subsection.

3.2.4 Investigation of various model-predicted measures of wave dissipation

In this subsection it is investigated which dissipation-related wave characteristic that can readily be computed by standard wave transformation models matches I_{rol} (Eq. 3.5) best. Earlier research into this topic has focussed on the dissipation of organized wave energy D_{br} (Lippmann & Holman, 1989), the energy of the surface roller, the white aerated mass at the breaking wave face, E_r (Van Enckevort & Ruessink, 2001; Ruessink et al., 2002a) and other parameters involving E_r , such as E_r/c^2 (Aarninkhof et al., 1997), where c is the phase speed of the wave field. So far, the focus of earlier research has primarily been on the match of time-averaged pixel intensities and the model-predicted wave characteristic in terms of the location of the dissipation peaks. We extend this approach by means of a quantitative comparison of video-derived and model-computed measures of wave dissipation and the inclusion of two additional wave characteristics, namely $\sqrt{E_r/c^3}$, suggested by Aarninkhof (1996) for further exploration, and the roller dissipation D_r , assuming that the generation of bubbles and foam is proportional to the transformation of kinetic roller energy to turbulence.

The cross-shore evolution of the wave characteristics listed above is computed with the wave transformation model described in Appendix D. It consists of two balance equations to describe the transformation of wave energy (Battjes & Janssen, 1978) and roller energy (Nairn et al., 1990; Stive & De Vriend, 1994) through the surf zone, using the Baldock et al. (1998) formulation for the dissipation of organized wave energy. Wave energy is converted into kinetic roller energy before ultimately being dissipated through the production of turbulence (Svendsen, 1984). These processes are governed by the wave dissipation parameter γ , which sets local breaker height as a function of water depth and wave steepness (Battjes & Janssen, 1978), and the roller dissipation parameter β , which represents the slope of the face of the breaking wave (Nairn et al., 1990). Default parameter settings involve $\beta = 0.10$ (Reniers & Battjes, 1997) and a γ parameterization according to Battjes & Stive (1985), who found γ to depend on the deep water wave steepness (Appendix D).

To investigate BIM performance for various model-predicted measures of wave dissipation, BIM was applied to a morphological data set acquired over a six-week period in October-November 1998 as part of the Coast3D field experiment at Egmond, The Netherlands (Ruessink et al., 2000). During the experiment, nearshore bathymetry was measured along 11 cross-shore profiles with 50 m spacing alongshore, using a 15-m high, amphibious vehicle called the WESP. In total, 21 surveys were performed, of which 11 cover only the inner bar. The measured depth is estimated to have an error of less than 15 cm, not accounting for unresolved bed forms having lengths less than $O(1\text{ m})$ and amplitudes less than $O(10\text{ cm})$. The survey data were interpolated to a rectangular grid with a cross-shore and alongshore spacing of 2 and 20 m, respectively. Hydrodynamic data are taken from Van Enckevort & Ruessink (2001). Offshore wave conditions (*rms* wave height $H_{\text{rms}0}$, peak period T_p and the energy-weighted mean wave angle $\bar{\theta}_0$) were measured with a directional wave buoy in 15 m water depth. Missing data, which occurred during 20% of time, were replaced by values from an identical buoy located approximately 15 km to the north. Offshore tidal levels are found from interpolation of water level data collected at tidal stations located 15 km north and south of Egmond, resulting in maximum errors of 0.1 m.

The time exposure and variance images used here were recorded hourly by the ARGUS video station, located on top of a 48-m high tower placed at the dunefoot 1500 m south of the mid of the field site. Since BIM presently applies to cross-shore arrays within the field of view of a single camera, only video data collected with camera 1 are considered here. This camera is equipped with a 9-mm lens, which yields a spatial resolution along the central array of the experiment area of 2 - 20 m in the cross-shore and about 50 m in the alongshore direction.

On the basis of the availability of good-quality bathymetric surveys and video images with sufficient wave breaking, a testbank was set-up, covering 192 intensity profiles sampled over four different days along four cross-shore arrays with 150 m spacing alongshore. During these four days, $H_{\text{rms}0}$ ranges between 0.5 and 1.8 m. BIM parameter settings involve a default value $p = 5$ for the intensity decay coefficient (Section 3.2.3). Sampling of raw intensity data involves the alongshore averaging over a distance of twice the local alongshore pixel resolution, centered around the y -coordinate of the array of interest. After pre-processing of the raw intensity data, 103 profiles were accepted for further analysis. This reduced data set provided an overall number of 239 dissipation peaks, 48 being located at the outer bar, 100 at the inner bar and the remaining 91 at the intertidal bar near the shoreline. To enable a quantitative comparison of the video-derived and model-computed measures of wave dissipation, the variables involved are normalized according to

$$D_{\text{o,n}}(x) = \frac{I_{\text{rol}}(x)}{\int_x I_{\text{rol}}(x)dx} \quad (3.16a)$$

$$D_{\text{c,n}}(x) = \frac{D_{\text{mod}}(x)}{\int_x D_{\text{mod}}(x)dx} \quad (3.16b)$$

where $D_{\text{o,n}}$ is the normalized, roller induced image intensity profile which is considered as a video-derived measure of wave dissipation, D_{mod} is any of the five model-computed

Table 3.1: BIM performance for different wave characteristics. Mean and standard deviation of Δx_D and ΔA_D per breaker bar and for the entire data set.

	$D_{c,n}$	$\overline{\Delta x_D}(m)$	$\sigma_{\Delta x}(m)$	$\overline{\Delta A_D}(-)$	$\sigma_{\Delta A}(-)$
Outer bar	D_{br}	-7.3	39.7	-0.034	0.463
	E_r/c^2	-6.0	22.0	-0.295	0.332
	E_r	-6.4	21.8	0.111	0.478
	$\sqrt{E_r/c^3}$	-6.2	21.9	-0.333	0.263
	D_r	-6.3	21.9	-0.070	0.415
Inner bar	D_{br}	-17.1	9.7	-0.037	0.383
	E_r/c^2	-5.7	9.9	-0.122	0.365
	E_r	-8.1	9.6	-0.012	0.384
	$\sqrt{E_r/c^3}$	-4.5	10.1	-0.315	0.245
	D_r	-6.9	9.8	-0.033	0.345
Intertidal bar	D_{br}	-9.6	10.4	0.103	0.808
	E_r/c^2	-2.0	9.3	0.760	1.107
	E_r	-7.4	8.3	-0.273	0.663
	$\sqrt{E_r/c^3}$	1.2	10.4	0.411	0.873
	D_r	-5.0	8.4	-0.096	0.811
Entire data set	D_{br}	-12.3	20.2	0.048	0.594
	E_r/c^2	-4.4	13.1	0.179	0.868
	E_r	-7.5	12.6	-0.087	0.544
	$\sqrt{E_r/c^3}$	-2.6	13.7	-0.042	0.673
	D_r	-6.0	12.7	-0.009	0.580

measures of wave dissipation identified above and $D_{c,n}$ is the normalized equivalent of D_{mod} . Notice that no Gaussian type filtering is applied to the model-computed measures of wave dissipation.

BIM performance is evaluated by means of a comparison of the corresponding peak locations (x_{D_o} , x_{D_c}) and peak areas (A_{D_o} , A_{D_c}) below $D_{o,n}(x)$ and $D_{c,n}(x)$. The location x_{D_o} is found directly from μ_G ; x_{D_c} is the location of the corresponding local maximum of $D_c(x)$. A_{D_o} and A_{D_c} are determined as the area below $D_{o,n}(x)$ and $D_{c,n}(x)$, within a distance σ_G at both sides of x_{D_o} and x_{D_c} , respectively. Results for the five wave characteristics investigated here are summarized in Table 3.1, by means of the mean $\overline{\Delta x_D}$ and standard deviation $\sigma_{\Delta x}$ of the horizontal deviations $\Delta x_D = x_{D_c} - x_{D_o}$, as well as the mean $\overline{\Delta A_D}$ and standard deviation $\sigma_{\Delta A}$ of the dimensionless area offset $\Delta A_D = (A_{D_c} - A_{D_o})/A_{D_o}$. Negative (positive) $\overline{\Delta x_D}$ indicate a seaward (shoreward) offset of x_{D_c} as compared to the associated x_{D_o} , while negative (positive) $\overline{\Delta A_D}$ reflect that $D_{c,n}$ underestimates (overestimates) the associated $D_{o,n}$ at a particular breaker bar.

Table 3.1 shows that the D_r matches $D_{o,n}$ best, since it combines moderate values of $\overline{\Delta x_D}$ per breaker bar with relatively small $\overline{\Delta A_D}$. The latter indicates a balanced distribution of the wave dissipation over the three breaker bars. The other characteristics are

rejected for various reasons. Although D_{br} yields similar deviations in terms of $\overline{\Delta A_D}$, the average seaward offset of x_{Dc} for D_{br} is approximately twice as large as the offset for D_r . Different performance of the E_r based characteristics is best observed from the resulting $\overline{\Delta A_D}$ per breaker bar. Owing to the division by c , which decreases with decreasing water depth, the characteristics E_r/c^2 and $\sqrt{E_r/c^3}$ yield $D_{c,n}$ that considerably underestimate $D_{o,n}$ at the outer bar, which is compensated by an overestimation of $D_{o,n}$ at the intertidal bar. E_r shows opposite behaviour, which again yields relatively large $\overline{\Delta A_D}$ at the outer and intertidal bar as compared to D_r .

BIM performance for the best case characteristic D_r is visualized in Figure 3.9. The absence of clear outliers demonstrates that the image pre-filtering technique based on the characteristics of $I_G(x)$ performs well. The difference in slopes of the line of equality and the best-fit line through the data demonstrates that the measured data x_{Do} and A_{Do} both show more variability than the associated x_{Dc} and A_{Dc} , at all breaker bars. This observation explains the large values for $\sigma_{\Delta x}$ and $\sigma_{\Delta A}$ reported in Table 3.1. Because D_r combines moderate seaward offsets of 6.3, 6.9 and 5.0 m of x_{Dc} at the outer, inner and intertidal bar with a well-balanced distribution of the wave dissipation per breaker bar, it is concluded that D_r outperforms the other wave characteristics considered here and therefore will be used as the intensity matching wave characteristic.

3.2.5 Sensitivity analysis BIM parameter settings

In this section, BIM sensitivity to variable settings of the model parameters is investigated. To that end, the wave breaking parameter γ and the roller dissipation parameter β of the wave transformation model, as well as the BIM parameter p are varied over a realistic range. Default settings are $\beta = 0.10$, $p = 5$ and γ according to Battjes & Stive (1985, see Appendix D). The sensitivity tests include the investigation of a new formulation for γ according to Ruessink et al. (2003a), who parameterize γ as a function of the local water depth and wave length, as well as a formulation for β according to Walstra et al. (1996), who developed an empirical expression for β as a function of local water depth, wave height and wave length. Table 3.2 summarizes the results by means of the mean and standard deviation of Δx_D and ΔA_D over the entire data set.

Table 3.2 demonstrates that that BIM behaviour is not very sensitive to variations of γ in the range 0.60 - 0.75. The onset of wave breaking delays with increasing values of γ , which induces a minor shoreward migration of x_{Dc} , hence a decrease in $\overline{\Delta x_D}$. Variable γ settings also affect the distribution of the wave dissipation over the three breaker bars. For $\gamma = 0.55$, $\overline{\Delta A_D}$ amounts to 0.254, -0.157 and -0.242 at the outer, inner and intertidal bar, respectively, indicating that $D_{c,n}$ overestimates $D_{o,n}$ at the outer bar and underestimates $D_{o,n}$ at the inner and intertidal bar. With increasing values of γ , $D_{c,n}$ at the outer bar decreases, while $D_{c,n}$ in the shallow surf zone increases. This thus explains improved BIM performance with increasing values of γ . For $\gamma = 0.80$ however, $\overline{\Delta A_D}$ is -0.254, -0.059 and 0.411 for the outer, inner and intertidal bar, respectively, indicating that $D_{c,n}$ underestimates $D_{o,n}$ at the outer bar, while overestimating $D_{o,n}$ at the inner bar. Best constant γ settings are found in between, in the range 0.65 - 0.70. The cross-shore varying γ parameterization according to Ruessink et al. (2003a) yields slightly improved error statistics as compared to the best constant γ settings. The γ

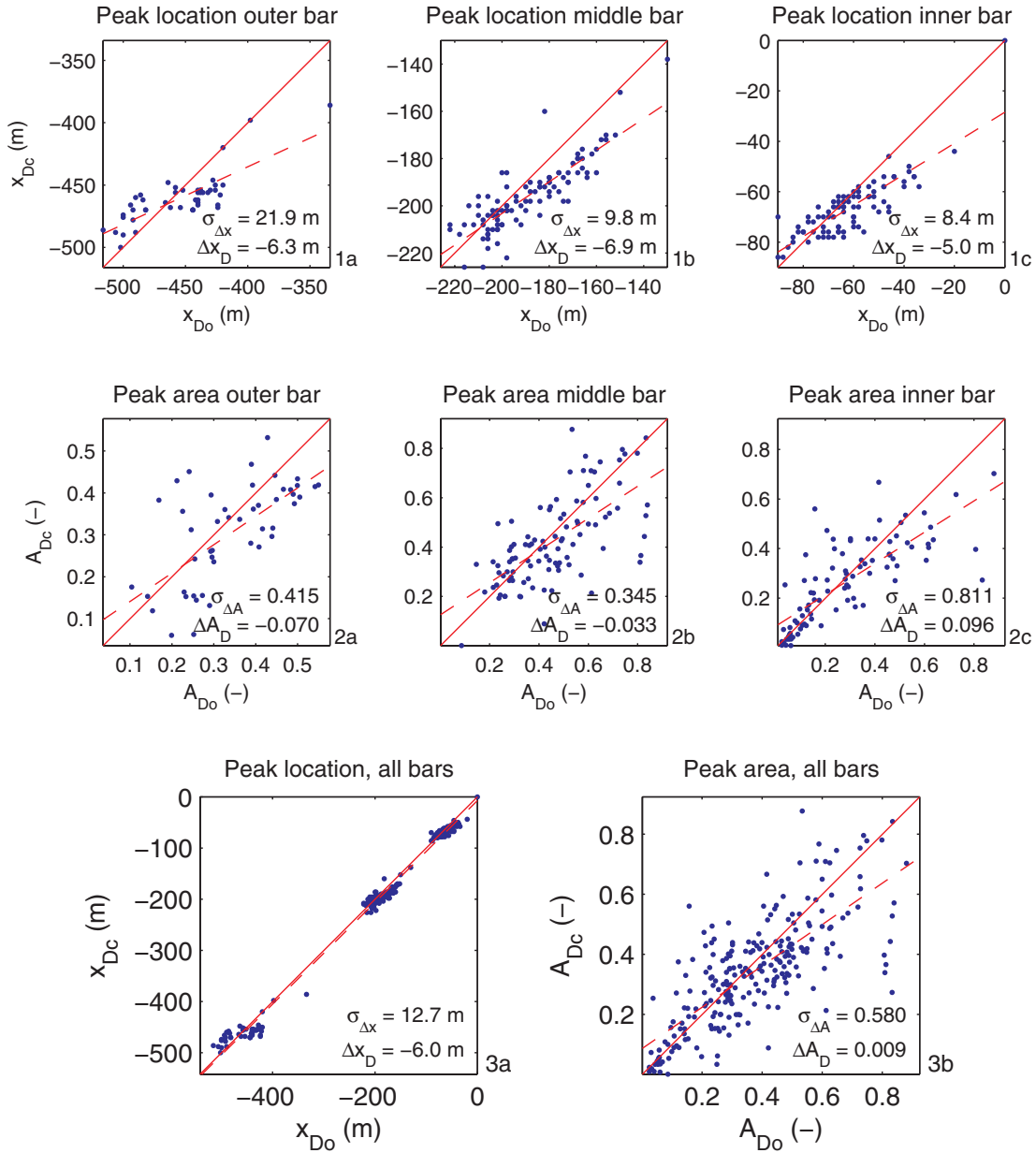


Figure 3.9: Stand-alone application of BIM to a multiple-barred beach at Egmond, The Netherlands. Comparison of $D_{o,n}$ and $D_{c,n}$ (wave characteristic D_r) in terms of the peak location per bar (1a-c), peak area per bar (2a-2c), peak location for all bars (3a) and peak area at all bars (3b). The dashed line is the best linear fit line of the data.

parameterization of Battjes & Stive (1985) however provides the best match between $D_{o,n}$ and $D_{c,n}$ across all bars. The latter parameterization is therefore adopted as a starting point for further analysis.

BIM performance is not very sensitive to variable β settings, particularly not in the range 0.075 - 0.125. With decreasing values of β , the dissipation of E_r is delayed, inducing a shoreward migration of the x_{Dc} . Since x_{Dc} is generally located seaward of

Table 3.2: BIM performance for different settings of the model parameters γ , β and p . RWS'03 refers to Ruessink et al. (2003a), BS'85 to Battjes & Stive (1985) and WMS'96 to Walstra et al. (1996).

		$\overline{\Delta x_D}(m)$	$\sigma_{\Delta x}(m)$	$\overline{\Delta A_D}(-)$	$\sigma_{\Delta A}(-)$
Entire data set	$\gamma = 0.55$	-8.2	11.8	-0.107	0.526
	$\gamma = 0.60$	-7.6	11.8	-0.059	0.544
	$\gamma = 0.65$	-6.9	11.8	-0.017	0.583
	$\gamma = 0.70$	-6.1	12.0	0.020	0.642
	$\gamma = 0.75$	-5.4	12.2	0.052	0.713
	$\gamma = 0.80$	-4.8	12.5	0.081	0.789
	γ RWS'03	-6.8	12.9	-0.030	0.487
	γ BS'85 (default)	-6.0	12.7	0.009	0.580
Entire data set	$\beta = 0.050$	-1.9	13.1	-0.071	0.565
	$\beta = 0.075$	-4.3	12.9	-0.023	0.569
	$\beta = 0.100$ (default)	-6.0	12.7	0.009	0.580
	$\beta = 0.125$	-7.3	12.6	0.028	0.589
	$\beta = 0.150$	-8.2	12.6	0.014	0.449
	β WMS'96	-3.7	12.3	0.049	0.584
Entire data set	$p = 1$	-6.0	12.7	0.070	0.739
	$p = 2.5$	-6.0	12.7	0.017	0.611
	$p = 5$ (default)	-6.0	12.7	0.009	0.580
	$p = 10$	-6.0	12.7	0.008	0.573
	$p = 15$	-6.0	12.7	0.009	0.572
	$p = 20$	-6.0	12.7	0.010	0.571
	$p = 30$	-6.0	12.7	0.010	0.571

x_{D_o} , BIM performance in terms of $\overline{\Delta x_D}$ improves with decreasing values of β . Lowering β however, is also associated with a flattening and widening of the roller dissipation profile, inducing an underestimation of $D_{o,n}$ for low β . Table 3.2 confirms this observations, showing negative $\overline{\Delta A_D}$ for small β under 0.10 and positive $\overline{\Delta A_D}$ for large β . Best results in terms of both $\overline{\Delta x_D}$ and $\overline{\Delta A_D}$ are found for β values in the range 0.10-0.125; the default value $\beta = 0.10$ is therefore adopted as a starting point for further analysis. It is noted that the β parameterization according to Walstra et al. (1996) shows good performance in terms of the horizontal error of the peak locations, albeit that the offset in peak area is relatively large.

Considering the background of the intensity interpretation model, variation of the foam removal parameter p is not anticipated to affect the x_{D_o} . This is confirmed by the results presented in Table 3.2, which show constant $\overline{\Delta x_D}$ and $\sigma_{\Delta x}$ for all settings of p . With decreasing values of p , I_G is subject to an increased correction for the effect of persistent foam, inducing a narrowing of the peaks of $D_{o,n}$ and increasing relative differences between the peak heights $D_{o,n}$. For large values of p , BIM performance is no longer sensitive to variable p settings, indicating that no correction is applied to I_G . On

the basis of the testbank and methodology considered here, it is concluded that best results are achieved for large values of p , suggesting that the effect of persistent foam affecting video-derived observations of wave breaking is less significant at Egmond than at Duck. Considering the virtual insensitivity, however, of the model results to variable settings of p exceeding 10, a value $p = 10$ is adopted as a starting point for further analysis.

3.2.6 Discussion on BIM performance

The analysis of BIM performance described above yields results which compare well to the work done by Van Enckevort & Ruessink (2001). Using E_r as the intensity matching wave characteristic, Van Enckevort & Ruessink (2001) find a landward offset of 6-10 m of x_{D_o} as regard to the associated x_{D_c} . Application of BIM on the basis of D_r as the intensity matching parameter yields $\overline{\Delta x_D}$ values of -6.3 m, -6.9 m and -5.0 m at the outer, inner and intertidal bar, respectively. These horizontal offsets are well in line with the Van Enckevort & Ruessink (2001) results. Comparison of the present BIM outcome to the results reported in Aarninkhof & Ruessink (2001) shows a considerable improvement of the match between $D_{o,n}$ and $D_{c,n}$. This can be attributed to the incorporation of the pre-processing technique for the selection of good quality video data only. Both comparisons confirm good performance of BIM with respect to the automated selection of video data on the basis of the Gaussian fit approach.

The sensitivity analysis to variable settings of three model parameters yields best results for $\beta = 0.10$, $p = 10$ and a γ parameterization according to Battjes & Stive (1985). Although the analysis of BIM performance yields reasonable results in terms of the mean deviations $\overline{\Delta x_D}$ and $\overline{\Delta A_D}$, it is observed that x_{D_o} and A_{D_o} show more variability than the associated x_{D_c} and A_{D_c} , which yields large $\sigma_{\Delta x}$ and $\sigma_{\Delta A}$ for all parameter settings, at each breaker bar. SBM capability to account for these variabilities needs further attention. Besides, it has to be noted that the analysis used here focusses on the match between $D_{o,n}$ and $D_{c,n}$ in the regions of wave breaking, hence around the breaker bars only. Any deviations between $D_{o,n}$ and $D_{c,n}$ in the trough regions were not taken into account. As we are interested in mapping subtidal bathymetry along the entire beach profile, it is concluded that the final calibration of the model parameters needs further consideration on the basis of the validation of SBM against field data.

BIM application at Duck (NC) shows that $\overline{D_{c,n}}$ overestimates $D_{o,n}$ in the trough regions, which induces an associated negative $\overline{\Delta A_D}$ in the bar regions. This mismatch is related to the BIM methodology for the pre-processing of raw video data, as will be demonstrated here. Figure 3.10 shows Duck results in terms of A_{D_c} and A_{D_o} , obtained from BIM application to 648 cross-shore intensity profiles, sampled from a total of 84 images collected at seven different days during the SandyDuck Experiment. Pre-processing of these data, including an additional constraint demanding that 95% of $\int D_c(x)dx$ occurs within a single camera field of view, yields a limited set of 63 intensity profiles which meet the criteria. Although A_{D_o} and A_{D_c} are well related (skill $R^2 = 0.83$), the results show a consistent, negative offset with respect to the line of equality ($\overline{\Delta A_D} = -0.382$), indicating that $D_{c,n}$ underestimates the associated $D_{o,n}$ in the bar region. Investigation of I_v (Figure 3.10b), the resulting $D_{o,n}$ (Figure 3.10c) and the

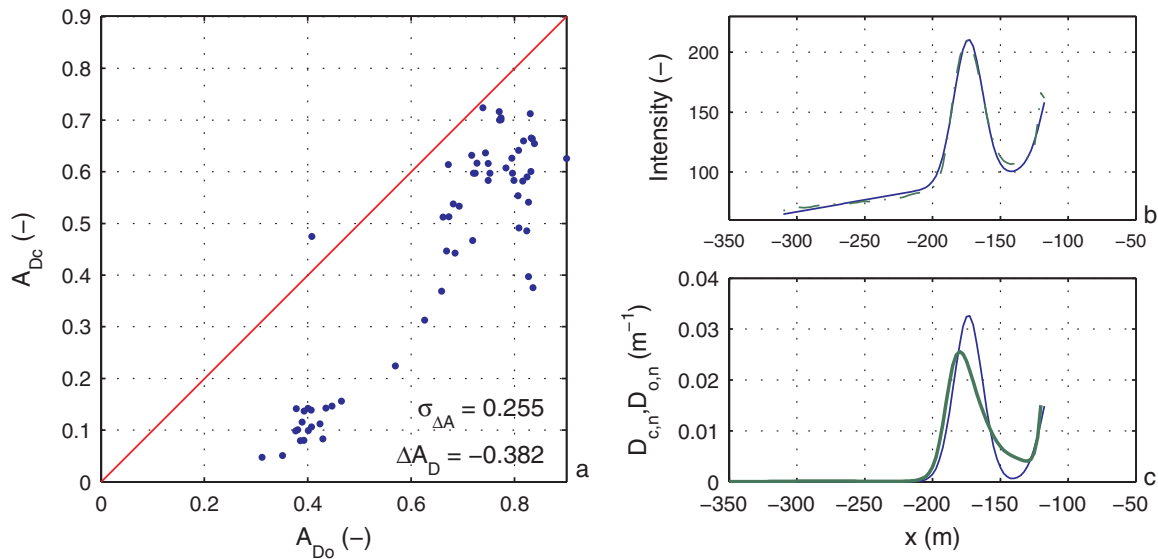


Figure 3.10: *Stand-alone application of BIM to a single-barred beach at Duck, NC (USA). Evaluation of BIM performance by means of a comparison of A_{Dc} and A_{Do} at the breaker bar (a). The consistent offset is explained with the help of (b) I_v (dashed line) versus I_G (solid line) at Duck array $y = 1100$ d.d. Oct. 2, 1997 GMT 19 hr. and (c) the associated $D_{c,n}(x)$ (bold line) versus $D_{o,n}(x)$ (thin line).*

associated $D_{c,n}$ (Figure 3.10c) shows that BIM applies an erroneous correction for background illuminations, based on the assumption of zero wave dissipation in the trough region at the lee side of a breaker bar. This assumption does not hold for the Duck bar configuration at October 2. Owing to the presence of a terrace-type inner bar close to the shoreline, dissipation of roller energy continues in the shallow region shoreward of the region of intense wave breaking. The non-zero dissipation rates in these shallow areas are observed from the raw intensity data (Figure 3.10b), before erroneously being removed by the BIM methodology to correct for background illuminations. As a result, $D_{c,n}$ exceeds $D_{o,n}$ in the trough region, which is compensated by an underestimate of $D_{o,n}$ at the breaker bar. This explains the consistent offset in terms of A_{Do} versus A_{Dc} . BIM performance at Duck can be improved by changing the model in a sense that the trend correction m_I is determined from the trend in $D_c(x)$ rather than from the raw intensity data only. This upgrade however is outside the scope of this thesis.

3.2.7 Conclusions

The Breaker Intensity Model (BIM) developed in this section performs the automated pre-processing and normalization of standard time-averaged video intensity data. Pre-processing involves the substitution of video-derived, cross-shore intensity profiles with a Gaussian approximation. It was found that this approach provides a sound base to remove noise from the raw video data and to exclude poor-quality data from further analysis. To remove the effect of persistent foam, a methodology was developed to isolate the roller-related contribution to time-averaged image intensity, based on a

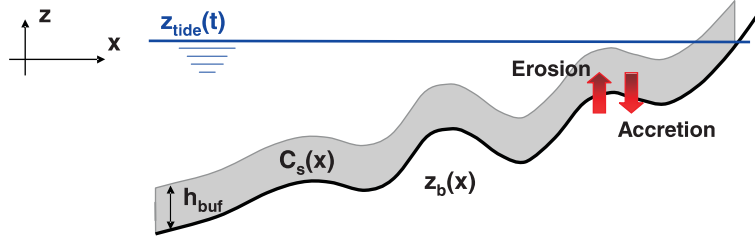


Figure 3.11: *Definition sketch of the model to map subtidal bathymetry.*

detailed investigation of the process of wave breaking as observed from intra-wave time-stack images. BIM is used to investigate the correspondence between normalized video observations of wave breaking and various model-predicted patterns of wave dissipation. It was found that D_r outperforms the other model-predicted wave characteristics that have been considered, suggesting that bubbles and foam are generated by the transition of kinetic roller energy into turbulence. Evaluation of BIM performance for variable settings of the model parameters yields best results for $\beta = 0.10$, $p = 10$ and a γ parameterization according to Battjes & Stive (1985). Although these settings yield reasonable results in terms of the mean deviations Δx_D and ΔA_D , it was found that x_{D_o} and A_{D_o} show much more variability than the associated x_{D_c} and A_{D_c} , inducing large $\sigma_{\Delta x}$ and $\sigma_{\Delta A}$ at all breaker bars. It has to be noted however, that these findings are based on the match between scaled video observations and model predictions of wave dissipation patterns in the areas of wave breaking only. Further detailing is necessary on the basis of the investigation of SBM capability to map subtidal bathymetry along the entire beach profile, including the trough regions.

3.3 Quantification of water depth from video observations of wave breaking

3.3.1 A model to map subtidal bathymetry: Approach

The Bathymetry Assessment Model (BAM) addresses the second sub-objective specified in Section 3.1 aiming to infer and update beach bathymetry on the basis of remote measurements of wave breaking. The BAM concept is generic in the sense that the input wave breaking information may originate from any measurement source, provided that this information relates to a wave breaking parameter that can be predicted with a wave transformation model. In the context of this work, BAM operates on a video-derived measure of wave dissipation $D_o(x)$, sampled from time averaged video imagery, and relates these to a model-computed measure of wave dissipation $D_c(x)$, determined from a one-dimensional parametric wave transformation model. Both $D_o(x)$ and $D_c(x)$ will be defined quantitatively in Subsection 3.3.2.

Within the context of the overall time-dependent model SBM, the sub-model BAM governs the morphodynamic updating of a coastal profile on the basis of vertical sediment fluxes, driven by differences between $D_o(x)$ and $D_c(x)$. The model is morpho-

dynamic in a sense that it accounts for a feedback mechanism between changes of bathymetry and the computed transformation of wave energy. It should be noted however, that the vertical sediment fluxes driving bathymetrical changes are determined from differences between $D_o(x)$ and $D_c(x)$ rather than a process-based approach that would quantify sediment transport rates from the local wave and current conditions. BAM aims for a partial update of the bottom elevation on the basis of each single image, without achieving a perfect match between $D_o(x)$ and $D_c(x)$. A perfect match would imply an over-fit on noisy intensity characteristics of a particular image. The embedding of BAM in the framework of the overall time dependent model SBM enables the model to resolve the evolution of coastal bathymetry from a sequence of video images, which provide a dominant signal in the evolution of video-observed patterns of wave breaking that exceeds the noise level.

BAM adopts a two-layer approach (Figure 3.11), consisting of the sea bed with elevation $z_b(x)$ and a sediment buffer layer with sediment availability $C_s(x)$, representing a sediment volume per unit area [m^3/m^2]. A positive difference $D_c - D_o$ drives an upward directed erosional sediment flux S_E from the sea bed to the buffer layer, causing local erosion of the sea bed and a local increase of C_s . A negative $D_c - D_o$ results in the opposite effect, driving a downward direct accretional sediment flux S_A which yields accretion of the sea bed and a decrease of C_s in the buffer layer. Cross-shore gradients of $C_s(x)$ drive the horizontal redistribution of sediment within the buffer layer from areas of large C_s (sediment surplus in the buffer layer due to sea bed erosion) to regions of small C_s (sediment shortage in the buffer layer due to sea bed accretion). The sediment buffer layer was included to guarantee conservation of mass within the overall system. Notice that C_s is not related to any physical process like wave breaking induced turbulence. It only provides a sediment buffer to enable erosion and accretion of the sea bed, while facilitating the redistribution of sediments within the coastal system.

In this section, the BAM model formulations are presented (Subsection 3.3.2) and model behaviour is investigated with the help of a synthetic data set (Subsection 3.3.3). The performance of SBM, involving the application of both BIM and BAM, is evaluated in Section 3.4 against field data collected at Egmond.

3.3.2 Model formulations BAM

BAM operates on a real-world time frame t , using a variable number of time steps with pre-defined spacing Δt to bridge the time gap $t_1 - t_0$ between successive, good-quality video images, collected at t_0 and t_1 (Figure 3.12). Every time t , the bathymetry $z_b(x, t)$ is estimated by updating the previous bathymetry $z_b(x, t - \Delta t)$ on the basis of a time-dependent vertical sediment flux $S(x, t)$, driven by differences between $D_c(x, z_b(t - \Delta t), t_1)$ and $D_o(x, t_1)$. D_c is computed from the tide and wave conditions at time t_1 , using the bathymetry at time $t - \Delta t$. To describe these processes mathematically, BAM solves time-dependent mass balance equations for the sea bed and the buffer layer, respectively

$$\frac{\partial z_b(x, t)}{\partial t} = - (S_E(x, t) + S_A(x, t)) \quad (3.17)$$

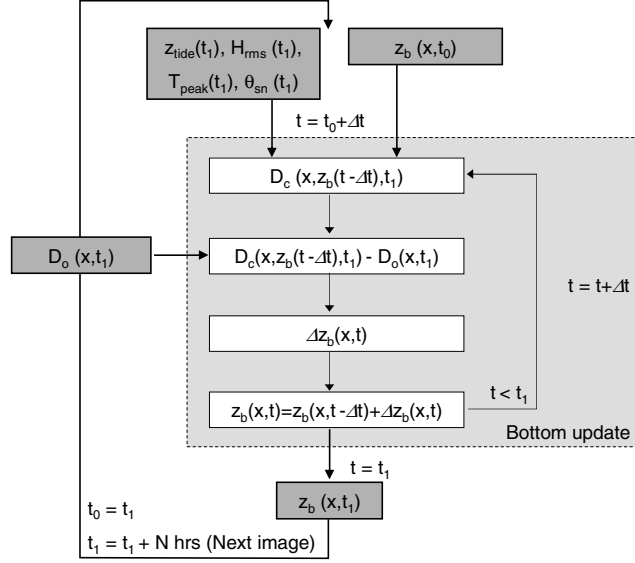


Figure 3.12: Operation of the model to map subtidal beach bathymetry. The diagram shows the time frame for the updating of bathymetry over the past period ranging from t_0 to t_1 , on the basis of $D_o(x, t_1)$, the tide and wave conditions at t_1 and the actual bathymetry $z_b(x, t)$. The duration of the time gap $t_1 - t_0$ (marked as N hours) depends on the availability of good quality video data.

$$\frac{\partial C_s(x, t)}{\partial t} - D \cdot \left(\frac{\partial^2 C_s(x, t)}{\partial x^2} \right) = S_E(x, t) + S_A(x, t) \quad (3.18)$$

In Eqs. (3.17) and (3.18), $S_E(x, t)$ and $S_A(x, t)$ represent the erosional and accretional sediment fluxes per unit area and per unit time [$m^3/m^2/s$] including pores, both driven by differences between $D_c(x)$ and $D_o(x)$. The diffusion term in Eq. (3.18) with diffusion coefficient D accounts for the redistribution of sediments in the buffer layer. Since the source terms in Eq. (3.17) and (3.18) are equal and opposite, the conservation of mass within the overall system of sea bed and buffer layer is guaranteed. The boundary conditions used at the seaward and shoreward end of the model are $\partial z_b / \partial x = 0$ and $\partial^2 C_s / \partial x^2 = 0$, stating that BAM does not allow for changes of bathymetry at the seaward and shoreward end of the model, nor diffusive sediment fluxes across the boundaries of the buffer layer.

Because wave dissipation rates increase with decreasing water depth, BAM renders a positive offset $D_c(x) - D_o(x) > 0$ into a local lowering of z_b and associated increase in C_s , and vice versa. The model formulations for S_E and S_A , which are applicable to regions where $D_c > D_o$ and $D_c < D_o$, respectively, read

$$S_E(x, t) = w_E \cdot F_{\text{dmp}}(x) \cdot \left(D_c(x, z_b(t - \Delta t), t_1) - D_o(x, t_1) \right) \quad (3.19)$$

$$S_A(x, t) = w_A \cdot F_{\text{dmp}}(x) \cdot \left(\frac{C_s(x, t)}{C_{s, \text{max}}(t)} \right) \left(D_c(x, z_b(t - \Delta t), t_1) - D_o(x, t_1) \right) \quad (3.20)$$

where w_E is the erosion parameter governing the time scale of bottom erosion, w_A the accretion parameter affecting the time scale of accretion and $C_{s, \text{max}}(t)$ is the cross-shore

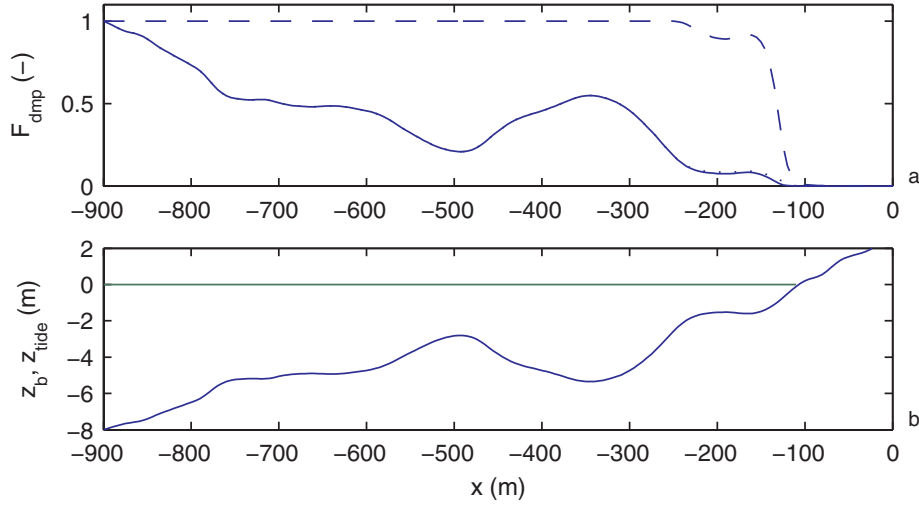


Figure 3.13: Appearance of the damping function F_{dmp} as typically applied at Egmond, The Netherlands. Visualization of (the components of) F_{dmp} (a) and a measured Egmond beach profile (b). The dashed line represents the tanh-part of Eq. 3.23, the dotted line (hardly visible behind the solid line) the effect of the $\frac{h(x)}{h_0}$ and the solid line the overall appearance of F_{dmp} .

maximum of $C_s(x, t)$ at time t . Both S_A and S_E are driven by differences between D_c and D_o . Following the conclusions of Section 3.2, D_c is set to equate the dissipation of roller energy D_r . The parameter D_o is obtained by scaling $D_{o,n}$ with the incoming wave energy flux, to arrive at a quantitative match of D_c and D_o . This yields

$$D_c(x, z_b(t - \Delta t), t_1) = D_r(x, z_b(t - \Delta t), t_1) \quad (3.21)$$

$$D_o(x, t_1) = E_0 c_{\text{gx}} D_{o,n}(x, t_1) \quad (3.22)$$

where $E_0 = \frac{1}{8} \rho g H_{\text{rms}}^2$ is the wave energy at deep water and c_{gx} is the cross-shore component of the wave group velocity, also at deep water. By scaling D_o and D_c with the incoming wave energy flux, high-energetic wave conditions have a stronger morphological impact than low-energetic conditions, which is in line with real-world coastal processes.

Eq. 3.20 shows that S_A also depends on the local sediment availability $C_s(x, t)$, normalized with $C_{s,\text{max}}(t)$. S_A approaches zero for very small C_s , thus preventing the occurrence of negative C_s in the buffer layer. Arbitrary settings of w_E and w_A generally yield an overall erosion $\int S_E dx$ which differs from the overall accretion $\int S_A dx$, thus allowing for the modelling of erosional or accretional coastal systems. As the overall system of sea bed and sediment buffer layer is mass conservative, erosion (accretion) of the sea bed is associated with a gain (loss) of sediment in the buffer layer. To model coastal systems with no net erosion or accretion at the sea bed, the parameters w_E and w_A can be set such that $\int S_E dx$ equals the overall accretion $\int S_A dx$ at every Δt .

Finally, Eqs. (3.19) and (3.20) embody an empirical damping function $F_{\text{dmp}}(x)$, which has been included for two-fold reasons. First, it aims to stimulate changes in

bathymetry in areas of low D_o and D_c , like the trough regions and the deep water part of the beach profile. Second, it aims to reduce sediment fluxes to zero at very shallow water, to avoid unrealistic BAM behaviour near the shoreline where the phase velocity c approaches zero, which causes D_r to become very large owing to its proportionality to E_r/c . Both objectives are addressed with the formulation

$$F_{\text{dmp}}(x) = 0.5 \left(\tanh \left(\frac{120h(x)}{L_{\text{deep}}} - \frac{15h_{\text{deep}}}{L_{\text{deep}}} \right) + 1 \right) \left(\frac{h(x)}{h_0} \right)^q \quad (3.23)$$

where $h(x)$ is local water depth, h_0 is the water depth at the seaward boundary of the model, L_{deep} is a representative deep water wave length for the field site or flume experiment of consideration, h_{deep} is a representative water depth near the outer end of the surf zone and q is an empirical power that needs calibration against measured data. L_{deep} and h_{deep} are considered as field site or flume experiment representative parameters, which do presently not vary with changing environmental conditions. The appearance of F_{dmp} typically applied at Egmond is shown in Figure 3.13, based on parameter settings $h_{\text{deep}} = 8$ m and $L_{\text{deep}} = 60$ m (estimated from a mean T_p of 6.2 s over the period 1999-2000) and $q=1.5$. Owing to the factor $\frac{h(x)}{h_0}$, F_{dmp} indeed stimulates morphological changes in the deeper trough regions as compared to the relatively shallow bar regions, while the tanh-part of Eq. (3.23) reduces F_{dmp} to zero in shallow water near the shoreline.

3.3.3 Evaluation of model behaviour against synthetic data

In this sub-section, the behaviour of BAM is investigated on the basis of a synthetic data set. Such a synthetic analysis involves the design of an artificial time series of beach profiles and hydrodynamic conditions, which provides the input for a wave transformation model to compute a data set of wave dissipation profiles. BAM interprets the wave dissipation profiles thus obtained as the ‘measured’ wave dissipation D_o , thus adopting an ideal data set to reconstruct the original set of beach profiles. This synthetic analysis enables us to verify the implementation of the BAM model formulations, to gain insight in BAM behaviour for different settings of w_A , w_E , D and q and to assess the model’s potential to reconstruct a target bathymetry for various hydrodynamic conditions and beach configurations, particularly in areas of poor information coverage like the trough regions. Results of the synthetic analysis are interpreted with respect to the outcome of a reference case, which is discussed in detail first.

Reference case

In the reference case, BAM is used to infer a bar-trough profile from an initially non-barred beach profile (Eq. 3.26) at $t = 0$ hr, on the basis of an artificially-generated time series of D_o . A wave transformation model is used to compute D_r profiles across a non-changing target bathymetry $z_b(x, t_1)$ during 50 consecutive hours. These D_r profiles provide the synthetic D_o for the reference case. During the 50 hour period, the tidal level z_{tide} varies according to

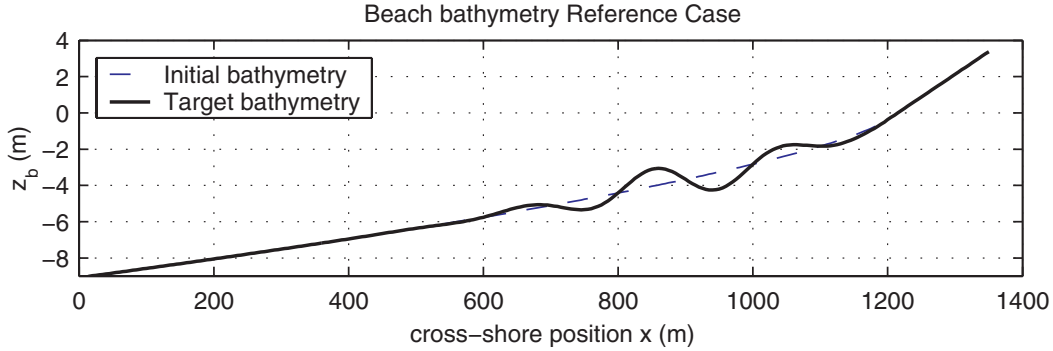


Figure 3.14: *Initial (dashed) and target (solid) beach bathymetry for reference case, synthetic tests BAM.*

$$z_{tide} = -A_{tide} \cdot \sin\left(\frac{2\pi \cdot t}{T_{tide}} - \pi\right) \quad (3.24)$$

where the tidal amplitude A_{tide} is set to 1 m and the period T_{tide} is 12 hours. The H_{rms0} of the shore-normal incident wave field is 1 m, with a T_p of 6.5 s.

The artificial bar-trough profile is taken from Bakker & De Vroeg (1988), who found tendencies in breaker bar behaviour along the Dutch coast that are quantitatively described by

$$z_b(x, t_1) = z_{b,mean} - A_b \cdot e^{-\left(\frac{x' - x_b}{R_b}\right)^2} \cdot \cos\left(\frac{2\pi(x' - x_b)}{L_b} - \phi_b\right) \quad (3.25)$$

In Eq. (3.25), x' is a cross-shore coordinate (positive in seaward direction), A_b is the maximum bar amplitude, x_b is the location of the maximum bar amplitude, R_b is a measure of the width of the barred part of the beach profile, L_b is the bar spacing and ϕ_b is the phase of the bar system. The Bakker & De Vroeg (1988) formulation describes sand bars as cosine-shaped perturbations to a mean beach profile $z_{b,mean}$. The bar amplitudes depend on the cross-shore location and the phase of the bar system. To represent a beach profile typically found at Egmond, the parameters are set to $A_b = 1$ m, $x_b = 300$ m, $R_b = 200$ m, $L_b = 200$ m and $\phi_b = 90^\circ$ (Roelvink, 1993). The mean beach profile elevation $z_{b,mean}$ is described by a simple power curve

$$z_{b,mean} - z_r = -A(x' - x_r)^b \quad (3.26)$$

where z_r is a reference elevation at location x_r , b is an exponent and A is a dimensional constant with unit $[m^{1-b}]$. Following Dean (1977), b is set to $2/3$ on the basis of the assumption of a uniform energy dissipation per unit volume of water under equilibrium conditions. Setting $A = 0.08m^{1/3}$ and $z_r = 0$ m at $x_r = -10$ m yields a representative Egmond profile with a 1:40 slope around the shoreline, which is interpolated to the shoreward-directed computational grid x of BAM (Figure 3.14).

BAM is applied with a time step Δt of 360 s. Default parameter settings for the reference case involve $w_E = 2.5 \cdot 10^{-5} m^3/m/N$, $D = 0.10 m^2/s$ and an initial sediment

availability $C_s = 1 \text{ m}^3/\text{m}^2$ along the entire profile. As the Bakker & De Vroeg (1988) formulation describes sand bars as a mass-conservative perturbation to a mean beach profile, the value of w_A is determined from the restriction of mass-conservation at the sea bed, which demands that the overall erosion $\int S_E dx$ equals the overall accretion $\int S_A dx$ at every time step Δt .

BAM behaviour for the reference case is illustrated in Figure 3.15. Deviations $D_c - D_o$ (Eqs. 3.21 and 3.22) drive a sediment flux $S_0 = S_E + S_A$, which causes accretion of the sea bed in the bar regions and erosion in the trough regions, with an associated decrease and increase in C_s , respectively, in the buffer layer. No changes of bathymetry occur outside the regions of wave dissipation. Diffusion induces a redistribution of sediment in the buffer layer, as can be seen from the flattening of the cross-shore distribution of C_s . Deviations $D_c - D_o$ and $z_b - z_{\text{target}}$ rapidly decrease during the first few hours, to reach a near-zero offset at $t = 50$ hr. Owing to the application of F_{dmp} , the model response time is small in the outer bar region, while increasing somewhat towards shallow water. Furthermore, it is observed that the time scale of profile adjustment in the trough regions is large as compared to the neighbouring bar regions. This originates from the observation that the accretion of sediment in the bar regions is associated with large deviations between D_c and D_o , along relatively small parts of the beach profile. The compensating erosion of sediment is driven by smaller deviations between D_c and D_o , which occur along larger portions of the beach profile. Running the model for a period considerably longer than 50 hours yields zero deviations $z_b - z_{\text{target}}$ at the sea bed and a uniform distribution $C_s = 1$ in the buffer layer, identical to the initial distribution of C_s at $t = 0$ hr. These observations confirm the conservation of mass at the sea bed and in the buffer layer.

To enable a quantitative comparison of different synthetic test cases, BAM performance is evaluated by means of the *rms* difference between the actual bathymetry $z_b(x, t)$ and the target bathymetry $z_{b,\text{end}}$ after 50 hours, quantified as

$$\epsilon_{\text{rms}}(t) = \sqrt{\frac{\sum \left(z_b(x, t) - z_{b,\text{end}}(x) \right)^2}{N_x}} \quad (3.27)$$

where N_x is the number of grid points in cross-shore direction. Figure 3.16 shows the evolution of ϵ_{rms} with time for the reference case. It confirms the earlier observation that profile deviations rapidly decrease during the first few hours and that the time scale of profile adjustment in the bar regions is small as compared to the trough regions. For large simulation times, ϵ_{rms} values approach zero, demonstrating the correct implementation of the BAM formulations.

In search of an objective characterization of BAM performance in terms of the evolution of $\epsilon_{\text{rms}}(t)$, a three-parameter exponential function

$$\epsilon_{\text{fit}}(t) = \epsilon_0 + \epsilon_1 \cdot e^{\left(\frac{-t}{\tau}\right)} \quad (3.28)$$

has been fitted to $\epsilon_{\text{rms}}(t)$, accounting for profile deviations in both the bar and trough regions. The model response time τ provides a measure for the time scale of error decay, while the profile adjustment ratio $\delta_\epsilon = \epsilon_0/(\epsilon_0 + \epsilon_1)$ yields a measure for the remaining

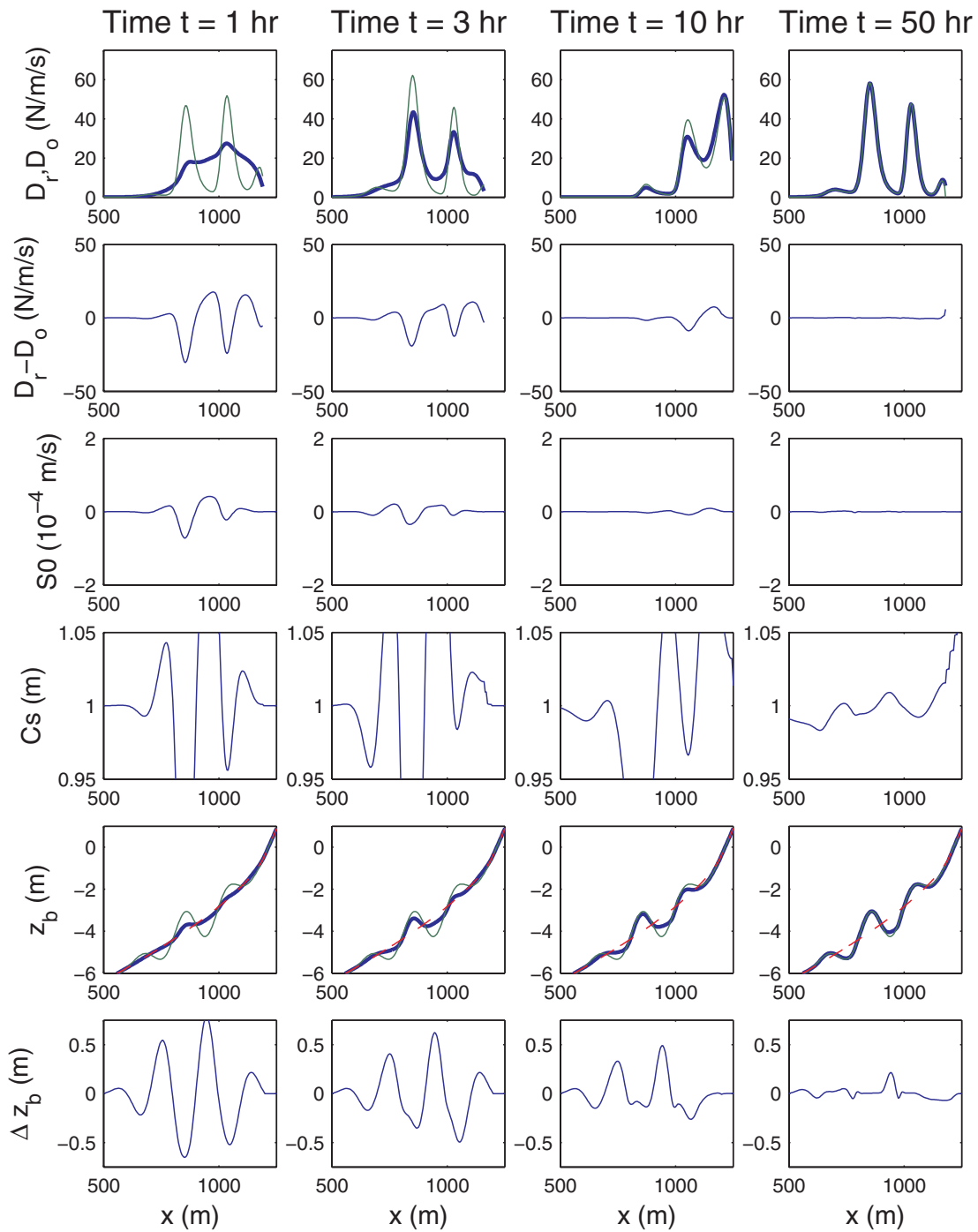


Figure 3.15: BAM behaviour reference case. Visualization of BAM results after 1, 3, 10 and 50 hours, by means of D_c versus D_o (upper row) and their deviation $D_c - D_o$ (second row), the sediment flux $S_0 = S_E + S_A$ (third row), the evolution of C_s (fourth row) and z_b (fifth row) driven by S_0 and the profile offset $\Delta z_b = z_b - z_{target}$. Bold lines refer to BAM outcome, fine lines represent D_o (first row) and z_{target} (fifth row) and the dashed line (fifth row) shows initial beach bathymetry.

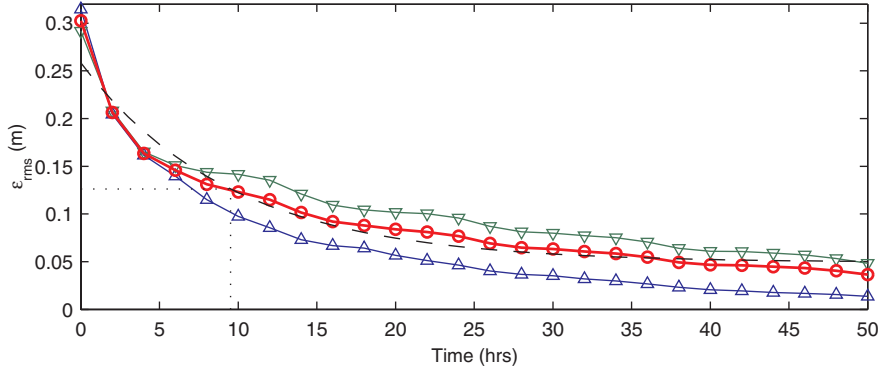


Figure 3.16: BAM application synthetic data. Evolution of ϵ_{rms} over time in the bar regions (\triangle), trough regions (∇) and along the entire profile (\circ). The dashed line represents ϵ_{fit} , which is used to quantify BAM performance.

profile deviations after 50 hours. Notice that τ represents the model response time associated with the computed error decay ϵ_1 after 50 hours, instead of the target decay $\epsilon_0 + \epsilon_1$. Good BAM performance therefore demands *both* τ and δ_ϵ to be small. A combination of large δ_ϵ with small τ indicates that BAM shows only limited reduction of the profile mismatch after 50 hours, albeit that this reduction was rapidly achieved. Values $\tau = 9.3$ hrs and $\delta_\epsilon = 19.3\%$ were found for the reference case. Notice that ϵ_{fit} , by nature of its definition, approaches a *constant* level $\epsilon_{\text{fit}} = \epsilon_0$ for large t , whereas the associated difference $\epsilon_{\text{rms}}(t)$ generally still shows a decreasing tendency for large t . As a result, ϵ_0 tends to overestimate $\epsilon_{\text{rms}}(t = 50)$, hence δ_ϵ represents an upper limit of the actual difference between the computed and the target bathymetry after 50 hours.

To gain insight in BAM behaviour for different settings of w_A , w_E , D and q and to assess the model's potential to reconstruct a target bathymetry for various hydrodynamic conditions and beach configurations, the synthetic analysis described above is performed for three different test series:

- Series A: Model sensitivity to variable parameter settings
- Series B: Model performance under variable tide and wave conditions
- Series C: Model sensitivity to variable bar morphology

BAM performance for the test series A-C is evaluated below in terms of τ and δ_ϵ .

Series A: Model sensitivity to variable parameter settings

Series A are meant to investigate BAM behaviour for different settings of the numerical model parameters. Test ranges for w_E , w_A , q and D and the results in terms of τ and δ_ϵ are summarized in Table 3.3.

Cases A1a-A1f are run in mass-conservative mode, which is realistic for the synthetic data set considered here. They show that w_E governs the time scale of profile adjustment. With increasing w_E , morphological changes per unit time increase, which

Table 3.3: BAM performance for different settings of w_E and w_A . Series A1 and A3 assume mass conservation at the bottom. This restriction does not apply to Series A2.

Case	w_E (ms^2/kg)	w_A (ms^2/kg)	q (-)	D (m^2/s)	τ (hrs)	δ_ϵ (%)
A1a	$0.5 \cdot 10^{-5}$	-	2	0.10	22.4	37.3
A1b	$1.0 \cdot 10^{-5}$	-	2	0.10	14.0	31.5
A1c	$2.5 \cdot 10^{-5}$	-	2	0.10	9.3	19.3
A1d	$5.0 \cdot 10^{-5}$	-	2	0.10	6.5	10.6
A1e	$10.0 \cdot 10^{-5}$	-	2	0.10	3.5	4.8
A1f	$25.0 \cdot 10^{-5}$	-	2	0.10	1.6	2.5
A2a	$2.5 \cdot 10^{-5}$	$0.25 \cdot 10^{-5}$	2	0.10	2.3	67.3
A2b	$2.5 \cdot 10^{-5}$	$0.50 \cdot 10^{-5}$	2	0.10	7.0	49.4
A2c	$2.5 \cdot 10^{-5}$	$1.25 \cdot 10^{-5}$	2	0.10	9.7	23.6
A2d	$2.5 \cdot 10^{-5}$	$2.5 \cdot 10^{-5}$	2	0.10	9.0	17.6
A2e	$2.5 \cdot 10^{-5}$	$5.0 \cdot 10^{-5}$	2	0.10	9.1	20.6
A2f	$2.5 \cdot 10^{-5}$	$12.5 \cdot 10^{-5}$	2	0.10	11.9	25.5
A2g	$25.0 \cdot 10^{-5}$	$5.0 \cdot 10^{-5}$	2	0.10	18.6	20.4
A2h	$25.0 \cdot 10^{-5}$	$12.5 \cdot 10^{-5}$	2	0.10	5.3	4.7
A3a	$2.5 \cdot 10^{-5}$	-	0.0	0.10	2.4	7.4
A3b	$2.5 \cdot 10^{-5}$	-	0.5	0.10	2.3	6.6
A3c	$2.5 \cdot 10^{-5}$	-	1.0	0.10	4.9	10.9
A3d	$2.5 \cdot 10^{-5}$	-	2.0	0.10	9.3	19.3
A3e	$2.5 \cdot 10^{-5}$	-	3.0	0.10	17.2	28.6
A4a	$2.5 \cdot 10^{-5}$	-	2	0	11.6	47.0
A4b	$2.5 \cdot 10^{-5}$	-	2	0.005	16.3	19.8
A4c	$2.5 \cdot 10^{-5}$	-	2	0.010	16.6	6.8
A4d	$2.5 \cdot 10^{-5}$	-	2	0.025	13.2	9.6
A4e	$2.5 \cdot 10^{-5}$	-	2	0.050	10.1	14.2
A4f	$2.5 \cdot 10^{-5}$	-	2	0.100	8.5	17.3
A4g	$2.5 \cdot 10^{-5}$	-	2	0.250	8.6	19.0

yields a decrease in both τ and δ_ϵ . BAM shows robust performance along the entire range of w_E values considered here. With increasing w_E , both τ and δ_ϵ approach zero, which confirms correct implementation of the BAM model formulations.

In A2a-A2f the assumption of mass-conservation at the sea bed is dropped. They show that BAM performance in terms of δ_ϵ is rather sensitive to the settings of w_A . Very small w_A hamper the generation of sand bars, while very large w_A hamper the deepening of the trough regions. The resulting profile deviations particularly occur in shallow water depths and negatively affect BAM performance after 50 hours. This observation suggests that the BAM outcome is governed by parameter settings rather than differences between D_o and D_c . This is not the case, however, as can be seen from the two additional test cases A2g and A2h. Cases A2g and A2h were designed to enable ongoing profile adjustment, by decreasing the model's response time through an

increase in w_E and w_A . Both parameters are increased with a factor 10 relative to the associated Cases A2b and A2c, respectively. The results show improved performance for both cases, with δ_ϵ dropping to about 5% for Case A2h, where w_E and w_A differ a factor 2. So, although the decoupling of w_E and w_A affects model performance in terms of τ and δ_ϵ at the time scale of 50 hours, BAM is capable of reconstructing $z_{b,\text{end}}$ on the basis of different values of w_E and w_A , albeit that τ increases with respect to the mass-conservative reference case.

Cases A3a-A3e show BAM performance for different values of the power q (Eq. 3.23), which governs the depth-dependent reduction of the sediment exchange between the sea bed and the buffer layer. The model response time τ increases with increasing values of q , due to a further reduction of the sediment fluxes between the bottom and the buffer layer, particularly in shallow water. Very small q settings show a tendency towards the formation of an unrealistic cliff near the shoreline, which negatively affects model performance for Case A3a. With increasing values of q , the ratio $\tau_{\text{bar}}/\tau_{\text{trough}}$ increases, indicating a relative decrease in the time scale of profile adjustment for the trough regions as compared to the bar regions. For $q = 3$, the response times for the bar and trough regions are approximately similar.

Series A4 investigate BAM sensitivity to variable setting of the diffusion coefficient D . For an initial sediment availability $C_s = 1 \text{ m}^3/\text{m}^2$, BAM performance is virtually unaffected by variable settings of the diffusion coefficient D . With decreasing C_s , BAM sensitivity to D increases, in a sense that a decrease in D hampers the generation of breaker bars, due to limited sediment availability for accretion. The results presented in Table 3.3 were obtained with a constant initial $C_s = 0.25 \text{ m}$. Even for such a small initial C_s , however, the sensitivity is limited as compared to the effect of variable settings of w_E , w_A or q .

Series B: Variable hydrodynamic conditions

Test series B aim to investigate BAM performance for variable tidal amplitude and wave height. Test ranges for A_{tide} and H_{rms0} are summarized in Table 3.4, including the results in terms of τ and δ_ϵ .

Test series B1a-B1c show that BAM performance generally improves with an increase in A_{tide} . This can be explained from the cross-shore migration of the wave dissipation peaks with variable z_{tide} (Van Enckevort & Ruessink, 2001), thus improving the D_o coverage along the beach profile. The slight decrease in BAM performance for Case B1d and B1e relates to profile deviations in the trough around $x = 950 \text{ m}$, which is less exposed to wave dissipation at water levels in excess of 1 m above mean sea level, and an emerging inner bar at low tide. BAM performance also improves with increasing wave height (Series B2a-B2h), again due to an improved coverage of D_o along the beach profile. In the case of a beach with multiple sand bars, improved D_o coverage involves an increase in the overall number of dissipation peaks, as well as a widening of each individual peak with increasing wave height. Test series B3a-B3f confirm the conclusions drawn from Series B1 and B2, saying that BAM performance benefits from increasing A_{tide} and H_{rms0} . The additional effect of including tidal variations decreases with increasing wave height. Very large wave heights, however, readily provide a good

Table 3.4: BAM performance for different hydrodynamic conditions. Stand-alone variation of A_{tide} (Series B1) and H_{rms0} (Series B2), and the combined effect (Series B3).

Case	A_{tide} (m)	H_{rms0} (m)	τ (hrs)	δ_{ϵ} (%)
B1a	0.0	1.0	8.9	26.6
B1b	0.5	1.0	9.7	22.4
B1c	1.0	1.0	9.3	19.3
B1d	1.5	1.0	7.9	23.8
B1e	2.0	1.0	8.1	27.9
B2a	0.0	0.6	14.8	87.2
B2b	0.0	0.7	18.9	68.3
B2c	0.0	0.8	14.8	47.5
B2d	0.0	0.9	9.1	39.2
B2e	0.0	1.0	8.9	26.6
B2f	0.0	1.1	8.9	11.9
B2g	0.0	1.2	6.7	7.0
B2h	0.0	1.3	5.3	6.3
B3a	0.0	0.5	10.4	93.0
B3b	1.0	0.5	27.5	78.5
B3c	0.0	1.0	8.9	26.6
B3d	1.0	1.0	9.3	19.3
B3e	0.0	1.5	3.3	12.0
B3f	1.0	1.5	4.8	13.7

coverage of wave dissipation information along the beach profile in themselves, which is negatively by the inclusion of tidal variations. This explains the marginal decrease in BAM performance for Case B3f as compared to B3e.

Series C: Systematic variation of bar morphology

Test Series C concern the investigation of BAM performance over a range of morphological configurations. These involve a systematic increase in bar height (Series C1), a widening of the surf zone (Series C2) and a nourishment case (Series C3) to represent a situation with no conservation of mass at the sea floor. The nourishment is schematized as a Gaussian-shaped sand mass of $200 \text{ m}^3/\text{m}^1$, located about 400 m off-shore, with a crest elevation at 3 m below mean level and a maximum height of 1.33 m with respect to the undisturbed equilibrium profile. The Bakker & De Vroeg (1988) bar morphology parameters and the results in terms of τ and δ_{ϵ} are summarized in Table 3.5.

Test cases C1a-C1d range from a weakly-developed sand bar system ($z_{\text{bar}} - z_{\text{trough}}$ about 1 m, bar slope 1:50) to a well-developed bar-trough system ($z_{\text{bar}} - z_{\text{trough}}$ about 4 m, bar slope 1:20). The results show that BAM performance decreases with increasing bar height, hence trough depth. Overall profile deviations are dominated by deviations found in the trough regions. Test Series C2 aim to investigate BAM performance for a

Table 3.5: BAM performance for different morphological configurations. Systematic variation of the bar height (Series C1) and the surf zone width (Series C2).

Case	A_b (m)	ϕ_b ($^\circ$)	L_b (m)	R_b (m)	x_b (m)	w_A	τ (hrs)	δ_ϵ (%)
C1a	0.5	90	200	200	300	-	5.7	7.3
C1b	1.0	90	200	200	300	-	9.3	19.3
C1c	1.5	90	200	200	300	-	8.0	45.4
C1d	2.0	90	200	200	300	-	8.5	57.0
C2a	1.0	90	150	150	200	-	7.3	28.8
C2b	1.0	90	200	200	200	-	5.8	27.2
C2c	1.0	90	300	300	300	-	3.4	25.5
C2d	1.0	90	400	400	400	-	2.3	25.4
C3a	0.0	-	-	-	-	$0.50 \cdot 10^{-5}$	36.9	88.0
C3b	0.0	-	-	-	-	$1.25 \cdot 10^{-5}$	31.6	29.1
C3c	0.0	-	-	-	-	$2.50 \cdot 10^{-5}$	16.2	14.4
C3d	0.0	-	-	-	-	$5.0 \cdot 10^{-5}$	9.0	5.4
C3e	0.0	-	-	-	-	$12.5 \cdot 10^{-5}$	3.8	1.2
C3f	0.0	-	-	-	-	$25.0 \cdot 10^{-5}$	2.1	0.8

three bar system with variable surf zone width, ranging from 400 m (Case C2a) to more than 1000 m (Case C2d). To account for sufficient coverage of D_o along the beach profile, Series C2 has been run with $H_{\text{rms}0} = 1.5$ m. The four test cases show very consistent behaviour, each achieving a δ_ϵ of about 25% after 50 hours. The relatively large τ for Cases C2a and C2b are induced by a slow profile adjustment in the relatively narrow trough regions. Finally, two important conclusions can be drawn from the nourishment case, which was run with different settings of w_A (Cases C3a-C3f). First, BAM shows the capability to reconstruct a target bathymetry in the case of a non-conservative sediment budget scenario ($\delta_\epsilon = 0.8\%$ for Case A3f). Second, the results for Series C3 confirm the findings obtained from Series A2 with respect to BAM performance for variable w_A , showing self-induced deviations near the shoreline if w_E exceeds w_A with a factor 5.

3.3.4 Discussion on BAM behaviour and applicability

The main objective of testing BAM on the basis of a synthetic data set was to investigate model behaviour for variable parameter settings and to assess its performance over a range of hydrodynamic conditions and morphological configurations. Regarding the latter, it was concluded that

- The time scale of profile adjustment is relatively small in the bar regions as compared to the trough regions, over the entire range of hydrodynamic conditions and beach configurations considered here.
- BAM performance improves with increasing wave height and increasing tidal amplitude. The additional effect of including tidal variations decreases with increasing wave height.

- The BAM concept is applicable over a wide range of morphological configurations. Model performance improves with decreasing bar amplitudes, while being rather insensitive to variations of the surf zone width.

Besides these conclusions on BAM applicability, the synthetic analysis has provided insight on two important aspects of BAM behaviour.

First, erroneous model deviations tend to accumulate near the shoreline. This was most clearly observed from the cases involving very small w_A settings, which hamper bar development at deeper water. The resulting lack of wave dissipation at deeper water yields an overestimate of D_c near the shoreline, which causes an unrealistic deepening of the beach profile near the shoreline. BAM has shown the capability to correct for these self-induced errors, albeit that the time scale involved is very large. This observation legitimizes the inclusion of a damping function F_{dmp} to reduce changes of bathymetry in shallow water. The favorable effect of F_{dmp} further appears from Case A3a, which shows the unrealistic development of a cliff near the shoreline if no h/h_0 dependent reduction of sediment fluxes is applied. Apart from these aspects, F_{dmp} is anticipated to be indispensable for SBM applications on the basis of field data, since the wave transformation models used here are not designed for use at very shallow water (Battjes & Janssen, 1978) and D_c theoretically becomes infinite at zero water depth (owing to its proportionality with E_r/c), while the associated video-derived D_o will not.

Second, the time scales of profile adjustment are governed by w_E , w_A and q . In mass-conservative mode, the model response time τ rapidly decreases with increasing values of w_E (hence w_A) and decreasing values of q . The bar regions show a more rapid decrease in τ for lower q than the trough regions. When applied in non-conservative mode, BAM still manages to reconstruct a target bathymetry, at least if w_E and w_A differ less than a factor 2, albeit that the time scale involved increases with increasing relative differences between w_E and w_A . Unrealistic BAM behaviour, caused by self-induced profile deviations near the shoreline, is observed for situations where w_E and w_A differ more than a factor 5. It is concluded that the settings w_E , w_A and q need to be chosen carefully, since the combination of their absolute values, governs the time scale of profile adjustment. Model validation against field data is needed to determine optimal settings for these parameters.

3.4 Validation of Subtidal Beach Mapper

3.4.1 Introduction

In Sections 3.2 and 3.3, the two sub-models that compose SBM were described individually and tested in stand-alone mode. In this section, we investigate the performance of the overall model SBM on the basis of a morphological data set, acquired during the first year after nourishing a beach in front of the Egmond boulevard. The center of the nourishment area is located approximately 2 km north of the field site of the extensive Coast3D experiment (Ruessink et al., 2000). In this validation section, we limit ourselves to a comparison of two SBM based bathymetries and the corresponding bi-annual field surveys across the nourished area. The background and morphological evolution

of the Egmond nourishment are discussed in more detail in Chapter 4, making use of both the inter- and subtidal beach mapper.

3.4.2 Validation of SBM at Egmond: Heuristic approach

To assess SBM performance at the time scale of 1 year, the model is applied to quantify the evolution of subtidal bathymetry along 2 cross-shore arrays, over a 12 month period starting September 1999. During this period, the WESP was used to bi-annually survey nearshore bathymetry, typically along 50 cross-shore profiles with 100 m spacing alongshore. The measured depth is estimated to have an error of less than 15 cm (Van Enckevort & Ruessink, 2001). The survey data were interpolated to a rectangular grid with a cross-shore and alongshore spacing of 10 m, yielding good-quality bathymetrical maps of September 1999, May 2000 and September 2000.

Offshore wave conditions (H_{rms0} , T_p and $\bar{\theta}_0$) were measured with a directional wave buoy at IJmuiden, located approximately 15 km to the south of the nourished site. Approximately 50% of the missing data, which occurred during 15% of time, could be replaced by values from an identical buoy approximately 75 km to the north. Absence of any wave data caused SBM to be non-applicable during the period October 18 - November 17, 1999. Offshore tidal levels are found from interpolation in water level data collected at tidal stations located 15 km north and south of Egmond.

Video data were collected hourly with an ARGUS video station, installed at 43 m above sea level on top of the Egmond lighthouse Jan van Speyk for the purpose of monitoring the morphological evolution of the nourished area. In the context of this validation study, images sampled from the offshore-directed camera 3 and the northward-oriented camera 1 are used to quantify changes of bathymetry along a central array $y = -130$ m and an outer array $y = -1500$ m, respectively. Both camera views cover the entire array of interest, which is a necessity for application of the present SBM model.

The stand-alone tests of BIM and BAM have readily shown that good SBM performance demands the specification of appropriate settings for at least six model parameters (γ , β , p , w_E , w_A and q). Considering the large variabilities $\sigma_{\Delta x}$ and $\sigma_{\Delta A}$ that result from a comparison of $D_{c,n}$ to $D_{o,n}$ (Subsection 3.2.5), a seventh parameter T_{hist} is introduced here. The maximum update period T_{hist} sets an upper limit for the duration $t_1 - t_0$ of bathymetry updating between successive good-quality video images. By doing so, we aim to avoid that SBM over-fits $z_b(x, t)$ on a single, potentially inaccurate, dissipation profile $D_o(x, t_1)$, induced by large $t_1 - t_0$. This situation may occur after data gaps in the video archive or periods of poor-quality images. For convenience sake, all seven parameters that affect SBM performance are listed here

- The breaker parameter γ . With decreasing γ , wave breaking occurs at deeper water, which yields a relative increase (decrease) of D_c at the outer (intertidal) bar. The different distribution of D_c over the breaker bars directly affects S_0 , which is driven by deviations $D_c - D_o$.
- The roller parameter β . A decrease in β delays the dissipation of roller energy. It is associated with a flattening, widening and shoreward migration of the peaks

of D_c . So, different β settings affect the shape and location of the peaks of D_c , hence S_0 .

- The persistent foam parameter p . A decrease in p is associated with an increased correction for the effect of persistent foam, inducing a narrowing of the peaks of D_o and increasingly different areas A_{D_o} at various bars. The different distribution of D_o over the breaker bars directly affects $D_c - D_o$, hence S_0 .
- The erosion parameter w_E and the accretion parameter w_A . The parameters w_E and w_A affect the absolute magnitude of S_0 , hence the time scale of profile adjustment. The response time τ of SBM increases with decreasing w_E and w_A , as well as increasing relative differences between w_E and w_A .
- The depth power q . The parameter q governs the depth dependent reduction of S_0 . With increasing q , the overall model response time τ decreases. The bar regions show a more rapid decrease in τ than the trough regions, indicating that an increase in q stimulates profile adjustment in the trough regions.
- The maximum update period T_{hist} . The parameter T_{hist} sets an upper limit for the duration $t_1 - t_0$ of bathymetry updating between successive good-quality video images. Large T_{hist} may induce unrealistic profile variabilities caused by overfitting on a single, potentially inaccurate, dissipation profile D_o .

Best parameter settings $\beta = 0.10$, $p = 1$, $w_E = 1 \cdot 10^{-7} \text{ ms}^2/\text{kg}$, $w_A = 2.5 \cdot 10^{-7} \text{ m}^3/\text{m}/N$, $q = 1.50$, $T_{\text{hist}} = 24$ hours and γ according to Battjes & Stive (1985) were heuristically found from a comparison of video-derived beach profiles at May 17 and August 28, 2000 with the corresponding surveyed profiles, along two different cross-shore arrays. The results thus obtained (Figure 3.17) demonstrate SBM's capability to reproduce the shoreward migration of the outer bar and the net accumulation of sand in the shallow surf zone along the central array $y = -130$ m. With vertical deviations of 5 to 15 cm in terms of the elevation of the bar crest and deviations of 20 to 40 cm at the seaward face of the bars, SBM performs well in the bar regions along this array. Although the model shows a correct tendency towards accretion in shallow water, the present parameter settings do not enable SBM to reproduce the generation of the intertidal bar over the summer period. Further stimulating morphological changes in shallow water through a decrease in q yields improved SBM performance along array $y = -130$ m, but also invokes unrealistically large accretion of sediment in the shallow zone of array $y = -1500$. The present settings thus represent a compromise. In the trough regions, the water depth is generally underestimated, except for the inner trough in May 2000. At deeper water, SBM results show an erroneous accretion at the seaward face of the nourishment, while the surveyed profiles indicate a 100 m onshore migration of the nourishment to become the new outer bar.

In terms of volume changes between the -8 and 0 m depth contours along the array $y = -130$ m, SBM finds a net accretion of 229 (273) m^3/m after eight (twelve) months, which are somewhat large as compared to the measured accretions of 219 (155) m^3/m . Accretion of sand at the dry beach is not included in this analysis. This explains the

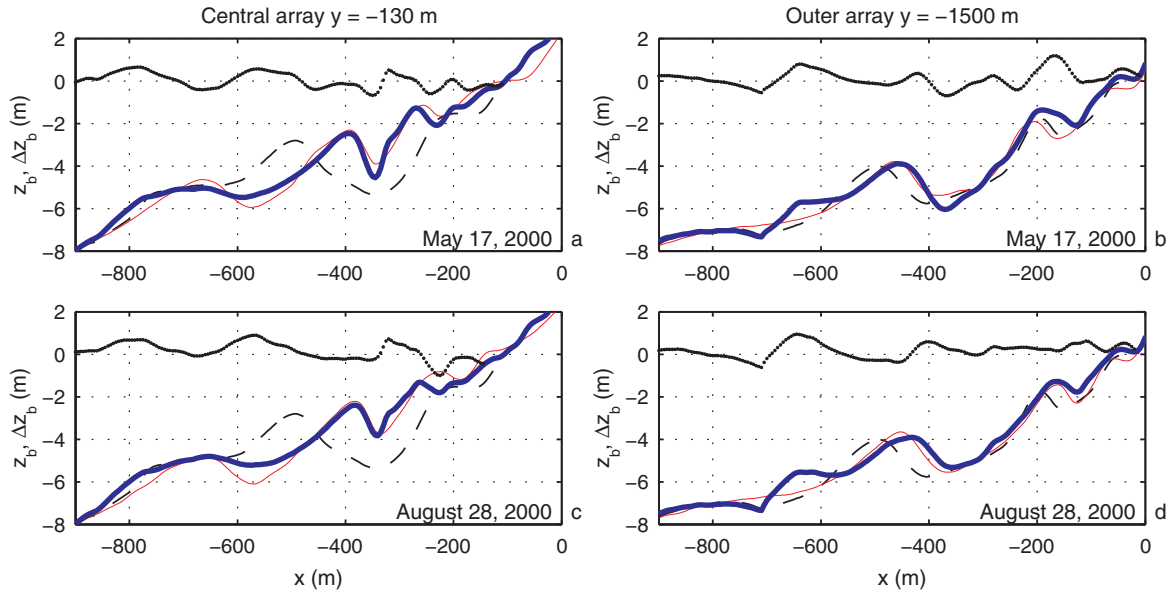


Figure 3.17: Validation of SBM against field data Egmond station Jan van Speyk. Modelled (bold line) bathymetry, surveyed (thin line) bathymetry and the difference $\Delta z_b = z_b - z_{\text{target}}$ (dotted line) at May 17, 2000 (a,b) and August 28, 2000 (c,d), for the central array $y = -130$ m (a,c) and the outer array $y = -1500$ m (b,d). The initial profile (dashed line) is surveyed in September 1999.

decrease in the *measured* accretion over the period May 2000 - September 2000, which is primarily related to a seaward shift of the 0 m contour. With a net erosion of $3 \text{ m}^3/\text{m}$ between the -8 and 0 m depth contours over the three-month summer period, erosion processes only marginally contribute to the decrease in the observed accretion. If we limit the volume analysis to the morphological changes between the -5 m and 0 m depth contours, the calculated accretion is 194 (236) m^3/m after eight (twelve) months, which are to be compared to a measured accretion of 244 (195) m^3/m . The increase in the measured accretion rates is induced by the onshore migration of the shoreface nourishment, thereby passing the -5 m depth contour. Thus, excluding the erroneous accretion at the seaward side of the shoreface nourishment from the volume analysis improves SBM performance in terms the calculated changes of beach volume, particularly after 12 months.

Table 3.6: Time- and profile-averaged error statistics on SBM performance along two different cross-shore arrays.

Alongshore position (m)	$\overline{\Delta z}$ (m)	Δz_{rms} (m)	$\overline{\Delta r}$ (-)	Δr_{rms} (-)
y=-1500 (camera 1)	0.14	0.39	0.089	0.241
y=-130 (camera 3)	0.08	0.39	-0.055	0.237

In search of an objective assessment of SBM performance, we follow Stockdon & Holman (2000) by quantifying model deviations in terms of the elevation errors Δz_b ,

$$\Delta z_b(x, t) = z_b(x, t) - z_{\text{target}}(x, t), \quad (3.29)$$

and the relative errors

$$\Delta r_b(x, t) = \frac{z_b(x, t) - z_{\text{target}}(x, t)}{z_{\text{MSL}} - z_{\text{target}}(x, t)}, \quad (3.30)$$

where z_{MSL} is the tidal elevation at mean sea level (MSL). This means that absolute profile deviations are normalized with the local water depth at MSL. Positive Δz_b indicate an underestimate of local water depth. The profile-averaged offsets $\overline{\Delta z}$ and $\overline{\Delta r}$ are computed as

$$\overline{\Delta z} = \frac{1}{N_x} \sum_{i=1}^{N_x} \Delta z_b(x), \quad (3.31)$$

$$\overline{\Delta r} = \frac{1}{N_x} \sum_{i=1}^{N_x} \Delta r_b(x), \quad (3.32)$$

where N_x is the number of cross-shore locations. Only Δz_b and Δr_b for $z_{\text{target}} < 0$ m are taken into account. The *rms* error of the differences, calculated as

$$\Delta z_{\text{rms}} = \sqrt{\frac{1}{N_x} \sum_{i=1}^{N_x} (\Delta z_b(x))^2}, \quad (3.33)$$

$$\Delta r_{\text{rms}} = \sqrt{\frac{1}{N_x} \sum_{i=1}^{N_x} (\Delta r_b(x))^2}, \quad (3.34)$$

is used to measure the variability of the differences. For the computed profiles shown in Figure 3.17, $\overline{\Delta z}$ (Δz_{rms}) is 0.01 m (0.35 m) in May 2000, and 0.14 m (0.43 m) in August 2000. The positive values found for $\overline{\Delta z}$ indicate an overestimate of the overall accretion for both profiles. The relative errors $\overline{\Delta r}$ (Δr_{rms}) are -0.007 (0.211) and -0.041 (0.261) for May 2000 and August 2000, respectively, indicating that *rms* profile deviations typically amount to 20 to 25 % of the local water depth at MSL. It is noted that these relative errors are largely driven by profile deviations in shallow water. Time-averaged statistics on profile deviations (Table 3.6) demonstrate that SBM performance is similar along the two cross-shore arrays, even though the D_o profiles involved were sampled from different cameras. These results are the more encouraging since the model validation was largely based on SBM performance along array $y=-130$ m.

To examine SBM performance along different parts of the beach profile, each measured profile along array $y=-130$ m was divided into six sections (Figure 3.18), representing the outer bar, the outer trough, the inner bar, the inner trough, the intertidal bar and the inner surf zone up to a beach elevation $z_b = 0$ m. With a Δz_{rms} of 22 cm in the inner bar region, the statistics per section (Table 3.7) show good SBM performance

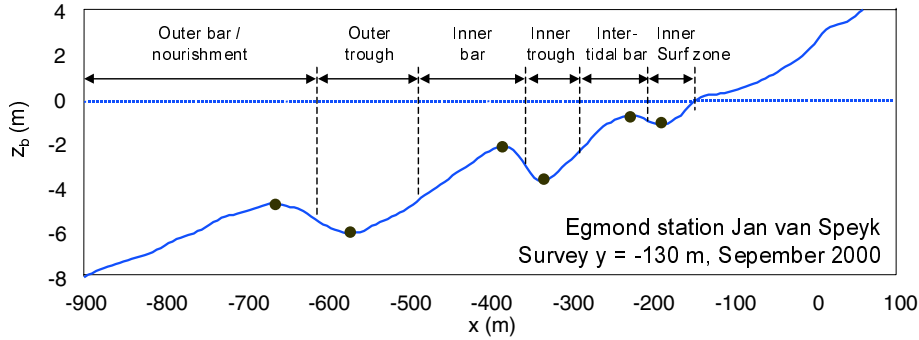


Figure 3.18: *Sub-division of beach profile in six regions for separate evaluation of SBM performance. The boundaries of each region are chosen at the middle point between the neighbouring bar crest and trough channel.*

there. The statistics confirm poor performance at the intertidal bar, as mentioned above. Maximum Δz_{rms} up to 52 cm are found in the trough regions. On the average, SBM underestimates water depths in the trough regions (positive $\overline{\Delta z}$) and overestimates water depth in the bar regions (negative $\overline{\Delta z}$). Relative errors increase with decreasing water depth.

3.4.3 SBM sensitivity to variable parameter settings

The SBM results presented in Sub-section 3.4.2 were obtained with parameter settings, that were found from a heuristic search into SBM performance along two Egmond arrays at $y = -130$ m and $y = -1500$ m. The objective of this sub-section is to provide further background on the model sensitivity to variable parameter settings, on the basis of a qualitative description of the outcome of a test series along array $y = -130$ m. To facilitate the interpretation of our findings, the seven model parameters are categorized by means of a hydrodynamic cluster (β , γ), a video cluster (p , T_{hist}) and a morphological cluster (w_E , w_A , q). Sub-section 3.4.3 is concluded with a brief recipe for model calibration.

Table 3.7: *SBM performance along different sections of Egmond Jan van Speyk profile $y = -130$ m. Mean statistics on Δz_b and Δr_b per section, obtained from the comparison of SBM results and surveyed bathymetries at May 17, 2000 and August 28, 2000.*

Section	$\overline{\Delta z}$ (m)	Δz_{rms} (m)	$\overline{\Delta r}$ (-)	Δr_{rms} (-)
Outer bar	0.20	0.37	0.028	0.058
Outer trough	0.47	0.52	0.080	0.087
Inner bar	-0.19	0.22	-0.063	0.070
Inner trough	0.07	0.46	0.029	0.131
Intertidal bar	-0.26	0.50	-0.253	0.446
Inner surf zone	-0.25	0.29	-0.384	0.514

Hydrodynamic parameters (β , γ)

To investigate model sensitivity to variable γ settings, γ was varied over the range 0.60-0.75 and compared to the default parameterization according to Battjes & Stive (1985). With decreasing γ , D_c at outer bar increases, which is compensated by a decrease in D_c in the shallow surf zone. A value $\gamma = 0.60$ causes D_c to overestimate D_o at the outer bar. Consequently, the elevation of the outer bar is significantly underestimated, in association with an appreciable decrease in the accretion in the outer trough. The opposite occurs in the shallow surf zone, where profile deviations decrease with increasing γ , due to larger accretion rates as a result of lower D_c . A large $\gamma = 0.75$ particularly causes an overestimate of the accretion in the outer and inner trough regions, in combination with a slight overestimate of the elevation of the outer bar. Apart from slightly improved results at the outer bar and in the trough regions, and a small increase in profile deviations in the shallow surf zone, SBM results with γ according to Battjes & Stive (1985) do not differ significantly from the results found for large γ .

Variation of β in the range 0.075-0.125 shows a significant deepening of the trough regions with decreasing β . This is induced by ongoing propagation of roller energy into the trough regions of nearly zero D_o , which causes D_c to overestimate D_o . This effect is particularly observed in the inner trough region. Owing to the flattening and widening of the D_c peaks, a decrease in β is also associated with a marginal increase in bar elevation, albeit that this effect is only of secondary importance as compared to the variability in trough depth. The β parameterization according to Walstra et al. (1996) shows good performance in the bar regions, but this is largely compensated by a significant overestimate of the accretion in the trough regions.

Video parameters (p , T_{hist})

To assess SBM sensitivity to p , the settings of p were varied over the range 0.5-5.0. The model outcome shows a deepening of the trough regions and the seaward face of the breaker bars with decreasing p . This is induced by a narrowing of the peaks of D_o , resulting from a more rigorous correction for the effect of persistent foam. A small value $p = 0.5$ yields an appreciable increase in the accretion in a narrow region around the bar crest. However, owing to the narrowing of the peaks of D_o , D_c increasingly overestimates the corresponding D_o at both sides of the dissipation maximum, which yields a deepening of the trough regions and the bar face. The opposite situation occurs for large p , which induces a non-realistic flattening of the overall beach profile. A decrease in p further stimulates bar generation in shallow water, while it hampers bar formation at deeper water.

The parameter T_{hist} limits the maximum morphological changes for a single image. The latter increases with increasing T_{hist} . An investigation of SBM outcome for $T_{\text{hist}} = 36$ hours as compared to 12 hours shows a slight increase in the accretion in deep surf zone section and at very shallow water. This implies that large T_{hist} improves SBM performance in the shallow surf zone, while the deep section benefits from lower T_{hist} . SBM sensitivity to variations of T_{hist} is primarily observed along regions which are less frequently exposed to wave breaking.

Morphological parameters (w_E , w_A , q)

The three morphological parameters w_E , w_A and q govern the time scale of profile adjustment. Changing the absolute values of w_E and w_A does not affect the overall patterns of erosion and sedimentation, but the time scale of profile adjustment changes. This implies that tendencies towards erosion or accretion become more apparent. For the central array $y=-130$ m, this means that an increase in w_E and w_A is associated with an increase in the erroneous accretion at the seaward side of the shoreface nourishment, additional erosion at the seaward face of the inner bar and additional accretion in the inner trough region, across the intertidal bar and in the inner surf zone. Changing the ratio of w_E and w_A directly affects the patterns of erosion and sedimentation along the beach profile. In the case of the synthetic analysis (Section 3.3.3), it was found that this aspect does affect the time scale of profile adjustment, but not the final result. As we aim for a gradual update of bathymetry on the basis of a time series of video images, instead of over-fitting bathymetry on a single, potentially inaccurate D_o , this aspect is of relevance here. The results obtained from varying the ratio w_A/w_E over the range 1.5-2.5 confirm that the tendencies towards accretion at the seaward side of the shoreface nourishment, in the trough regions and in shallow water are stimulated with an increase in w_A/w_E .

Lowering q implies a depth-dependent increase in the time scale of profile adjustment, the effect of which increases with decreasing water depth. Variation of q over the range 1.0-2.5 shows that small q particularly stimulate the tendency towards accretion in the region of the intertidal bar. However, existing tendencies towards erosion or accretion at deeper parts of the surf zone are also stimulated, albeit less rigorously. This is observed from a slight increase in the erroneous accretion seaward of the shoreface nourishment and some additional erosion of the seaward face of the inner bar for small q . Thus, the morphological parameters w_E , w_A and q are coupled in a sense that a decrease in q increases the time scale of profile adjustment, which is primarily governed by the absolute values and ratio of w_E and w_A .

In summary: A recipe for SBM calibration

In search of the calibration of SBM, it is important to realize that the *patterns* of erosion and accretion are driven by differences between D_o and D_c , which are affected by the hydrodynamic parameters β and γ , the breaker intensity parameter p and the ratio w_A/w_E . The *time scale* of profile adjustment is governed by the absolute values and ratio of w_E and w_A , the depth power q and, to a lesser extent, the maximum update period T_{hist} . The calibration of SBM largely relies on setting appropriate values for the time scale parameters, to obtain a model that resolves the morphological changes along the beach profile, without over-fitting on inaccuracies of D_o . A recipe for SBM calibration involves a three-step approach, where steps 2 and 3 may be iterative:

- Step 1: Hydrodynamic parameters. It was found that SBM shows fair performance with default settings for γ and β that match the settings reported by other researchers (Battjes & Stive, 1985; Reniers & Battjes, 1997) as part of careful

calibration studies of the wave model. It is therefore recommended to adopt the Battjes & Stive (1985) parameterization for γ and set β to 0.10.

- Step 2: Video parameters. The test runs considered in this study have shown best SBM performance for $T_{\text{hist}} = 24$ hours and $p = 1$. These values are recommended as the default settings to start from. T_{hist} may be lowered if small numbers of inaccurate images drive unrealistic bathymetrical changes. The settings of p may be reconsidered if the SBM results show too much flattening of the beach profile or deepening of the trough regions.
- Step 3: Morphological parameters. To obtain insight in the prevailing tendencies for erosion and accretion, it is recommended to start from a concise analysis of SBM sensitivity to variable q , w_E , w_A and w_A/w_E . In absence of any other calibration data, profile evolution at the intertidal beach may be compared to the corresponding IBM output at the location of the array of interest. If necessary, the settings of T_{hist} and p (Step 2) may be reconsidered, to damp the erroneous contribution of small numbers of poor quality images and to stimulate or hamper the deepening of the trough regions.

Presently, it involves a heuristic search to arrive at best settings for the morphological parameters w_E , w_A and q , thereby accounting for pre-existing expert knowledge on the anticipated erosion or accretion of the coastal system of interest and its morphodynamic behaviour in general. By saying so, we acknowledge that the present calibration procedure involves an important subjective component, particularly at Step 3. The development of a more objective methodology for SBM calibration is subject of further research.

3.4.4 Discussion on SBM performance Egmond

In this section, SBM was applied to map subtidal bathymetry along two Egmond arrays spaced approximately 1400 m alongshore. The application has demonstrated the model's capability to reproduce the dominant morphological changes during the first year after placing a shoreface nourishment, including the shoreward migration of the outer bar and the net accretion of sand in the nearshore part of the surf zone. The *rms* error of the vertical deviations along the beach profile typically amounted 40 cm for both cross-shore arrays. This result compares well to the Δz_{rms} of 90 cm, reported by Stockdon & Holman (2000) for their model to map subtidal bathymetry from video-based estimates of wave celerity. Relative errors Δr_{rms} increase with decreasing water depth. Furthermore, SBM shows a tendency to overestimate the overall accretion across the surf zone.

Detailed investigation of the calculated profile evolution over one year (Figure 3.19) demonstrates that profile deviations at deeper water ($x = -800$ m) are induced by the inclusion of a limited number of poor quality dissipation profiles D_o . Once developed, SBM does not provide an erosional difference $D_c - D_o$ to remove the erroneous accretion at deeper water. The latter observation also applies to the outer trough region ($x = -550$ m), where SBM gradually lowers the bed elevation over the period September 1999

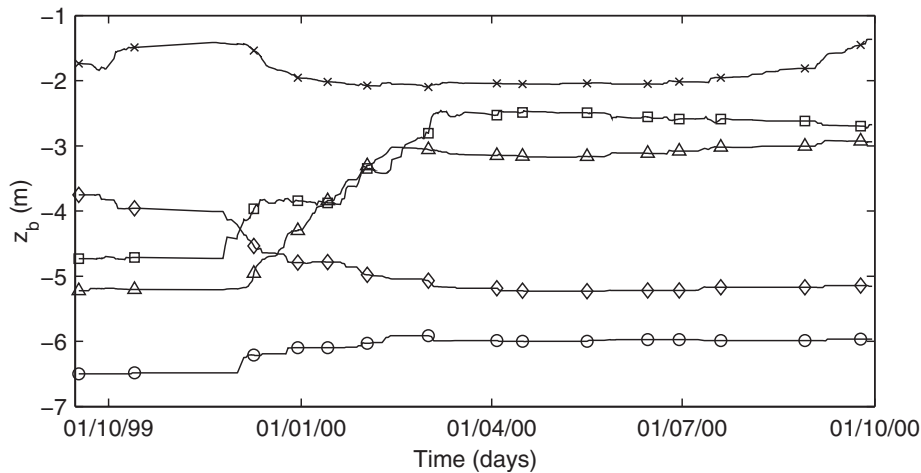


Figure 3.19: Time series of bed elevation along the central array $y = -130$ m at locations $x = -800$ m (\circ), $x = -550$ m (\diamond), $x = -400$ m (\square), $x = -325$ m (\triangle) and $x = -225$ m (\times). Notice that the markers are plotted every 50th data point, hence do not represent all data.

to April 2000. At that point however, SBM lacks a difference $D_c - D_o$ to induce the desired further lowering of the outer trough. Instead, inaccurate D_o cause a minor accretion of the outer trough region during the summer period. Similar tendencies are observed in the inner trough region ($x = -325$ m), where the accumulation of small errors also yields an erroneous accretion over the summer period. Notice furthermore that the inner surf zone time series at $x = -225$ m shows an favorable increase in the bed elevation in September 2000, which compensates for the vertical offset in the inner surf zone at August 28, that was reported earlier (Figure 3.17).

It is thus concluded that profile deviations after one year are induced by the combined effect of (i) the occasional inclusion of poor quality D_o , (ii) lack of erosional differences $D_c - D_o$ to compensate for erroneous accretions at deeper water and (iii) the accumulation of small errors over time, induced by inaccurate D_o . Mechanisms (i) and (ii) dominate erroneous profile evolution in areas that are hardly exposed to wave dissipation, while the importance of mechanism (iii) increases with decreasing water depth. Once again, this stresses the importance of setting an appropriate model response time, since the effect of both mechanisms (i) and (iii) increases with decreasing model response time.

The SBM sensitivity analysis along array $y = -130$ m (Subsection 3.4.3) has shown that the model response time is governed by the absolute values of w_E and w_A , their ratio w_A/w_E , the depth power q and, to a smaller extend, T_{hist} . Investigating SBM results along multiple cross-shore arrays, it was found that the model response time is also affected by the number of images that meet the BIM acceptance criteria on D_o quality. The latter number varies for different arrays. Along the outer array $y = -1500$ m, the number of processed images over the period September 15, 1999 to October 1, 2000 exceeds the number for the central array $y = -130$ with about 40% (Figure 3.20). This yields an increase in the cumulative bathymetry update time, defined as

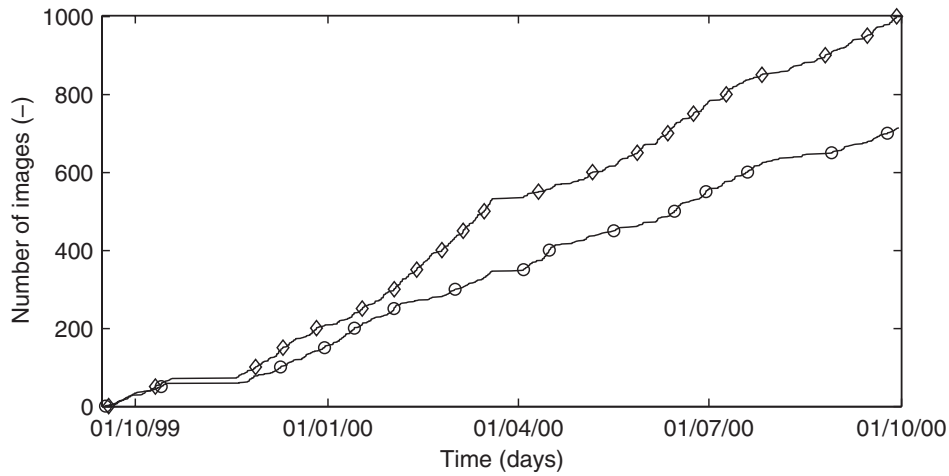


Figure 3.20: *Evolution of the cumulative number of video images that meet the BIM acceptance criteria on D_o quality, for arrays $y = -130$ m (o) and $y = -1500$ m (\diamond). Horizontal sections denote periods of missing data.*

the sum of all time gaps $t_1 - t_0$ between successive good-quality images after potentially being reduced to a maximum T_{hist} . The cumulative bathymetry update time amounts 271 and 242 days for the arrays $y = -1500$ and $y = -130$ m, respectively, indicating an inherent decrease in the model response time for the outer arrays. This effect contributes importantly to the accretion of sand in the shallow surf zone, found for the outer array.

3.5 Discussion on SBM behaviour

In the preceding sections, the behaviour and performance of the two sub-models BIM and BAM has been investigated in stand-alone mode, and together by means of a 12 month validation of SBM against field data collected at Egmond. In this section, the description of SBM is finalized with a discussion on some general characteristics of SBM behaviour and suggestions for further model development.

3.5.1 General characteristics of present SBM behaviour

SBM is based on a two-layer approach, consisting of a sea bed with elevation z_b and a buffer layer with sediment availability C_s . The exchange of sediment between the sea bed and the buffer layer is driven by differences between D_o and D_c . Erosion of the sea bed causes a local increase in C_s in the buffer layer, while the sediment needed for accretion is extracted from the buffer layer, inducing a local decrease in C_s . Cross-shore gradients of C_s drive a redistribution of sediment in the buffer layer, from areas of large C_s (sea bed erosion) to areas of low C_s (sea bed accretion). This does *not* imply that SBM can only be applied for the mapping of bathymetrical changes, driven by cross-shore transport. The model accounts for coastal changes induced by alongshore transport, by enabling a non-zero net exchange of sediment between the sea bed and

the buffer layer. In other words, the sediment involved with a net accretion (erosion) of the sea bed is extracted from (added to) the buffer layer, thus inducing a decrease (increase) in the mean sediment availability in the buffer layer.

The validation of SBM against Egmond field data has shown that, depending on the array of interest, a number of 700 to 1000 video-based dissipation profiles D_o meet the BIM acceptance criteria over a 12 month period. This corresponds to 60 to 80 useful D_o profiles per month, which provides sufficient temporal resolution to resolve changes of coastal bathymetry in the surf zone. The data set of 700 useful images for the central array $y = -130$ m yields a mean bathymetry update period of 8.1 hours per image, with a standard deviation of 9.0 hours. With the time gap between successive, accepted D_o profiles being relatively small as compared to the time scale of morphological changes in the surf zone, SBM takes benefit from additional information on a virtually unchanged bathymetry, provided by consecutive video images. A single image provides information on D_o in the regions of wave breaking, which cover only limited parts of the beach profile. The regions of coverage vary with the hydrodynamic conditions, in a sense that wave breaking occurs further off-shore with decreasing tidal levels and increasing wave heights (Kingston et al., 2000; Van Enkevort & Ruessink, 2001). Thus, by including multiple images on a virtually unchanged bathymetry, the information coverage along the beach profile improves, which positively affects SBM performance.

SBM performance on the basis of a time series of video images is strongly governed by the time scale of profile adjustment as specified through the model parameters w_E , w_A , q and, to a less extend, T_{hist} . Besides, the model response time has been shown to depend on the number of dissipation profiles D_o that meet the BIM acceptance criteria. Setting an appropriate time scale is an important step in the process of setting up a model that resolves the morphological changes along the beach profile over the period of interest, without over-fitting on inaccuracies of D_o . So far, all model parameters were set manually, using a heuristic search to arrive at a set of parameter values which yield reasonable performance along two different cross-shore arrays. The development of an objective methodology to set the model response time is a key issue for furthering the applicability and performance of SBM.

3.5.2 Furthering SBM performance and applicability

In Subsection 3.4.4, it was concluded that profile deviations after one year result from the combined effect of (i) the occasional inclusion of poor quality D_o , (ii) lack of erosional gradients $D_c - D_o$ to compensate for erroneous accretions at deeper water and (iii) the accumulation of small errors over time, induced by inaccurate D_o . These three mechanisms provide a useful framework for the identification of measures to improve SBM accuracy. Four suggestions are presented here:

- As regard to Mechanism (i): Exclude the limited number of poor quality video images that are responsible for profile deviations in regions of non-frequent wave breaking. Ideally, this can be achieved relatively easily by tightening the operational BIM criteria for the acceptance of D_o profiles. However, it may also be necessary to introduce additional criteria, for instance on the location and height

of the D_o peaks in relation to the incoming wave energy. The latter criterion is inspired by preliminary investigations on error-inducing images. For reasons unexplored yet, some early morning time exposure images happen to show a bright, wave dissipation-*like* band of high pixel intensities at deep water under very mild wave conditions, which could be held responsible for unrealistic accretion at deeper water. Further investigation on the intensity characteristics of error-inducing images is necessary to arrive at a robust criterion for their rejection.

- As regard to Mechanism (ii): Include additional information on the anticipated changes of bathymetry in regions of non-frequent wave breaking. These regions particularly concern the deep water sections of the beach profile and the trough regions. They are characterized by small D_c and D_o , which drive a nearly zero, inaccurate sediment exchange between the sea bed and the buffer layer. A regular sediment transport model may provide additional information on the anticipated erosion or accretion in these regions. Alternately, existing knowledge on long-term beach profile evolution may be used to fit the trough bathymetry with the bar bathymetry derived from video.
- As regard to Mechanism (iii): Introduce a threshold on D_o and/or D_c , or $D_c - D_o$, demanding that SBM may only carry out bathymetrical changes in regions that exceed the empirical threshold. This approach assumes that most inaccurate video intensity data are found from regions of small D_o , which are then responsible for the accumulation of small errors over time.
- As regard to Mechanisms (i) and (iii): Develop an objective methodology for the automatic determination of an appropriate model response time. Ideally, the model response time (or bathymetrical changes per single image) reflects the accuracy of the video data and the potential for coastal changes, governed by the transport capacity of the external forcing conditions (waves and tides). The model response time should increase with increasing data accuracy and transport capacity, and should also be corrected for the inherent dependency on the number of video images that meet the BIM acceptance criteria. This approach can be implemented through automated determination of the settings of w_E , w_A , q and T_{hist} during the course of an SBM run.

To further SBM applicability, the key issue is to set-up the model in 2DH mode, so that it can be used to map subtidal bathymetry in coastal areas, operating directly on (merged) plan-view images (e.g., Figure 3.1). At the moment, SBM is only applicable along 1D cross-shore arrays, which have to be located within the field of view of a single video camera. Extending SBM for application at 2DH grids involves a two-step approach. First, the input wave dissipation information D_o needs to be provided in 2DH mode. As a 2DH area of interest is generally covered by the views of multiple cameras, this implies that pixel intensities sampled from different cameras need to be levelled to arrive at smooth transitions between the cameras spanning the area of interest. The latter operation may be less trivial, owing to the considerable variability of image intensity characteristics for variable camera orientations with respect to the position of

the sun. Second, the SBM model formulations need to be converted into 2DH mode. As the 1D version of SBM accounts for bathymetrical changes driven by cross-shore and alongshore transport gradient, this can readily be achieved by running the present model along multiple arrays and interpolating the output to a 2DH grid. However, for computational ease, it may be beneficial to fully convert the model formulations into 2DH mode. Although this is a straightforward step for the wave model that calculates D_c , this modification demands further consideration for the intensity interpretation code (BIM) and the assimilation code (BAM).

3.6 Conclusions

The work presented in this chapter aimed to address the main objectives 1 and 2 of this thesis (Section 1.4) for the subtidal part of the beach, through development and validation of a new model to quantify subtidal beach bathymetry from ten-minute time-averaged video observations of wave breaking and the tide and wave conditions offshore. To that end, three sub-objectives were formulated as a guideline for model development (Subsection 3.1.3). The three sub-objectives are successively evaluated here.

To develop a methodology to quantitatively interpret good-quality video observations of wave breaking

- To quantitatively interpret video observations of wave breaking, a Breaker Intensity Model (BIM) was developed which samples intensity data from time-averaged video images, verifies data quality, removes the effect of persistent foam by isolating the roller-related contribution to time-averaged image intensity and normalizes the raw video information to allow for a quantitative comparison to normalized model-computed measures of wave dissipation.
- The substitution of video-derived cross-shore intensity profiles with a Gaussian approximation (as part of the pre-processing procedure) provides a sound base to remove noise from the raw video data and to exclude poor-quality data from further analysis. For Egmond, a number 60 to 80 video-based dissipation profiles per month typically meets the BIM acceptance criteria.
- Out of all model-predicted measures of wave dissipation considered here, time-averaged video observations of wave breaking relate best to the dissipation of roller energy D_r , which is proportional to the ratio of the roller energy E_r and the phase speed c .
- Averaged over the entire validation data set, BIM shows reasonable performance in terms of the mean location and area per dissipation peak, albeit that the video-observed variability in these parameters considerably overestimates the variability predicted from a common wave decay model.

To develop a methodology to quantify the temporal evolution of subtidal bathymetry

- To quantify the temporal evolution of subtidal bathymetry, a Bathymetry Assessment Model (BAM) was developed which continuously updates beach bathymetry through assimilation of video-derived (D_o) and model-predicted (D_c) measures of wave dissipation.
- For synthetic data, the BAM assimilation procedure benefits from increasing wave heights, increasing tidal ranges and decreasing trough depths, while being hardly sensitive to variable surf zone width. The BAM concept is applicable over a wide range of morphological configurations.
- The time scale of profile adjustment is governed by the morphological parameters (i.e. the accretion parameter w_A , the erosion parameter w_E , the depth power q and, to a less extent, the maximum update period T_{hist}), as well as the number of video images that meet the BIM acceptance criteria. The model response time in dissipative areas (like the bar regions) is small as compared the neighbouring trough regions.

To assess the accuracy of the Subtidal Beach Mapper (SBM)

- SBM application along two cross-shore Egmond arrays spacing approximately 1400 m alongshore has demonstrated the model's capability to reproduce the dominant morphological changes during the first year after placing a shoreface nourishment, including the shoreward migration of the outer bar and the net accretion of sand in the nearshore part of the surf zone.
- The *rms* error of the vertical deviations along the entire beach profile typically amounts 40 cm for both arrays. Marginal deviations in the order of 10 to 20 cm are found at the seaward face of the bars, which increase up to 20 to 40 cm near the bar crest. Maximum deviations up to 80 cm are found in the trough region, owing to lack of wave dissipation information. The accretion of sediment in the shallow surf zone is underestimated, which contributes importantly to the increase in relative errors with decreasing water depth.
- Deviations between the computed and measured beach profile after one year were found to result from the combined effect of (i) the occasional inclusion of poor D_o , (ii) lack of erosional gradients $D_c - D_o$ to compensate for erroneous accretion at deeper water and (iii) the accumulation of small errors over time, induced by inaccurate D_o .
- The analysis of SBM sensitivity to variable parameter settings has shown that model performance is strongly governed by the user-specified time scale of profile adjustment. The development of an objective methodology to set the model response time is a key issue for furthering the applicability and performance of SBM.

Considering the overall *rms* error of 40 cm, we conclude that SBM shows promising performance at Egmond. This conclusion finds support in the observation that alternative alternative model concepts, which quantify local water depth from the linear dispersion equation (Eq. 3.1) and video-based estimates of the incident wave frequency σ and wave number k , usually meet difficulties in shallow water (owing to the non-linearity of the wave field). Bathymetrical information obtained from SBM (like bar position and bar crest elevation) can be used for the validation of coastal profile models or in direct support of coastal zone management. The opportunities in this respect are discussed in more detail in Chapter 4.

Chapter 4

Video monitoring in support of Coastal Zone Management

4.1 Introduction

4.1.1 Motivation and approach

This chapter addresses the third main objective of this thesis (Section 1.4) by investigating the utility of video monitoring techniques for Coastal Zone Management (CZM) and science. The analysis particularly focusses on models to quantify intertidal (IBM, Chapter 2) and subtidal (SBM, Chapter 3) bathymetry from video. The utility of video-based monitoring techniques is not only determined by the availability of generically applicable, accurate and robust video interpretation methods, but also by their capability to address problems of end-user interest. In other words, useful video-based monitoring techniques provide information of direct end-user's relevance. An evaluation of the utility of ARGUS video imaging should therefore be intimately related to the objectives of the end-users of video-derived monitoring data, in this case coastal managers and/or coastal scientists.

During the last two decades of the 20th century, the use of video monitoring at distinctive field sites worldwide (Subsection 1.3.1) was primarily science-driven (Holman et al., 1993). The aim was to improve our understanding of nearshore morphodynamic processes. The unique character of the ARGUS technique in terms of the wide coverage of spatiotemporal scales made it a highly appreciated instrument for research purposes. The utility of ARGUS video imaging for coastal scientists can be assessed directly from the output of conference papers and reviewed journal publications.

The last few years reveal a tendency towards the use of ARGUS video imaging in direct support of coastal management (Van Koningsveld et al., 2003). The degree of success is determined by the capability of video interpretation models to provide information of direct management interest. This capability can be assessed by identifying the role of quantitative coastal state information within policy development cycles and demonstrating the capability of IBM and SBM to quantify this information from video. So, to evaluate the utility of ARGUS video imaging for CZM, it is necessary to adopt an established framework for coastal policy development, which explicitly treats the

role of quantitative state information, i.e. IBM- and SBM-derived indicators of coastal evolution.

Although the utility of ARGUS video imaging for coastal science is briefly discussed in Section 4.5, this chapter mainly evaluates the utility of video monitoring techniques for coastal management, with a particular focus on the monitoring of a combined beach and shoreface nourishment at Egmond (the Netherlands).

4.1.2 Objectives and outline of this chapter

This chapter presents an approach to evaluate the utility of ARGUS video monitoring, especially methods to quantify inter- and subtidal bathymetry, for coastal management and science. Thus, further detailing Objective 3 of this thesis (Section 1.4) with a focus on the utility for CZM, the sub-objectives of this chapter are:

- to adopt an established framework that explicitly treats the information need and decision procedures in the field of CZM;
- to use IBM and SBM to quantify time series of video-based indicators of coastal evolution, particularly at Egmond;
- to evaluate the utility of video-based monitoring techniques for CZM in the context of the framework identified above.

Considering the central role of the case example Egmond, this chapter starts with a brief description of the Egmond coastal system (Subsection 4.2.1) and the recent CZM history of the site (Subsection 4.2.2). Subsequently, Subsection 4.2.3 discusses a ‘frame of reference’ for policy development (Van Koningsveld & Mulder, 2002; Van Koningsveld, 2003), which explicitly treats the information need and decision procedures in the field of CZM. The utility of video monitoring for CZM is evaluated against the background of this ‘frame of reference’ (Section 4.5), using the results obtained from the application of IBM (Section 4.3) and SBM (Section 4.4) at Egmond. This chapter concludes with a summary of our findings in the context of the three sub-objectives identified above.

4.2 The Egmond site: Coastal system and management issues

4.2.1 Nearshore processes at Egmond

Egmond is situated along the central part of the Dutch coast also known as the Holland coast, stretching from the Hoek van Holland harbour moles in the south to the Texel inlet channel near Den Helder in the north (Figure 4.1). This coastal stretch has a length of about 120 km and mainly consists of dune areas, sandy beaches and multiple-barred nearshore zones. Major man-made structures in the area are the harbour moles at Hoek van Holland, Scheveningen and IJmuiden and the Hondsbossche Seawall near

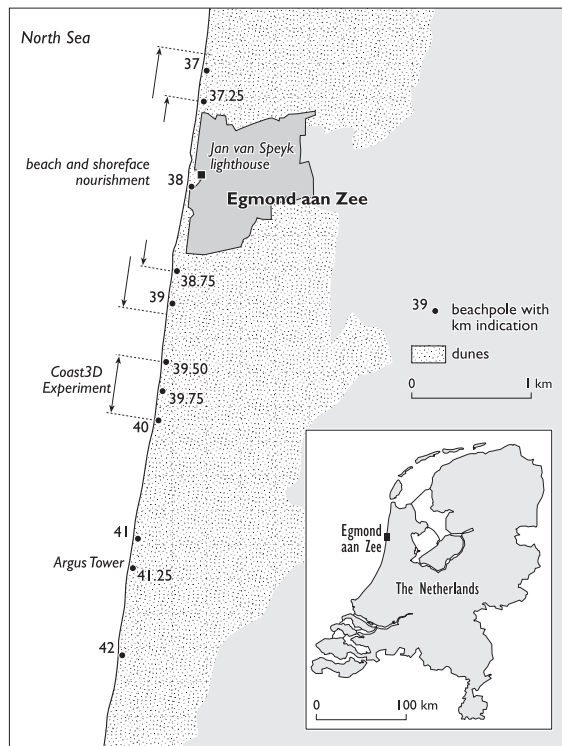


Figure 4.1: *Situation of Egmond along the Holland coast.*

Petten. Egmond is located in the northern half of the central Dutch coast, in between the IJmuiden harbour moles and the Hondsbossche Seawall.

The surf zone at Egmond is characterized by two shore-parallel subtidal nearshore sandbars. The crest of the outer bar lies below mean water depths of -3.5 to -4.0 m NAP and is at times fairly straight, but it often shows irregularity and some rhythmicity with typical length scales of several kilometers (Figure 4.2). The crest of the inner bar has an irregular alongshore planview with most of the time a crescentic appearance, and lies below a mean bed level of -1.5 to -2.5 m NAP (Van Rijn et al., 2002). The bars have a multi-annual lifetime during which they evolve in a cyclic manner. Bar birth near the shoreline is followed by offshore migration across the surf zone and decay offshore, the latter being associated with the formation of a new bar near the shoreline (Wijnberg & Terwindt, 1995). Near Egmond, the cycle return period of the bar system is about 15 years (Wijnberg, 1995).

On a smaller scale, Egmond often shows the presence of a swash bar at the intertidal beach. Kroon (1994) identifies three phases in the behaviour of this swash bar: (1) the initial generation and growth near the low- to mid-tide water line, (2) its stabilization or shoreward migration and (3) its disappearance, either by merging with the upper dry beach during mild wave conditions, or by flattening during rough wave conditions. Phases (1) and (2) are associated with low to moderate wave conditions. The cross-shore migration of the swash bar is related to variations in the tidal amplitude over a spring-neap tide cycle, which decouples the morphological behaviour of the swash bar and the subtidal bar system.

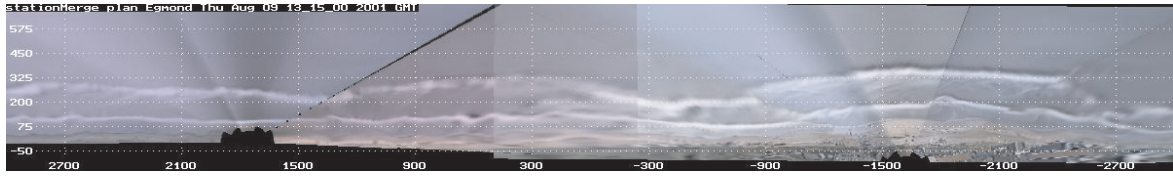


Figure 4.2: *Combined plan view image d.d. August 9, 2001 GMT 13 hr, covering 6 km of Egmond shoreline. The combined image is obtained from rectification and successive merging of ten time exposure images, sampled from the Egmond video stations Coast3D (located about 3 km south of town near km 41.25, Figure 4.1) and Jan van Speyk (located in the center of town near km. 38.00, Figure 4.1).*

The investigation of historic maps shows a shoreline retreat of about 300 m near Egmond over the period 1686 to present (Ligtendag, 1990). Over the period 1964 to 1992, however, the coastline (-1 m depth contour) near Egmond is approximately stable (Van Rijn, 1997). The mean width of the dry beach is approximately constant, albeit that large fluctuations are observed between different years (Boers, 1999). The beach near Egmond is erosive at the -8 m depth contour, showing a retreat of about 0.5 to 1 m/year over the period 1964 to 1992.

Coastal changes at Egmond are driven by a wave climate with a yearly mean wave height H_{m0} of 1.2 m and a mean period T_{m0} of about 5 sec, showing considerable seasonal fluctuations. Waves predominantly approach the shore from south-westerly and north-north-westerly directions. The asymmetrical, semi-diurnal tidal curve induces northward directed currents during the four-hour flood period and southward directed currents during the 8 hour ebb period. The mean tidal range at Egmond is 1.65 m, with a maximum of 2.0 m at spring tide and a minimum of 1.4 m at neap tide.

4.2.2 Coastal Zone Management at Egmond

Coastal policy in the Netherlands has primarily been aimed at the protection against flooding of the lowland areas situated landward of the coastline. Prior to 1980, this has been achieved by building groynes, dikes and seawalls. During the 80's, the scope of coastal policy gradually widened towards other coastal functions like ecological values, supply of drinking water, recreation and residential and industrial functions. This initiated a historic decision in 1990, to stop any further coastal retreat by maintaining the coastline at the position of that date, adopting a new policy called 'Dynamic Preservation' (e.g., De Ruig, 1998). The objective of this policy is to provide safety against flooding in combination with sustainable preservation of the functions and values of dunes and beaches. As it aims to take advantage of natural dynamic processes, the principal intervention measure is sand nourishment.

Implementation of the Dynamic Preservation policy demands an objective assessment of the state of the coastal system. For this purpose, the concept of the Momentary Coastline (MCL) has been developed (e.g., Hamm et al., 2002). The MCL represents the momentary horizontal position of the coastline, determined from the sand volume in a cross-shore profile between the dunefoot at an elevation H above mean low water

(MLW) and the depth contour at an equal depth H below MLW. The MCL is computed every year on the basis of annual surveys of bathymetry (named JARKUS surveys) along cross-shore profiles with 250 m alongshore spacing. The anticipated position of the MCL for the next year is predicted from the ten-year trend in the evolution of the MCL and compared to the location of the so-called Basal Coastline (BCL), which reflects the 1990 coastline and acts as the reference state.¹ If the anticipated MCL is located shoreward of the BCL, an intervention by means of sand nourishment is necessary.

One decade of Dynamic Preservation has shown that the coastal area in front of the Egmond boulevard was nourished with an average sediment volume of almost $150 \text{ m}^3/\text{m}/\text{year}$ over the period 1990-1997, while much smaller volumes of 0 and $25 \text{ m}^3/\text{m}/\text{year}$ were sufficient for the neighbouring coastal stretches south and north of town, respectively. So, in front of the Egmond boulevard, the nourished sand was disappearing much faster than in the neighbouring regions, potentially due to the seaward shift of the location of the BCL.

In an attempt to mitigate sand losses, the authorities decided to intervene by means of a combined beach and shoreface nourishment, which was placed in April and August 1999, respectively. The $200 \text{ m}^3/\text{m}$ beach nourishment had a length of 1500 m alongshore; the $400 \text{ m}^3/\text{m}$ shoreface nourishment, placed at 5 m water depth at the seaward face of the outer bar, covered a length of 2200 m. To monitor the effect of the combined nourishment on the evolution of nearshore bathymetry, an ARGUS video station was deployed on top of the Jan van Speyk lighthouse in May 1999, about 3 km north of the Argus tower which hosts the Coast3D video station, installed in December 1997 (Figure 4.1). The application of video monitoring techniques within a CZM context is evaluated in this chapter.

4.2.3 A framework to evaluate the utility of video monitoring in support of Coastal Management

Video monitoring techniques provide quantitative information on the state of a coastal system. Successful use of this information for scientific purposes does not necessarily guarantee its utility in the field of CZM. The latter demands insight in the information need of coastal managers. The role of quantitative state information in the context of policy development cycles is revealed by Van Koningsveld & Mulder (2002).

On the basis of the analysis of Dutch coastal policy over the last two decades, Van Koningsveld & Mulder (2002) found that successful policy development demands the use of a systematic ‘frame of reference’ (Figure 4.3). This involves the explicit definition of strategic and operational objectives, for use with a 4-step decision recipe consisting of (1) a quantitative state concept, (2) a bench marking procedure, (3) a procedure for CZM interventions and (4) an evaluation procedure. For the Dynamic Preservation policy (Sub-section 4.2.2), the strategic objective was ‘... *to guarantee a sustainable safety level and sustainable preservation of values and functions in the dune area ...*’. In terms of safety against flooding, the associated operational objective was

¹This is true, except for a limited number of regions (including the coastal towns of Egmond, Bergen and Callantsoog) where the BCL is shifted seaward to guarantee safety against flooding (Rakhorst, 1994)

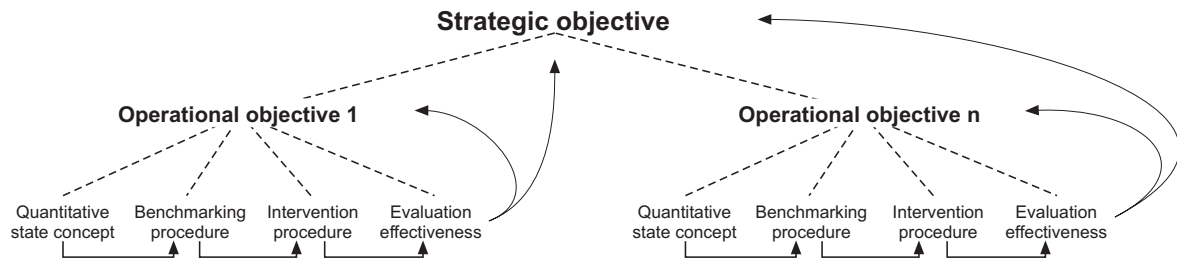


Figure 4.3: *Basic frame of reference as a tool for policy development (after: Van Koningsveld & Mulder, 2002). This approach explicitly reveals the role of quantitative state information within policy development cycles.*

specified as ‘... the coastline will be maintained at its position in the year 1990’. To quantitatively assess the state of the coastal system (Step 1), the MCL indicator was developed and compared to the corresponding BCL (Step 2). If necessary, nourishment schemes are carried out (Step 3) which are evaluated every five years (Step 4). A recent evaluation by Roelse (2002) demonstrates that the Dynamic Preservation policy has successfully met its operational objective: By nourishing a mean volume of 6 Mm^3 sand per year, the Dutch coastline is indeed preserved at its 1990 position (and in fact even gained 560 hectares of beach front over the period 1990-1998, an over 100% increase as compared to the ten-year period before).

Video monitoring techniques can thus contribute to policy development cycles by means of the quantitative assessment of Coastal State Indicators (CSIs) for use in Step 1 of the basic frame of reference. Van Koningsveld et al. (2003) define CSIs as a reduced set of parameters that can simply, adequately and quantitatively describe the dynamic state and evolutionary trends of a coastal system and include relevant information to provide a basis for decision making in the field of CZM. At the moment, the Dutch intervention strategy for ‘regular’ maintenance is based on a single CSI (the MCL indicator), accounting for the only operational objective (maintenance of coastline position) of the Dynamic Preservation policy. It is questionable whether this narrow focus is sufficient. Being associated with time scales of 1 to 10 years and space scales in the order of 1 to 10 kilometers only, the BCL procedure ignores coastal fluctuations at smaller and larger spatiotemporal scales. Ignoring these scales, the BCL procedure may therefore not properly account for integral coastal safety and other functions like beach recreation, nature conservation and swimmer safety.

The former was already noted by Mulder (2000), who suggested that the Dynamic Preservation policy yields a non-sustainable system at the time scale of decades. His observation has initiated the implementation of a no-regret policy demanding the ‘preservation of the total sand volume in the coastal system’ - even though it is acknowledged that key aspects of this policy (like the definition of the reference sections and the efficiency of arbitrary dumping locations) need further refinement. Despite these useful developments for the larger spatiotemporal scales, no operational objectives have yet been incorporated for smaller time and space scales.

So to evaluate the utility of video monitoring techniques for Coastal Management, it is necessary to demonstrate our capabilities to quantify either *established* CSIs (particu-

larly the MCL indicator) from video, or *additional* CSIs that contribute to established operational objectives by addressing alternative spatiotemporal scales, or *new* CSIs which cater for entirely new operational objectives. A sound embedding of video-derived CSIs in a basic frame of reference for policy development is a prerequisite for successful application of video monitoring techniques in support of coastal management. These aspects are further treated in Section 4.5, after a brief overview of IBM (Section 4.3) and SBM (Section 4.4) results at Egmond.

4.3 Video-based assessment of intertidal CSIs

4.3.1 Data set of intertidal bathymetries

To quantify morphological changes at the intertidal beach in front of the Egmond boulevard, IBM was applied to map intertidal beach bathymetry between the elevation contours of 0 and +1 m with respect to the Dutch Reference Level (NAP). Plan view bathymetrical maps were generated on a monthly basis during the first (Caljouw, 2000) and second (Nipius, 2002) year after placing the combined beach and shoreface nourishment (Figure 4.4). The Caljouw (2000) data set covered a coastal strip of 1400 m alongshore, centered around the video station on top of the Jan van Speyk lighthouse. Improved user functionality of the operational model and advanced preprocessing of the raw intensity data (Appendix B.1) enabled Nipius (2002) to cover a distance of 2000 m alongshore. Both Caljouw (2000) and Nipius (2002) used the site-specific shoreline elevation model according to Janssen (1997), instead of the more generic elevation model presented in this thesis. Vertical differences between both models are in the order of 10-20 cm, which yields an horizontal offset of about 4-8 m. This offset is small compared to the overall shoreline variability over the two-year period of interest. Thus, the application of the Janssen model has only a small effect on the accuracy of our observations of the video-derived evolution of intertidal beach bathymetry.

The initial intertidal morphology of June 1999, two months after the implementation of the beach nourishment, was characterized by a highly irregular shoreline, with an erosion hot-spot at about 500 m south of the video station and considerable accretion at 200 m north of the station (Figure 4.4). The width of the beach varied by more than 60 m within a distance of 700 m. After a calm summer period during which only minor foreshore changes were observed, a sequence of storm events in October and November 1999 caused significant erosion of the beach, in particular at the location of minimum beach width at about 400 m south of the video station. Besides, a flattening of the beach profile was observed from the divergence of the elevation contours. During the winter months, ongoing erosion was observed all along the area of interest. In March 2000, this had resulted in a coastal retreat of 30 m in the north, and more than 40 m in the south. At some locations, virtually no sub-aerial beach was left, despite the nourishment activities which were executed only 9 months previously. Between April and June 2000, a degree of recovery (about 20 m additional beach width) was observed; full restoration of the morphological configuration of June 1999 had however not been achieved.

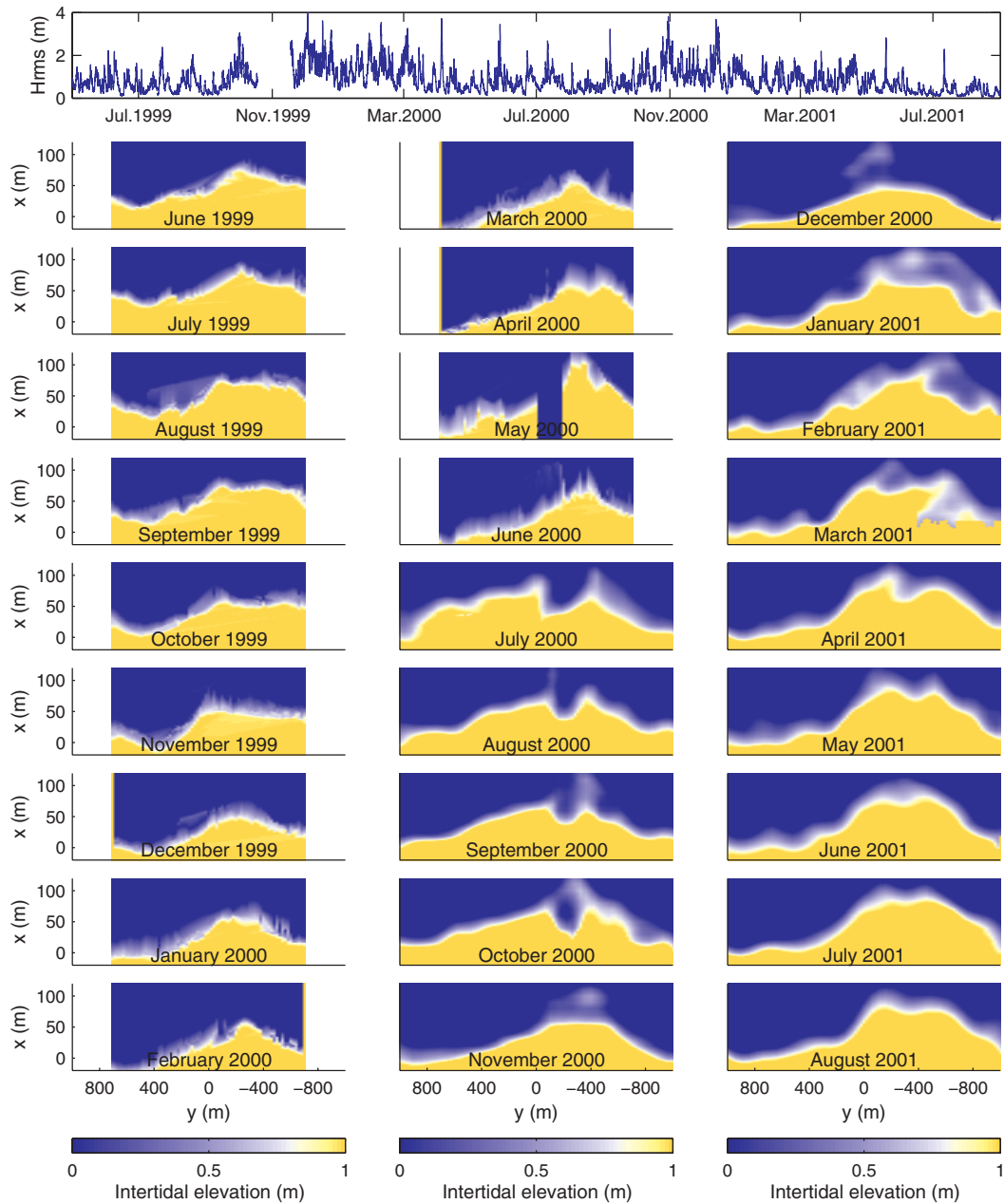


Figure 4.4: Video-observed evolution of intertidal bathymetry at Egmond over the period June 1999 - August 2001. Monthly, plan view maps of the intertidal beach bathymetry between the NAP +0 and NAP +1 m elevation contours. The dry beach is located at the lower side of each panel. The video station is located near the origin of the horizontal coordinate axis, which is positively directed south. Elevations at the sub-aqueous (sub-aerial) beach are manually set to zero (one). Until June 2000, intertidal bathymetries are obtained from linear interpolation of IBM-derived shorelines. Afterwards, an advanced quadratic Loess interpolator (Plant et al., 2002) is used. The upper panel shows H_{rms} for the period of interest.

Persistent erosion forced the coastal authorities to place a second beach nourishment along the strip between 0 and 800 m south of the video station by the end of June 2000. Shoreline retreat of 10-20 m per month continued along the nourished section over the period August-September 2000, as the nourished sand transferred from the intertidal beach to restore an erosion hot-spot around 700 m south of the video station. Rough wave conditions in November and December 2000 resulted in further erosion, and a shoreward shift of the shoreline by 15-20 m, relative to the initial beach conditions measured in June 1999. Early in 2001, a ‘slug’ of sand entered the intertidal zone directly north of the video station, causing a net local accretion in the order of 50 m, accompanied by the flattening of the beach profile and the development of strong morphological irregularities in the intertidal zone. The redistribution of sediments alongshore, combined with an overall accretionary trend, resulted in an increasingly smoothed shoreline in April 2001, with this trend continuing through to the end of the summer in August 2001. Interestingly, the plan-shape morphological configuration of August 2001, characterized by a seaward extension of the foreshore directly north of the video station and a contrasting erosion hot-spot approximately 600 m to the south, is remarkably similar to the initial situation in June 1999, despite the nourishment effort in July 2000. The latter observation suggests that the morphological evolution of the intertidal beach is at least partly governed by larger-scale phenomena, for example the presence of a depression in the outer bar (Nipius, 2002), although the mechanism of shoreline instabilities induced by strongly-oblique waves (Murray et al., 2001) may also play a role.

In summary, two years of video-based monitoring of intertidal coastal changes at a nourished beach in Egmond have shown significant variability in its morphodynamic behaviour, which would have been hard to measure with traditional survey techniques. Averaged over the area of interest, a strong seasonal variability is observed. Besides, considerable spatial variability occurs through redistribution of sediments within the area of interest. These variabilities obscure the identification of chronic erosion, hence the design of appropriate interventions. Apart from this, they may also hamper coastal functions like recreation, with non-favorable economic consequences for local beach communities. Better insight in these variabilities at the smaller temporal and spatial scales is expected to contribute importantly to the design of effective mitigation measures in the field of coastal management. A limited set of carefully chosen CSIs should contribute at this point by providing a simple, objective quantification of the morphological variabilities within a complex coastal system and by enabling a sound embedding of quantitative state information within policy development cycles.

4.3.2 Video-observed evolution of intertidal CSIs Egmond

In search of a simple, objective quantification of intertidal morphodynamics at the nourished beach in Egmond, this sub-section introduces the CSIs beach width and intertidal beach volume and assesses their evolution for the two-year data set of monthly intertidal bathymetries described above.

The CSI ‘beach width’ is determined as the horizontal, cross-shore distance W between the position of the dunefoot and a representative elevation contour at the inter-

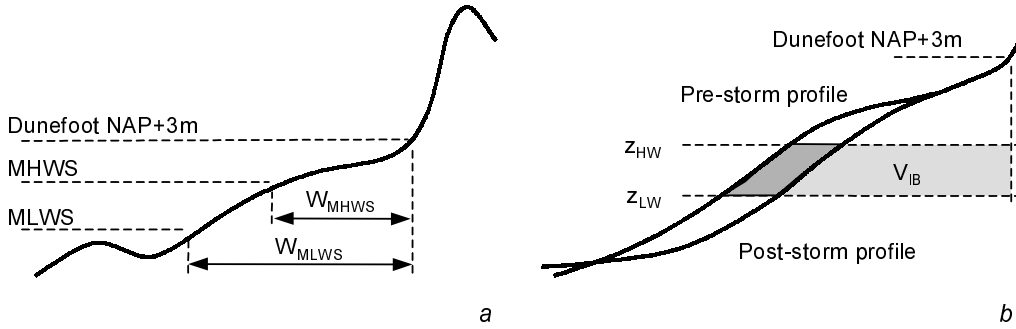


Figure 4.5: *Definition sketch of the CSI's beach width (a) and intertidal volume (b).*

tidal beach (Figure 4.5a). In the Netherlands, the position of the dunefoot is defined as the location of the NAP +3 m contour, which is surveyed every two years. The position of the elevation contours marking the water levels of Mean Low Water Spring (MLWS) and Mean High Water Spring (MHWS) are adopted to constrain W at the seaward side, which yields beach width indicators W_{MLWS} and W_{MHWS} for low-tide and high-tide, respectively. At the moment, W_{MLWS} and W_{MHWS} at Egmond are set at NAP -0.76 and NAP +0.90 m, respectively. These numbers are re-considered every ten years, to account for sea level rise and amplitude variations of the astronomical components that compose the tidal signal.

Similar to the MCL indicator, the CSI ‘intertidal beach volume’ is defined as a sand volume V_{IB} within a reference section of the cross-shore profile, bordered by the position of the dunefoot at the shoreward side and the location of the high and low tide elevation contours at the seaward side (Figure 4.5b). For IBM application at Egmond, representative values of NAP-0.4 m and NAP +1.0 m are adopted for the elevations z_{LW} and z_{HW} of the low and high tide beach contour, respectively. Variations ΔV_{IB} of V_{IB} between successive months directly reflect patterns of erosion and accretion.

The evolution of W_{MLWS} , W_{MHWS} and ΔV_{IB} at Egmond over the period June 1999 - August 2001 has been determined for nine neighbouring coastal sections with an alongshore length of 200 m each (Nipius, 2002). As IBM identifies a shoreline near the highest point of wave run-up, IBM-based bathymetries typically cover the area between the elevation contours of NAP-0.4 m and NAP +1.0 m. So, to quantify W_{MLWS} from the location of the NAP-0.76 m contour, IBM results are linearly extrapolated along cross-shore arrays. Furthermore, volumetric changes ΔV_{IB} are normalized with the vertical range $z_{HW} - z_{LW}$, to enable a comparison with earlier intertidal bathymetries by (Caljouw, 2000) which cover the area between the elevation contours of NAP +0.0 m and NAP +1.0 m. As a result, ΔV_{IB} reported here represents a volume change per m height and per m alongshore.

The temporal evolution of W_{MLWS} , W_{MHWS} and ΔV_{IB} for the example beach Sections 3 and 7 (Figure 4.6) characterizes the dominant morphological changes identified earlier, without however addressing any spatial variabilities. The beach width variability shows a strong seasonal component (particularly in Section 7), while significant ΔV_{IB} in Section 3 (July 2000) and 7 (January 2001) represent the additional beach nourishment and mid-winter intertidal accretion noted earlier. These time series do not reveal the

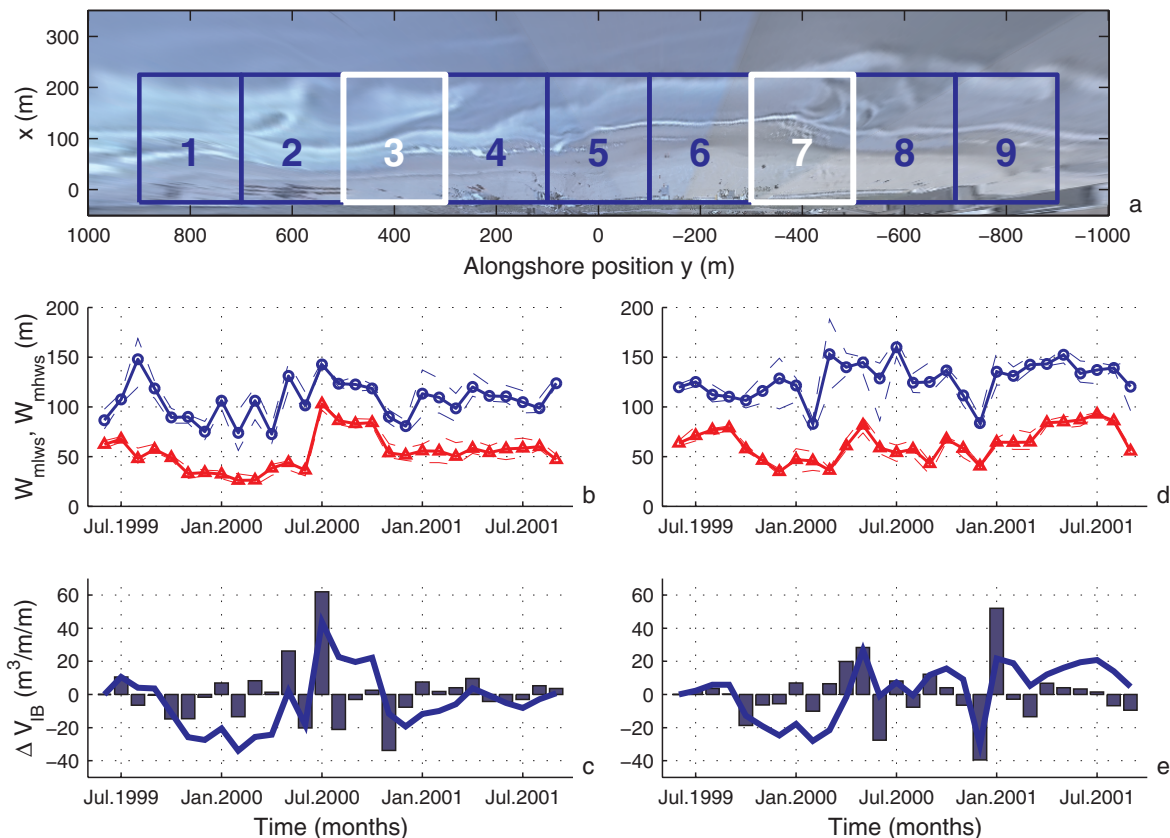


Figure 4.6: *Quantification of video-derived CSIs at Egmond. Evolution of beach width (b,d) and intertidal beach volume (c,e) within Sections 3 (b,c) and 7 (d,e) over the period June 1999 - August 2001. Beach width is quantified by means of the cross-shore distance between the dunefoot and the low tide (o) and high tide (Δ) elevation contour, respectively. The fine, dashed lines (b,d) reflect the uncertainty range, determined from the minimum and maximum beach width within each section.*

remarkable spatial coherence of the morphological changes. The latter is particularly observed from the persistent nature of the shoreline perturbation immediately north of the light house, whereas well-established theories on beach morphodynamics would anticipate a diffusive redistribution of sediments alongshore. The utility of video-derived intertidal CSIs in support of CZM will be evaluated in Section 4.5.

4.4 Video-based assessment of subtidal CSIs

4.4.1 Data set of subtidal beach profiles

To illustrate the practical use of SBM, two example application are treated here, namely (1) a beach evolution scenario and (2) a bar assessment scenario. The beach evolution scenario (1) matches the validation case (Subsection 3.4.2) and involves the use of SBM to deduce the morphological evolution of the surf zone in front of the Egmond boulevard

during the first year after implementation of the 1999 shoreface nourishment. The beach evolution scenario starts from a surveyed initial profile. The bar assessment scenario (2) concerns the use of SBM to measure a barred beach profile in absence of any other information on the surf zone bathymetry. To do so, SBM updates an arbitrary, non-barred initial profile on the basis of a limited number of video images, typically spanning a one-week period. Both applications are briefly discussed below.

The beach evolution scenario (1) involves the use of SBM to quantify coastal profile evolution at Egmond over the period September 15, 1999 - October 1, 2000, along two cross-shore arrays located immediately in front and 1500 m north of the Jan van Speyk video station. Rather than in the validation phase, when the focus was on the quantification of SBM accuracy at two discrete moments in time (Section 3.4), we now consider the morphological *evolution* of the two arrays $y = -130$ m and $y = -1500$ m throughout the entire 12 month period of interest, on the basis of 715 (1003) SBM-based beach profiles, respectively.

Both arrays show a gradual evolution of the subtidal bathymetry (Figure 4.7), except probably for the deep water part of the outer array $y = -1500$ m around the NAP-6 m depth contour, which marks the seaward end of the horizontal field of view of the camera of consideration. Along the central array, the shoreface nourishment shows a minor lowering and associated seaward migration over the period December 1999 - May 2000, followed by a recovery during the successive summer months. Deployment of the shoreface nourishment induces an over 100 m onshore migration of the former bar during the first six months. The intertidal bar simultaneously migrates offshore to form a well-developed three-bar system with the shoreface acting as the new outer bar. Morphological changes during the successive period April 2000 - October 2000 are characterized by a further increase in the crest elevation of the inner bar and the accretion of sand in the inner trough and inner surf zone regions, yielding a net increase in the beach volume along the central array. Though being located outside the nourished area, the bathymetrical evolution along the outer array $y = -1500$ m also shows a shoreward migration of the outer bar, which occurs over the entire period of interest. After an initial eight-month period of deepening, the outer trough is subject to net accretion of sand during the summer of 2000. Though less-pronounced as compared to the central array, the shallow part of the beach profile above the NAP -2 m contour is subject to net accretion of sand during the first eight months after deployment of the shoreface nourishment, followed by stabilization.

The bar assessment scenario (2) involves the use of SBM to measure a barred beach profile, by updating a non-barred initial bathymetry on the basis of a sub-sample of the Coast3D data set (Ruessink et al., 2000, also described in Subsection 3.2.4), covering the period October 16 - October 24, 1998. Time-averaged image intensity are sampled along cross-shore arrays with 50 m spacing alongshore and averaged across the Coast3D area of interest, located between 1250 and 1750 m north of the video station. The initial bathymetry is arbitrarily set to a combined straight profile, with two sections sloping 1:170 and 1:85 outside and within the surf zone, respectively. Except for the erosion and sedimentation parameters w_E (Eq. 3.19) and w_A (Eq. 3.20), SBM was run with the standard parameter settings established in Subsection 3.4.2. The parameters w_E and w_A were both set at $12.5 \cdot 10^{-7} \text{ ms}^2/\text{kg}$, to enable relatively large bathymetrical

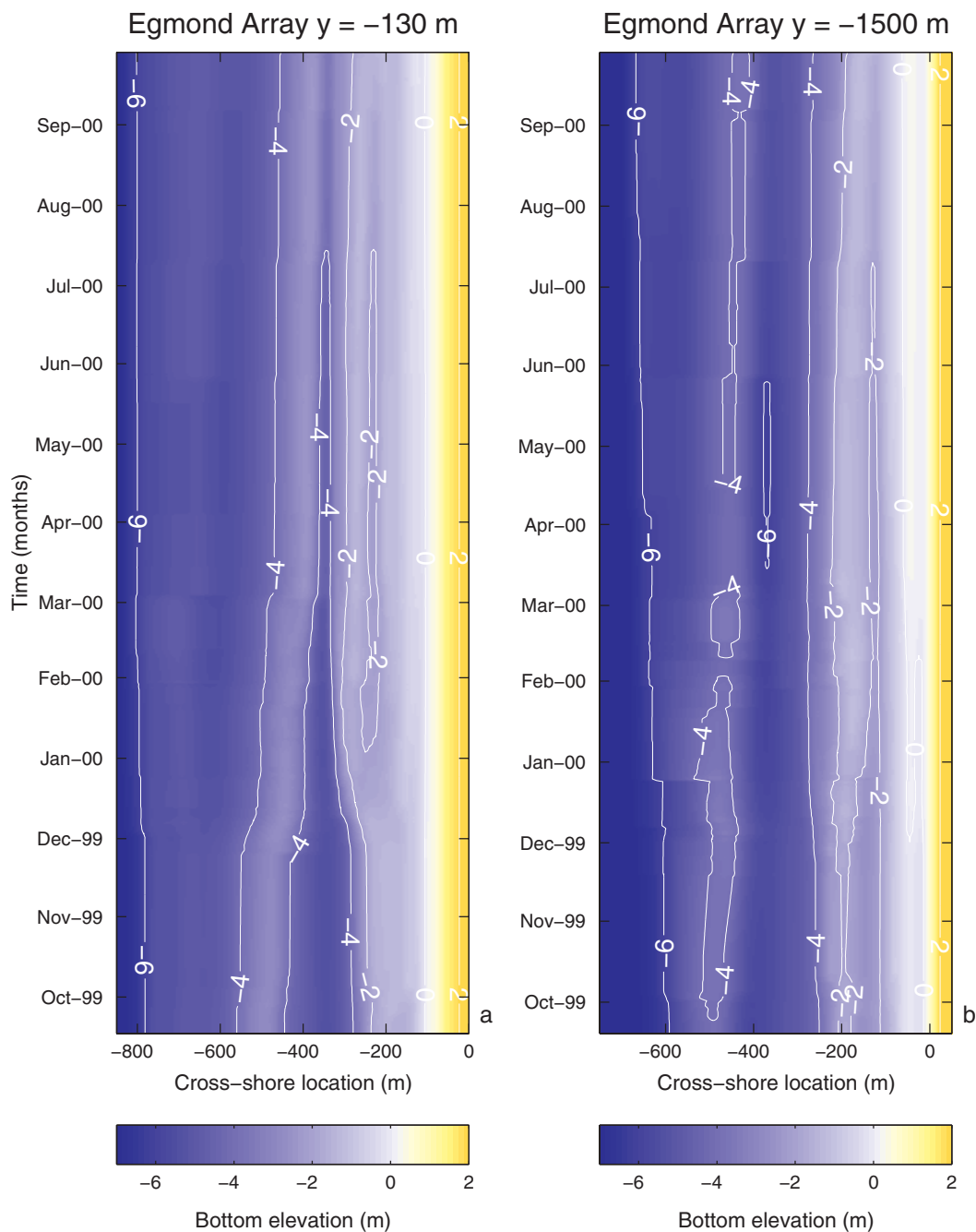


Figure 4.7: *Video-derived morphological evolution of subtidal beach bathymetry at Egmond. Timestack of SBM-based beach profiles along the central array $y = -130$ m and the outer array $y = -1500$ m over the period September 15, 1999 - October 1, 2000.*

changes over a short period of time by means of a decrease in the model response time τ (Eq. 3.28). Overall, 48 video-derived, alongshore-averaged dissipation profiles D_o met the BIM acceptance criteria. The resulting bathymetrical evolution over the eight-day period of interest, as well as the final beach profile at October 24 are shown in Figure 4.8 and compared to the surveyed beach profile at October 24, also averaged over a distance

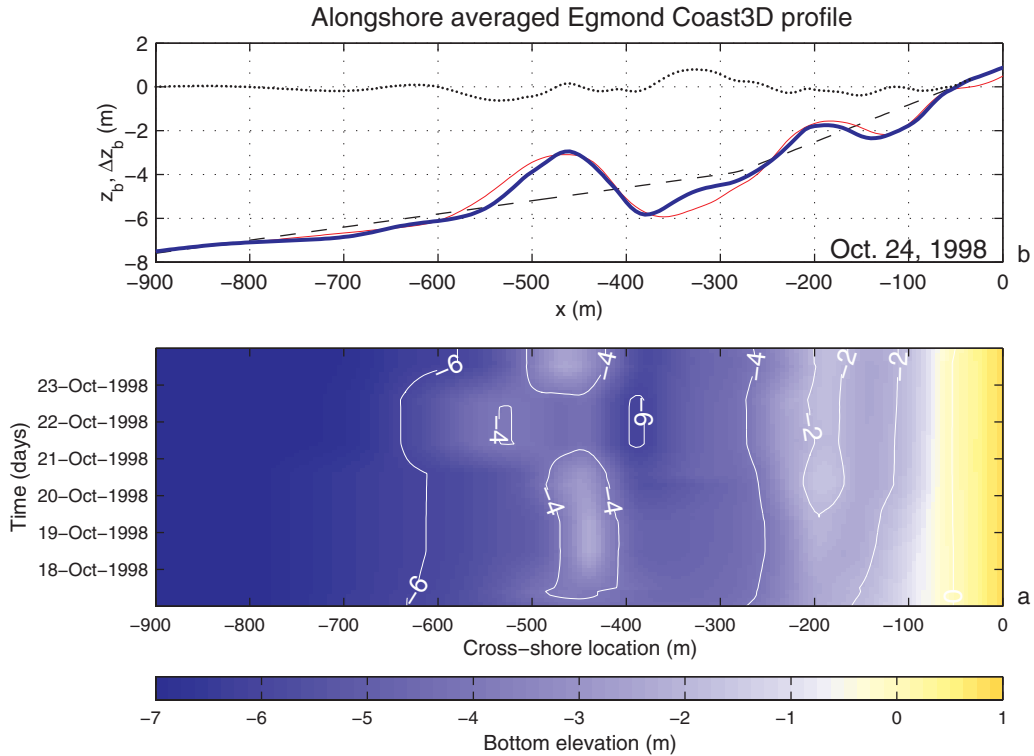


Figure 4.8: *Quantification of a barred beach profile from an arbitrary initial profile. Eight-day timestack (a) of SBM-based beach profiles and the resulting modelled (bold line) and surveyed (thin line) beach profile (b) at October 24, 1998. The dashed line reflects the arbitrarily chosen initial profile at October 16. Beach profiles are alongshore-averaged over the area of the Coast3D field experiments at Egmond.*

of 500 m alongshore. Video-based profile adjustment starts with the generation of an outer bar and the deepening of the outer and inner trough regions, two days later followed by the generation of the inner bar. The non-realistic, seaward migration of the outer bar at October 21 is induced by the combination of noisy, video-derived wave dissipation profiles D_0 and a small model response time τ , which is corrected in the days after on the basis of good-quality data. Despite an overestimate of the bottom elevation in the outer trough region, it is concluded that the final beach profile at October 24 shows very good agreement with the surveyed profile, particularly in terms of the elevation and volume of the breaker bars and the deepening of the inner trough region and the section seaward of the outer bar.

In summary, the application of SBM to quantify subtidal coastal changes after deployment of a shoreface nourishment and to map a barred beach profile from an arbitrary initial profile has demonstrated the potential for the use of video techniques for the monitoring of surf zone morphodynamics on a weekly to monthly basis. The interpretation of SBM results in terms of a limited set CSIs is a prerequisite, however, for successful use of the model in the context of policy development cycles, as addressed in the next subsection.

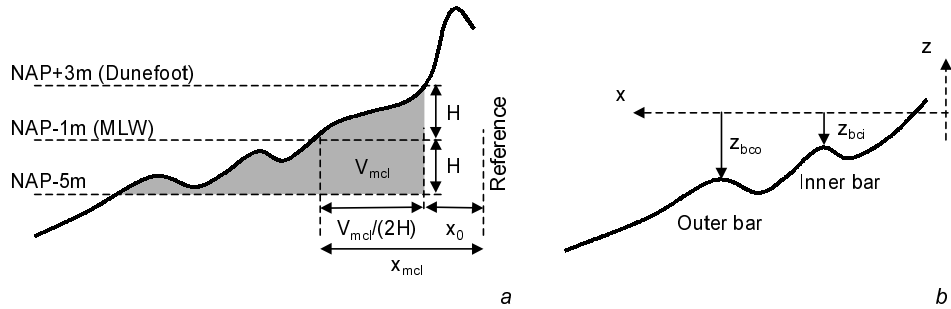


Figure 4.9: Definition sketch of (a) the Momentary Coastline position x_{mcl} at Egmond and (b) the crest elevation z_{bco} (z_{bci}) of the outer (inner) bar. The crest elevation is defined with respect to Dutch datum NAP, which is approximately 20 cm below mean sea level.

4.4.2 Video-observed evolution of subtidal CSIs Egmond

In search of a simple, objective characterization of the morphological changes in the surf zone, this sub-section adopts the well-established MCL indicator (Section 4.2.2) as a means to present the gain or loss of sand at the coastline. Besides, it introduces a new CSI named z_{bc} , which reflects the elevation of the bar crest. The evolution of both CSIs is quantified for the one-year data set of SBM-derived Egmond Jan van Speyk beach profiles described above.

The Momentary Coastline position x_{mcl} (e.g., Hamm et al., 2002) is an aggregated measure for the location of the MLW coastline contour. It is quantified from the sand volume in the beach profile between the dunefoot at an elevation H above MLW and the depth contour at an equal depth H below MLW (Figure 4.9a). With the dunefoot being defined as the NAP +3 m contour and MLW being approximately NAP -1 m at Egmond, x_{mcl} is determined from the sand volume between the NAP +3 m and NAP -5 m surface elevation contours. By nature, the SBM-derived data set of beach profiles does not reflect morphological changes of the sub-aerial beach.

The second CSI z_{bc} reflects the elevation of the crest of a sand bar and can be quantified for both the outer (z_{bco}) as well as the inner (z_{bci}) bar. It is defined as the maximum local profile elevation between two neighbouring trough sections. The parameter z_{bc} may be relevant for coastal safety, since the water depth over a bar strongly governs the direct wave attack at the shoreline, but also for military applications, for instance when planning a landing operation on hostile territory.

The evolution of x_{mcl} , z_{bci} and z_{bco} for the central and outer Egmond arrays over the period September 15, 1999 - October 1, 2000 (Figure 4.10) could directly be determined from the data set of SBM derived beach profiles. Owing to a welded inner surf zone with a poorly developed bar-trough system, no z_{bci} was found for the central array $y = -130$ m before February 2000 and near the end of September 2000. It should be noted that variations of x_{mcl} are entirely driven by bathymetrical changes of the sub-aqueous beach.

The seaward shift of x_{mcl} , which amounts to 15 (35) m for the outer (central) array, confirms the net accretion of sediment reported in Section 4.4.1. Both arrays show a

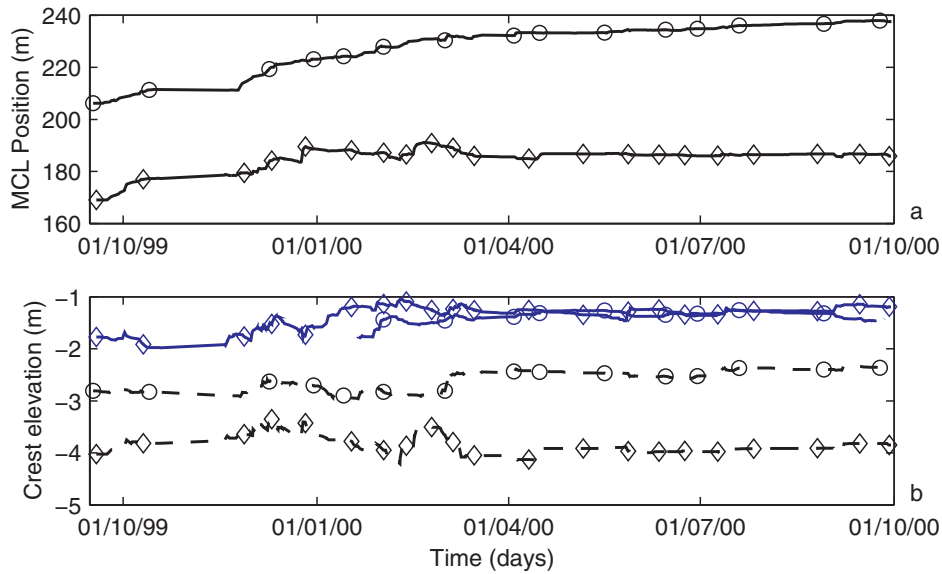


Figure 4.10: Video-derived evolution of the momentary coastline position x_{mcl} (a) and the bar crest elevation z_{bc} (b) at Egmond, over the period September 15, 1999 - October 1, 2000. The evolution is quantified from SBM results along the central array $y = -130$ m (\circ) and the outer array $y = -1500$ m (\diamond) of the Jan van Speyk station. z_{bc} has been determined for both the outer bar (dashed line) and the inner bar (solid line). Markers indicate every 50th data point.

rapid accretion during the first six months after completion of the combined beach-shoreface nourishment. Along the central array $y = -130$ m, this phase is followed by a period of stabilization during spring and, again, a tendency towards accretion during the successive summer months. Along the outer (northern) array $y = -130$ m, evolution of x_{mcl} after the initial phase of accretion is characterized by a slight erosion during spring, followed by a period of stabilization over summer.

During the first six months after completion of the nourishment works, z_{bci} and z_{bcc} show a net increase in the crest elevation of both subtidal bars, which is associated with the rapid onshore migration of the bar system over that period. After this initial phase of rapid profile adjustment, both arrays show a fairly stable inner bar over the period of interest. At the same time, the central array $y = -130$ m shows a minor tendency towards an ongoing increase in z_{bcc} , whereas the outer array $y = -1500$ m shows a distinct lowering of z_{bcc} . Interestingly, z_{bcc} along the central array exceeds z_{bcc} along the outer array with more than a meter. The utility of this information for coastal protection and/or military purposes is evaluated in the next section.

4.5 Discussion on the utility of Argus

A discussion on the utility of ARGUS video imaging is intimately related to the objectives of the end-users of video-derived monitoring data (Section 4.1). Twenty years of ARGUS-based science have contributed importantly to our understanding of nearshore morpho-

dynamic processes (e.g., Lippmann & Holman, 1990; Holland et al., 1998; Alexander, 2001; Van Enckevoort, 2001). The unique character of the ARGUS technique in terms of the cover of a wide range of spatiotemporal scales inspired a wealth of scientific publications, thus demonstrating a great utility for coastal scientists. Besides, it is acknowledged that much of the research work also embodies an - often indirect - relevance for CZM purposes, for instance:

- A fundamental understanding of the morphodynamics of a coastal system may contribute importantly to decision making in the field of coastal management. For example, is a scheduled intervention to mitigate local beach erosion still necessary if we know that the erosion is part of seasonal cycle?
- The availability of high-resolution, video-derived coastal state information is of significant importance for studies involving model improvement and data-model integration. Long-term, detailed data sets on nearshore processes provides enhanced opportunities for improvement and validation of process-based models and enable development of sophisticated data-driven model concepts (including neural networks, Ruessink et al., 2002b) to describe coastal morphodynamics. Improved performance of these models will optimize the design of coastal interventions like beach nourishments.
- Knowledge on the alongshore uniformity (Van Enckevoort & Ruessink, 2003a,b) of the morphodynamics of a coastal system facilitates the selection of an appropriate numerical model to assess the impact of various coastal interventions, thus reducing overall project costs.

Over the last few years, there has been a tendency towards the use of ARGUS video imaging in direct support of coastal management (Van Koningsveld et al., 2003). The utility of ARGUS in this respect can be evaluated in the context of the basic frame of reference for policy development (Section 4.2.3). To do so, video techniques should be used to quantify either *established* CSIs (particularly the MCL indicator) from video, or *additional* CSIs that contribute to established operational objectives by addressing alternative spatiotemporal scales, or *new* CSIs which cater for entirely new operational or strategic objectives. This categorization provides a useful scheme to assess the CZM utility of ARGUS in general, and the video-based CSIs quantified in this thesis in particular.

Established operational objective, established CSI

As stated in Section 4.2, the primary operational objective of Dutch CZM is to maintain the coastline at its 1990 position, using the MCL indicator to obtain quantitative information on the state of the coastal system. In Section 4.4, the MCL indicator was quantified from video on a daily to weekly basis. It is therefore concluded that the ARGUS technique shows a favorable utility in a sense that it provides the desired quantitative state information, although its degree of utility may be limited by the present accuracy of video-based estimates of x_{mcl} .

The accuracy of the video-derived x_{mcl} is limited by (1) the inherent model accuracy of SBM (Section 3.4), (2) the partial inclusion of morphological changes at the intertidal beach and (3) the neglect of morphological changes at the sub-aerial beach. As a result, video-based estimates of x_{mcl} are less accurate than their survey-based counterparts, that are presently used by coastal managers. The accuracy of x_{mcl} can be improved by (1) furthering the performance of SBM itself, particularly in the trough regions (Section 3.5.2), (2) embedding IBM results within the SBM environment, to achieve improved performance at the intertidal beach and to enable the cross-shore migration of the shoreward boundary condition of SBM, and (3) incorporating techniques to quantify morphological changes at the sub-aerial beach (e.g., Holman et al., 1991) and dunefoot oscillations. The combination of improved capabilities to quantify the momentary coastline position x_{mcl} from video and beneficial ARGUS key characteristics (high spatiotemporal resolutions, low costs) is expected to positively affect the utility of ARGUS.

Established operational objective, additional CSI

The present BCL procedure is associated with spatiotemporal scales in the order of 1 to 10 km and 1 to 10 years (Section 4.2.3), thus ignoring the three-dimensional character of beach morphodynamics at smaller space (hundreds of meters) and time (weeks to months) scales. As a result of these smaller-scale variabilities, the operational objective to maintain the coastline at its 1990 position may locally not be met. This problem increasingly occurs with local beach nourishments becoming the most important measure for coastal interventions.

Rather than using a suit of complex video analysis techniques or expensive field surveys to quantify x_{mcl} with sufficient resolution alongshore and in time, we can adopt alternative, relatively simple CSIs like the intertidal beach volume V_{IB} or the bar crest elevation z_{bc} and add these to the bench marking procedure for the operational objective ‘coastline maintenance’. This approach is motivated from earlier investigations, which have demonstrated the importance of morphological feedback mechanisms within coastal systems. Examples include the governing role of the outer bar phase for the morphodynamics of the breaker bar system (Wijnberg, 1995), the dependency of intertidal morphological changes on the (inner) surf zone bathymetry in front (De Boer, 2000; Kannan et al., 2003) and the relation between dune erosion during storm events and the location of the water contour line (Thornton et al., 2003). As the MCL indicator primarily reflects surf zone morphology, variations of the video-derived CSIs V_{IB} and z_{bc} are likely to correlate with variations of x_{mcl} . This justifies the use of relatively simple, video-based CSIs V_{IB} and z_{bc} for the evaluation of the operational objective ‘coastline maintenance’ at spatiotemporal scales of hundreds of meters and weeks to months.

Apart from a detailed investigation of the correlation between variations of V_{IB} , z_{bc} and x_{mcl} , practical use of the smaller-scale CSIs for CZM purposes demands a sound embedding in an additional basic frame of reference for the operational objective ‘coastline maintenance’. This involves an accurate definition of the new CSIs (particularly the elevation of the upper and lower plane bordering V_{IB} , the alongshore spacing of successive V_{IB} estimates and their resolution in time), the design of bench marking procedures

(development of methods to predict the evolution of V_{IB} and/or z_{bc} at the time scale of interest, determination of CSI standards) and an intervention procedure for situations where the predicted state of the small-scale CSI does not meet the CSI standard. The associated intervention may typically be a relatively small, local beach nourishment. Considering (i) the importance of the operational objective ‘coastline maintenance’, (ii) the close correspondence of a basic frame of reference for V_{IB} to existing CZM procedures and (iii) the relative ease of the video analysis techniques involved, future use of V_{IB} in a CZM context is realistic.

In summary, the incorporation of smaller-scale operational objectives for coastline maintenance to enable year-round exploitation of beaches calls for tailored interventions, which demand high-resolution monitoring in time and space. Given its key characteristics (high-resolution, low costs) and the video-based CSIs quantifiable so far (V_{IB} , z_{bc}), the utility of the ARGUS video technique for smaller-scale coastline maintenance is qualified as highly-promising.

New operational objective, new CSI

Apart from contributing to existing operational objectives, video-derived quantitative state information can also be explored in support of new objectives, not embedded (yet) in the Dutch field of CZM. For example, as regard to recreation, an operational objective formulated as ‘*near coastal resorts, a minimum beach width of 75 m will be maintained during the entire tourist season*’ would directly contribute to the existing strategic objective for CZM, which states the ‘... *sustainable preservation of values and functions* ...’. Implementation of such a new operational objective again demands an accurate definition of a representative CSI and the determination of bench marking and intervention procedures. Notice that the detailing of these aspects is primarily driven by functional demands. For instance, for this particular operational objective, it is likely to determine the CSI beach width on the basis of the shoreline location at mean low tide, since the intertidal beach contributes importantly to the recreational value of a coastal system. The definitions suggested here allow for the occurrence of smaller beach widths during winter months and storm conditions, when the value ‘recreation’ is less crucial. The utility of ARGUS in this respect depends on the successful embedding of new operational objectives in CZM practice and our capabilities to derive the appropriate quantitative state information from video.

In summary

The unique characteristics of the ARGUS video technique enable the long-term, cost-efficient monitoring of coastal regions over a wide range of spatiotemporal scales. Over the last two decades, this has stimulated the successful use of ARGUS in the context of many fundamental research studies, all aiming to contribute to our understanding of coastal morphodynamics. The use of ARGUS video monitoring in direct support of CZM demands a sound embedding of video-derived quantitative state information within policy development cycles, through quantification of a limited set of accurately defined CSIs. Exploration of the potential use of IBM- and SBM-derived CSIs confirms

the utility of ARGUS in this respect, albeit that some video-based CSIs, particularly x_{mcl} , undeniably require more accurate quantification.

Apart from the CSIs quantified from IBM or SBM and discussed in this chapter, there is wealth of complementary, video-based quantitative state information that contributes to the utility of ARGUS as well. Examples include statistics on local wave breaking to assess the efficiency of an artificial surfing reef at the Gold Coast, Australia (Turner et al., 2003), the occurrence and spacing of rip currents (Reintjes, 2002) to evaluate swimmer safety, the monitoring of channel evolution in support of shipping operations and statistics on people density at the beach to evaluate the spatial and temporal variability of beach use (*pers. comm.* J. Jimenez, UPC, Barcelona, Spain). Again, this quantitative information needs a sound embedding in a basic frame of reference approach, to be useful in direct support of CZM purposes. The latter issue is subject to present research in the framework of the EU-funded CoastView project.

4.6 Conclusions

The work presented in this chapter aimed to address the third main objective of this thesis (Section 1.4), by evaluating the utility of video-based monitoring techniques, particularly methods to quantify intertidal and subtidal bathymetry, for coastal management and science. To that end, three sub-objectives were formulated (Subsection 4.1.2), which are successively evaluated here.

To adopt an established framework that explicitly treats the information need and decision procedures in the field of CZM

- Van Koningsveld & Mulder (2002) provide a basic frame of reference for policy development, which explicitly shows the role of quantitative coastal state information (or Coastal State Indicators, CSIs) in relation to decision making in the field of CZM.
- The utility of video-based monitoring techniques, particularly methods to quantify intertidal and subtidal bathymetry, should be determined from the model's capability to quantitatively assess time series of CSIs.

To use IBM and SBM to quantify time series of video-based indicators of coastal evolution

- Both IBM and SBM are capable of mapping coastal bathymetry with sufficient accuracy to resolve inter- and subtidal morphological changes at spatiotemporal scales of hundreds of meters and weeks to months. This implies that model inaccuracies are small relative to the morphological changes at these scales.
- The definition of the CSIs presented here (beach width, intertidal beach volume, bar crest elevation) may need further consideration, depending on the detailed definition of the operational objective involved.

-
- The time series of CSIs considered so far do not reveal the remarkable spatial variability of the morphological changes at Egmond, as observed from the persistent nature of the shoreline perturbation immediately north of the light house.

To evaluate the utility of video-based monitoring techniques for CZM in the context of the framework identified above

- SBM-derived cross-shore beach profiles directly allow for the quantification of the Momentary Coastline Indicator x_{mcl} , which plays a central role in the field of Dutch CZM. Provided that the (partial) neglect of intertidal and sub-aerial changes and relatively large profile deviations in trough regions do not significantly reduce the accuracy of video-based estimates of x_{mcl} , it is concluded that the ARGUS technique shows a favorable utility in support of CZM at this point.
- IBM-derived intertidal bathymetrical maps enable the quantification of the evolution of beach width at low (W_{MLWS}) and high (W_{MHWS}) tide, and intertidal volumetric changes ΔV_{IB} . To assess their utility in direct support of CZM, it is necessary to demonstrate their correlation to x_{mcl} so that CSIs contribute to the established operational objective ‘coastline maintenance’. Alternatively, CSIs should address new operational objectives, for instance related to recreation.

Apart from its utility for CZM, the scientific utility of ARGUS video monitoring directly appears from the wealth of journal and conference publications, inspired by the use of the system. Present research efforts focus on the use of video-derived coastal state information for model improvement and data-model integration purposes. Detailed observations of the evolution of morphological parameters like shoreline location, intertidal beach volume and bar crest elevation provide enhanced opportunities for improvement and validation of process-based models and enable development of sophisticated data-driven model concepts (including neural networks) to describe coastal morphodynamics. Indeed the ARGUS video technique provides unique opportunities for the cost-efficient, synoptic and long-term monitoring of coastal environments over a wide range of spatiotemporal scales. With local beach nourishments becoming the most important measure for coastal interventions, the importance of smaller-scale CSIs within the field of CZM is expected to increase. It is a challenge for both coastal managers and scientists to derive the appropriate quantitative state information from ARGUS video imagery and to facilitate a sound embedding of this information in policy development cycles.

Chapter 5

Conclusions

The central aim of this thesis was *to quantify nearshore bathymetry from shore-based video imagery at spatiotemporal scales of direct management and research interest*. To achieve this central aim, three main objectives were formulated (Section 1.4), which are successively evaluated here.

Main objective 1: To develop robust methods to extract inter- and subtidal beach bathymetry from shore-based video imagery

In the framework of this study, two complementary methods were developed to derive inter- and subtidal beach bathymetry from shore-based video imagery.

The Intertidal Beach Mapper (IBM) composes the three-dimensional beach surface between the shoreline contours at low and high tide by mapping a series of beach contours, sampled throughout a tidal cycle. To that end, it delineates a shoreline feature from time-averaged video imagery on the basis of the visual contrast between the sub-aerial and sub-aqueous parts of the beach. To distinguish between these parts, the model explores the clustering of pixel intensities in both the color and luminance domains. The corresponding shoreline elevation is estimated from the tide and wave conditions at the time of image collection, accounting for the effects of tide- and storm-induced water level variations outside the surf zone, wave set-up at zero water depth and swash oscillations at infragravity and incident wave frequencies. Wave set-up at zero water depth is determined from an innovative wave propagation model, based on the self-similarity of bores in the inner surf zone. Empirical parameterizations involving the offshore wave height and period, and the intertidal beach slope are used to quantify the vertical excursion of the swash oscillations. In the absence of a generic criterion to separate between sub-aerial and sub-aqueous pixels over a wide range of hydrodynamic and atmospheric conditions at different sites, IBM necessarily operates on individual images. The new method was found to be robust, generic, flexible in use and capable of resolving three-dimensional morphological features including emerging intertidal bars.

The Subtidal Beach Mapper (SBM) quantifies surf zone bathymetry through assimilation of video-observed and model-predicted patterns of wave dissipation. SBM features two sub-models. The Breaker Intensity Model (BIM) samples time-averaged video intensities along a cross-shore array, excludes poor-quality images and interprets the resulting

intensity patterns in terms of a wave dissipation parameter. The latter involves a correction for the effect of persistent foam, which is visible at time-averaged video images but not predicted by common wave propagation models. The wave dissipation as measured from video is fed into the Bathymetry Assessment Model (BAM). BAM updates an initial beach bathymetry, either surveyed or determined from a previous video image, through assimilation of measured and modelled patterns of wave dissipation. This is achieved by raising the bottom elevation in areas where the measured dissipation rate exceeds the computed dissipation and vice versa. Since the model includes video data with high resolution in time, it allows for nearly continuous monitoring of surf zone bathymetry. It was found that time-averaged video observations of wave breaking relate best to the dissipation of roller energy D_r , albeit that the video-observed variability in D_r considerably overestimates the variability predicted from a common wave decay model. The time scale of profile adjustment is mainly governed by a limited set of morphological model parameters and is relatively small in dissipative areas (like the bar regions) as compared the neighbouring trough regions. Synthetic model tests demonstrated the applicability of SBM over a wide range of morphological configurations.

The two models are complementary by nature since they largely operate on different parts of the beach profile. At high tide, however, the sub-aqueous intertidal beach is part of the computational domain of SBM. Because of this spatial overlap, information on the elevation of the intertidal beach can be used as a shoreward boundary condition of SBM. This interesting link between both models is unexplored yet.

Main objective 2: To determine the accuracy of IBM and SBM through calibration and validation against existing bathymetric data sets

Validation of IBM against a data set of GPS-surveyed shorelines at Egmond has shown that mean vertical deviations resulting from the shoreline detection technique increase with increasing distance from the video station; deviations induced by model estimates of the corresponding shoreline elevation are relatively constant alongshore. The overall mean vertical deviation is less than 15 cm along 85% of the 2 km study region, which corresponds to a horizontal offset of 6 m. The scatter of overall model deviations (15-20 cm) is dominated by uncertainties resulting from the shoreline detection model. Model application at three distinctive field sites worldwide confirms IBM's reasonable applicability and performance over a wide range of hydrodynamic and atmospheric conditions.

Application of SBM along two cross-shore Egmond arrays spacing approximately 1400 m alongshore has demonstrated the model's capability to reproduce the dominant morphological changes during the first year after placing a shoreface nourishment, including the shoreward migration of the outer bar and the net accretion of sand in the nearshore part of the surf zone. The *rms* error of the vertical deviations along the entire beach profile typically amounts 40 cm for both arrays. Marginal deviations in the order of 10 to 20 cm are found at the seaward face of the bars, which increase up to 20 to 40 cm near the bar crest. Maximum deviations up to 80 cm are found in the trough region, owing to lack of wave dissipation information. The accretion of sediment in the shallow surf zone is underestimated, which contributes importantly to the increase in relative er-

rors with decreasing water depth. The analysis of SBM sensitivity to variable parameter settings has shown that model performance is strongly governed by the user-specified time scale of profile adjustment. The development of an objective methodology to set the model response time is a key issue for furthering the applicability and performance of SBM.

Main objective 3: To assess the utility of video-based monitoring techniques, particularly IBM and SBM, for application in support of coastal management and science

The availability of generically applicable, accurate and robust video interpretation models *in itself* does not guarantee the utility of video-based monitoring techniques. Useful video-based monitoring techniques also need to provide quantitative state information of direct end-users relevance. Van Koningsveld & Mulder (2002) provide a basic frame of reference for policy development, which explicitly shows the role of quantitative coastal state information (or Coastal State Indicators, CSIs) in relation to decision making in the field of CZM. The utility of video-based monitoring techniques for coastal management is governed by their capability to quantitatively assess time series of CSIs.

The application of IBM and SBM for the monitoring of a combined beach and shoreface nourishment at Egmond has shown that both models are capable of mapping coastal bathymetry with sufficient accuracy to resolve inter- and subtidal morphological changes at spatiotemporal scales of hundreds of meters and weeks to months. This implies that model inaccuracies are small relative to the morphological changes at these scales. SBM-derived cross-shore beach profiles directly allow for the quantification of the Momentary Coastline Indicator x_{mcl} , which plays a central role in the field of Dutch CZM. Provided that the (partial) neglect of intertidal and sub-aerial changes and relatively large profile deviations in trough regions do not significantly reduce the accuracy of video-based estimates of x_{mcl} , it is concluded that the ARGUS technique shows a favorable utility in support of CZM at this point. IBM-derived intertidal bathymetrical maps enable the quantification of the evolution of low-tide and high-tide beach width, as well as intertidal volumetric changes. To assess their utility in direct support of CZM, it is necessary to demonstrate their correlation to x_{mcl} so that CSIs contribute to the established operational objective ‘coastline maintenance’. Alternatively, CSIs should contribute to additional, smaller-scale operational objectives for smaller-scale coastal variability, driven by public and economic demands on beach recreation. The definition of the CSIs presented here may need further consideration, depending on the detailed definition of the operational objective involved.

The scientific utility of ARGUS video monitoring appears from the wealth of journal and conference publications, inspired by the use of the system. In the context of this work, the application of high-resolution video monitoring has revealed a remarkable spatial coherence of the morphological changes at Egmond, as observed from the persistent nature of the shoreline perturbation immediately north of the light house. Of particular scientific interest is the use of video-derived coastal state information for model improvement and data-model integration purposes. Detailed observations of the evolution of morphological parameters like shoreline location, intertidal beach volume

and bar crest elevation provide enhanced opportunities for improvement and validation of process-based models and enable development of sophisticated data-driven model concepts (including neural networks) to describe coastal morphodynamics. The use of video-derived morphological parameters for model improvement and data-model integration purposes is expected to be one of the focal points of ARGUS-based research in the nearby future.

In summary

The ARGUS video technique provides unique opportunities for the cost-efficient, synoptic and long-term monitoring of coastal environments over a wide range of spatiotemporal scales. Taking advantage of these favorable characteristics, the intertidal and subtidal beach mapper have successfully addressed the central aim of this work by *quantifying nearshore bathymetry from shore-based video imagery at spatiotemporal scales of direct management and research interest*. Furthermore, it is shown that video-based CSIs can resolve morphological changes at spatiotemporal scales of hundreds of meters and days to months. Existing CSIs quantified from traditional survey techniques do not easily include these smaller scales. With local beach and shoreface nourishments becoming the most important measure for coastal interventions, the importance of smaller-scale CSIs within the field of CZM is expected to increase. It is a challenge for both coastal managers and scientists to derive the appropriate quantitative state information from ARGUS video imagery and to facilitate a sound embedding of this information in policy development cycles.

References

- AARNINKHOF, S. G. J. (1996), Quantification of bar bathymetry from video observations. MSc thesis, Delft University of Technology.
- AARNINKHOF, S. G. J. & J. A. ROELVINK (1999), Argus-based monitoring of intertidal beach morphodynamics. In: Proc. Coastal Sediments'99, New York: ASCE, pp. 2429–2444.
- AARNINKHOF, S. G. J. & B. G. RUESSINK (2001), Video observations of wave breaking and the implication for wave decay modelling. In: Proc. Coastal Dynamics'01, New York: ASCE, pp. 979–988.
- AARNINKHOF, S. G. J., P. C. JANSSEN & N. G. PLANT (1997), Quantitative estimations of bar dynamics from video images. In: Proc. Coastal Dynamics'97, New York: ASCE, pp. 365–374.
- AARNINKHOF, S. G. J., M. CALJOUW & M. J. F. STIVE (2000), Video-based, quantitative assessment of intertidal beach variability. In: Proc. 27th Int. Conf. on Coastal Engineering, New York: ASCE, pp. 3291–3304.
- AARNINKHOF, S. G. J., N. G. PLANT, I. L. TURNER & K. S. KINGSTON (2002), Shoreline identification from video imagery: Intercomparison and ground truthing of four detection models. In prep. .
- ALEXANDER, P. S. (2001), Quantitative analysis of nearshore morphological variability based on video imaging. MSc thesis, Oregon State University.
- ALPORT, M., J. BASSON, G. P. MOCKE, J. NAICKER & C. SALTAU (2001), Discrimination and analysis of video imaged shorelines and nearshore processes. In: Proc. of Coastal Dynamics Conf., Lund, Sweden, ASCE, pp. 989–997.
- BAKKER, W. T. & J. H. DE VROEG (1988), Is de kust veilig? Analyse van het gedrag van de Hollandse kust in de laatste 20 jaar. Nota GWAO 88.017, Rijkswaterstaat, Dienst Getijdewateren. (In Dutch).
- BALDOCK, T. E., P. HOLMES, S. BUNKER & P. VAN WEERT (1998), Cross-shore hydrodynamics within an unsaturated surf zone. *Coastal Engineering* 34, pp. 173–196.
- BATTJES, J. A. (1974), Surf similarity. In: Proc. 14th Int. Conf. on Coastal Engineering, New York: ASCE, pp. 466–480.
- BATTJES, J. A. & J. P. F. M. JANSSEN (1978), Energy loss and set-up due to breaking of random waves. In: Proc. 16th Int. Conf. on Coastal Engineering, New York: ASCE, pp. 570–587.
- BATTJES, J. A. & M. J. F. STIVE (1985), Calibration and verification of a dissipation model for random breaking waves. *Journal of Geophysical Research* 90, pp. 9159–9167.
- BEETS, D. J., L. V. D. VALK & M. J. F. STIVE (1992), Holocene evolution of the coast of holland. *Marine Geology* 103, pp. 423–443.
- BELL, P. S. (1999), Shallow water bathymetry derived from an analysis of X-band marine radar images of waves. *Coastal Engineering* 37, pp. 513–527.
- BIRKEMEIER, W. A. & K. T. HOLLAND (2001), The corps of engineers' field research facility:

- More than two decades of coastal research. *Shore & Beach* 69, pp. 3–12.
- BIRKEMEIER, W. A. & C. MASON (1984), The crab: A unique nearshore surveying device. *Journal of Survey Engineering* 110, pp. 1–7.
- BOERS, M. (1996), Simulation of a surf zone with a barred beach. 1. Wave heights and wave breaking. *Communications on Hydraulic and Geotechnical Engineering*, Report No. 96-5, Delft University of Technology, Netherlands.
- BOERS, M. (1999), Suppleties bij Egmond en Bergen. Rapport RIKZ-99.030 (in Dutch), Rijkswaterstaat Rijks Instituut voor Kust en Zee.
- BOERS, M. & J. VAN DE GRAAFF (1995), Mass and momentum balance in the surf zone. In: *Proc. Coastal Dynamics'95*, New York: ASCE, pp. 257–268.
- BOSBOOM, J., S. G. J. AARNINKHOF, A. J. H. M. RENIERS, J. A. ROELVINK & D. J. R. WALSTRA (1997), Unibest-TC 2.0. Overview of model formulations. Report H2305.42, Delft Hydraulics.
- CALJOUW, M. (2000), Video-based monitoring of the Egmond beach- and shoreface nourishments. MSc thesis, Delft University of Technology.
- CERC (1984), Shore protection manual. Vicksburg MS, USA: Department of the Army, US Army Corps of Engineers.
- CHICKADEL, C. & R. A. HOLMAN (2002a), Measuring longshore current with video techniques. In: *Eos Trans. AGU*, 82(47), Fall Meet. Suppl.
- CHICKADEL, C. & R. A. HOLMAN (2002b), Optical measurements of low frequency cross-shore flows. In: *Eos Trans. AGU*, 83(47), Fall Meet. Suppl., p. F717.
- CHICKADEL, C. C., R. A. HOLMAN & M. H. FREILICH (2003), An optical technique for the measurement of longshore currents. Accepted for publication in *Journal of Geophysical Research*.
- CLARKE, L. B. & B. T. WERNER (2003), Synoptic imaging of nearshore bathymetric patterns. *Journal of Geophysical Research* 108(C1), pp. 5.1–5.13.
- DAVIDSON, M., D. HUNTLEY, R. HOLMAN & K. GEORGE (1997), The evaluation of large (km) intertidal beach morphology on a macrotidal beach using video images. In: *Proc. Coastal Dynamics'97*, New York: ASCE, pp. 385–394.
- DAVIDSON, M. A. & B. D. MORRIS (2002), The use of video remote sensing for the evaluation of high resolution wave parameters and sub-tidal morphology. Submitted to *Coastal Engineering*.
- DE BOER, A. (2000), Beach volume changes on a meso-tidal sandy coast. In: *Proc. 27th Int. Conf. on Coastal Engineering*, New York: ASCE, pp. 3076–3087.
- DE RUIG, J. H. M. (1998), Coastline management in the netherlands: Human use versus natural dynamics. *Journal of Coastal Conservation* 3, pp. 203–210.
- DE VRIEND, H. J. (1997), Prediction of aggregated-scale coastal evolution. In: *Proc. Coastal Dynamics'97*, New York: ASCE, pp. 644–653.
- DE VRIEND, H. J., M. CAPOBIANCO, T. CHESHER, H. E. DE SWART, B. LATTEUX & M. J. F. STIVE (1993), Approaches to long-term modelling of coastal morphology: a review. *Coastal Engineering* 21, pp. 225–269.
- DEAN, R. G. (1977), Equilibrium beach profiles: US Atlantic and Gulf coast. *Ocean Engineering report No. 12*, University of Delaware, Newark, DE.
- DRONKERS, T. (2001), Intertidal morphodynamics at Narrowneck Reef. Intra-annual video observations and predictions of long-term shoreline response. MSc thesis, Delft University of Technology.
- DUGAN, J. P., W. D. MORRIS, K. C. VIERRA, C. C. PIOTROWSKI, G. J. FARRUGGIA & D. C. CAMPION (2001a), Jetski-based nearshore bathymetric and current survey system.

- Journal of Coastal Research 17(4), pp. 900–908.
- DUGAN, J. P., C. C. PIOTROWSKI & J. Z. WILLIAMS (2001b), Water depth and surface current retrievals from airborne optical measurements of surface gravity wave dispersion. *Journal of Geophysical Research* 106(C8), pp. 16903–16915.
- FRAGAKIS, C. (2002), Preface to the special issue shore nourishment in europe. *Coastal Engineering* 47(2), pp. 79–80.
- GALLAGHER, E. L., S. ELGAR & E. B. THORNTON (1998), Observations and predictions of megaripple migration in a natural surf zone. *Nature* 394, pp. 165–168.
- GARCEZ FARIA, A. F., E. B. THORNTON, T. C. LIPPMANN & T. P. STANTON (2000), Undertow over a barred beach. *Journal of Geophysical Research* 105, pp. 16999–17010.
- GODA, Y. (1975), Irregular wave deformation in the surf zone. *Coastal Eng. Jpn* 18, pp. 13–27.
- GREIDANUS, H. (1997), The use of radar for bathymetry in shallow seas. *The Hydrographic Journal* 83, pp. 13–18.
- GUILLÉN, J., M. J. F. STIVE & M. CAPOBIANCO (1999), Shoreline evolution of the Holland coast on a decadal scale. *Earth Surface Processes and Landforms* 24, pp. 517–536.
- GUILLÉN, J., O. CHIC, E. OJEDA, A. PALANQUES & S. AARNINKHOF (2002), Monitorización de las playas de la ciudad de barcelona utilizando imagenes de video: Evolucion de la linea de costa en respuesta a temporales y regeneración artificial (2001-2002). In: *Proc. of JORNADAS Conf, Almeria, Spain*.
- GUZA, R. T. & E. B. THORNTON (1982), Swash oscillations on a natural beach. *Journal of Geophysical Research* 87, pp. 483–491.
- GUZA, R. T. & E. B. THORNTON (1985), Observations of surf beat. *Journal of Geophysical Research* 90, pp. 3161–3172.
- HAMM, L., M. CAPOBIANCO, H. H. DETTE, A. LECHUGA, R. SPANHOFF & M. J. F. STIVE (2002), A summary of european experience with shore nourishments. *Coastal Engineering* 47, pp. 237–265.
- HERBERS, T. H. C., S. ELGAR, R. T. GUZA & W. C. O'REILLY (1995), Infragravity-frequency (0.005-0.05 hz) motions on the shelf, ii, free waves. *Journal of Geophysical Research* 25, pp. 1063–1079.
- HOLLAND, K. T. (2001), Application of the linear dispersion relation with respect to depth inversion using remotely sensed imagery. *IEEE Transactions on Geoscience and Remote Sensing* 39(9), pp. 2060–2072.
- HOLLAND, K. T. & R. A. HOLMAN (1993), The statistical distribution of swash maxima on natural beaches. *Journal of Geophysical Research* 98(C6), pp. 10271–10278.
- HOLLAND, K. T. & R. A. HOLMAN (1997), Video estimation of foreshore topography using trinocular stereo. *Journal of Coastal Research* 13(1), pp. 81–87.
- HOLLAND, K. T. & J. A. PULEO (2001), Variable swash motions associated with foreshore profile change. *Journal of Geophysical Research* 106, pp. 4613–4623.
- HOLLAND, K. T., B. RAUBENHEIMER, R. T. GUZA & R. A. HOLMAN (1995), Runup kinematics on a natural beach. *Journal of Geophysical Research* 100, pp. 4985–4993.
- HOLLAND, K. T., R. A. HOLMAN, T. C. LIPPMANN, J. STANLEY & N. PLANT (1997), Practical use of video imagery in nearshore oceanographic field studies. *Journal of Oceanic Engineering* 22, pp. 81–92.
- HOLLAND, K. T., A. H. SALLENGER JR, B. RAUBENHEIMER & S. ELGAR (1998), Swash zone morphodynamics and sediment transport processes. In: *Proc. 26th Int. Conf. on Coastal Engineering*, New York: ASCE, pp. 2799–2811.
- HOLLAND, K. T., J. A. PULEO & T. N. KOONEY (2001), Quantification of swash flows using

- video-based particle image velocimetry. *Coastal Engineering* 44, pp. 65–77.
- HOLLAND, K. T., J. A. PULEO, N. PLANT & J. M. KAIHATU (2002), Littoral environmental nowcasting system (lens). In: *Proc. of IEEE Oceans Conf.*, pp. 1234–1240.
- HOLMAN, R. A. & A. H. J. SALLENGER (1985), Setup and swash on a natural beach. *Journal of Geophysical Research* 90, pp. 945–953.
- HOLMAN, R. A. & A. H. J. SALLENGER (1986), High-energy nearshore processes. *Transactions, American Geophysical Union* 67, pp. 1369–1371.
- HOLMAN, R. A., T. C. LIPPMANN, P. V. O’NEILL & K. HATHAWAY (1991), Video estimation of subaerial beach profiles. *Marine Geology* 97, pp. 225–231.
- HOLMAN, R. A., A. H. J. SALLENGER, T. C. LIPPMANN & J. W. HAINES (1993), The application of video image processing to the study of nearshore processes. *Oceanography* 6, pp. 78–85.
- HOUWMAN, K. T. (2000), Tide, wind- and wave-driven flow processes in the nearshore zone. Ph.D. thesis, Dept. of Physical Geography, Utrecht University, Netherlands.
- HUNT, I. A. (1959), Design of seawalls and breakwaters. *Proc. Am. Civil Eng.* 85, pp. 123–152.
- HUNTLEY, D. A., R. T. GUZA & A. J. BOWEN (1977), A universal form of shoreline run-up spectra? *Journal of Geophysical Research* 82, pp. 2577–2581.
- IRISH, J. L. & W. J. LILLYCROP (1999), Scanning laser mapping of the coastal zone: the shoals system. *ISPRS Journal of Photogrammetry & Remote Sensing* 54, pp. 123–129.
- JANSSEN, P. C. (1997), Intertidal beach level estimations from video images. MSc thesis, Delft University of Technology.
- KAMINSKY, G. M., P. RUGGIERO, G. GELFENBAUM & C. PETERSON (1997), Long term coastal evolution and regional dynamics of a us pacific northwest littoral cell. In: *Proc. Coastal Dynamics Conf.*, Plymouth, UK, New York: ASCE, pp. 614–623.
- KANNAN, S., T. C. LIPPMANN & J. H. LIST (2003), The relationship of nearshore sandbar configuration to shoreline change. In: *Proc. Coastal Sediments’03*, New York: ASCE.
- KINGSTON, K. S., B. G. RUESSINK, I. M. J. VAN ENCKEVORT & M. A. DAVIDSON (2000), Artificial neural network correction of remotely sensed sandbar location. *Marine Geology* 169, pp. 137–160.
- KINGSTON, K. S., C. MALLET, N. G. PLANT & M. A. DAVIDSON (2003), Inter-tidal mapping of morphological features from remotely sensed data. Submitted to *Marine Geology*.
- KNAAPEN, M. A. F. (1996), Optimizing bathymetry estimates gained by video imaging of breaking waves. Report H2443, Delft Hydraulics.
- KOMAR, P. (1998), *Beach and nearshore sedimentation*, 2nd ed. Upper Saddle River, NJ, USA: Prentice-Hall.
- KONICKI, K. M. & R. A. HOLMAN (2000), The statistics and kinematics of transverse sand bars on an open coast. *Marine Geology* 169, pp. 69–101.
- KROON, A. (1994), Sediment transport and morphodynamics of the beach and nearshore zone near Egmond, The Netherlands. Ph.D. thesis, Physical Geography, Utrecht University.
- KURIYAMA, Y. (2003), Sediment budget analysis with aerial photographs. In: *Proc. Coastal Sediments’03*, New York: ASCE.
- LEU, L. G., Y. Y. KUO & C. T. LIU (1999), Coastal bathymetry from the wave spectrum of SPOT images. *Coastal Engineering Journal* 41, pp. 21–41.
- LIGTENDAG, W. A. (1990), Van IJzer tot Jade, een reconstructie van de zuidelijke Noordzee kust in de jaren 1600 en 1750. Rapport MDLK-K-9041 (in Dutch), Rijkswaterstaat Meetkundige Dienst.
- LIPPMANN, T. C. & R. A. HOLMAN (1989), Quantification of sand bar morphology: a video technique based on wave dissipation. *Journal of Geophysical Research* 94, pp. 995–1011.

- Coastal Engineering, ASCE, pp. 637–650.
- PULEO, J. A. & K. T. HOLLAND (2001), Estimating swash zone friction coefficients on a sandy beach. *Coastal Engineering* 43, pp. 25–40.
- RAKHORST, H. D. (1994), Standaardisatie bepaling BKL en TKL. Rapport NH-94.ANV.015 (in Dutch), Rijkswaterstaat Directie Noord-Holland.
- RANASINGHE, R., G. SYMONDS & R. HOLMAN (1999), Quantitative characterisation of rip dynamics via video imaging. In: *Proc. of Coastal Sediments Conf., Long Island (NY, USA)*, New York: ASCE, pp. 987–1002.
- RANASINGHE, R., G. SYMONDS, K. BLACK & R. HOLMAN (2000), Processes governing rip spacing, persistence, and strength in a swell dominated microtidal environment. In: *Proc. 27th Int. Conf. on Coastal Engineering*, New York: ASCE, pp. 454–467.
- RAUBENHEIMER, B. & R. T. GUZA (1996), Observations and predictions of wave run-up. *Journal of Geophysical Research* 101, pp. 25575–25587.
- RAUBENHEIMER, B., R. T. GUZA & S. ELGAR (1996), Wave transformation across the inner surf zone. *Journal of Geophysical Research* 101, pp. 25589–25597.
- REINTJES, C. M. (2002), Muilocaties voor de kust bij Egmond aan Zee. Relatie tussen muilocaties en volumeveranderingen. IMAU Report R 02-02, Instituut voor Marien en Atmosferische Onderzoek Utrecht, Faculteit Ruimtelijke Wetenschappen, Universiteit Utrecht.
- RENIERS, A. J. H. M. & J. A. BATTJES (1997), A laboratory study of longshore currents over barred and non-barred beaches. *Coastal Engineering* 30, pp. 1–22.
- RENIERS, A. J. H. M., J. A. ROELVINK & A. R. DONGEREN (2000), Morphodynamic response to wave-group forcing. In: *Proc. 27th Int. Conf. on Coastal Engineering*, New York: ASCE, pp. 3218–3228.
- RENIERS, A. J. H. M., G. SYMONDS & E. B. THORNTON (2001), Modelling of rip currents during rdex. In: *Proc. Coastal Dynamics'01*, New York: ASCE, pp. 493–499.
- RENIERS, A. J. H. M., J. A. ROELVINK & E. B. THORNTON (2003), Morphodynamic modeling of an embayed beach under wave group forcing. Accepted for publication in *Journal of Geophysical Research*.
- ROELSE, P. (2002), Water en Zand in balans. Evaluatie zandsuppleties na 1990; een morfologische beschouwing. Report RIKZ-2002.003 (In Dutch), Rijkswaterstaat Rijks Instituut voor Kust en Zee.
- ROELVINK, J. A. (1993), Dissipation in random wave groups incident on a beach. *Coastal Engineering* 19, pp. 127–150.
- ROONEY, J., C. FLETCHER, B. MATHEW, D. EVERSOLE, L. SIANG-CHYN, B. RICHMOND & A. GIBBS (2003), Dynamics of sandy shorelines in maui, hawaii: Consequences and causes. In: *Proc. Coastal Sediments'03*, New York: ASCE.
- RUSSINK, B. G. & M. C. J. L. JEUKEN (2002), Dunefoot dynamics along the dutch coast. *Earth Surface Processes and Landforms* 27, pp. 1043–1056.
- RUSSINK, B. G., K. T. HOUWMAN & P. HOEKSTRA (1998a), The systematic contribution of transporting mechanisms to the cross-shore sediment transport in water depths of 3 to 9 m. *Marine Geology* 152, pp. 295–324.
- RUSSINK, B. G., M. G. KLEINHANS & P. G. L. v. BEUKEL (1998b), Observations of swash under highly dissipative conditions. *Journal of Geophysical Research* 103(C2), pp. 3111–3118.
- RUSSINK, B. G., I. M. J. VAN ENCKEVORT, K. S. KINGSTON & M. A. DAVIDSON (2000), Analysis of observed two- and three-dimensional nearshore bar behaviour. *Marine Geology* 169, pp. 161–183.
- RUSSINK, B. G., J. R. MILES, F. FEDDERSEN, R. T. GUZA & S. ELGAR (2001), Modeling

- the alongshore current on barred beaches. *Journal of Geophysical Research* 106, pp. 22451–22463.
- RUSSINK, B. G., P. S. BELL, I. M. J. VAN ENCKEVORT & S. G. J. AARNINKHOF (2002a), Nearshore bar crest location quantified from time-averaged x-band radar images. *Coastal Engineering* 45, pp. 19–32.
- RUSSINK, B. G., H. F. P. VAN DEN BOOGAARD & S. G. J. AARNINKHOF (2002b), Integration of Argus video data and nearshore sandbar models. Report Z3290, Delft Hydraulics.
- RUSSINK, B. G., D. J. R. WALSTRA & H. N. SOUTHGATE (2003a), Calibration and verification of a parametric wave model on barred beaches. *Coastal Engineering* 48, pp. 139–149.
- RUSSINK, B. G., K. M. WIJNBERG, R. A. HOLMAN, Y. KURIYAMA & I. M. J. VAN ENCKEVORT (2003b), Intersite comparison of interannual nearshore bar behavior. *Journal of Geophysical Research* 108(C8).
- RUSS, J. C. (1995), *The image processing handbook*. 2nd Edition. Boca Ration, Florida: CRC Press, Inc.
- SALLENGER, A. H. J., W. KRABILL, R. SWIFT & J. BROCK (2001), Quantifying hurricane-induced coastal changes using topographic lidar. In: *Proc. Coastal Dynamics Conf.*, Lund, Sweden, New York: ASCE, pp. 1007–1016.
- STIVE, M. J. F. (1980), Velocity and pressure field of spilling breakers. In: *Proc. 17th Int. Conf. on Coastal Engineering*, New York: ASCE.
- STIVE, M. J. F. & H. J. DE VRIEND (1994), Shear stress and mean flow in shoaling and breaking waves. In: *Proc. 24th Int. Conf. on Coastal Engineering*, New York: ASCE, pp. 594–608.
- STIVE, M. J. F. & A. J. H. M. RENIERS (2003), Sandbars in motion. *Nature* 299, pp. 1855–1856.
- STIVE, M. J. F., S. AARNINKHOF, L. HAMM, H. HANSON, M. LARSON, K. W. WIJNBERG, R. J. NICHOLLS & M. CAPOBIANCO (2002), Variability of shore and shoreline evolution. *Coastal Engineering* 47(2), pp. 211–235.
- STOCKDON, H. F. & R. A. HOLMAN (2000), Estimation of wave phase speed and nearshore bathymetry from video imagery. *Journal of Geophysical Research* 105, pp. 22015–22033.
- STOCKDON, H. F., R. A. HOLMAN & A. H. SALLENGER (2002), Parameterization of incident and infragravity swash variance. In: *Eos Trans. AGU*, 83(47), Fall Meet. Suppl., p. F746.
- SUZUKI, K., S. TAKAHASHI, N. YAMAGATA, O. HORITA, Y. KURIYAMA, S. AARNINKHOF, R. G. & I. ELSHOFF (2002), Field obserbation of miyazaki beach using argus video technique. In: *Proc. of coastal engineering Japan (Volume 47)*, Society of Civil Engineering.
- SVENDSEN, I. A. (1984), Wave heights and set-up in a surf zone. *Coastal Engineering* 8, pp. 303–329.
- SVENDSEN, I. A., P. A. MADSEN & J. BUHR HANSEN (1978), Wave characteristics in the surf zone. In: *Proc. 16th Int. Conf. on Coastal Engineering*, New York: ASCE, pp. 520–539.
- SYMONDS, G., R. A. HOLMAN & B. BRUNO (1997), Rip currents. In: *Proc. Coastal Dynamics'97*, New York: ASCE, pp. 584–585.
- THORNTON, E., T. DALRYMPLE, T. DRAKE, E. GALLAGHER, B. GUZA, A. HAY, R. HOLMAN, J. KAIHATU, T. LIPPMANN & T. OZKAN-HALLER (2000), State of nearshore processes research: II. Technical Report NPS-OC-00-001, Naval Postgraduate School, Monterey, California.
- THORNTON, E. B. & R. T. GUZA (1983), Transformation of wave height distribution. *Journal of Geophysical Research* 88, pp. 5925–5938.
- THORNTON, E. B., J. L. SWAYNE & J. R. DINGLER (1998), Small-scale morphology across the surf zone. *Marine Geology* 145, pp. 173–196.

- THORNTON, E. B., L. A. EGLEY, A. SALLENGER & R. PARSONS (2003), Erosion in southern monterrey bay during the 1997-1998 el nino. In: Proc. Coastal Sediments'03, New York: ASCE.
- TURNER, I. L. & V. M. LEYDEN (2000), System description and analysis of shoreline change: August 1999 - February 2000. Report 1, Northern Gold Coast Coastal Imaging System. WRL Technical Report 00/12, 85 pp., Water Research Laboratory, University of New South Wales.
- TURNER, I. L., V. M. LEYDEN, G. SYMONDS, J. MCGRATH, A. JACKSON, T. JANCAR, S. G. J. AARNINKHOF & I. E. ELSHOFF (2000), Predicted and observed coastline changes at the gold coast artificial reef. In: Proc. 27th Int. Conf. on Coastal Engineering, New York: ASCE, pp. 1836–1847.
- TURNER, I. L., S. G. J. AARNINKHOF, T. D. T. DRONKERS & J. MCGRATH (2003), Czm applications of argus coastal imaging at the gold coast, australia. Accepted for publication in *Journal of Coastal Research* .
- VAN ENCKEVORT, I. M. J. (2001), Daily to yearly nearshore bar behaviour. Ph.D. thesis, Physical Geography, Utrecht University.
- VAN ENCKEVORT, I. M. J. & B. G. RUESSINK (2001), Effects of hydrodynamics and bathymetry on video estimates of nearshore sandbar position. *Journal of Geophysical Research* 106, pp. 16969–16979.
- VAN ENCKEVORT, I. M. J. & B. G. RUESSINK (2003a), Video observations of nearshore bar behaviour. part 1: alongshore uniform variability. *Continental Shelf Research* 23, pp. 501–512.
- VAN ENCKEVORT, I. M. J. & B. G. RUESSINK (2003b), Video observations of nearshore bar behaviour. part 2: alongshore non-uniform variability. *Continental Shelf Research* 23, pp. 513–532.
- VAN KONINGSVELD, M. (2003), Matching Specialist Knowledge with End User Needs. Ph.D. thesis, Department of Civil Engineering, University of Twente.
- VAN KONINGSVELD, M. & J. P. M. MULDER (2002), Sustainable coastal policy in the netherlands. a small- and large scale approach. In: Proc. 28th Int. Conf. on Coastal Engineering, New York: ASCE, pp. 3594–3605.
- VAN KONINGSVELD, M., M. A. DAVIDSON & D. A. HUNTLEY (2003), Matching science with coastal management needs; the search for appropriate coastal state indicators. Subm. to *Journal of Coastal Reserach* .
- VAN RIJN, L. C. (1997), Sediment transport and budget of the central coastal zone of holland. *Coastal Engineering* 32, pp. 61–90.
- VAN RIJN, L. C., B. G. RUESSINK & J. P. M. MULDER (2002), Coast3D - Egmond. The behaviour of a straight sandy coast on the time scale of storms and seasons. Amsterdam: AQUA publications.
- WALSTRA, D. J. R., G. P. MOCKE & F. SMIT (1996), Roller contributions as inferred from inverse modelling techniques. In: Proc. 25th Int. Conf. on Coastal Engineering, New York: ASCE, pp. 1205–1218.
- WENSINK, G. J., G. H. F. M. HESSELMANS & C. J. CALKOEN (1998), The bathymetry assessment system. In: Proc. of the Oceanology '98 Conf., Brighton, UK, pp. 361–370.
- WIJNBERG, K. M. (1995), Morphologic behaviour of a barred coast over a period of decades. Ph.D. thesis, Physical Geography, Utrecht University.
- WIJNBERG, K. M. & HOLMAN (1997), Cyclic bar behavior viewed by video imagery. In: Proc. Coastal Dynamics'97, New York: ASCE, pp. 375–384.
- WIJNBERG, K. M. & J. H. J. TERWINDT (1995), Quantification of decadal morphological

- behaviour of the central Dutch coast. *Marine Geology* 126, pp. 301–330.
- WORLEY, C. R., T. C. LIPPMANN, J. W. HAINES & A. H. SALLENGER (1997), An aerial video system for rapidly measuring sand bar morphology. In: *Proc. Coastal Dynamics'97*, New York: ASCE, pp. 346–354.
- WRIGHT, L. D. & A. D. SHORT (1984), Morphodynamic variability of surf zones and beaches: a synthesis. *Marine Geology* 56, pp. 93–118.

Appendix A

Photogrammetry

A.1 Geo-referencing of oblique video data

Standard photogrammetric procedures (Holland et al., 1997) enable the transformation from real world coordinates (x, y, z) to image coordinates (u, v) on the basis of the collinearity equations (Eq. 1.1). The latter contain 11 coefficients $L_1 - L_{11}$, which are described as

$$\begin{aligned} L &= -(x_c m_{31} + y_c m_{32} + z_c m_{33}) \\ L_1 &= \frac{(u_0 m_{31} + f m_{11})}{(\lambda_u L)} \\ L_2 &= \frac{(u_0 m_{32} + f m_{12})}{(\lambda_u L)} \\ L_3 &= \frac{(u_0 m_{33} + f m_{13})}{(\lambda_u L)} \\ L_4 &= -(L_1 x_c + L_2 y_c + L_3 z_c) \\ L_5 &= \frac{(v_0 m_{31} + f m_{21})}{\lambda_v L} \\ L_6 &= \frac{(v_0 m_{32} + f m_{22})}{\lambda_v L} \\ L_7 &= \frac{(v_0 m_{33} + f m_{23})}{\lambda_v L} \\ L_8 &= -(L_5 x_c + L_6 y_c + L_7 z_c) \\ L_9 &= \frac{m_{31}}{L} \\ L_{10} &= \frac{m_{32}}{L} \\ L_{11} &= \frac{m_{33}}{L} \end{aligned} \tag{A.1}$$

In Eq. (A.1), (x_c, y_c, z_c) are the camera xyz -coordinates, (u_0, v_0) are the image center uv -coordinates, f is the effective focal length and λ_u and λ_v are the horizontal and vertical scale factors. The m -coefficients describe the successive rotations around the

azimuth ϕ , tilt τ and roll σ ,

$$\begin{aligned}
m_{11} &= \cos \phi \cos \sigma + \sin \phi \cos \tau \sin \sigma \\
m_{12} &= -\sin \phi \cos \sigma + \cos \phi \cos \tau \sin \sigma \\
m_{13} &= \sin \tau \sin \sigma \\
m_{21} &= -\cos \phi \sin \sigma + \sin \phi \cos \tau \cos \sigma \\
m_{22} &= \sin \phi \sin \sigma + \cos \phi \cos \tau \cos \sigma \\
m_{23} &= \sin \tau \cos \sigma \\
m_{31} &= \sin \phi \sin \tau \\
m_{32} &= \cos \phi \sin \tau \\
m_{33} &= -\cos \tau
\end{aligned} \tag{A.2}$$

The theoretical formulations presented here are valid for use with distortion-free lenses. Owing to the incorporation of λ_u and λ_v , the formulations embody a correction for the slightly non-squareness of individual pixels. The latter is induced by a minor difference in sampling frequency between the camera and image acquisition hardware, which causes a minor mismatch between the number of horizontal picture elements at the camera CCD and the number of columns at the image frame buffer, where the image processing system stores the video data.

A.2 Calibration of intrinsic camera model parameters

Video lenses generally show a radial distortion, which increases with decreasing focal length and decreasing lens quality. This distortion essentially appears from radially varying deviations Δr between the video-observed locations of individual pixels and their theoretical positions at a rectangular pixel grid, which depend on the distance to the image center (u_0, v_0) , see Figure A.1a. Holland et al. (1997) parameterize the radial deviations Δr by means of an odd-order polynomial, according to

$$\Delta r = k_1 r^3 + k_2 r, \tag{A.3}$$

where

$$r = \sqrt{(u - u_0)^2 + (v - v_0)^2}. \tag{A.4}$$

The values of the distortion coefficients k_1 and k_2 are obtained by fitting Eq. (A.3) to the radial deviations Δr (Figure A.1b), measured in the laboratory with the help of a control points testfield (Holland et al., 1997). Using an iterative approach, the calibration procedure also yields best settings for the horizontal and vertical scale factor λ_u and λ_v and the image center coordinates u_0 and v_0 .

In summary, calibration of the video hardware in the laboratory (preceding the actual installation in the field) yields values for the intrinsic camera model parameters $(\lambda_u, \lambda_v, k_1, k_2, u_0, v_0)$, whereas the image geometry solution, defined by means of a four angle vector $[\phi, \tau, \sigma, \delta]$, is found from the geo-referencing procedure involving a

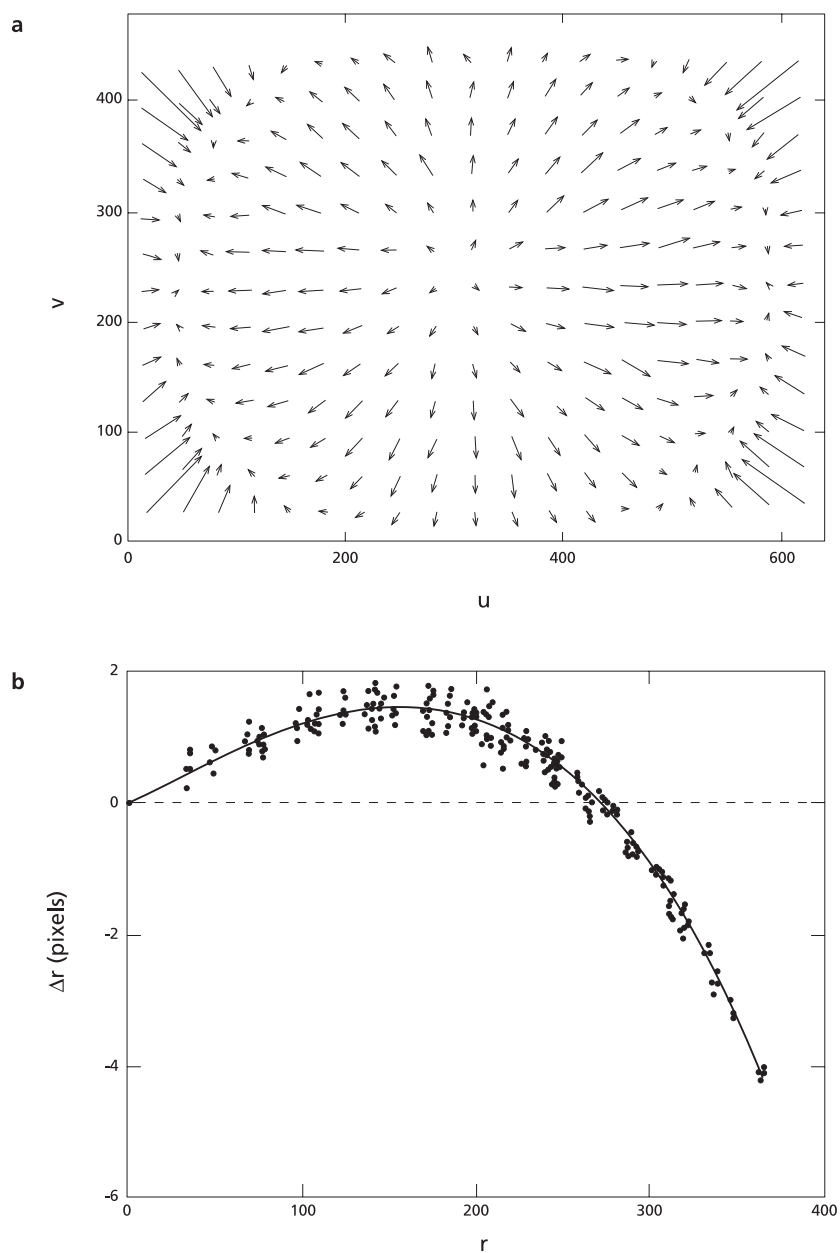


Figure A.1: *Radial distortion of video lenses. Examples of (a) radial distortion of raw video data and (b) the corresponding best fit polynomial to perform the distortion correction.*

minimum number of two Ground Control Points as well as the intrinsic camera model parameters.

Appendix B

Detailed aspects of the shoreline detection model

B.1 Preprocessing of raw intensity data

To identify the location of the shoreline at the interface of dry and wet, raw image intensities are sampled within a region of interest covering both the sub-aerial and sub-aqueous beach. Preprocessing of these raw intensity data involves a two-step approach:

- Filtering of raw intensities. To remove outliers, raw HSV data are filtered by settling a limited intensity range $\mu_i - \alpha_i \cdot \sigma_i < I_i < \mu_i + \alpha_i \cdot \sigma_i$ for each intensity band I_i (where $i = 1 \dots 3$ for hue, saturation and value respectively). μ_i and σ_i represent the mean and standard deviation of I_i . Data within this range are selected for further analysis. The coefficient α_i is set such that 99% of the raw data are covered, with a lower limit 0 for $\mu_i - \alpha_i \cdot \sigma_i$ and an upper limit 1 for $\mu_i + \alpha_i \cdot \sigma_i$.
- Scaling of filtered intensity data. To improve contrast between the clusters of dry and wet pixels, the HSV color bands I_i of the filtered intensity data are scaled between 0 and 1, using a linear transformation to project intensity data in the range $I_{i,\min} < I_i < I_{i,\max}$ on the extended domain $[0 \ 1]$.

The effect of both operations is illustrated in Figure B.1.

B.2 Filtering histograms of scaled intensities

To enable the discrimination of two unique clusters of dry and wet pixels, the histogram of scaled image intensities is low-pass filtered with the help of a two-dimensional, symmetrical Hanning filter. This operation causes individual, spiky bins of the histogram to merge, which yields a smoother histogram of intensity data. Histogram smoothing increases with increasing window width w_{han} of the Hanning filter. A side-effect of the filtering operation is the introduction of an artificial shift of the location of minimum probability ('saddle point') towards the cluster with the smaller number of occurrences

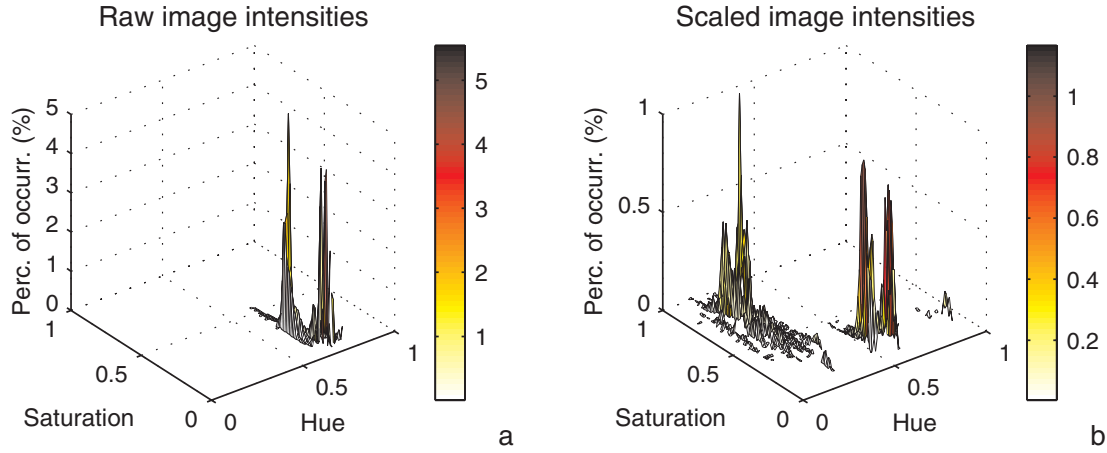


Figure B.1: *Preprocessing of raw HSV image intensities. Histogram of intensity data in hue-saturation space, before (a) and after (b) filtering and subsequent scaling.*

(Figure B.2, away from the middle point in between the centers of mass of both clusters. In operational mode, w_{han} has to be set such that it is large enough to enable the identification of two unique clusters of dry and wet pixels, without inducing a considerable artificial offset of the saddle point between both clusters. An iterative approach is adopted to determine best settings for w_{han} , which starts from small w_{han} and ends if two unique clusters are revealed, or w_{han} exceeds the empirically set maximum window width $w_{\text{han,max}}$. In the latter case, the image of consideration is rejected from further analysis owing to insufficient visible contrast between the sub-aerial and sub-aqueous beach (c.f. Section B.3).

The magnitude of the artificially introduced shift of the saddle point towards the smaller cluster increases with (i) increasingly different cluster sizes and (ii) increasing w_{han} of the Hanning filter. To account for this artificial offset, an empirical correction dS is applied according to:

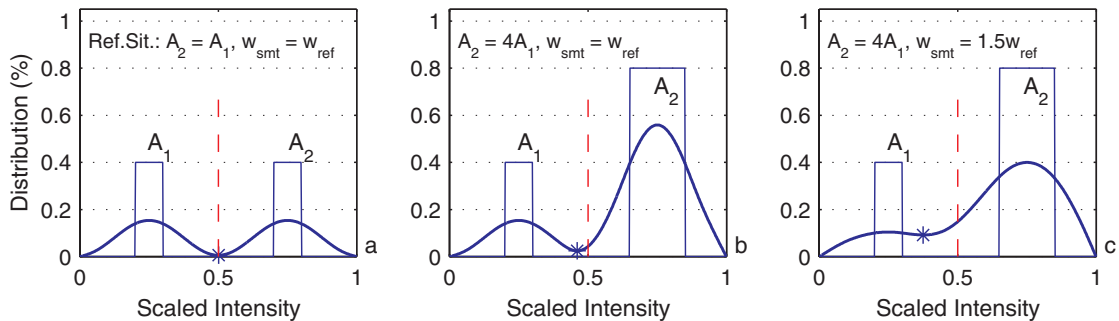


Figure B.2: *Filtering induced off-set of the location of minimum probability (*) in between two clusters of observations (one-dimensional case). Illustration of the effect of increasing cluster area (b) and increasing window width (c), with respect to the reference situation with equal cluster size (a).*

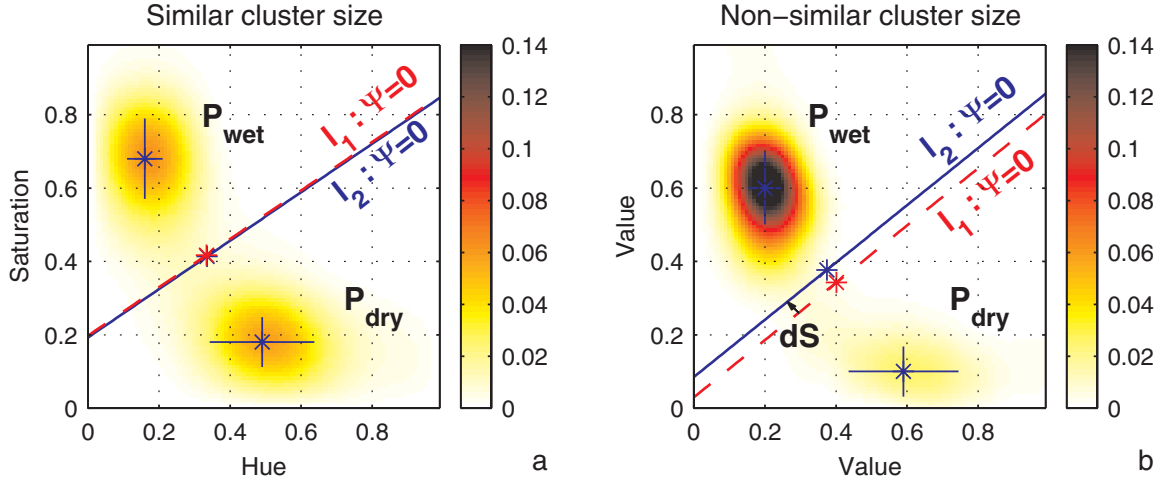


Figure B.3: Correction of the filtering-induced artificial off-set of the location of the saddle point of the histogram. The lines l_1 and l_2 represent the discriminator function before and after application of the correction, in case of similar (a) and strongly non-equal (b) cluster sizes.

$$dS = f_{sign} \cdot \left(\frac{w_{\text{han}}}{\hat{w}_{\text{han,max}}} \cdot \frac{N_{\text{wet}} - N_{\text{dry}}}{N_{\text{wet}} + N_{\text{dry}}} \right) \cdot d\hat{S}_{\text{max}} \quad (\text{B.1})$$

In Eq. (B.1), f_{sign} is a sign function which arranges the correction to be in the right direction (i.e. towards the larger cluster), w_{han} is the window width of the Hanning filter which yields two unique clusters of pixels and $\hat{w}_{\text{han,max}}$ is the maximum window width tolerated by the shoreline detection model. The parameters N_{wet} and N_{dry} represent the number of pixels in the wet and dry cluster respectively, based on a initial discrimination between dry and wet (i.e. with no correction on the smoothing induced shift). Finally, $d\hat{S}_{\text{max}}$ is the user-defined maximum shift of the location of the saddle point, which is expressed as a portion of the absolute distance ΔP between the two peaks P_{dry} and P_{wet} of the histogram. The parameter $d\hat{S}_{\text{max}}$ can be used for calibration purposes; a reasonable value for application over a wide range of beaches is 0.2 - 0.3. Notice that significant shifts ($dS \geq 0.5d\hat{S}_{\text{max}}$) are only obtained in case of a large width of the Hanning window in combination with strongly non-equal cluster sizes, for instance a w_{han} of $0.8 \cdot \hat{w}_{\text{han,max}}$ in combination with only 20% dry pixels within the region of interest. Figure B.3 illustrates the operation of Eq. (B.1), based on the application of the shoreline detection model to the 04/12/1998 GMT 10 hr. time exposure image of Noordwijk, with different user-defined regions of interest. The parameter $d\hat{S}_{\text{max}}$ is set to $0.2 \cdot \Delta P$ for both situations. Similar cluster sizes (53% dry pixels) yield a $dS = 0.007 \cdot \Delta P$, hardly visible in Figure B.3a. Non-similar cluster sizes however (only 20% dry pixels) yield a correctional shift $dS = 0.069 \cdot \Delta P$ towards the largest cluster (Figure B.3b).

B.3 Assessment of dry-wet contrast in pixel intensities

The IBM shoreline detection model considers three parameters to evaluate the distinctive potential of a discriminator function Ψ . All three are based on the filtered histogram of image intensities. The parameters are (i) the filter width w_{han} that reveals two unique clusters, (ii) the relative cluster size and (iii) the spread of the intensity values within each cluster. To allow for reliable identification of clusters of dry and wet pixels, Ψ needs to pass empirical criteria on parameters (i) and (ii):

1. w_{han} is not allowed to exceed $\hat{w}_{han,max}$, which is set to half the width of the domain of I_x and I_y . Both I_x and I_y are ranging between 0 and 1.
2. Either one of the two clusters should cover at least 10% of the overall number of pixels.

If both the color-based discriminator function Ψ_c and the luminance-based function Ψ_l obey these criteria, analysis is continued with an evaluation of Ψ_c and Ψ_l in terms of parameter (iii). This involves the standard deviations σ_{dry} and σ_{wet} of the intensity data per cluster normalized with their corresponding distances ΔP_{dry} and ΔP_{wet} to the discriminator line l (Fig. A-4). The parameters σ_{dry} and σ_{wet} are computed as the vectorized sum of the standard deviations σ_x and σ_y per cluster in the I_x and I_y domain respectively. The latter are represented by the crosses projected at each cluster in Figure B.4.

The discriminator functions Ψ_c and Ψ_l are evaluated in terms of the ratios $\sigma_{dry}/\Delta P_{dry}$ and $\sigma_{wet}/\Delta P_{wet}$. The detection model aims to minimize the largest of the two ratios, as dry-wet contrast increases with decreasing ratios $\sigma_{dry}/\Delta P_{dry}$ and $\sigma_{wet}/\Delta P_{wet}$. The discriminator function which performs best in this respect is adopted for shoreline detection.

B.4 Empirical demands on shoreline persistency

Application of the discriminator function Eq. (2.1) to scaled intensity data sampled within the region of interest yields a surface of Ψ values that spans the region of interest. Surface contour techniques are used to determine the location of the shoreline from the $\Psi = 0$ elevation contours. To avoid the inclusion of erroneous shoreline contours, for example induced by artificial features on the beach, an individual contour is only accepted if it meets at least one empirical criterion on shoreline persistency. The three empirical criteria on shoreline persistency demand that an individual shoreline contour is only accepted if

- It covers at least 75 neighbouring pixels in image space
- It covers at least 200 m alongshore

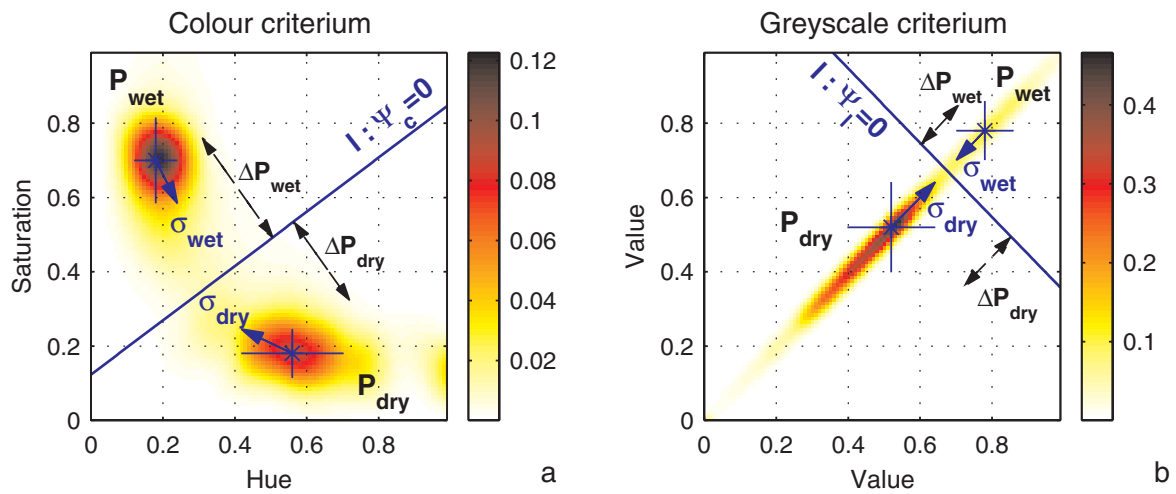


Figure B.4: *Dry-wet contrast as observed from pixel clustering in color (a) and luminance (b) space. Both histograms originate from a single Noordwijk image d.d. 04/12/1998 10:00 GMT. The crosses represent the σ_x and σ_y of the intensity data within each cluster. Hardly any contrast is found in luminance space, whereas two well-separated clusters of pixels are found in color space. Hence, Ψ_c is adopted for shoreline detection.*

- It covers at least half the alongshore length of the region of the interest

Application of these criteria effectively remove erroneous $\Psi = 0$ contours at the dry beach, while enabling IBM to resolve 3-dimensional morphology including emerging intertidal bars.

Appendix C

Formulation and implementation of the inner surf zone model

In the framework of this study, a two-layer hydrodynamic model has been developed to describe wave height decay in the inner surf zone, based on the self-similarity of hydrodynamic processes in this shallow region. This appendix provides a detailed description of the governing equations of the inner surf zone model and briefly addresses their implementation in a numerical code.

C.1 Background inner surf zone model

The inner surf zone model describes an onshore-propagating bore that passes a location x at time $t = 0$ (Figure C.1). The bore motion is periodic with period T . The upper layer is located above trough level and features a bore with height H_2 , propagating onshore with velocity V over a sloping bottom with elevation z_b . The lower layer with thickness H_1 is located between the bottom and the trough level and features a net offshore mass flux to balance the onshore mass flux in the upper layer.

On the basis of detailed flume measurements by Stive (1980) and his interpretation of the Peregrine & Svendsen (1978) of a quasi-steady breaking wave (Figure 2.10), the instantaneous layer thickness h_1 (h_2) and particle velocity v_1 (v_2) in the lower (upper) layer are parameterized as:

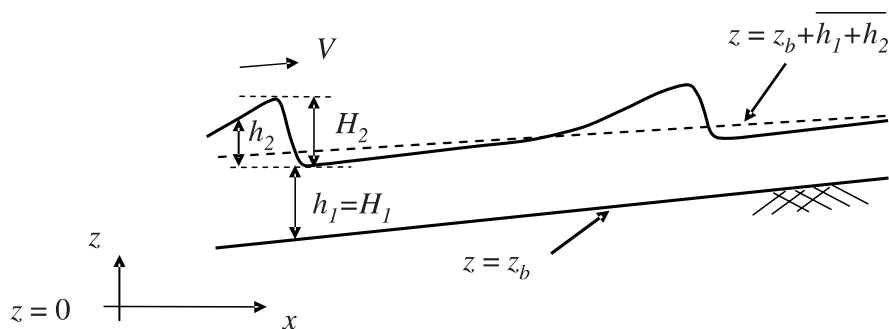


Figure C.1: *Definition sketch inner surf zone model.*

$$\frac{h_1}{H_1} = 1 \quad (\text{C.1a})$$

$$\frac{h_2}{H_2} = \left(1 - \frac{t}{T}\right)^{a_1} \quad \text{with } a_1 = 5 \quad (\text{C.1b})$$

$$\frac{v_1}{V} = a_2 \left(1 - \frac{t}{T}\right)^2 + a_3 \quad \text{with } a_2 = 0.44, \ a_3 = -0.18 \quad (\text{C.1c})$$

$$\frac{v_2}{V} = a_4 e^{a_5 \left(1 - \frac{t}{T}\right)} + a_6 \quad \text{with } a_4 = 0.0024, \ a_5 = 6, \ a_6 = -0.18 \quad (\text{C.1d})$$

where T is the wave period. To facilitate further elaboration of these formulations, we transform these formulations to a reverse time frame t_* defined as $t_* = 1 - t/T$, which yields:

$$\frac{h_1}{H_1} = 1 \quad (\text{C.2a})$$

$$\frac{h_2}{H_2} = t_*^{a_1} \quad (\text{C.2b})$$

$$\frac{v_1}{V} = a_2 t_*^2 + a_3 \quad (\text{C.2c})$$

$$\frac{v_2}{V} = a_4 e^{a_5 t_*} + a_6 \quad (\text{C.2d})$$

Notice that this transformation does not affect any of the wave-averaged properties that are evaluated in the context of the inner surf zone model.

C.2 Model formulations

The intra-wave parameterizations (C.2) for the layer thickness and particle velocity in the inner surf zone are formulated in terms of three unknowns H_1 , H_2 and V . Balance equations for the conservation of mass and momentum in the overall two-layer system provide two conditions for the inner surf zone model. The system of equations is closed through the assumption of a shallow water approximation for V . The three model equations are discussed here.

C.2.1 Time averaged momentum balance equation

The momentum balance equation is formulated on the basis of the conservation of horizontal momentum within an inner surf zone control volume, bordered by vertical planes and extending from the bottom level z_b to the water surface $z_b + h_1 + h_2$ (Fig. C.1). Accounting for the horizontal force effectuated by the sloping bottom and the effect of bottom friction, the momentum balance equation reads:

$$\frac{\partial}{\partial t} \int_{z_b}^{z_b+h_1+h_2} \rho v dz = -\frac{\partial}{\partial x} \int_{z_b}^{z_b+h_1+h_2} (p + \rho v^2) dz - p_b \frac{\partial z_b}{\partial x} - \tau_b \quad (\text{C.3})$$

where the horizontal particle velocity v is defined as $v = v_1$ for $z_b < z < z_b + h_1$ and $v = v_2$ for $z_b + h_1 < z < z_b + h_1 + h_2$. Weakly varying acceleration terms (like $v \frac{\partial v}{\partial x}$) have been neglected. In Eq. (C.3), $p = \rho g (z_b + h_1 + h_2 - z)$ is the instantaneous hydrostatic pressure for $z_b < z < z_b + h_1 + h_2$, p_b is the hydrostatic pressure near the bottom, $\frac{\partial z_b}{\partial x}$ is the local beach slope and τ_b represents the bottom friction, modelled as $\tau_b = \frac{1}{2} \rho f_w v_1 |v_1|$, where f_w is a friction coefficient. Averaging over time causes the left-hand side of Eq. (C.3) to become zero, owing to the periodic character of the bore motion. After substitution of v with v_1 and v_2 , the time-averaged momentum balance equation for the inner surf zone model reads

$$\begin{aligned} & \frac{\partial}{\partial x} \int_0^1 \int_{z_b}^{z_b+h_1+h_2} p dz dt_* + \frac{\partial}{\partial x} \int_0^1 \int_{z_b}^{z_b+h_1} \rho v_1^2 dz dt_* + \frac{\partial}{\partial x} \int_0^1 \int_{z_b+h_1}^{z_b+h_1+h_2} \rho v_2^2 dz dt_* + \\ & + \int_0^1 p_b \frac{\partial z_b}{\partial x} dt_* + \int_0^1 \tau_b dt_* = 0 \end{aligned} \quad (\text{C.4})$$

Modelling the individual terms

Taking into account the parameterizations (C.2), the individual terms of Eq. (C.4) can be formulated in terms of the unknown H_1 , H_2 and V . Doing so for the hydrostatic pressure term yields

$$\begin{aligned} \int_0^1 \int_{z_b}^{z_b+h_1+h_2} p dz dt_* &= \int_0^1 \int_{z_b}^{z_b+h_1+h_2} \rho g (z_b + h_1 + h_2 - z) dz dt_* = \\ &= \frac{1}{2} \rho g \int_0^1 (h_1 + h_2)^2 dt_* = \frac{\rho g H_1^2}{2} + \frac{\rho g H_1 H_2}{a_1 + 1} + \frac{\rho g H_2^2}{4a_1 + 2} \end{aligned} \quad (\text{C.5})$$

The wave-induced fluxes of horizontal momentum through the lower and upper layer (second and third term of Eq. C.4) are formulated as

$$\begin{aligned}
\int_0^1 \int_{z_b}^{z_b+h_1} \rho v_1^2 dz dt_* &= \int_0^1 \int_{z_b}^{z_b+h_1} \rho V^2 (a_2 t_*^2 + a_3)^2 dz dt_* = \\
&= \rho H_1 V^2 \int_0^1 (a_2 t_*^2 + a_3)^2 dt_* = \rho H_1 V^2 \left(\frac{a_2^2}{5} + \frac{2a_2 a_3}{3} + a_3^2 \right) \\
\int_0^1 \int_{z_b+h_1}^{z_b+h_1+h_2} \rho v_2^2 dz dt_* &= \int_0^1 \int_{z_b+h_1}^{z_b+h_1+h_2} \rho V^2 (a_4 \cdot e^{a_5 t_*} + a_6)^2 dz dt_* = \\
&= \rho V^2 \int_0^1 (a_4 \cdot e^{a_5 t_*} + a_6)^2 h_2 dt_* = \rho V^2 H_2 A
\end{aligned} \tag{C.6}$$

where A represents the numerically-computed value of the integral $\int_0^1 (a_4 e^{a_5 t_*} + a_6)^2 t_*^{a_1} dt_*$. The forcing terms accounting for the effects of the horizontal force effectuated by the sloping bottom and bottom friction read

$$\int_0^1 p_b \frac{dz_b}{dx} dt_* = \frac{dz_b}{dx} \int_0^1 \rho g (h_1 + h_2) dt_* = \rho g \left(H_1 + \frac{H_2}{a_1 + 1} \right) \frac{dz_b}{dx} \tag{C.7a}$$

$$\int_0^1 \tau_b dt_* = \int_0^1 \left(\frac{1}{2} \rho f_w v_1 |v_1| \right) dt_* = \frac{\rho f_w V^2 B}{2} \tag{C.7b}$$

where B represents the numerically-computed integral $\int_0^1 (a_2 t_*^2 + a_3) |a_2 t_*^2 + a_3| dt_*$.

Momentum balance equation

Substitution of the formulations derived above in Eq. (C.4) yields the following momentum balance equation:

$$\begin{aligned}
\frac{d \left(\frac{\rho g H_1^2}{2} + \frac{\rho g H_1 H_2}{a_1 + 1} + \frac{\rho g H_2^2}{4a_1 + 2} \right)}{dx} &+ \frac{d \left(\rho H_1 V^2 \left\{ \frac{a_2^2}{5} + \frac{2a_2 a_3}{3} + a_3^2 \right\} \right)}{dx} + \frac{d(\rho V^2 H_2 A)}{dx} = \\
&= -\rho g \left(H_1 + \frac{H_2}{a_1 + 1} \right) \frac{dz_b}{dx} - \frac{\rho f_w V^2 B}{2}
\end{aligned} \tag{C.8}$$

This equation can be solved numerically after writing it in finite difference form (Section C.3).

C.2.2 Time averaged mass balance equation

The mass balance equation states that at the time scale of the wave period T , the net shoreward mass flux M_2 in the upper layer needs to be compensated by a net seaward mass flux M_1 through the lower layer. Both fluxes are obtained by integrating the flow velocities over the layer thickness and subsequently averaging over time. This yields:

$$M_1 = \int_0^1 \int_{z_b}^{z_b+h_1} (\rho v_1) dz dt_* = \rho V \int_0^1 (a_2 t_*^2 + a_3) h_1 dt_* = \rho V H_1 \left(\frac{a_2}{3} + a_3 \right) \quad (\text{C.9a})$$

$$M_2 = \int_0^1 \int_{z_b+h_1}^{z_b+h_1+h_2} (\rho v_2) dz dt_* = \rho V \int_0^1 (a_4 \cdot e^{a_5 \cdot t_*} + a_6) h_2 dt_* = \rho V H_2 C \quad (\text{C.9b})$$

where C represents the numerically-computed value of the integral $\int_0^1 (a_4 e^{a_5 t_*} + a_6) t_*^{a_1} dt_*$. Conservation of mass demands that $M_1 + M_2 = 0$, hence

$$\rho V H_1 \left(\frac{a_2}{3} + a_3 \right) + \rho V H_2 C = 0 \quad (\text{C.10})$$

C.2.3 Bore velocity

The system of equations is closed through the assumption of a shallow water approximation for V ,

$$V = \sqrt{g \cdot h_{\text{bore}}} = \sqrt{g(H_1 + \delta H_2)} \quad (\text{C.11})$$

where δ is an empirical bore velocity coefficient, which accounts for uncertainties in the magnitude of the water depth h_{bore} at the bore crest and the error in application to a non-uniform bore.

C.3 Solving the model equations

The model equations are solved numerically with the help of a forward stepping integration method. To that end, the mass and momentum balance equations are iteratively evaluated. Starting from known boundary conditions for $H_1(x_i)$ and $H_2(x_i)$ at the seaward end x_i of the inner surf zone model, the model initially assumes ΔH_1 between x_i and the next computational point x_{i+1} to be zero. This assumption enables the quantification of ΔH_2 from Eqs. (C.8) and (C.11), using a first-order Taylor approximation to estimate finite difference terms in the momentum balance equation. The Taylor approximations are formulated as:

$$\begin{aligned}
\Delta \left(\frac{\rho g H_1^2}{2} + \frac{\rho g H_1 H_2}{a_1 + 1} + \frac{\rho g H_2^2}{4a_1 + 2} \right) &\cong \rho g H_1 \Delta H_1 + \frac{\rho g H_2}{a_1 + 1} \Delta H_1 + \\
&\quad + \frac{\rho g H_1}{a_1 + 1} \Delta H_2 + \frac{\rho g H_2}{2a_1 + 1} \Delta H_2 \\
\Delta \left(\left\{ \frac{a_2^2}{5} + \frac{2}{3} a_2 a_3 + a_3^2 \right\} \rho V^2 H_1 \right) &\cong 2 \left\{ \frac{a_2^2}{5} + \frac{2}{3} a_2 a_3 + a_3^2 \right\} \rho V H_1 \Delta V + \\
&\quad + \left\{ \frac{a_2^2}{5} + \frac{2}{3} a_2 a_3 + a_3^2 \right\} \rho V^2 \Delta H_1 \\
\Delta (\rho V^2 H_2 A) &\cong 2 \rho A H_2 V \Delta V + \rho V^2 A \Delta H_2 \\
\Delta V &\cong \frac{\delta \sqrt{g}}{2\sqrt{H_1 + \delta H_2}} \Delta H_2 + \frac{\sqrt{g}}{2\sqrt{H_1 + \delta H_2}} \Delta H_1 \\
\Delta z_b &\cong m \Delta x
\end{aligned} \tag{C.12}$$

where m is the local beach slope. Substitution of these expressions in the momentum balance equation (C.8) yields

$$\begin{aligned}
f_1 \cdot \Delta H_2 + f_2 \cdot \Delta V + f_3 \cdot \Delta H_1 &= -(term_1 + term_2) \Delta x \\
\Delta V &= f_4 \cdot \Delta H_2 + f_5 \cdot \Delta H_1
\end{aligned} \tag{C.13}$$

where

$$\begin{aligned}
term_1 &= \rho g m \left(H_1 + \frac{H_2}{a_1 + 1} \right) \\
term_2 &= \frac{\rho f_w V^2 B}{2}
\end{aligned} \tag{C.14}$$

and appropriate terms are gathered in the factors $f_1 \dots f_5$. Substitution of the expression for ΔV in the first order Taylor approximation of the momentum balance equation enables the quantification of ΔH_2 given an initial estimate of ΔH_1 :

$$\Delta H_2 = - \frac{(f_3 + f_2 f_5) \Delta H_1 + (term_1 + term_2) \Delta x}{(f_1 + f_2 f_4)} \tag{C.15}$$

After this initial step, the mass balance equation is evaluated to verify mass conservation within the system at x_{i+1} . If necessary, the estimate of $H_1(x_{i+1})$ is refined on the basis of the sign of $M_1 + M_2$, which enables an improved estimate of ΔH_2 , hence H_2 . This process turns out to rapidly converge in about 5-15 iteration steps.

Appendix D

Formulations wave transformation model

In the framework of this study, a parametric wave transformation model was used to quantify wave set-up throughout the surf zone as part of IBM's shoreline elevation model (Section 2.3.3) and to generate model-predicted wave dissipation patterns for assimilation with video-derived observations of wave breaking in the context of SBM (Section 3.2.4). The wave model consists of three coupled differential equations which describe the time-averaged, cross-shore evolution of organized wave energy E , roller energy E_r and wave set-up η . Assuming the wave field to be narrow-banded in frequency and direction, the wave energy balance equation (Battjes & Janssen, 1978) reads

$$\frac{d}{dx}(Ec_g \cos \bar{\theta}) = -D_{br} - D_f \quad (\text{D.1})$$

where c_g is the wave group velocity, $\bar{\theta}$ is the mean wave angle and D_{br} and D_f represent energy dissipation due to wave breaking and bottom friction, respectively. The organized wave energy is calculated as $E = \frac{1}{8}\rho g H_{rms}^2$, where ρ is the water density, g is the gravitational acceleration and H_{rms} is the *rms* wave height. As wave heights inside and outside the surf zone are best described by a Rayleigh distribution (Thornton & Guza, 1983; Baldock et al., 1998), we adopt the Baldock et al. (1998) formulation to model D_{br} ,

$$D_{br} = \frac{1}{4}\rho g \alpha f_p e^{-\left(\frac{H_b}{H_{rms}}\right)^2} (H_b^2 + H_{rms}^2) \quad (\text{D.2})$$

where α is a dissipation parameter (commonly set to 1), f_p is the peak frequency and H_b is the wave height where waves start breaking, which is generally defined as a fraction of the local water depth (Battjes & Janssen, 1978),

$$H_b = \frac{0.88}{k} \tanh\left(\frac{\gamma kh}{0.88}\right) \quad (\text{D.3})$$

In this formulation, k is the wave number and h represent local water depth. The Battjes & Janssen (1978) and Baldock et al. (1998) formulations for D_{br} yield similar wave dissipation rates in the range of moderate H_{rms}/H_b less than 0.75. The mildly-sloping beaches considered in the framework of this thesis are characterized by such

moderate H_{rms}/H_b , which justifies the use of default γ settings according to Battjes & Stive (1985), who calculate γ from the deep water wave steepness $s_0 = H_{\text{rms}0}/L_0$ as $\gamma = 0.5 + 0.4 \tanh(33s_0)$. In line with Bosboom et al. (1997), D_f is described as a function of the local orbital velocity

$$D_f = \frac{1}{8\sqrt{\pi}} \rho f_{\text{fr}} \left(2\pi f_p \frac{H_{\text{rms}}}{\sinh(kh)} \right)^3 \quad (\text{D.4})$$

where f_{fr} is a bottom friction coefficient. Linear wave theory is used to calculate c_g and Snell's law is applied to determine the evolution of $\bar{\theta}$ throughout the surf zone from the $\bar{\theta}_0$ measured offshore.

Standard wave transformation models like the Battjes & Janssen (1978) model describe the decay of organized wave energy reasonably well, however, the location of initial wave set-up is consistently predicted too far seaward. This has initiated the modelling of the foamy rollers at the face of breaking waves (Svendsen, 1984). Such a roller is a turbulent bore-like mass of water, which is developed in the transition zone where potential wave energy is converted into kinetic energy before ultimately being dissipated through the production of turbulence. Parametric wave transformation models account for this effect through incorporation of a balance equation for roller energy (Nairn et al., 1990; Stive & De Vriend, 1994)

$$\frac{d}{dx} (2E_r c \cos \bar{\theta}) = -D_r + D_{\text{br}} \quad (\text{D.5})$$

where E_r is the roller energy density, c is the phase speed and D_r is the dissipation of roller energy, given by

$$D_r = 2\beta g \frac{E_r}{c} \quad (\text{D.6})$$

thus representing the power per unit time performed by the shear stress at the interface of the foamy wave roller and the water surface. The slope β of the breaking-wave front directly affects the rate of roller dissipation, such that roller advection length increases with decreasing β . Inclusion of the roller concept particularly improves model predictions of wave-induced alongshore currents (Reniers & Battjes, 1997; Ruessink et al., 2001)

Finally, the wave set-up η is determined from the depth-integrated and time-averaged cross-shore momentum balance equation, given by

$$\frac{d\eta}{dx} = -\frac{1}{\rho g h} \frac{dS_{\text{xx}}}{dx} \quad (\text{D.7})$$

where $S_{\text{xx}} = (n + n \cos^2 \bar{\theta} - \frac{1}{2})E + 2E_r \cos^2 \bar{\theta}$, with $n = c_g/c$, is the cross-shore component of the radiation stress tensor (Longuet-Higgins & Stewart, 1964), which accounts for the contribution of organized wave energy as well as roller energy.

Appendix E

Video-based shoreline detection models

Aarninkhof et al. (2002) assess the behaviour and performance of four video-based shoreline detection models, at four distinctive video sites world-wide. The three detection models involved besides IBM are briefly discussed below.

E.1 ShoreLine Intensity Maximum (SLIM) model

Swash motions at the shoreline may generate foam and produce a distinct shore-parallel band of high light intensity in time exposure images. (Plant & Holman, 1997) name the bright band the shoreline intensity maximum (SLIM). Changes in the SLIM position are assumed to be correlated to changes in the tide level. As the tide rises and falls, the SLIM moves onshore and offshore, visually marking beach elevation contour lines. The approach used by (Plant & Holman, 1997) (also described by (Madsen & Plant, 2001) is to identify the map co-ordinates of the shoreline and then assign an estimated tidal elevation to them, thus producing bathymetric data. The *rms* elevation error of this technique appears to be about 10 cm (or 1 m in horizontal sense at Duck, NC), after removing an offset bias. This error level is comparable to direct bathymetric survey error.

Following (Madsen & Plant, 2001), SLIM positions are located by fitting a superposition of quadratic and Gaussian-shaped functions to intensities along a cross-shore transect that included the entire intertidal zone. The intensity function that they used was

$$\hat{I}(t_i, y_j, x) = I_0^{ij} + I_1^{ij}x + I_2^{ij}x^2 + A_{\text{slim}}^{ij} \exp \left[- \left(\frac{x - X_{\text{slim}}^{ij}}{L_{\text{slim}}^{ij}} \right)^2 \right] \quad (\text{E.1})$$

where I_0 , I_1 , I_2 , parameterize the quadratic function and A_{slim} , X_{slim} and L_{slim} parameterize the Gaussian function's amplitude, position, and width (Figure E.1). While the X_{slim} is the only parameter used to generate bathymetric data, the other parameter estimates are used to interpret the quality of each estimated shoreline position

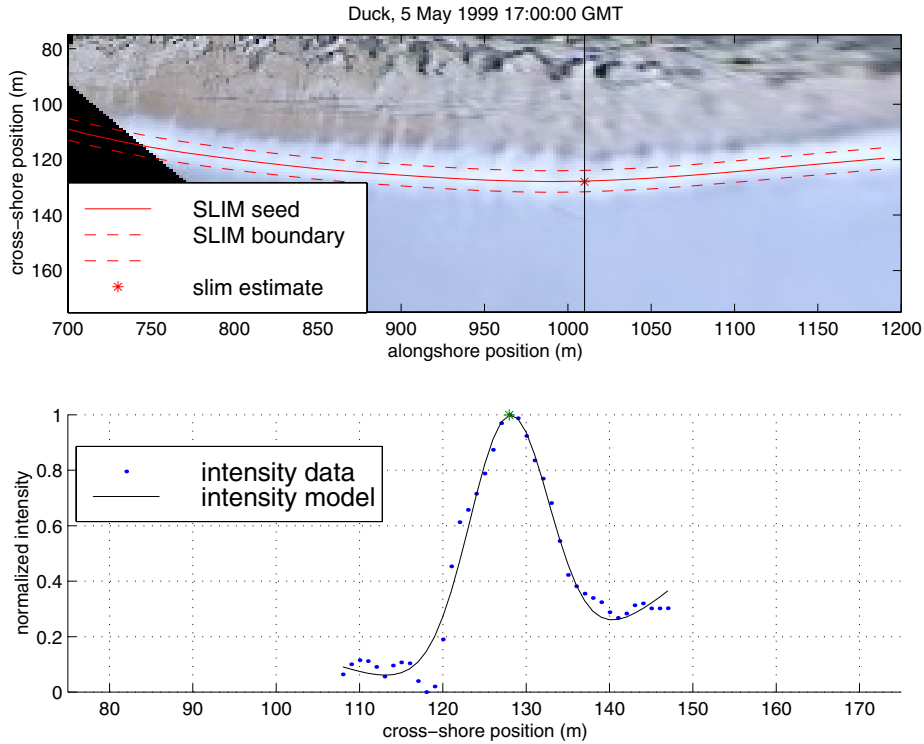


Figure E.1: *Background of SLIM approach.*

(see Madsen & Plant, 2001, for more detail). The parameters were estimated using a non-linear (Gauss-Newton) regression algorithm.

E.2 Artificial Neural Network (ANN) model

The ANN model (Kingston et al., 2003) adopts the Aarninkhof & Roelvink (1999) approach of differentiating between wet and dry pixels to delineate a shoreline feature. This delineation is based on differences in the color characteristics of sand and water, which are quantified with an Artificial Neural Network model. See Kingston et al. (2000) for an overview of the general operation and implementation of Artificial Neural Networks, applied to coastal morphological systems.

Artificial Neural Networks simulate non-linear models of an input-output system. The network is constructed through tuning to a training data set. In this case the inputs are taken to be the Red-Green-Blue (RGB) values of a pixel. The output in the training data set is a binary classification of either water (0) or sand (1). The shoreline identification using an ANN implemented the following steps

- A region of interest in an image is selected. This contains both land and water pixels bounding one or more shoreline features.
- A classification surface, y is produced for the region of interest.

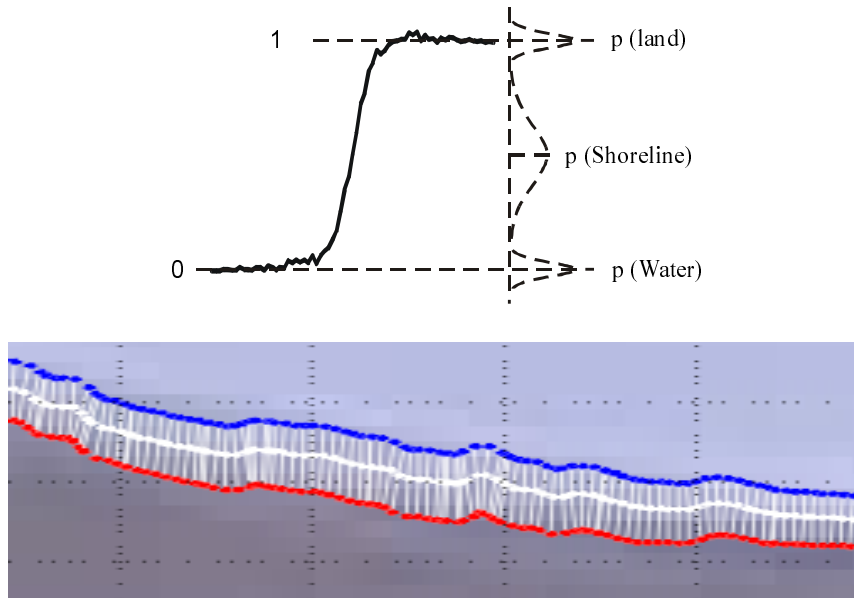


Figure E.2: *Background of ANN approach.*

- A histogram of values of y is generated. This allows the probability density function of the classified region to be inferred. The histogram will tend to contain two modes, centered on 0 and 1 corresponding to water and land values respectively.
- 5% and 95% percentiles of intermediate region of the histogram (i.e., the region that is, with high probability, not beach and not water) of y are calculated. These allow inference of the location of the shoreline threshold value (taken as the average of the 5% and 95% percentiles) and the corresponding 95% confidence intervals.
- These percentiles are then used to produce contours on y . The spread of the contours gives an indication of the confidence with which a shoreline has been identified in image parameter space
- Each point along the shoreline contour is considered and the corresponding points of the 5% and 95% confidence interval contours are identified.

E.3 Colour Channel Divergence (CCD) model

The CCD model (Turner et al., 2000; Turner & Leyden, 2000) is based upon the physical principal that ambient light from the sky is reflected by the ocean surface in a manner that is sufficiently different to distinguish it from land features. More particularly, to the naked eye the ocean usually appears blue under a wide range of light conditions, and it is this high reflectivity of light at wave lengths corresponding to the blue colors that is used within the CCD model to distinguish the waterline. The first step to applying this model is to separate color images into their individual red, green and blue components. The color of each pixel is thus defined as the triplet corresponding

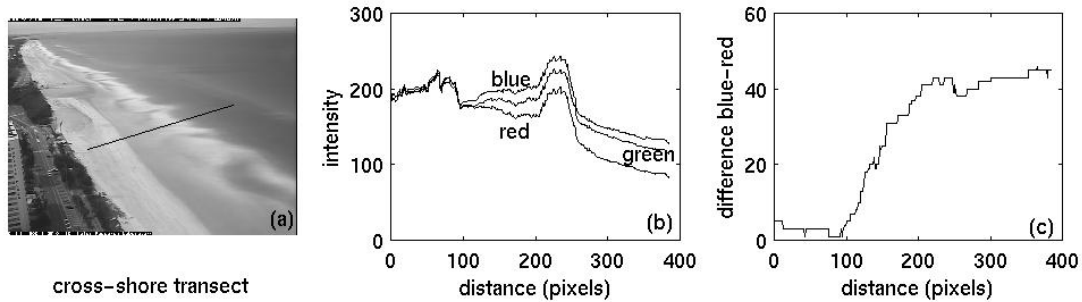


Figure E.3: *Background of CCD approach.*

to the intensity of each of the three fundamental colors. The waterline at any location alongshore can then be found by locating the point where the individual RGB color components of the image diverge, with 'ocean' pixels exhibiting higher intensity in the blue color band. To illustrate, Figure E.3a shows a typical time-exposure color image obtained from an Argus system, in this case looking north along the Gold Coast. An arbitrary cross-shore transect is indicated. In Figure E.3b the intensity of each separated color band (normalized in the range of 0 - 255) along this same transect are shown. Moving seawards, initially the intensity of each of the individual RGB color components are similar, resulting from the 'white' color of the beach. At a critical point all three separate color bands can be seen to dip, then rapidly diverge. The physical interpretation of this characteristic waterline signal is that the coincident decrease in all three color bands corresponds to the upper swash limit, with color divergence occurring at a point in the mid swash zone where the beach face is usually covered by swash during the ten-minute period during which the time-exposure image is created. Moving further seawards along the transect, the coincident maxima in all three (now diverged) color bands corresponds to the intensity maximum resulting from wave breaking in the nearshore, as detected by the SLIM model.

The detection of the waterline by the CCD model utilizes the divergence of color bands in the swash zone to define the cross-shore position of the shoreline at regular increments alongshore. Referring to Figure E.3c, the difference in intensity between the blue and red color bands is calculated, and a threshold divergence value is selected to define the waterline. This procedure is repeated at multiple shore-normal transects alongshore, to define the waterline along the entire region of interest. The particular threshold divergence value to define the waterline may be selected by calibration with available survey data; or alternatively, any value can be chosen for a particular site, which as long as this remains constant, can be used to assess the relative landward and seawards translation of the waterline.

List of Figures

1.1	The ARGUS world	5
1.2	Overview of standard ARGUS image types	6
1.3	Time series of pixel intensities sampled from Duck, camera 3	6
1.4	Example of cross-shore intensity timestack sampled from Duck, camera 3 d.d. 14/11/1997 at 17:00 GMT	7
1.5	Geo-referencing of oblique video data	8
1.6	Merged, plan-view image of Noordwijk, The Netherlands d.d. 20/10/1998 at 10:00 GMT	9
1.7	Pixel resolution maps for the five-camera configuration of Egmond station “Jan van Speyk” (May 1999)	10
2.1	Mapping intertidal beach bathymetry from video.	17
2.2	Time exposure images of Noordwijk, Netherlands.	19
2.3	Conversion of image intensities to HSV color space	20
2.4	Clustering of nearshore image intensities in hue-saturation space.	20
2.5	Filtered histogram of pixel intensities.	21
2.6	Shoreline detection on the basis of pixel intensity clustering.	21
2.7	Video-based estimates of the shoreline location at Noordwijk, Netherlands.	22
2.8	The effect of tide, wave set-up and swash on the shoreline location as observed from time-averaged video imagery.	23
2.9	Wave characteristics in the surf zone	26
2.10	Intra-wave surface elevation and flow velocity of an inner surf zone bore	27
2.11	Definition sketch inner surf zone model	27
2.12	Parameterizations of intra-wave layer thickness and flow velocity of the inner surf zone model	28
2.13	Sensitivity of lower layer flow field to tuning parameter μ	31
2.14	Calibration and validation of the inner surf zone model	32
2.15	Operational use of the inner surf zone model.	34
2.16	Assessment of IBM model accuracy on the basis of bathymetrical data	37
2.17	Overview of the Egmond data set for IBM validation	38
2.18	Assessment of IBM model accuracy against GPS-surveyed shorelines	38
2.19	Error quantification IBM per sub-model	40
2.20	Error quantification IBM overall model	41
2.21	Time exposure images of Duck NC (USA), Teignmouth (UK) and Egmond (NL)	43
2.22	Performance of shoreline detection models at Duck NC, Teignmouth and Egmond	44
2.23	Variability of the location of the filtered clusters of dry and wet pixels in the color and luminance domain	45

3.1	Video observation and model prediction of wave breaking at Palm Beach, Australia	54
3.2	Image intensity profile versus modelled wave parameter $\frac{E_T}{c^2}$	55
3.3	Quantification of subtidal beach bathymetry. Model layout	56
3.4	Example of the Gaussian fit technique to a cross-shore intensity profile at Egmond, Netherlands	59
3.5	Time series of pixel intensities during SandyDuck Experiment 1997	61
3.6	Description of individual wave breaker in BIM	62
3.7	Conceptual behaviour of BIM	63
3.8	Calibration intensity interpretation model	65
3.9	Stand-alone application of BIM to a multiple-barred beach at Egmond, The Netherlands	70
3.10	Stand-alone application of BIM to a single-barred beach at Duck, NC (USA) . .	73
3.11	Definition sketch of the model to map subtidal bathymetry	74
3.12	Operation of the model to map subtidal beach bathymetry	76
3.13	Appearance of the damping function F_{dmp} as typically applied at Egmond, The Netherlands	77
3.14	Initial and target beach bathymetry for reference case, synthetic tests BAM . .	79
3.15	BAM behaviour reference case	81
3.16	BAM application synthetic data. Evolution of profile deviations over time. Reference case.	82
3.17	Validation of SBM against field data Egmond station Jan van Speyk	90
3.18	Sub-division of beach profile for separate evaluation of SBM performance	92
3.19	Time series of bed elevation at individual locations	96
3.20	Evolution of cumulative number of accepted images overtime, for different cross-shore arrays.	97
4.1	Situation of Egmond along the Holland coast	105
4.2	Combined plan view image of the Egmond video stations Coast3D and Jan van Speyk	106
4.3	Basic frame of reference as a tool for policy development	108
4.4	Video-observed evolution of intertidal bathymetry Egmond, June 1999 - August 2001	110
4.5	Definition sketch intertidal CSIs	112
4.6	Quantification of video-derived CSIs at Egmond	113
4.7	Video-derived morphological evolution of subtidal beach bathymetry at Egmond	115
4.8	Quantification of a barred beach profile from an arbitrary initial profile	116
4.9	Definition sketch subtidal CSIs	117
4.10	Video-derived, temporal evolution of two subtidal CSIs at Egmond	118
A.1	Radial distortion of video lenses	141
B.1	Preprocessing of raw HSV image intensities	144
B.2	Filtering-induced off-set of the location of minimum probability	144
B.3	Correction of the filtering-induced artificial off-set of the location of the saddle point of the histogram	145
B.4	Dry-wet contrast as observed from pixel clustering in color and luminance space	147
C.1	Definition sketch inner surf zone model	149

E.1	Background of SLIM approach	158
E.2	Background of ANN approach	159
E.3	Background of CCD approach	160

List of Tables

1.1	Characterization of remote sensing techniques commonly used for the monitoring of changes of coastal bathymetry. ‘+’ (‘+/-’) symbols indicate that a particular technique has been applied with good (fair) results. Empty boxes denote situations that were incorporated in the overview presented here.	4
2.1	Overview of wave conditions flume experiments by Stive (1980).	26
2.2	Overview of wave conditions flume experiments by Boers (1996).	33
2.3	Characterization of IBM model deviations. Percentage of area of interest with $ \mu_{\delta z} $ below threshold value.	40
2.4	Sensitivity of IBM model performance to variable K_{osc}	41
2.5	Characterization of hydrodynamic regime per field site.	42
2.6	Performance of each shoreline detection model, quantified by means of the <i>rms</i> value of Δz_i per site.	43
2.7	Bulk statistics (mean and standard deviation) on the overall data set of 29551 Egmond shoreline samples.	46
3.1	BIM performance for different wave characteristics. Mean and standard deviation of Δx_D and ΔA_D per breaker bar and for the entire data set.	68
3.2	BIM performance for different settings of the model parameters γ , β and p . RWS’03 refers to Ruessink et al. (2003a), BS’85 to Battjes & Stive (1985) and WMS’96 to Walstra et al. (1996).	71
3.3	BAM performance for different settings of w_E and w_A . Series A1 and A3 assume mass conservation at the bottom. This restriction does not apply to Series A2.	83
3.4	BAM performance for different hydrodynamic conditions. Stand-alone variation of A_{tide} (Series B1) and H_{rms0} (Series B2), and the combined effect (Series B3).	85
3.5	BAM performance for different morphological configurations. Systematic variation of the bar height (Series C1) and the surf zone width (Series C2).	86
3.6	Time- and profile-averaged error statistics on SBM performance along two different cross-shore arrays.	90
3.7	SBM performance along different sections of Egmond Jan van Speyk profile $y = -130$ m. Mean statistics on Δz_b and Δr_b per section, obtained from the comparison of SBM results and surveyed bathymetries at May 17, 2000 and August 28, 2000.	92

List of Symbols

Abbreviations

BIM	Breaker Intensity Model
BAM	Bathymetry Assessment Model
CSI	Coastal State Indicator
CZM	Coastal Zone Management
IBM	Intertidal Beach Mapper
MCL	Momentary Coastline
SBM	Subtidal Beach Mapper

Roman symbols

A_{br}	combined intensity contribution roller and foam to $I(x)$
A_{rol}	roller induced intensity contribution to $I(x)$
A_G	height of $G(x)$
C_s	sediment availability BAM
D	diffusion coefficient
D_c	model-computed measure of wave dissipation
$D_{c,n}$	normalized model-computed measure of wave dissipation
D_o	video-derived measure of wave dissipation
$D_{o,n}$	normalized video-derived measure of wave dissipation
D_r	roller dissipation
E	wave energy
E_r	roller energy
F_{dmp}	damping function BAM
G	Gaussian type curve of intensity
H_{rms}	root mean square wave height
H_b	maximum wave height
H_0	significant wave height
H_1	lower layer thickness inner surf zone model
H_2	bore height inner surf zone model
I	pre-processed pixel intensity profile
I_G	Gaussian approximation of I_v
I_{min}	minimum intensity along $I(x)$
I_{max}	maximum intensity along $I(x)$

I_{rol}	roller induced intensity profile
I_{v}	raw pixel intensity profile
I_0	background intensity level
K_{osc}	empirical swash coefficient
L	Walton vector [$L_1..L_1$]
L_0	deep water wave length
L_c, L_a	cross-bore/boresight size of single pixel
L_{deep}	representative deep water wave length
N_{u}	Horizontal image size (pixels)
$P_{\text{dry}}, P_{\text{wet}}$	Clusters of dry/wet pixels
Q_{b}	fraction of breaking waves
R	distance to video camera
R_{ig}	infragravity swash height
R_{ss}	sea swell swash height
$S_{\text{E}}, S_{\text{A}}$	erosional/accretional sediment flux BAM
T	wave period
T_{hist}	maximum update period SBM
T_{p}	wave peak period
T_{nl}	dimensionless non-linearity parameter
V	bore speed inner surf zone model
V_{IB}	intertidal beach volume
W_{MHWS}	high-tide beach width
W_{MLWS}	low-tide beach width
$a_1 .. a_6$	empirical coefficients inner surf zone model
c	phase velocity
c_{g}	wave group velocity
f	camera focal length
f_{red}	reduction factor persistent foam
f_{w}	friction coefficient
g	gravitational acceleration
h	water depth
h_{deep}	representative water depth at deep water
h_1, h_2	instantaneous layer thickness inner surf zone model
h_0	water depth at seaward end of SBM
i_{br}	pixel intensity signal individual breaker
k	wave number
k_1, k_2	lens distortion coefficients
m	beach slope
m_1	cross-shore intensity trend
p	hydrostatic pressure
p	calibration coefficient BIM
p_{b}	hydrostatic pressure near bottom
p_1, p_2	Polynomials discriminator function Ψ
q	calibration coefficient SBM
r	radial image coordinate

t	time
t_*	intra-wave time t/T
u, v	horizontal/vertical image coordinate
u_0, v_0	image center coordinates
v_1, v_2	horizontal particle velocity inner surf zone model
w_E, w_A	erosion/accretion parameter BAM
x	horizontal cross-shore coordinate
x_{mcl}	Momentary Coastline indicator
y	horizontal alongshore coordinate
z	vertical coordinate
x_c, y_c, z_c	camera location
z_{sl}	shoreline location derived from video
z_b	bottom elevation with respect to mean sea level
z_{sl}	beach elevation at x_{sl}
z_0	offshore water level

Greek symbols

α	wave breaking parameter
β	roller dissipation parameter
γ	wave breaking parameter
δ	camera horizontal field of view
δ	calibration parameter inner surf zone model
ΔI_{br}	intensity increase at arrival of breaker
Δt	time step
Δx_{osc}	horizontal swash zone width
Δx_{trans}	transition zone width inner
η	set-up/set-down of mean water level
ζ	swash exceedence level
η_{osc}	vertical swash excursion
η_{sl}	wave set-up at shoreline
$\bar{\theta}_0$	mean wave angle
λ	intensity decay factor after passage roller
λ_u	horizontal image scale factor
λ_v	vertical image scale factor
μ	velocity correction parameter inner surf zone model
μ_G	location of $G(x)$
ξ_o	deep water Iribarren number
ρ	fluid density
σ	camera roll
σ	wave frequency
σ_G	measure for width of $G(x)$
σ_I	standard deviation of intensity signal
τ	camera tilt

τ_b	bottom shear stress
ϕ	camera azimuth
Ψ	Discriminator function pixel intensities

Model performance indicators

$\mu_{\delta_{zd}}, \sigma_{\delta_{zd}}$	mean / standard deviation detection related errors IBM
$\mu_{\delta_{ze}}, \sigma_{\delta_{ze}}$	mean / standard deviation elevation related errors IBM
$\mu_{\delta_z}, \sigma_{\delta_z}$	mean / standard deviation overall errors IBM
$\overline{\Delta x_D}, \sigma_{\Delta x}$	mean / standard deviation of peak location error BIM
$\overline{\Delta A_D}, \sigma_{\Delta A}$	mean / standard deviation of peak area error BIM
ϵ_{rms}	<i>rms</i> value elevation errors BAM synthetic data
τ	model response time BAM synthetic data
δ_ϵ	profile adjustment ratio BAM synthetic data
$\overline{\Delta z}, \Delta z_{rms}$	mean / <i>rms</i> value of elevation errors SBM
$\overline{\Delta r}, \Delta r_{rms}$	mean / <i>rms</i> value of relative elevation errors SBM

Acknowledgements

In the Spring of 1996 Marcel Stive suggested to his first graduated MSc. student that the good interaction until then deserved an intensified continuation. That moment marks the beginning of this PhD. study. A position suited perfectly to my personal interests involving a 50% affiliation with Delft University of Technology and a 50% affiliation with WL|Delft Hydraulics was created. The research was funded from the EU-sponsored PACE and SAFE projects, under contract numbers MAS3-CT95-0002 and MAS3-CT95-0004, respectively.

The first few months of my professional life were mostly dedicated to an extensive field campaign at Noordwijk, conducted with students from Utrecht and Delft and supervised by Aart Kroon. Aart's enthusiastic (and inevitably humorous) 'field classes' on nearshore morphodynamics have given me a much better feeling for coastal processes. Thanks Aart, for your help throughout my entire PhD. Over the years, we have become very good friends, which we enthusiastically celebrate during the third weekend of November at the annual 'Smartlappenfestival' in Utrecht. I'll sing you a nice song next time. Besides, I gratefully acknowledge the collaboration with the other 'argonauts' at Utrecht University, in particular Irene van Enkevort, Susanne Quartel, Bas van Dam and (as of late) Gerben Ruessink. Many thanks for revealing to me the charm of scatter plots and offering me a quiet desk when the work needed to be done on the text of this thesis.

Back to 1997. Being a youngster involved in two EU-projects means that you get to attend six-monthly meetings at gorgeous locations all across Europe, where wise men discuss state-of-the-art research at a level that initially goes far beyond your understanding. Fortunately, Judith Bosboom was also a neophyte to the European nearshore community. Judith, I've really enjoyed our trips to these meetings and the weekend off that was often included. Thanks for opening my eyes to modern art, I trust my lessons in football (including the excursion to Real Madrid) have not been a waste of time. During the Thessaloniki meeting the idea for the inner surf zone model was inspired by Rob de Meijer's 'unrolling fire hose' interpretation of a shoreward progressing wave in the swash zone. I hope, Rob, you still recognize some of your initial ideas in the inner surf zone model presented in this thesis.

During my PhD study, I have had the chance to bring two longer-term visits to the Coastal Imaging Lab of Rob Holman. When you enter Corvallis, you see a sign saying 'Oregon State University. Open minds, Open doors'. I can't think of a better way to characterize the place. The five months total I spent at OSU turned out to be very productive. In fact, it was John 'I-know-where-your-data-lives' Stanley (also CEO of Obnoxious Enterprises) who suggested the use of HSV color information for shoreline detection. Without Rob's support on the use of the SandyDuck timestacks, no BIM would ever have been developed. The time spent in Oregon outside work was just as enjoying: tailgating on Saturday morning for a Beavers football game, a three-day trip to California with Graham Symonds, running the stairs of Reser stadium with Rob, playing tennis with the one and only 'slum-lady' Ann Morey, early-day fishing with her husband Dana Ross, watching the Portland Trailblazers with Ken Kingston and

Howard 'Speedy' Southgate (by the way, what's the capital of Montana?) and weekend skiing on Mount Hood with Joep Halters who happened to be in the neighborhood (well, Austin, Texas). Needless to say that 'Tex' had to see a rodeo every week. Thanks Rob, Kathy, John and all the other OSU folks, for your hospitality, collaboration and the Friday nights at the Bombs Away. Couldn't have been better.

After two and a half years, the EU-funding ended but the work was not done yet. At that point, the research became part of the Delft Interfaculty Research Centre for 'Observation of the Earth and Earth's crust' (DIOC), supported by Delft University of Technology and headed by Prof. Roland Klees. Thank you Roland, for actively reminding me of getting the job done and funding an additional few months for writing this thesis. From 1998 onward, the work was co-funded by the Ministry of Public Works Rijkswaterstaat, Delft Cluster Project Coasts 03.01.03 and WL|Delft Hydraulics. I am indebted to Sander Hoogewoning and Arno de Kruif for stimulating the ongoing development and operationalization of ARGUS analysis tools, and for their efforts to achieve a sound embedding of ARGUS within the Rijkswaterstaat organization.

The Delft Cluster project and the VOP research framework with Rijkswaterstaat had a clear focus on the evaluation of a combined beach and shoreface nourishment in Egmond. Inspired by Dano Roelvink, this focus has initiated the birth of the BAM concept. Thanks Dano, for actively stimulating these developments and for occasionally reminding me to work towards the final result rather than losing myself in a myriad of interesting details along the road. The input of Gerben Ruessink, who joined WL|Delft Hydraulics in 2000, has been of major importance for the development of SBM and the completion of this thesis. Thanks a lot Gerben, for your guidance, daily assistance and successful attempt to reduce the size of my earliest manuscript by at least 40%. Even though I would have gladly involved you in the committee as my co-promotor, formal rules were to prevail. You nonetheless have fulfilled that role in an informal but enthusiastic manner.

Another characteristic of the ARGUS community that fits well with the nature of this PhD candidate is the intensive interaction and collaboration with ARGUS co-researchers across the world. Besides students – I gratefully acknowledge Pieter Janssen, Jan-Kees van Noort, Mark Caljouw, Thomas Dronkers, Leann Nipius, Paul de Groot and Anna Cohen who all contributed to the development of ARGUS over the last few years – I'd like to mention a few very special colleagues from abroad, in particular Nathaniel Plant, Ian Turner and Ken Kingston. Thanks Nathaniel, for providing the core routines this thesis (and other peoples work!) is based on and assisting on the data analysis for the model comparison study. Thanks Ian, for your massive contribution to getting my very first paper out in Coastal Engineering. Thanks Ken, for your ongoing contribution to the ARGUS Runtime Environment, which has definitely improved the robustness of the techniques developed in my research. I gratefully acknowledge all three of you (including Sheila, Susan and all the kids) for your hospitality during trips to Waveland, Sydney and Plymouth, and for showing me a glimpse of young parenthood. Yes, I certainly do owe all of you a beer.

Marcel Stive provided constant support during my entire study period. Marcel, I consider it a privilege to have had the chance to work with you for eight years now. Thanks a lot for your guidance, constructive comments, flexibility, pleasant company

at many trips abroad and continuous trust in what we're doing ("Marcel, Dirk-Jan and I like to head for the hotel, cause we have our presentation tomorrow". "Don't worry guys, you're naturals"). The way you've introduced me to the scientific coastal community is invaluable. I also acknowledge all members of my PhD committee. The work has definitely benefited from our discussions and your review of the draft version of this thesis. I consider it an honor, Jurjen, to become your first scientific grandson.

Besides the research itself, professional enjoyment is essentially governed by the people you work with every day. I give my hearty thanks to all of my colleagues at Delft University and WL | Delft Hydraulics, particularly the ARGUS group (Irv Elshoff, Kathelijne Wijnberg, Mark van Koningsveld, Robin Morelissen, Cynthia Reintjes, Thijs van Kessel and Dano Roelvink). We're not done yet with ARGUS! Irv, you have been involved with ARGUS from the very first day I entered De Voorst. With your indefatigable dedication, fondness for state-of-the-art technology and high quality working standards, you've brought the system to the level where we are today. I admire your perseverance during ARGUS field installations, when creativity is needed to get the images coming in. Thanks a lot for your major input over the years, the open communication and your 24-hours-a-day willingness to help. Special thanks also to Bert Jagers, whose indispensable assistance on troubleshooting at a few crucial moments throughout my research is gratefully acknowledged.

Obviously, all colleagues are special, but some are more special than others. The most special ones are the guys you share an office with for more than five years, while becoming very good friends. Dirk-Jan Walstra and Mark van Koningsveld, I truly appreciate the interaction, collaboration and escalation of nonsense we experienced over the years. I realize it's superfluous to describe the atmosphere in ZS115, since Van Koningsveld (2003) previously gave a detailed outline of that (cheers Mark, here's the first official reference to your thesis). Still, I trust Mark's listing of 'silly stuff' will continue to expand in the future. Following the long-standing tradition of our room, I feel highly honored having you guys as my 'paranymphen'.

Getuige onze telefoonrekening speelt de familie een belangrijke rol in ons leven. Beste pa & ma, Ivo & Anke, Miran & Wieger: Na de entree van Wieger en de trouwdag van Ivo & Anke wordt dit alweer onze derde heugelijke gebeurtenis dit jaar. Er was wat doorzettingsvermogen voor nodig, ik hoef jullie niet uit te leggen waar ik die van mee heb gekregen. Bedankt voor alle steun! Beste Cor & Ineke, Arjan & Anouk: Goed voorbeeld doet volgen, bij deze sluit ik me aan in de rij der doctoren. Ik prijs me gelukkig dat ik na Deurningen ook in Denekamp een hecht nest heb gevonden. Tot slot: Lieve Saskia, jarenlang was mijn proefschrift 'bijna af', nu is het ook echt zo ver. Dankjewel voor je liefdevolle geduld, aandacht en stimulans al die tijd (en oh ja, niet te vergeten de catering). Vanaf nu alleen nog maar leuke dingen in de weekends! Zou me niet verbazen, Sas, als je binnenkort weer snakt naar een paar Independence Days.

Stefan Aarninkhof
Delft, October 2003

Curriculum Vitae

Stefan Aarninkhof werd geboren op 1 augustus 1972 in het Twentse Hengelo, om na ruim een week te verhuizen naar Deurningen waar hij de eerste 18 jaar van z'n leven zou doorbrengen. Van 1984 tot 1990 doorliep hij het VWO aan Lyceum De Grundel in Hengelo. In de voetsporen van z'n vader koos hij vervolgens voor de opleiding Civiele Techniek, en wel aan de Technische Universiteit Delft. Op 19 april 1996 studeerde hij onder begeleiding van prof.dr.ir. Marcel Stive, prof.dr.ir. Jurjen Battjes en dr.ir. Dano Roelvink met lof af bij de sectie Waterbouwkunde. Het afstudeeronderwerp getiteld 'Optische Waarneming van Brekerbanken' zou de opmaat blijken voor z'n promotiewerk.

Van 1996 tot 2002 had hij een deeltijd-aanstelling als Toegevoegd Onderzoeker bij de sectie Waterbouwkunde van de Faculteit Civiele Techniek en Geowetenschappen aan de Technische Universiteit Delft. Begeleid door prof.dr.ir. Marcel Stive, dr. Gerben Ruessink en dr.ir. Dano Roelvink werkte hij aan de ontwikkeling van technieken om de morfologie van de brandingszone af te leiden uit tijdgemiddelde video waarnemingen. Dit onderzoek is beschreven in dit proefschrift.

Vanaf 1 juni 1996 is hij als onderzoeker-adviseur in deeltijd werkzaam geweest bij de afdeling Marine & Coastal Management van WL|Delft Hydraulics. Dit dienstverband is per 1 november 2002 omgezet in de huidige voltijdsaanstelling.